FLORIDA INTERNATIONAL UNIVERSITY

Miami, Florida

LOW-RISE IRREGULAR SHAPED BUILDINGS

A dissertation submitted in partial fulfillment of

the requirements for the degree of

DOCTOR OF PHILOSOPHY

in

CIVIL ENGINEERING

by

Manuel A. Matus

2023

To: Interim Dean Ines Triay
College of Engineering and Computing

This dissertation, written by Manuel A. Matus, and entitled Low-rise Irregular Shaped Buildings, having been approved in respect to style and intellectual content, is referred to you for judgment.

We have read this dissertation and recommend that it be approved.

Arindam Gan Chowdhury

Amal Elawady

Nipesh Pradhananga

Ioannis Zisis, Major Professor

Date of Defense: November 1, 2023

The dissertation of Manuel A. Matus is approved.

Interim Dean Ines Triay
College of Engineering and Computing

Andrés G. Gil
Vice President for Research and Economic Development
And Dean of the University Graduate School

Florida International University, 2023

ACKNOWLEDGMENTS

I wish to begin by expressing my heartfelt appreciation to my major professor, Dr. Ioannis Zisis, for his unwavering guidance, encouragement, trust, remarkable patience, and steadfast support throughout my academic journey. I am deeply grateful for his trust in me when he hired me as an undergraduate student. I can never adequately convey my gratitude for the countless opportunities he provided me. Furthermore, I am immensely thankful for the chance to participate in multiple research projects that extended beyond my initial scope of work. Having Dr. Zisis as my advisor allowed me to witness his unwavering dedication, humility, and genuine concern for his students, as he consistently made himself available to address any queries.

In addition, I extend my gratitude to Dr. Arindam Gan Chowdhury for his invaluable support and guidance during my studies, as well as his patience. I would also like to express my appreciation to Dr. Amal Elawady and Dr. Nipesh Pradhananga for their cooperation and tremendous support throughout my dissertation work.

I am indebted to my colleagues at the Wall of Wind Experimental Facility (WOW-EF), namely Walter Conklin, James Erwin, and Roy-Liu Marquez, for the wonderful moments we shared, their assistance, guidance, laughter, and unwavering support.

To my dear friends, Dr. Ziad Azzi, Dr. Krishna Sai Vutukuru, Dr. Johnny Estephan, Dr. Karim Mustafa, Dr. Hrishikesh Dev Sarma, and Dr. Sudip Subedi, I extend my sincerest gratitude for the years we spent together during our studies and for the enduring friendships we formed. Your words of encouragement were a source of great strength and made my journey considerably more manageable. I would like to acknowledge my friends Dr. Karim Mustafa and Dr. Hrishikesh Dev Sarma, as the three of us worked endlessly to

design and build the small wind tunnel used during this investigation.

I would like to offer a special acknowledgment to Dr. Maryam Refan and Jason Gkountis, both of whom made a significant impact on me. I will always cherish our meaningful conversations during their time at the WOW-EF.

I would like to extend my deepest gratitude to my beloved wife, Zarahi Prieto Arteaga. Her extraordinary patience, boundless love, profound understanding, unwavering support, and constant encouragement served as the cornerstone of my strength, enabling me to persevere on this remarkable journey.

Finally, my heartfelt thanks go to my mother, Albertina Contreras Aranguiz as well as my two brothers, Sergio Matus and Mirko Matus, for their love and unwavering support throughout my journey, despite being far from home.

ABSTRACT OF THE DISSERTATION

LOW-RISE IRREGULAR SHAPED BUILDINGS

by

Manuel A. Matus

Florida International University, 2023

Miami, Florida

Professor Ioannis Zisis, Major Professor

The United States has faced significant economic and human losses due to various natural disasters (including extreme wind events), with these calamities causing nearly $1,359 billion in economic losses and claiming the lives of 6,890 individuals. Coastal regions in the United States, despite occupying only 10% of the nation's land area, are especially vulnerable to the devastating impact of hurricanes and are home to 40% of the U.S. population. The American landscape has approximately 111 million buildings, with single-family homes representing the majority at 89.7% of the total count, and low-rise residential buildings make up 70% of the entire constructed environment. As architectural designs evolve towards more intricate and non-standard shapes, there is a growing need for further research focused on low-rise structures with irregular configurations. To address this need, comprehensive wind tunnel testing was carried out at Florida International University's Wall of Wind (WOW) Experimental Facility, using realistic models inspired by diverse low-rise building designs found in South Florida, including shapes like T, L, C, and S. These tests revealed that low-rise buildings with irregular floor plans exhibit distinct mean pressure distributions on roof and wall sections, different from those of rectangular

buildings. In cases where separated flow occurs, the re-entrant flow re-attaches to the downwind windward wall, leading to significant changes in stagnation point location and the development of turbulent air recirculation. Some side walls (under the effect of turbulent recirculating flows) experience notable decreases in suction pressures, transitioning from positive values near the 90-degree joint to negative values near the upwind edge. Irregularly shaped buildings tended to generate higher positive critical pressure coefficients on roof sections and generally experienced reduced development of negative critical pressure coefficients on some areas of roof sections compared to rectangular buildings. While suction pressure coefficients on roof sections aligned relatively well with current wind provisions, with some exceptions, it was consistently observed that the walls of buildings with irregular shapes exceeded the positive and negative pressure coefficient limits specified in the existing wind provision design guidelines making such structures more prone to damage.

TABLE OF CONTENTS

CHAPTER PAGE

LIST OF TABLES

TABLE PAGE

LIST OF FIGURES

FIGURE PAGE

1. INTRODUCTION

The United States has experienced significant economic and human losses due to various natural disasters. The combined impact of these events has resulted in staggering economic losses of approximately 2,575.7 billion dollars and tragically claimed the lives of 15,958 individuals, between 1980 and 2023. Among all the natural disasters, Tropical Cyclones, commonly known as hurricanes, stand out as the most devastating natural disaster, contributing to a substantial portion of the economic losses and human casualties, amounting to 1,359 billion dollars and 6,890 deaths respectively (Smith et al., 2020, NOAA 2023).

Hurricanes are particularly known for their severe impact on coastal regions worldwide, and in the United States, the East and Southeast coasts are especially susceptible to such extreme wind events (FEMA - Figure 1). Notably, even though coastal areas only account for 10% of the total land mass in the country, they accommodate 40% of the US population, making such areas vulnerable "hazardous hotspots" (NOAA 2013, Iglesias et al., 2021, Zulian 2022, Wilson et al., 2010).

The surge in population in US coastal cities has led to a substantial increase in housing units, rising from 16.1 million to 49.4 million between 1960 and 2010, representing 39% of the total housing in the country (Wilson et al., 2010, NOAA 2013). This rapid urbanization and expansion in coastal areas have further exacerbated the risk and potential impact of natural disasters, making it crucial to implement effective mitigation and preparedness measures to protect both lives and property.

The United States boasts a vast array of approximately 111 million buildings, each category contributing to the nation's diverse landscape. Commercial buildings account for 5.2%, symbolizing the thriving business hubs; industrial structures represent 0.3%,

signifying centers of industrial prowess; multifamily residential buildings make up 4.5%, creating communal living spaces, and the largest segment is single-family homes, encompassing a substantial 89.7% of all buildings. The preference for single-family living extends to approximately 75% of households, inclusive of manufactured homes, reflecting the American dream of owning a private dwelling.

In exploring the architectural heights, the data reveals that one-story residential buildings encompass 32.9% of the US housing units, catering to accessibility and convenience. Simultaneously, two-story residential buildings claim approximately 36.4% of the US housing units, striking a balance between space and functionality. Together, these low-rise residential structures harmoniously compose a remarkable 70% of the entire US built-up environment, showcasing the nation's affinity for cozy living spaces.

Delving further into the dimensions of these abodes, most single-family homes boast generous spaces ranging from 1000 to 2500 square feet, accommodating the aspirations and comforts of families. In contrast, multifamily homes are designed with a more efficient use of space, typically ranging from 500 to 1,500 square feet, offering a suitable solution for those seeking compact yet functional living arrangements (Potter 2020, Fu et al., 2012, Reyna et al., 2022). This fascinating interplay of building sizes underscores the versatility of the American housing landscape.

To mitigate the impacts of devastating hazards caused by extreme wind events, researchers have delved into the realm of civil infrastructure. Through meticulous wind tunnel testing encompassing a wide array of structures, structure components, materials, and more, researchers have sought to better comprehend the effects of such forces on structures and the built environment. The invaluable knowledge attained from these

investigations has paved the way for the formulation of essential building codes and wind provisions, meticulously designed to ensure the safe construction of structures, minimize wind-induced damages, and fortify the resiliency of the built environment. Thus, enhancing the ability of structures to withstand the forces of nature and safeguarding the communities that thrive within it.

In both the US and around the globe, the design and construction of structures are influenced by a multitude of factors. These factors encompass changes in societal norms, political landscapes, technological advancements, and the ever-evolving body of knowledge, among others. Over time, the significance of these factors may fluctuate, leading to varying degrees of impact on the way structures are built. As a result, the dynamic interplay of these elements can significantly shape the approach to construction practices and design principles over the years. Additionally, a great emphasis on maintaining the harmony between structures and the surrounding environment plays a key role in the overall structure's shapes (Friedman 1995, Jacobs 2006, Konior 2022, Lehman 2011, and Bassas et al., 2020).

In the modern urban landscape, an evident trend has emerged where buildings have embraced elaborate and diverse shapes, moving away significantly from the conventional square and rectangular designs. This shift is particularly pronounced in the increasing prevalence of tall and super-tall structures. As a result of these intricate architectural forms, extensive research has been conducted to comprehend the effects of wind-induced loads on buildings with irregular shapes. A multitude of investigations (Irwin 2009, Xie 2014, Kim et al., 2014, Kim et al., 2015, Zhang et al., 2020, Tamura et al., 2017, Xie 2012, Nagar et al., 2020, Xu et al., 2017, Yi et al., 2015, Sharma et al., 2018, Kourakis 2005, Rajdip et

al., 2016, Daemei et al., 2019, Yan et al., 2016, Wang et al., 2023, Gomez et al., 2005, Mashalkar et al., 2015, Souvik et al., 2014, Yi et al., 2016, Yi et al., 2017, Yi et al., 2020, Zhao et al., 2017, and Rajabi et al., 2022) have been carried out to explore the complex aerodynamic performance of mid- and high-rise structures characterized by such intricate shapes. These studies aim to gain a comprehensive understanding of how these irregularly shaped buildings respond to wind-induced forces. However, it is worth noting that there is a limited number of investigations focusing on low-rise structures with irregular shape plans, leading to a gap in knowledge and understanding regarding the performance of such buildings (Lee et al., 2016, Paterson et al., 1992, Stathopoulos et al., 1993, Zhang et al., 2014, Parackal et al., 2016, Shao et al., 2019, Uematsu et al., 2022, Verma et al., 2022, Sharma et al., 2023 and Sarma et al., 2023, Shao et al., 2019).

The current wind provisions, providing valuable design guidance for low-rise buildings, were established through wind tunnel experiments conducted on simplified regular-shaped models (such as square and rectangular) nearly five decades ago (Akins et al., 1977, Davenport et al., 1977, and Stathopoulos, 1979). More recent studies by the National Institute of Standards and Technology (NIST) and Tokyo Polytechnic University (TPU) have addressed this issue by conducting research on low-rise structures and developing aerodynamic databases specifically tailored for designing such buildings. These databases are valuable resources made available to the public. However, it is essential to recognize that these recent studies were also limited to idealized models with regular plans (Ho et al., 2005, NIST 2004, Tamura et al., 2005, Tamura 2012).

In light of the advancements in wind engineering and the evolving architectural landscape, there remains a need for further research focusing on low-rise buildings with

irregular shapes (herein referred to as: irregular shaped buildings, buildings with irregular shape, irregularly shaped buildings, buildings with irregular plans, buildings with complex shapes, buildings with intricate shapes, non-regular buildings, etc.). By conducting comprehensive studies that encompass a broader range of architectural designs, we can enhance our understanding and improve the safety and performance of low-rise structures in diverse and dynamic environments. Such endeavors will contribute significantly to the continual improvement and innovation in the design practices of low-rise buildings with complex shapes. Addressing this knowledge gap in research and updating design guidelines to account for the complexities of irregularly shaped low-rise buildings is crucial in ensuring their structural integrity and safety in today's rapidly evolving built environment. By conducting further studies and incorporating the latest advancements in wind engineering, we can enhance our ability to create resilient and sustainable structures that meet the challenges of the modern architectural landscape.

To evaluate the performance of low-rise buildings characterized by irregular shapes, large-scale (1 to 50 scale) and small-scale (1 to 100 scale) wind tunnel testing was conducted on a range of intricate models at the Wall of Wind (WOW) Experimental Facility (EF), situated at Florida International University (FIU) in Miami, Florida. To design the models for testing, the initial and crucial step involved conducting an extensive survey using satellite images obtained from residential areas in South Florida (Figure 2). These high-resolution satellite images offered a detailed and comprehensive perspective of the diverse low-rise buildings that adorned the region, effectively capturing a wide variety of architectural forms and intricate designs. The data collected from this survey formed the foundation for creating realistic and representative models that accurately simulated the

complexities of real-world low-rise structures with irregular shapes (Ahmed et al., 2016, Ahmed et al., 2023). The survey yielded invaluable insights into the prevailing shapes commonly found in the field, revealing that the most typical forms included T-, L-, C-, and S-shapes. From these identified shapes, multiple models were developed which varied in aspect ratios and roof end configuration (e.g., gable vs. hip roof ends). A total of 22 models with irregular shape plans were investigated by instrumenting each model with 300+ pressure taps distributed on all walls and roof sections to obtain the pressure distribution under wind induced loading.

The data acquired from all models was utilized to generate contour plots for both mean and peak pressure coefficients (Cp). These plots offered insights into the comprehensive pressure distribution on the wall and roof sections, contingent upon the direction of the wind. Moreover, the overall critical peak pressure coefficients were assessed, drawing valuable insights into how building shape irregularities influenced the development of these peak pressure coefficients. Furthermore, a comparison between the experimental data gathered from wind tunnel testing and the current wind provisions specified for components and cladding in low-rise buildings, as outlined in ASCE 7-22 – C&C, was carried out. This analysis aimed to evaluate the suitability of these minimum design guidelines for structures with irregular shapes. Additionally, smoke visualization tests were performed during these experiments, supplying valuable visual data regarding the interaction and development of mixed flows.

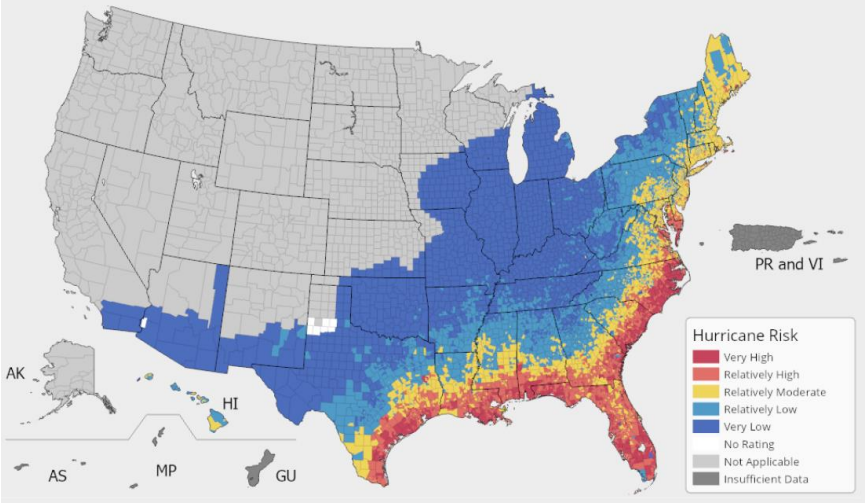

Figure 1. FEMA hurricane risk index map

Figure 2. Satellite image – South Florida residential area, 08/03/2023, Google Maps.

2. LITERATURE REVIEW

Buildings with intricate shapes have become popular as advancements in technology in multiple fields (e.g., architecture, materials, construction techniques, etc.) have emerged. A great number of such structures can be observed in the famous tall and super-tall buildings like Burj Khalifa, Taipei 101, Petronas Towers, among others. Current wind provisions provide guidance for the design of structures with intricate shapes, and most importantly, wind tunnel testing is highly encouraged as complex shapes portray a challenge when obtaining accurate design values. Wind tunnel testing can be a valuable

tool for understanding and mitigating wind-induced loads and vibrations, ensuring the safety and reliability of structures in challenging wind environments. In fact, the American Society of Civil Engineers (ASCE) recommends the utilization of wind tunnel testing in various scenarios:

1) Wind tunnel testing is deemed prudent when the architectural design of a building or structure possesses intricate or irregular shapes that elude comprehensive analysis through simplified analytical methods. This applies especially when the structure significantly departs from conventional shapes and configurations.

2) Tall structures, typically exceeding 500 feet in height, frequently necessitate wind tunnel testing as a mandatory step. This is imperative to evaluate wind-induced loads, pressures, and dynamic responses, given that these lofty edifices are more vulnerable to wind-induced vibrations and dynamic behaviors.

3) When architectural designs feature inventive elements, non-standard components, or unconventional architectural characteristics, the accurate comprehension of aerodynamic behavior and wind loads on the structure may mandate the inclusion of wind tunnel testing.

4) Structures sensitive to wind effects, such as expansive bridges, stadium roofs, and slender towers, might require wind tunnel testing to scrutinize their stability, dynamic reactions, and wind-induced forces comprehensively.

5) In geographical areas prone to elevated wind velocities, it is often advisable to incorporate wind tunnel testing as an integral component of the structural design process. This step ensures the safety and stability of the structure under conditions of extreme wind.

6) In situations where the primary aim is to formulate strategies for mitigating wind-related issues or to fine-tune the design of elements vulnerable to wind effects (e.g., cladding, rooftop equipment), the integration of wind tunnel testing can supply invaluable data for realizing these objectives.

In specific instances, local building codes and standards may dictate the necessity of wind tunnel testing for particular structure types, heights, or locations. This requirement ensures adherence to safety and performance criteria.

Numerous inquiries have been undertaken to gain deeper insights into structures with intricate configurations. Nevertheless, these investigations have predominantly concentrated on medium to tall buildings (Gomez et al., 2005; Mashalkar et al., 2015; Souvik et al., 2014; Yi et al., 2017; Zhao et al., 2017; Rajdip et al., 2016; Rajabi et al., 2022). For instance, Gomez et al. (2005) scrutinized the overall pressure distribution on 100-meter-tall structures with L- and C-shapes at a 1:100 scale (see Figure 3). Their findings revealed a complex pattern of pressures around the various wall sections, diverging from those obtained from the conventional square model. Similarly, other researchers, including Mashalkar et al. (2015), investigated structures with C-, I-, L-, and T-shape, ultimately affirming the critical role of structural form in withstanding wind forces. Souvik et al. (2014) explored pressure distribution on a building shaped like a "+" (see Figure 4) and highlighted substantial alterations in pressure distribution when compared to a rectangular model, particularly in response to varying wind directions. This indicated a significant dependency on the interaction between the protruding sections.

Yi et al. conducted multiple studies (2016, 2017, 2023) that delved into the impact of building shape on overall pressure distribution. Their investigations focused on an L-shaped building at a scale of 1 to 500, revealing notable variations in pressure distribution

at the corners of L-shaped structures. While these studies concentrated on medium to tall buildings, they offered valuable insights into the intricacies of buildings with unconventional shapes and the associated uncertainties in their safe design.

Comparatively fewer studies have explored the performance of low-rise buildings, and only a limited number have specifically addressed low-rise structures with irregular floor plans, and some have stated that determining the wind loads on low-rise buildings is more complex than tall buildings due to the variety of geometrical configurations found on the field (Stathopoulos 1982). For instance, Stathopoulos et al. (1993) examined airflow around buildings with L-shaped floor plans using computational modeling (see Figure 5). The study identified intricate recirculating flows on the windward and leeward sides, especially at cornering angles, underscoring the limitations of computational models in accurately predicting flow interactions. It is important to note that the computational model did yield valuable insights into other aspects of building walls and roof sections.

Parackal et al. (2016) conducted an investigation to assess wind-induced pressures on 1- and 2-story buildings with complex configurations (see Figure 6). This study noted that the design pressures specified in the Australian wind loading standards (AS 4055 and AS/NZS 1170.2) were based on wind tunnel studies conducted between 1970 and 1990 using simplified models with regular floor plans. The results of this investigation showed that the roof sections experienced higher suction forces near the edges and ridgelines, attributed to flow separation and vortex formation. Interestingly, when compared to the wind loading standards, the results were found to be conservative for one of the wind standards but inadequate for the other. However, both wind standards provided acceptable design loads for wall cladding in 1- and 2-story buildings, according to the author.

Shao et al. (2018, 2019) carried out an extensive examination of models with T- and L-shaped floor plans (see Figure 7). The research investigated two L-shaped and three T-shaped models, making this one of the few studies that specifically examined the impact of low-rise irregular building plans on overall pressure distribution against U.S. current wind provisions. Their findings revealed the development of substantial suctions at the roof eaves near re-entrant corners, as well as significant positive and negative pressures on the side walls near re-entrant corners when subjected to oblique wind directions. Additionally, they attributed wind load distributions on such buildings to wind separation from leading edges and the presence of upwind or downwind roof blocks. This investigation also evaluated the design guidelines provided by ASCE 7-10, concluding that the provided GCp (in ASCE 7-10) values were sufficient for designing T- and L-shaped buildings. However, they found that for ASCE 7-10 roof zone 2 was inadequate and loads were underestimated when compared to the experimental values.

Given the scarcity of research on low-rise structures featuring irregular floor plans, it became evident that conducting further studies on this subject is of utmost significance. These additional investigations are essential for gaining a deeper comprehension of how such structures perform when subjected to wind-induced forces. Expanding the body of research in this area would serve to bridge the existing knowledge gap related to low-rise residential buildings with complex shapes, ultimately facilitating the reduction of damage and enhancing their resilience in the face of extreme wind events.

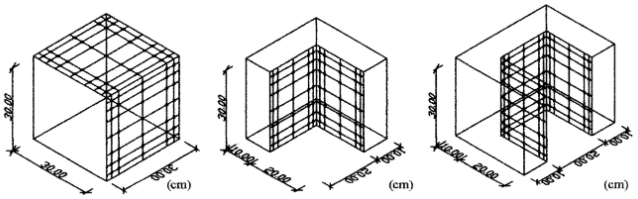

Figure 3. Buildings studied by Gomez et al., 2005.

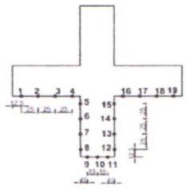

Figure 4. Building studied by Souvik et al., 2014.

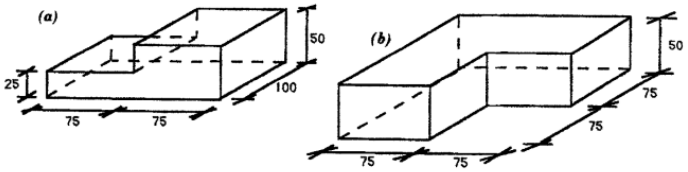

Figure 5. Building studied by Stathopoulos et al., 1993.

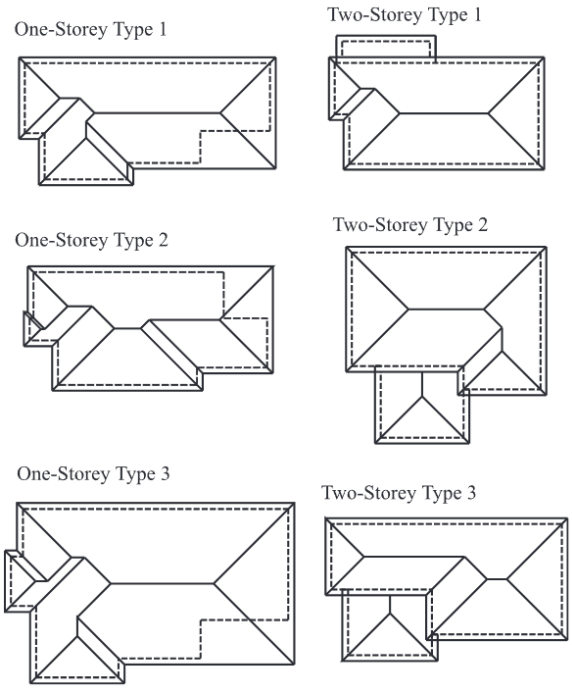

Figure 6. Buildings studied by Parackal et al., 2016.

Experimental configurations: Building dimensions, pressure tap layout and wind direction (θ).

Model	Plan	H (m)	L (m)	W (m)	l_1 (m)	l_2 (m)	w (m)
RG	Rectangular	5	20	10	5	–	–
RH1			15	10	7.5	5	–
RH2			20	10	7.5	5	–
LH1	L-shaped		17.5	17.5	7.5	10	10
LH2			17.5	22.5	7.5	10	10
TH1	T-shaped		25	17.5	7.5	10	10
TH2			30	17.5	7.5	10	10
TH3			25	22.5	7.5	10	10

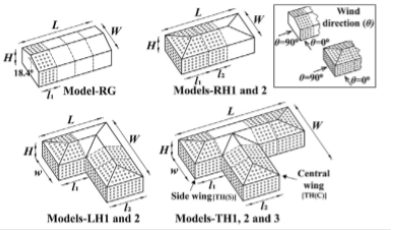

Figure 7. Buildings studied by Shao et al., 2018 and 2019.

3. SATELLITE IMAGERY

The built environment encompasses a diverse array of residential and commercial structures, with residential areas representing the predominant portion of the civil engineered landscape. In the United States, an astounding 70% of all structures fall within the category of low-rise residential buildings. The continuous evolution of factors such as political, technological, societal, and economic changes has left a profound impact on the design of structures. This evolution has led to the creation of buildings with intricate and distinctive shapes, presenting challenges in the design process that are both complex and counterintuitive.

To comprehensively assess the performance of low-rise structures with such complex shapes, it was imperative to identify the most common shapes that encompass the wide spectrum of variations found in real-world scenarios. To achieve this, an extensive survey of satellite aerial photographs from residential areas in South Florida was conducted. Thousands of satellite images were collected from these areas and meticulously analyzed. Each aerial image was examined using an online tool developed by Russell et al. in 2007, which facilitated the labeling of structures with different shapes, including T-, L-, C-, and R-shapes. Moreover, dimensional information from the images was obtained, and all relevant data related to the labeled buildings were saved into an XML text file to be

utilized as input for a Rapid Convolutional Neural Network algorithm developed by Ahmed et al. in 2016 and 2023.

The survey yielded insightful findings, revealing that T-, L-, and C-shapes were among the most adopted shapes by low-rise structures. Furthermore, the aspect ratios of these identified shapes exhibited considerable variation. To assess the impact of varying aspect ratios on these complex shapes, measures from multiple wall sections were diligently obtained and recorded. These measurements played a pivotal role in the design process of the subsequent test models. Additionally, the square footage of the models was considered to ensure that the test models closely resembled real low-rise residential buildings, contributing to the validity and accuracy of the research.

Through this rigorous survey and analysis, valuable insights were garnered into the prevalent shapes of low-rise buildings, shedding light on the dynamic interplay of factors that influence their design.

4. LARGE SCALE TESTING

4.1. MODELS

Based on the results obtained from the satellite imagery survey, a series of eleven models (1 to 50 scale) were meticulously designed to be tested at the Wall of Wind Experimental Facility (WOW-EF), with ten representing large-scale irregular-shaped structures, and one serving as a regular-shaped benchmark for comparison and validation. The aim was to explore the impact of shape variations within the same floor plan on overall pressure distributions. To achieve this, three models were crafted to represent T-shaped structures, three for L-shaped structures, and four for structures with C-shape. Having multiple models for each shape allowed for the "exaggeration" of aspect ratios, yielding

clearer insights into the effects of shape variations, and capturing the diversity of aspect ratios found in real-world structures. It must be noted that four of the ten models possessed flat roofs to see the effect of irregular shape plans on different roof types.

The rectangular model, identified as the regular shape model, was designed and constructed to serve as a reference for comparison and to validate the findings from the irregular-shaped models. All models were fabricated with 3/8-inch-thick laser-cut-plexiglass sections and instrumented with pressure-taps throughout their surfaces, including walls and roof sections, to record the overall wind-induced pressures. The total number of pressure-taps for each gable-roof model were 362, 346, 360, 344, 374, 378 and 354 for models $T1_{gable}$, $T2_{gable}$, $L1_{gable}$, $L2_{gable}$, $C1_{gable}$, $C2_{gable}$ and $R1_{gable}$, respectively. The total number of pressure-taps for each flat-roof model were 362, 362, 364 and 374 for models $T1_{flat}$, $L1_{flat}$, $C1_{flat}$ and $C2_{flat}$.

The dimensions for all models, presented in Figure 8 to Figure 17, are provided in inches at a scale of 1 to 50. The square footage (full-scale) for each model was as follows: T1 - 1465 square feet, T2 - 1221 square feet, L1 - 1465 square feet, L2 - 1221 square feet, C1 - 1465 square feet, C2 - 1709 square feet, and R1 - 1953 square feet. This comprehensive approach to model design and instrumentation allowed for a detailed investigation of the aerodynamic performance of these structures with intricate shapes, shedding light on their behavior under wind-induced loads and the effects of various aspect ratios on pressure distributions.

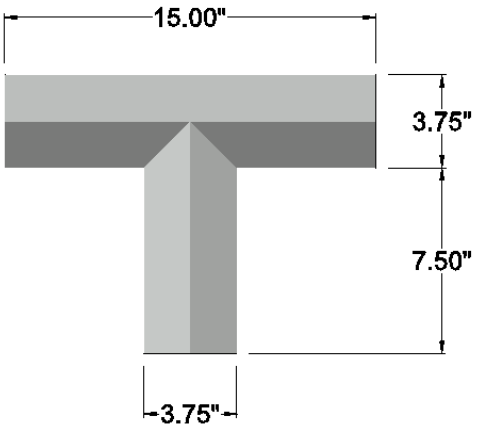

Figure 8. Model $T1_{gable\&flat}$ dimensions - top view

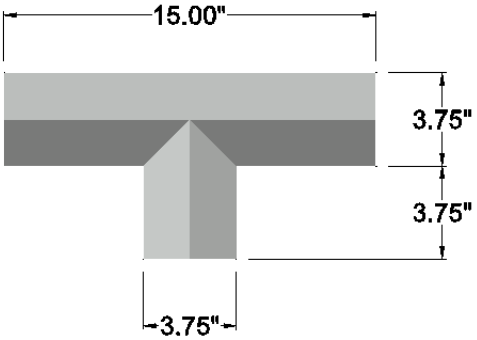

Figure 9. Model $T2_{gable}$ dimensions - top view

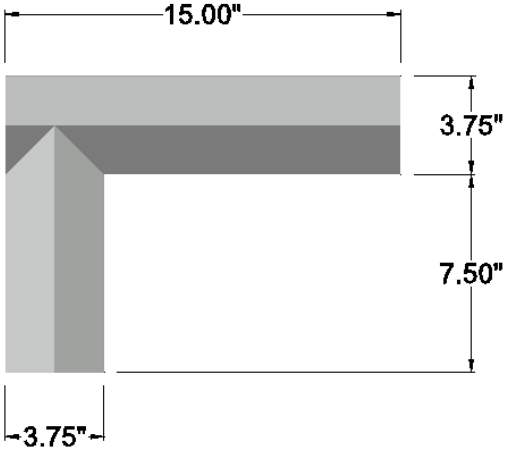

Figure 10. Model $L1_{gable\&flat}$ dimensions - top view

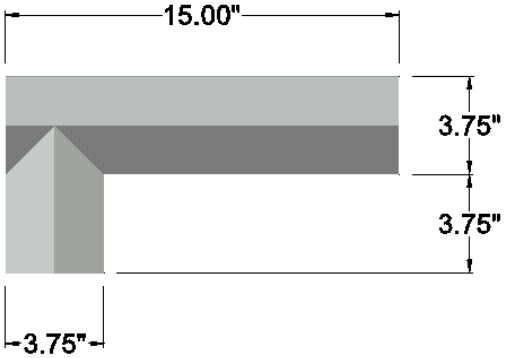

Figure 11. Model $L2_{gable}$ dimensions - top view

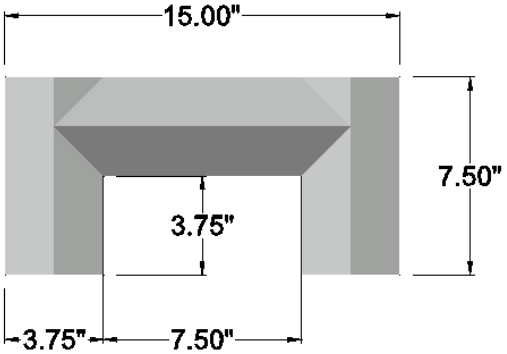

Figure 12. Model $C1_{gable\&flat}$ dimensions - top view

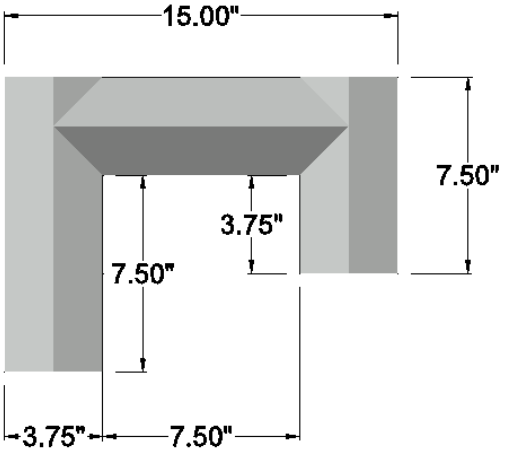

Figure 13. Model $C2_{gable\&flat}$ dimensions - top view

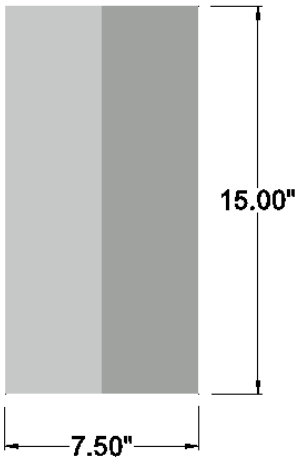

Figure 14. Model $R1_{gable}$ dimensions - top view

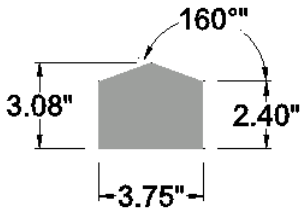

Figure 15. Elevation view (all irregular shape models sections wit gable roof)

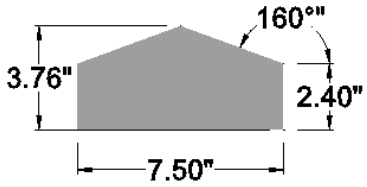

Figure 16. Elevation view (regular shape model with gable roof)

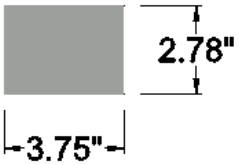

Figure 17. Elevation view (all irregular shape models sections with flat roof)

4.2. METHODOLOGY

Wind tunnel testing is a widely adopted and effective tool for assessing the response of structures subjected to wind-induced loading, particularly in cases where the structure's shape is aerodynamically complex. All large-scale models, for this investigation, underwent testing at the Wall of Wind (WOW) Experimental Facility (EF) located at

Florida International University in Miami, Florida, USA. This remarkable facility is a full/large-scale wind tunnel equipped with twelve 700-horsepower electric fans capable of generating wind speeds of up to 157 mph. The facility's design includes a flow-management box with adjustable components, enabling the modification of wind characteristics such as turbulence intensity and wind profiles. It must be noted that accurate simulation of wind properties is very important in order to obtain accurate results (Uematsu et al., 1999, Stathopoulos, 1984, Holmes, et al., 1990, Akins et al., 1977, Bachlin et al., 1983, Stathopoulos et al., 1983, Tieleman 1992). By employing spires and automated floor roughness components, the facility can achieve various terrain exposures (ASCE 7-22 - Figure 18). Moreover, a 16-ft diameter steel turntable is used to mount the models, allowing for tests to be conducted at multiple wind directions. The wind tunnel test section spans an area of 20-ft by 14-ft (width and height), providing ample space for full- and large-scale testing (Chowdhury et al., 2017).

The capability of conducting large-scale and full-scale testing enables the examination of building models of increased size. This not only allows for the assessment of complete structures but also facilitates the examination of smaller components, such as cladding elements, that contribute to the overall behavior of the structure. Additionally, the ability to test large-scale models permits the installation of a greater number of instruments, resulting in enhanced resolution and detailed insights into the response of structures and structural components and reduce Reynolds number effects (Chowdhury et al., 2017, Mooneghi et al., 2014, Mooneghi et al., 2016, Moravej 2018). However, wind tunnels have a limitation regarding eddies sizing, and depending on the prevailing wind conditions as well as the surrounding environment, these eddies may vary in size between small and

large eddies. When the scale of the model is increased, the ability of the wind tunnel to produce bigger eddies is reduced, resulting in a flow with lack of large eddies, in other words, lack of low-frequency turbulence (Mooneghi et al., 2016, Moravej 2018).

The scale of 1 to 50 was chosen for wind tunnel testing as it offered the largest scale while still allowing for a full range of turbulence, including both low and high-end turbulence intensities. Given the large-scale size, the roughness elements needed to extend up to the turntable to achieve the best possible alignment between wind speed (U) and turbulence intensity (I_u) profiles (Figure 19). To accurately measure the wind characteristics within the wind tunnel setup, six Turbulent Flow Instruments (TFI) Cobra Probes were strategically installed at the center of the turntable at various heights: 1.5 inches, 1.75 inches, 2.75 inches, 3 inches, 4.5 inches, and 6 inches. It is worth noting that for models with irregular shaped plans, the mean roof height was 2.75 inches, while for the rectangular model, it was 3 inches.

The mean wind speed (U) and turbulence intensity (I_u) profiles, as depicted in Figure 20, closely matched the Engineering Sciences Data Unit (ESDU) profiles for a simulated Open terrain (z0=0.02 m). Also, by using the power law it was found that the $1/\alpha$ value produced by the wind tunnel attained a value of 0.1, closely matching with the value provided by ASCE 7-22 for open terrain and thus confirming the validity of the setup and results obtained. Additionally, the Power Spectrum Density profile (Figure 21) demonstrated the wind tunnel's capability to generate both high-frequency and low-frequency turbulence.

Subsequently, the models were placed at the center of the turntable and connected to three Thermal Control Units (TCU) via Zoc33/64Px, and data was sampled with a

Scanivalve system, which consisted of a DSM4000 and an SPC4000 along with their corresponding hardware components. The system had the capability to accommodate a total of 384 pressure taps connected concurrently, with a sampling frequency of 520 Hz. The testing of all models was conducted across a range of wind directions, spanning from 0 to 345 degrees in 15-degree increments (clockwise direction) and for a 1-minute duration (Figure 22). The full-scale data sampling frequency and test time were obtained with Equation 1, where frequency and time attained values of 30.58 Hz and 17 minutes, assuming full-scale speed was equal to 84 mph. All data was then post-processed with a transfer function to compensate for any distortion caused by the urethane tubing length used to tap onto the models' pressure tap (Irwin et al., 1979).

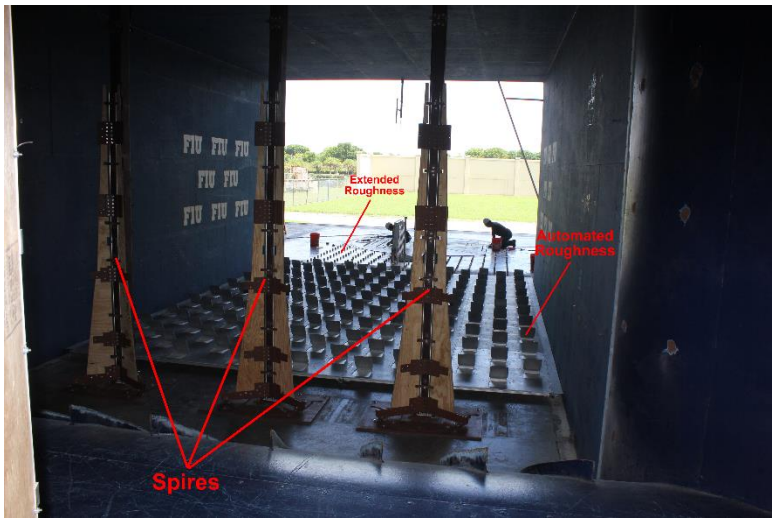

Figure 18. Wind tunnel spires and automated roughness elements

Figure 19. Extended roughness elements

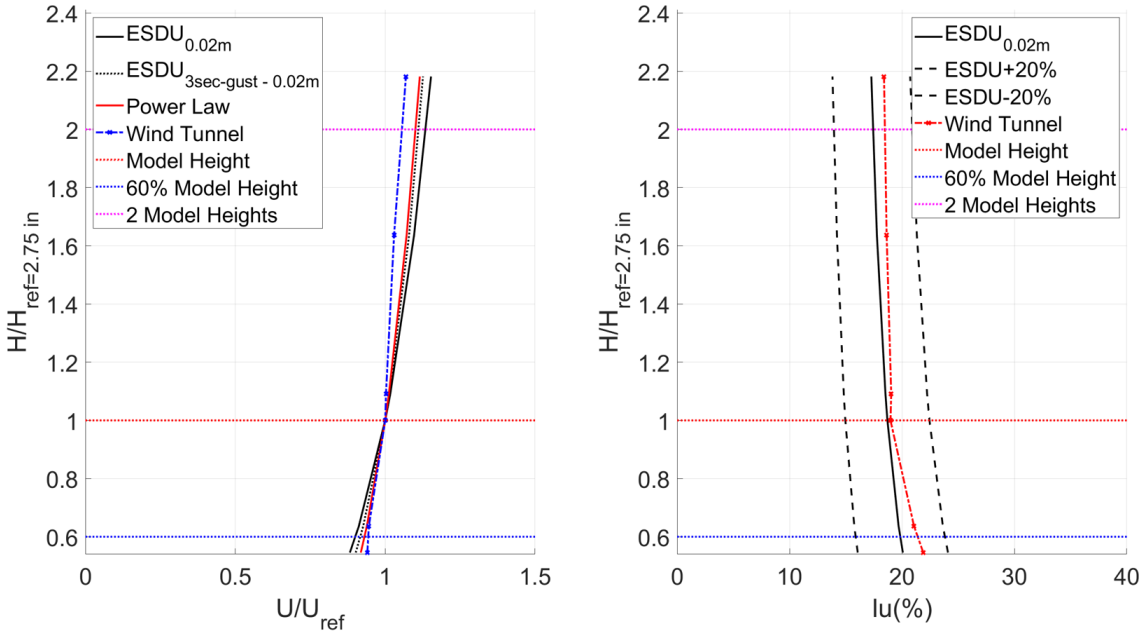

Figure 20. Wind speed (U) and turbulence intensity (I_u) profiles

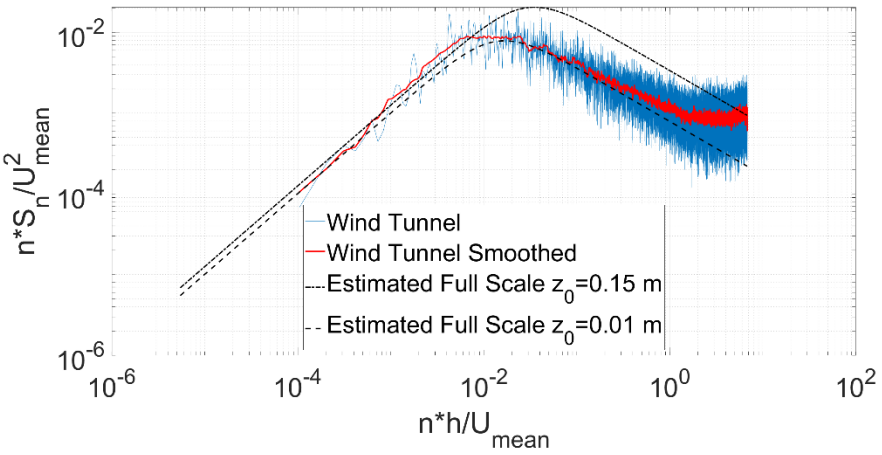

Figure 21. Power Spectrum Density profile at 2.75 inches height

$$\frac{T_{fs}U_{fs}}{L_{fs}} = \frac{T_m U_m}{L_m} \qquad \textit{Equation 1}$$

where T=Time; U=Wind Speed; L=Dimensional Scale; fs=Full-scale and m=Model

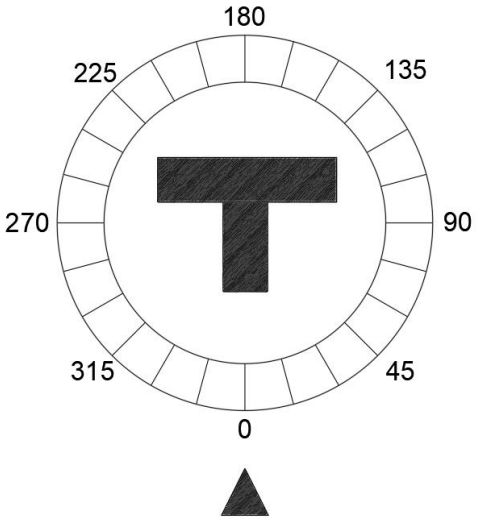

Figure 22. Wind directions

4.3. RESULTS LARGE SCALE STUDY

4.3.1. PRESSURE COEFFICIENTS

Pressure coefficients (C_p) were derived utilizing Equation 2, wherein t signifies the value within the time series, ($p-p_0$) signifies the differential pressure (for each pressure tap)

extracted from the Scanivalve data gathered across various experiments, ρ signifies the air density, and U_{MHR} signifies the mean wind speed at the model's mean roof height (MRH). The usage of such unitless coefficients "enables the transfer of model experimental results to full-scale, and the establishment of reference values for cataloging the aerodynamic properties of given geometric forms" (Simiu, 2019 – 4th Edition). In addition, current wind provisions, which provide GC_p values for the design of civil infrastructure, also provide GC_p values in the form of 3-second gust ($GC_{p,3s}$) (ASCE 7-22).

In this study, the outcomes are displayed using mean pressure coefficients ($C_{p,mean}$) and critical pressure coefficients ($C_{p,critical}$). In order to obtain these values, the data was treated with an Extreme Value Analysis (EVA) Best Linear Unbiased Estimation (BLUE) method (Lieblein, 1974) with a non-exceedance value set to 78%. To illustrate these coefficient values, contour plots were generated for each model shape and wind direction, representing both mean and critical values. Given the number of models and wind directions, producing a substantial quantity of contour plots would not be feasible for presentation. Hence, for the $C_{p,mean}$, solely the contour plots for 0-degree wind direction will be utilized to convey findings that are equally applicable to other wind directions (mean pressure coefficient contour plots, for cornering angles, are presented in the Appendix). In the process of assessing $C_{p,\ critical}$ values, a comprehensive analysis was conducted on each pressure tap located on the models, covering all wind directions. From this analysis, only the highest positive and negative values were singled out for consideration. As a result, the contour plots depicting $C_{p,\ critical}$ values for each model will encompass both positive and negative contours, offering a comprehensive representation of the extremes in the pressure coefficients from all wind directions.

$$C_p(t) = \frac{p - p_0}{\frac{1}{2}\rho U_{MRH}^2}$$ *Equation 2*

4.3.1.1. MEAN PRESSURE COEFFICIENTS

Contour plots were created for each model across all wind directions, offering valuable insights into the interplay between wind patterns and structures featuring irregular shapes. Figure 23 provides information regarding the orientation of the walls in all contour plots presented in this investigation. In this section, solely the contour plots corresponding to the 0-degree wind direction are showcased (Figure 24 to Figure 34). It is important to acknowledge that intricate flow interactions and developments were also evident in other wind directions. Nevertheless, the observations gathered from the 0-degree plots were generally applicable to the other wind directions as well. To facilitate the discussion, the models have been positioned in a manner where the wind, corresponding to a 0-degree wind direction, originates from the lower portion of the page. Likewise, the cardinal directions—North, West, South, and East — are denoted as the Top, Left, Bottom, and Right sides of the page, respectively. Furthermore, for clarity, the wall and roof sections will be denoted as "upwind" and "downwind" sections, respectively (for instance, "upwind windward wall" and "downwind windward wall" - as illustrated in Figure 24).

When examining the outcomes derived from model $T1_{gable}$ at a wind direction of 0 degree (depicted in Figure 25), a discernible pattern emerged: walls facing the oncoming wind exhibited positive pressure values, while the side and leeward walls manifested negative pressure values. These observations aligned closely with anticipated norms and fell within the expected range. However, a noteworthy pressure distribution was observed on both the windward and side walls when an extending section, forming a 90-degree

angle, was appended to either of the two wall segments. For instance, directing attention to the "upwind windward wall," a mean pressure coefficient of 0.68 was registered, with the most pronounced positive pressure occurring at the upper center of the wall. In contrast, a distinct pressure coefficient development was observed on the "downwind windward wall," where the average pressure coefficient peaked at approximately 0.51 (toward the left side) along one of the wall's edges. This represented a substantial 25% reduction in the development of positive pressure coefficients. Along the side walls, a distinct pattern emerged: the "downwind side walls" registered exclusively negative pressures, with the most extreme negative value reaching -0.83 and progressively diminishing toward the leeward wall side. The "upwind side wall" also experienced negative pressures, yet a noteworthy 33% decrease in the magnitude of negative pressures was observed, with the highest negative pressure coefficient settling at -0.27. Moreover, a gradual pressure decline was observed along these wall sections, but the values shifted to the positive realm near the juncture of the perpendicular-to-parallel walls, attaining a pressure coefficient value of 0.37.

When comparing models $T1_{gable}$ and $T2_{gable}$ (Figure 25 and Figure 26), a consistent pressure distribution pattern emerged, in alignment with the description provided earlier. However, a notable discrepancy arose in the pressure development of the "upwind side wall" for model $T2_{gable}$. Remarkably, these particular side walls experienced predominantly positive pressures, with the most pronounced suction pressure coefficient registering at a mere -0.11 - a remarkable 86% reduction when compared to a “downwind side wall.” Another noteworthy distinction surfaced in the pressure distribution over the roofs of these two models, with model $T1_{gable}$ experiencing somewhat lower suction pressure values. This

phenomenon can be attributed to the extension of the protruding section further upwind, creating a flow disruption that mitigates the formation of high suction zones across the roof sections. Consequently, model $T2_{gable}$ experienced heightened suction values when compared to those observed in model $T1_{gable}$.

Models $L1_{gable}$ and $L2_{gable}$ (Figure 27 and Figure 28) demonstrated similar overall effects as described for $T1_{gable}$ and $T2_{gable}$ (Figure 25 and Figure 26). However, a notable distinction arose concerning the pressure development on the "downwind windward wall." This wall, in comparison to the T models, exhibited significant elongation on the development of positive pressure development (stagnation pressure). The extension of this wall caused the positive pressure zone to extend along its length, reaching up to the junction with the "downwind side wall." Despite this elongation, the overall pressure coefficient value remained unaffected, maintaining a reading of 0.5. This value signified a reduction of 30% when contrasted with the 0.71 value recorded for the "upwind windward wall." Furthermore, it was noted that the leeward wall exhibited elevated suction pressure coefficient values on the side without a 90-degree wall joint (west side of leeward wall). In comparison to the findings from a rectangular model, the “leeward wall” of model $L1_{gable}$ demonstrated a 109% upsurge in the mean pressure coefficient value (-0.23 vs. -0.48). Additionally, an intriguing phenomenon manifested on the "parallel to the wind" roof section located upwind. Here, the suction values appeared to shift towards the west side. This effect became more pronounced when the length of the "perpendicular to wind" section surpassed that of the "parallel to wind" section. A theoretical explanation suggests that the pressure buildup occurred at the 90-degree joint formed by the wall sections, creating a blockage effect. This, in turn, led to the generation of pressure differentials that

compelled air to escape over the roof sections. Consequently, a complex mixing of air separations arose from both the roof edge of the "upwind windward wall" and the roof edge of the "upwind side wall" pushing the overall separation bubble away from the positive pressure pocket at the 90-degree walls joint.

Upon examining the pressure distribution of model $C1_{gable}$ (Figure 23), it was observed that the "upwind windward walls" remained exhibiting the highest positive pressure development, reaching values as high as 0.66. From this intricate C-shape, a unique configuration emerged between the "inner side walls" and the "downwind windward wall," which surprisingly led to an intensified reduction in positive pressure coefficients experienced by the latter. Specifically, the "downwind windward wall" experienced a 33.3% decrease in positive pressure coefficient compared to the pressure development on the "upwind windward wall." This reduction occurred primarily at the center of the "downwind windward wall." It appears that the separations originating from both "upwind windward walls" converged and interacted at the center of the "downwind windward wall," resulting in a complex blending of two previously separated flows. This interaction led to a less potent generation of positive pressures. The "inner side walls" predominantly experienced positive pressures, with the most substantial values appearing near the edge of the "downwind windward wall." Meanwhile, the "outer side walls" exhibited the anticipated pressure development pattern. The most negative values emerged near the separation zone and progressively diminished towards the leeward side of the wall. The most pronounced suction effect encountered by the "outer walls" (side walls) reached a magnitude of -0.68, while the "inner side wall" registered a value of -0.14, indicating a remarkable 80% reduction in suction forces. Furthermore, a similar phenomenon observed

in models with an L-shape was witnessed in the development of the "parallel to wind" roof sections of model $C1_{gable}$. A complex blending of airflows stemming from the "upwind windward walls," "inner side walls," and "downwind windward wall" resulted in the concentration of negative pressure coefficients along the outer edges of the roof sections. However, the most significant peaks were still situated near the edges of the protruding roof sections and in proximity to the 90-degree wall joints, reaching values of -1.38.

Overall, model $C2_{gable}$ (Figure 30) underwent similar pressure developments than those observed in model $C1_{gable}$. However, some interesting observations were made. For example, the “upwind windward walls” remained being the sections with the highest positive pressure development, however, a reduction of pressure was observed between the “west upwind windward wall” and the “east upwind windward wall.” The wall that protruded the most in the upwind direction attained a pressure coefficient value of 0.7, while the “east upwind windward wall” experienced a mean pressure coefficient value of 0.62, showing an 11% reduction. Furthermore, due to the extension of the “west section” an increased reduction on the positive pressure development on the “downwind windward wall” was observed to reach a 46% reduction. In addition, the "west inner side wall" demonstrated an amplified negative pressure development, reaching a value of -0.34, which signifies a notable 142% escalation in comparison to the "inner side walls" of model $C1_{gable}$. Additionally, the extension of a section towards the upwind direction resulted in a diminished impact of the roof on the negative pressure development. This alteration lessened the influence of the "positive pressure entrapment" created between the 90-degree wall joints, leading to a reduced effect on the displacement of negative pressure developments towards the outer perimeter of the roof section.

Regarding the models featuring flat roofs (depicted in Figure 31 to Figure 34), the pressure distributions on the wall sections were notably similar to those observed in the models with gable roofs. However, significant differences in pressure coefficients emerged on the roof sections, where the flat-roof models exhibited higher magnitudes of negative suction pressures. To illustrate, a comparison between models $T1_{gable}$ and $T1_{flat}$ (Figure 25 and Figure 31) revealed that the model with a flat roof exhibited an approximately 19% increase in the mean pressure coefficient across the roof section edges near the “upwind windward wall”, with values transitioning from -0.47 in model $T1_{gable}$ to -0.58 in model $T1_{flat}$. Furthermore, the regions of highest suction were identified along the roof edges adjacent to the 90-degree wall joints, particularly along the edges of the "downwind windward walls."

As for model $L1_{flat}$ (Figure 32), the primary disparity between gable and flat roofs was the notably elevated pressure coefficients experienced on the roof sections, particularly those perpendicular to the wind direction. Models featuring flat roofs encountered a negative pressure increase from -0.8 to -0.85. However, it is important to highlight that a conspicuous enlargement in the size of the separation/suction bubble between the two models was the primary observation. The interactions between the walls remained consistent with those observed and described for model $L1_{gable}$ (Figure 27). As previously mentioned in model $L1_{gable}$, an increase in pressure coefficients on one side of the leeward wall was observed. In the case of model $L1_{flat}$, the same phenomenon was noted.

Similarly, models $C1_{flat}$ and $C2_{flat}$ (Figure 33 and Figure 34) exhibited a wall pressure distribution like the patterns observed in models with gable roofs. The distinguishing factor, consistent with the previous two models, was the expansion of areas

experiencing negative pressures on the various roof sections. Notably, a discernible impact of the interaction between the "inner side walls" and the "downwind windward wall" led to a significant negative pressure distribution aligned with the direction of the "inner side walls." This distribution extended to the leeward side of the roof sections. This effect was noticeably diminished when the extension of the "inner side wall" towards the upwind direction was increased (e.g., west side inner wall), as observed in Figure 34.

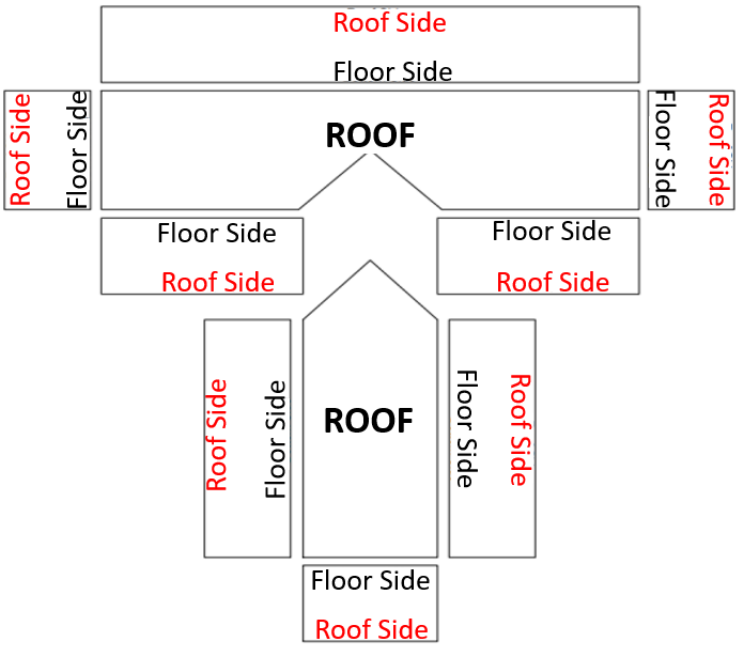

Figure 23. Contour plots walls orientation

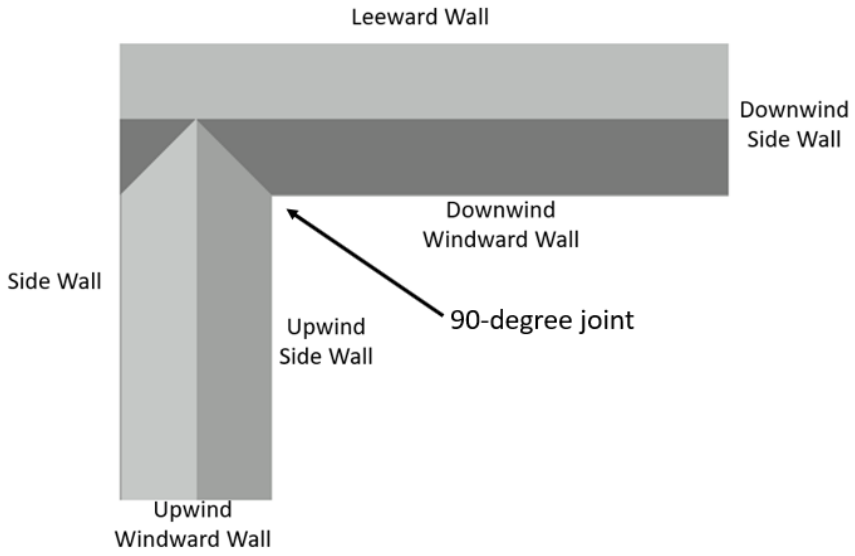

Figure 24. Wall and roof sections labeling

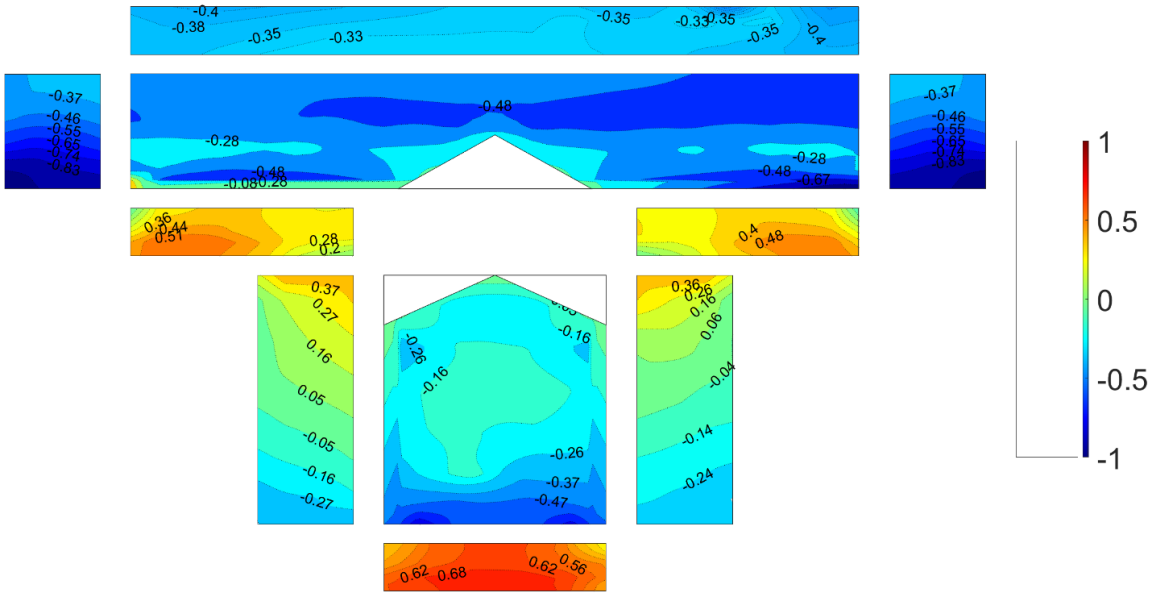

Figure 25. Model $T1_{gable\_2019}$ $C_{p,mean}$ – 0 degree.

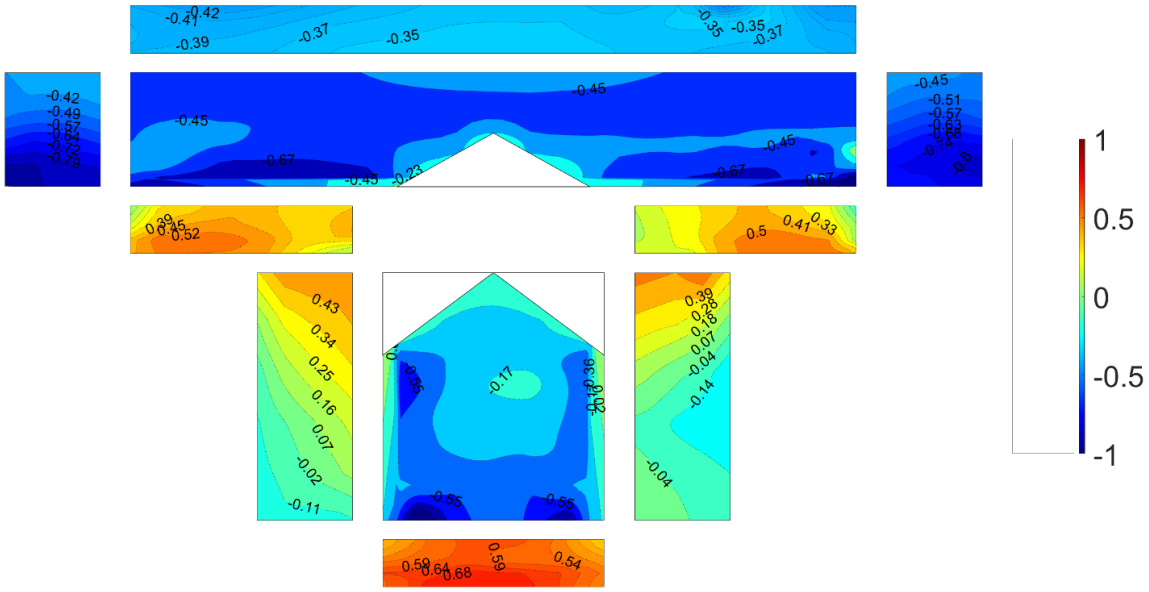

Figure 26. Model $T2_{gable\_2019}$ $C_{p,mean}$ – 0 degree.

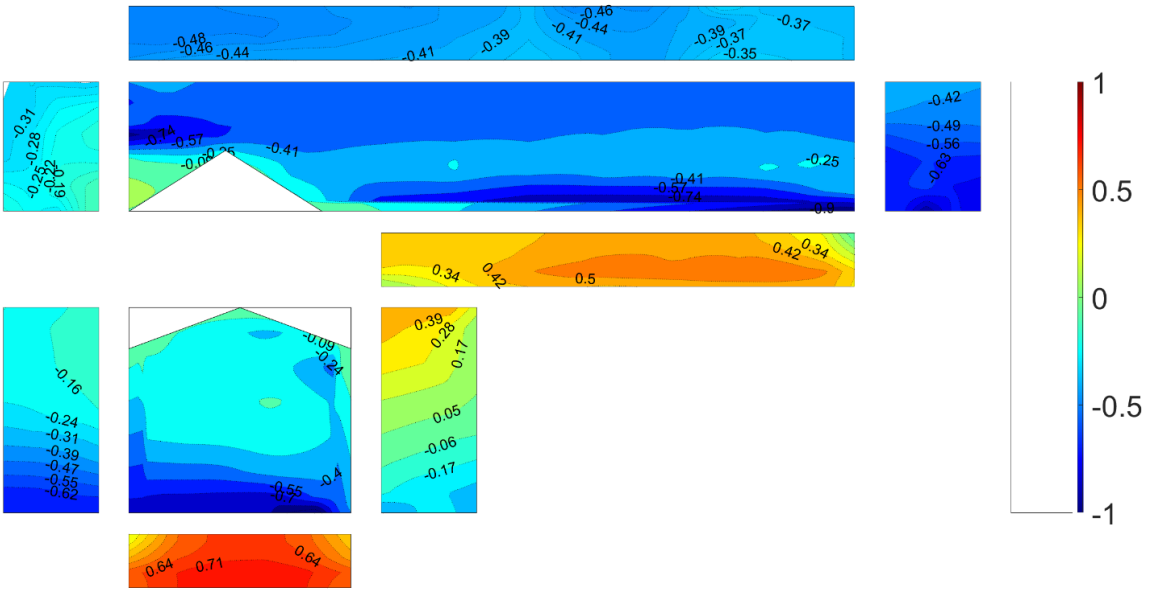

Figure 27. Model $L1_{gable\_2019}$ $C_{p,mean}$ – 0 degree.

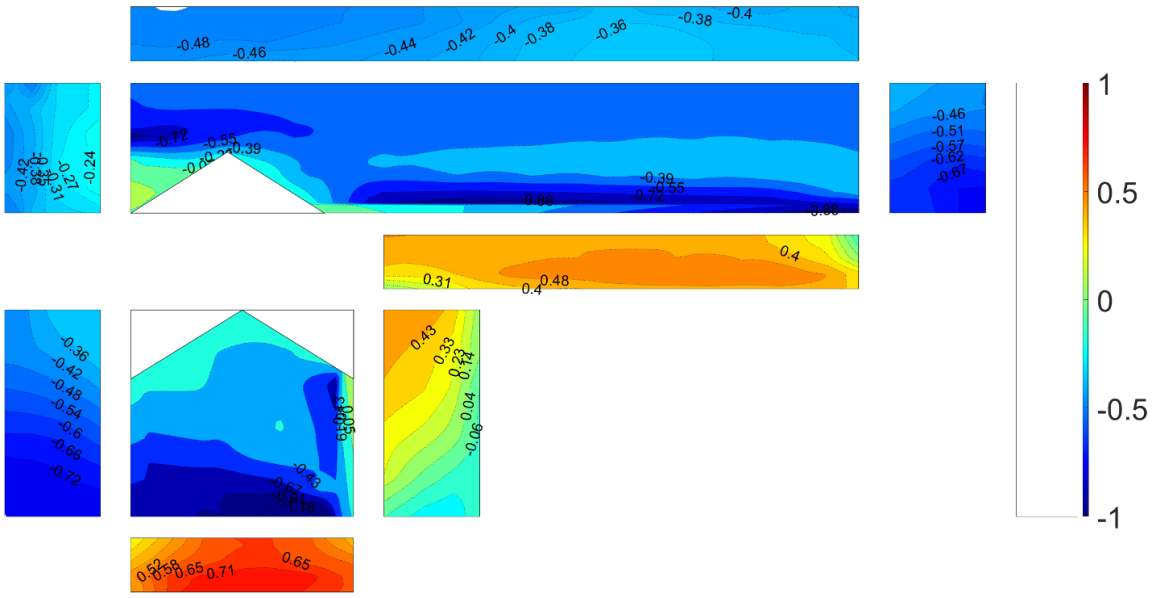

Figure 28. Model $L2_{gable\_2019}$ $C_{p,mean}$ – 0 degree.

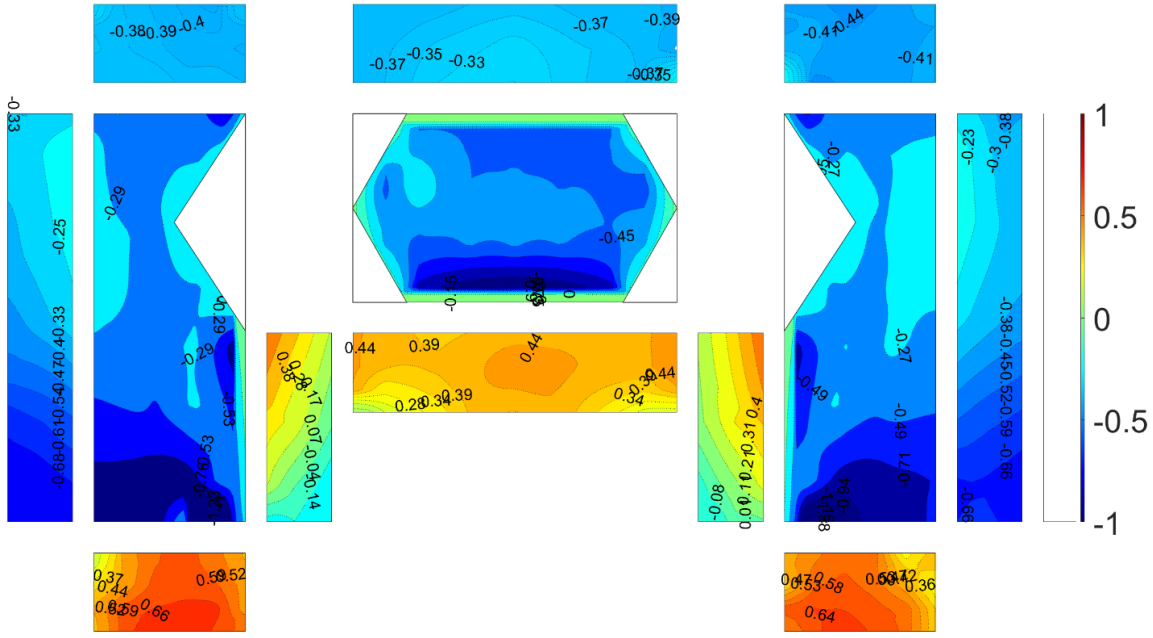

Figure 29. Model $C1_{gable\_2019}$ $C_{p,mean}$ – 0 degree.

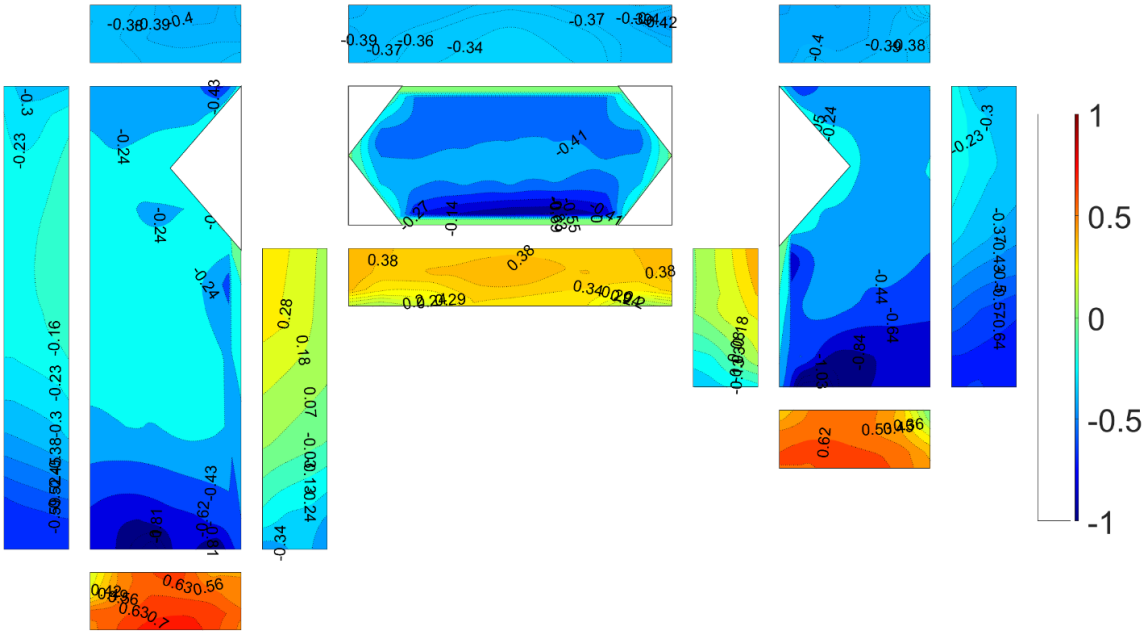

Figure 30. Model $C2_{gable\_2019}$ $C_{p,mean}$ - 0 degree.

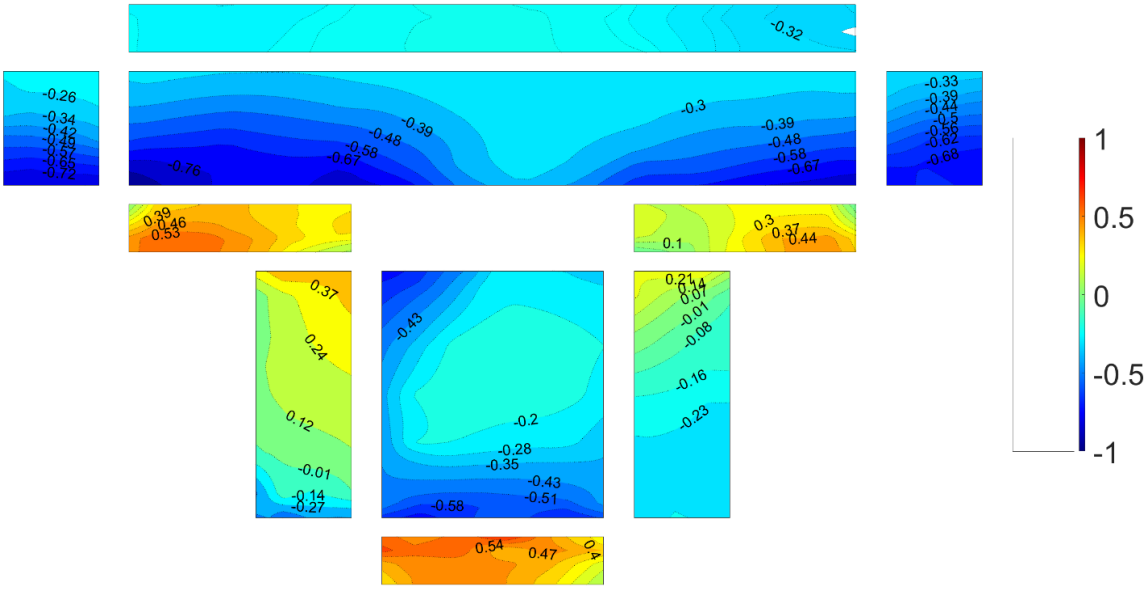

Figure 31. Model $T1_{flat\_2020}$ $C_{p,mean}$ – 0 degree.

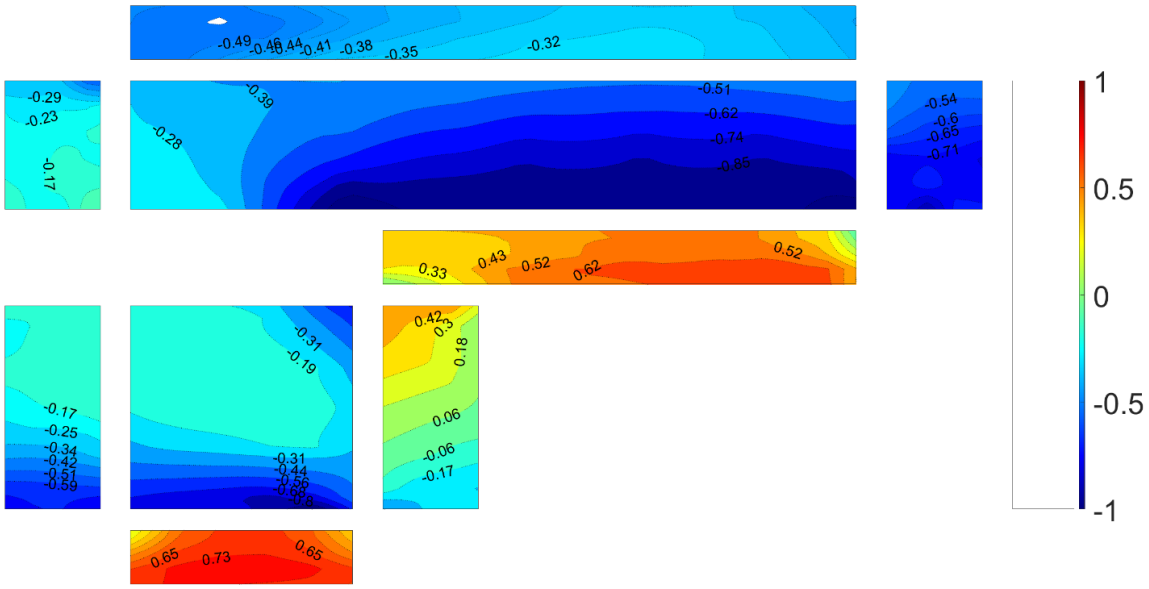

Figure 32. Model $L1_{flat\_2020}$ $C_{p,mean}$ – 0 degree.

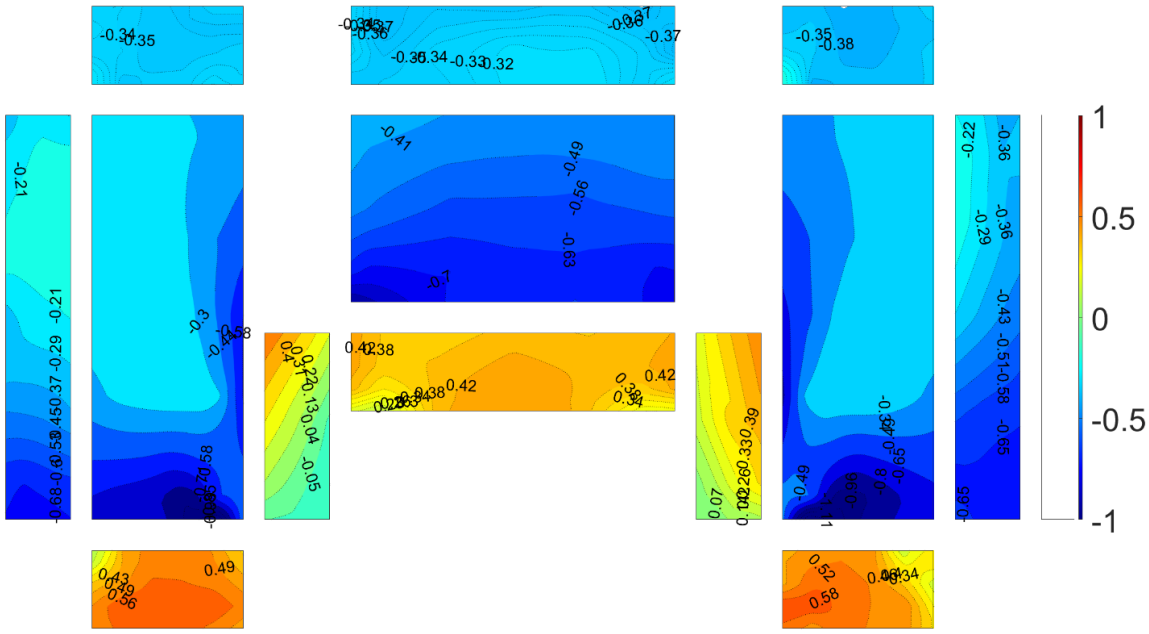

Figure 33. Model $C1_{flat\_2020}$ $C_{p,mean}$ – 0 degree.

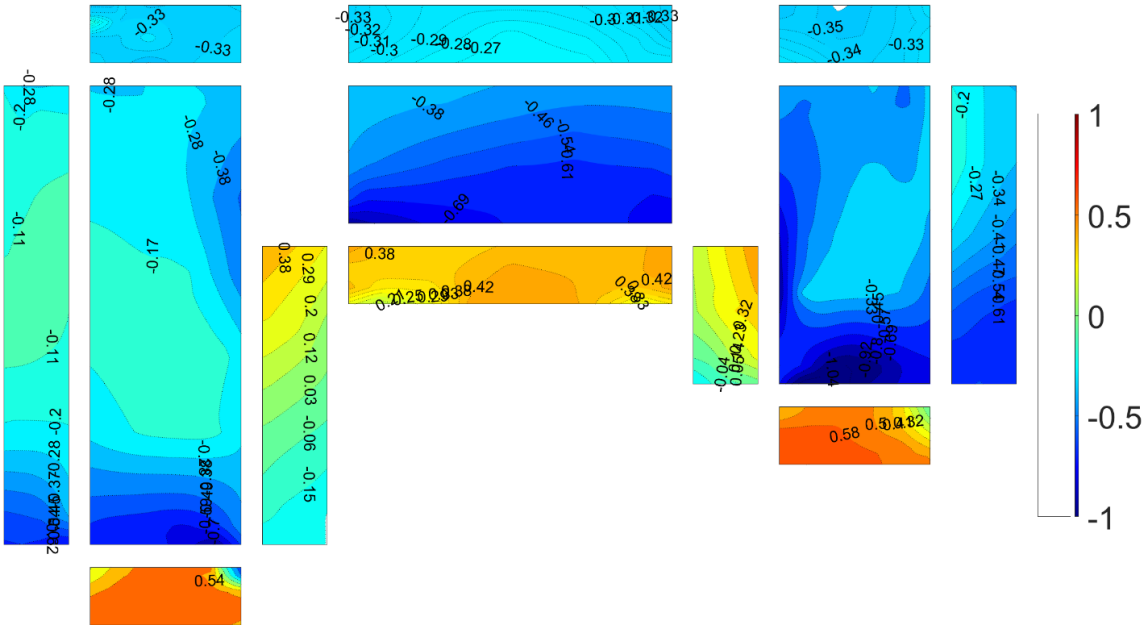

Figure 34. Model C2$_{flat_2020}$ $C_{p,mean}$ – 0 degree.

4.3.1.2. CRITICAL PRESSURE COEFFICIENTS

Contour plots were generated for each model with irregular shapes to illustrate the critical peak pressure coefficient ($C_{p,\ critical}$) (Figure 35 to Figure 48). These plots aimed to identify the specific regions within the models that are more susceptible to encountering the highest positive and negative forces. These critical peak pressure coefficient plots will be referred to as the plots showing the maximum and minimum values for both positive and negative critical graphs. The primary goal of creating these plots is to provide a visual representation that encompasses the most challenging scenarios across all wind directions. These plots play a crucial role in offering valuable insights to ensure structural integrity during the design phase. However, it is important to emphasize that these critical values might not occur simultaneously. This underscores the necessity for a comprehensive analysis of these values.

The critical values (both positive and negative) for each pressure tap were determined by choosing the highest peak Cp value among all wind directions, as well as the lowest peak Cp value among all wind directions. Please note these peak critical values (in the form of 3s peaks) were obtained by the BLUE method.

When examining the positive pressures acquired from all models, it became evident that the walls were more prone to experiencing elevated positive pressures. This observation was anticipated across all models, irrespective of their floor plan shapes. To facilitate a straightforward comparison among the outcomes of models with irregular shapes, the walls were categorized based on their orientation: North, West, South, and East. Here, North pertains to walls facing the upper portion of the page, West indicates walls oriented towards the left side, South refers to walls facing the bottom of the page, and East designates walls positioned along the right side.

Upon evaluating the maximum $C_{p,\,critical}$ values for the walls in the $T1_{gable\_2019}$ model (Figure 35), which align with the North, West, South, East, and roof sections, the measured values were 1.53, 1.61, 1.66, 1.51 and 1.20, respectively. In comparison to the values from the rectangular model (Figure 47), model $T1_{gable\_2019}$ exhibited a up to 12% rise in wall positive values. Remarkably, the roof of model $T1_{gable\_2019}$ experienced a staggering 75% increase in the highest value recorded across the entire roof area. Within the roof sections of this model, the roof edges adjacent to the 90-degree wall joints were notably influenced by a complex interplay of flow mixing. Upon examining the minimum $C_{p,\,critical}$ values (Figure 36), it became apparent that the recorded values were as follows: -2.36, -2.50, -2.50, -2.82, and -3.75, corresponding to the North-wall, West-wall, South-wall, East-wall, and roof sections, respectively. These values translated to walls experiencing a potential

increase of up to 16% in their minimum $C_{p,\ critical}$ values, while the roof, on the other hand, demonstrated an 16% reduction in the observed values when compared to results obtained from the model with regular shape (Figure 48).

Upon examining the findings from model $T2_{gable\_2019}$ (Figure 37), a similar trend to that observed in model $T1_{gable\_2019}$ (shown in Figure 35) was apparent. Maximum $C_{p,\ critical}$ values on wall sections displayed an upward shift of as much as 6%, and concurrently, the roof encountered a noteworthy 41% rise in its maximum $C_{p,\ critical}$ values. Roof edges located adjacent to the wall sections forming a 90-degree angle (e.g., "downwind windward walls" and "upwind side walls") were observed to develop positive pressure pockets that resulted in increased maximum $C_{p,\ critical}$ areas. As for the minimum $C_{p,\ critical}$ values of model $T2_{gable\_2019}$ (as seen in Figure 38), the walls exhibited an increase of up to 12%, whereas the roof demonstrated a reduction of 16% in the occurrence of highly negative $C_{p,\ critical}$ values, when compared to model with regular shape plan (Figure 47 and Figure 48).

The outcomes for Models $L1_{gable\_2019}$ and $L2_{gable\_2019}$ are presented in Figure 39 through Figure 42. Upon analyzing the contour plots and numerical data, it became evident that walls in both models exhibited an increase of up to 6% and 17% in their maximum $C_{p,\ critical}$ values when compared to the results of the regularly shaped model. The specific values for each model were 1.46, 1.57, 1.54, and 1.50 for the $L1_{gable}$ model, and 1.61, 1.54, 1.58, and 1.66 for the $L2_{gable}$ model. Note these values correspond to walls facing north, west, south, and east. For both of these models, a remarkable escalation of 54% and 56% was observed in the maximum $C_{p,\ critical}$ values on the roofs, respectively. Interestingly, these models' walls, exhibited minimum $C_{p,\ critical}$ values that were 33% and 36% higher compared to those obtained from Model R, attaining values of -2.55, -2.18, -2.32, -2.37

and -2.62, -1.9, -2.32 and -2.24, respectively (e.g., north-, west-, south- and east-wall). Conversely, when compared to model R, the roof sections of these models showed a reduction in minimum $C_{p,\,critical}$ values by as much as 18% and 24%, respectively.

In the case of Model $C1_{gable\_2019}$, the maximum $C_{p,\,critical}$ values (as depicted in Figure 43) demonstrated an augmentation in pressures, reaching up to 20%. Notably, this increase was particularly pronounced in the "downwind windward wall," which experienced the most substantial rise in pressure when contrasted with the regularly shaped model while the roof sections of this model exhibited a significant 73% surge in the development of maximum $C_{p,\,critical}$ values. Notably, the protruding roof sections were the specific areas where the highest maximum $C_{p,\,critical}$ values were observed to form. As was observed in previous models, roof edges adjacent to walls forming a 90-degree joint were most susceptible to the development of increased maximum $C_{p,\,critical}$ values. When focusing on the minimum $C_{p,\,critical}$ values (Figure 44), it was noted that these values underwent an increase of up to 20% in comparison to the values of the walls in Model R. Concurrently, there was a decrease of 11% in the minimum $C_{p,\,critical}$ values of the roof sections of the same model.

Upon scrutinizing the values derived from the maximum and minimum $C_{p,\,critical}$ contour plots of Model $C2_{gable\_2019}$ (Figure 45), it was observed that the walls experienced a more modest upswing in maximum $C_{p,\,critical}$ values, as well as a substantial increase in these values within the roof sections – 10% and 54%, respectively. The roof's 54% increase in maximum $C_{p,\,critical}$ values still concentrated on the edges adjacent to walls forming a 90-degree joint. Conversely, the walls within Model $C2_{gable}$ exhibited heightened values in minimum $C_{p,\,critical}$ values, up to 20%, whereas the values in the roof sections experienced

a decrease of 27% (Figure 46), when compared to model R minimum $C_{p,\ critical}$ values (Figure 48).

To obtain a comprehensive visual overview of the acquired $C_{p,\ critical}$ values, a graph and table were generated and are included below. In Figure 49, you can observe the highest individual $C_{p,\ critical}$ values observed for various wall and roof sections across all models featuring gable roofs. This graph revealed that wall sections within irregularly shaped buildings tended to exhibit elevated minimum $C_{p,\ critical}$ values. Interestingly, roof sections of models with irregular shapes displayed a reduction in their minimum $C_{p,\ critical}$ values compared to the regular-shaped model. Furthermore, roof sections of irregularly shaped models demonstrated significantly higher maximum $C_{p,\ critical}$ values compared to the results from the model with a rectangular plan shape.

Table 1 presents a summary of percentage variations in comparison to the results from all walls facing north, west, south and east, as well as roof sections with regular shapes. A secondary table was generated obtaining the highest value observed to develop from all walls, and the difference between the worst value of all rectangular model walls was estimated (

Table 1. Wall and roof sections highest maximum vs minimum $C_{p,\ critical}$ variation percentages – 2019 experiments (gable roofs)

Model Section	$T1_{gable\_2019}$		$T2_{gable\_2019}$		$L1_{gable\_2019}$		$L2_{gable\_2019}$		$C1_{gable\_2019}$		$C2_{gable\_2019}$	
	MAX	MIN	MAX	MIN	MAX	MIN	MAX	MIN	MAX	MIN	MAX	MIN
North Wall	100 %	113 %	104 %	112 %	96 %	133 %	106 %	136 %	101 %	106 %	97 %	94 %
West Walls	109 %	95 %	104 %	97 %	106 %	89 %	104 %	78 %	113 %	89 %	100 %	93 %
South Walls	112 %	116 %	106 %	106 %	104 %	117 %	107 %	117 %	120 %	127 %	110 %	120 %
East Walls	102 %	116 %	104 %	106 %	101 %	106 %	112 %	101 %	109 %	104 %	102 %	107 %
Roof	175%	84 %	141 %	84 %	154%	82 %	156 %	76 %	173 %	91 %	154 %	83 %

). From the table, it was noted that all models underwent an increase in the development of maximum critical pressure coefficients, with the highest increase being 17%. On the other hand, the walls mostly underwent an increase in the development of

minimum critical pressure coefficients, with the most critical increase reaching a 9% increase.

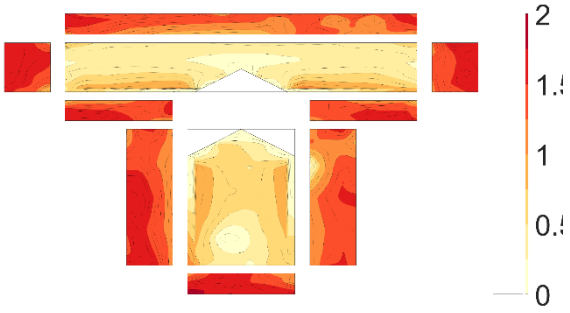

Figure 35. $T1_{gable\_2019}$ maximum $C_{p,\,critical}$

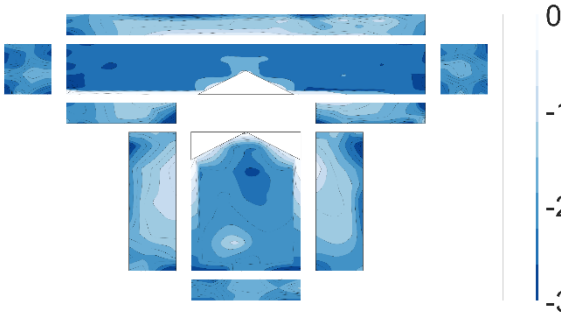

Figure 36. $T1_{gable\_2019}$ minimum $C_{p,\,critical}$

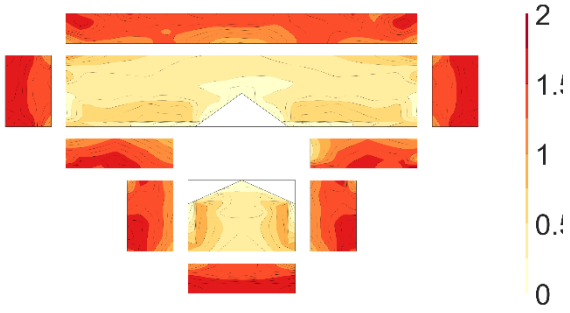

Figure 37. $T2_{gable\_2019}$ maximum $C_{p,\,critical}$

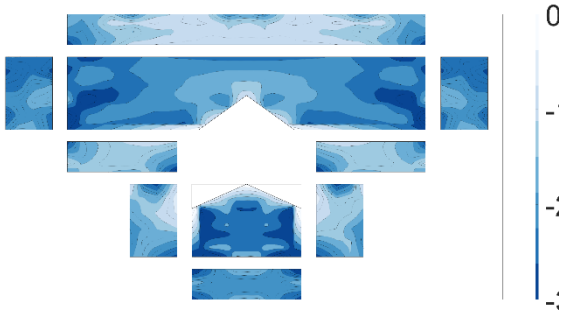

Figure 38. $T2_{gable\_2019}$ minimum $C_{p,\,critical}$

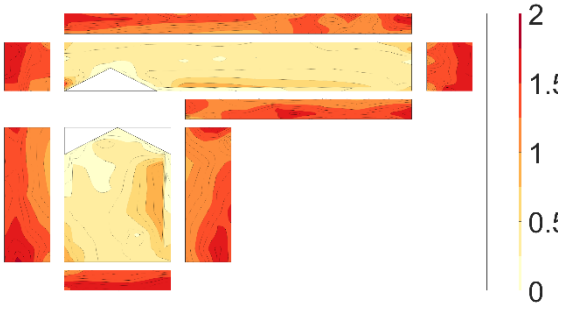

Figure 39. $L1_{gable\_2019}$ maximum $C_{p,\,critical}$

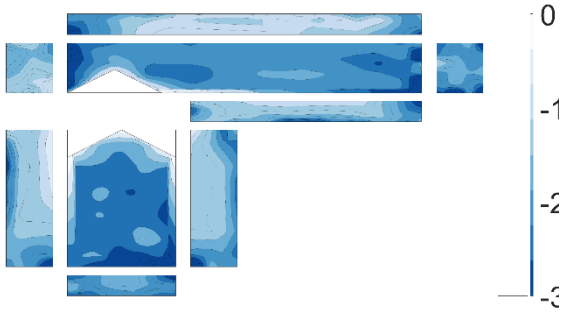

Figure 40. $L1_{gable\_2019}$ minimum $C_{p,\,critical}$

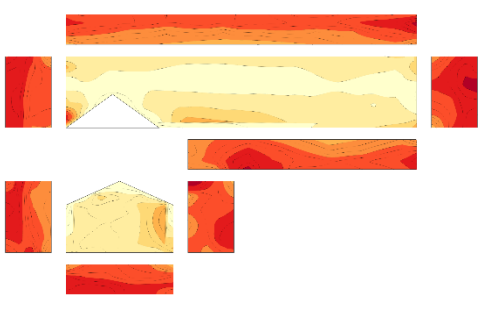

Figure 41. $L2_{gable\_2019}$ maximum $C_{p,\,critical}$

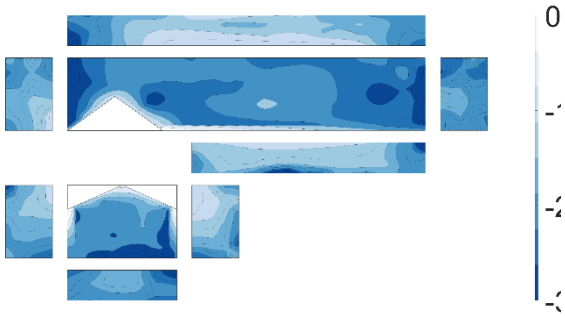

Figure 42. $L2_{gable\_2019}$ minimum $C_{p,\,critical}$

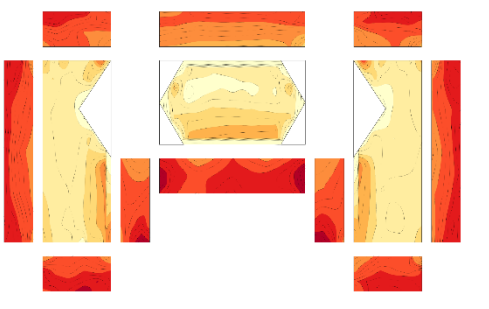

Figure 43. $C1_{gable\_2019}$ maximum $C_{p,\,critical}$

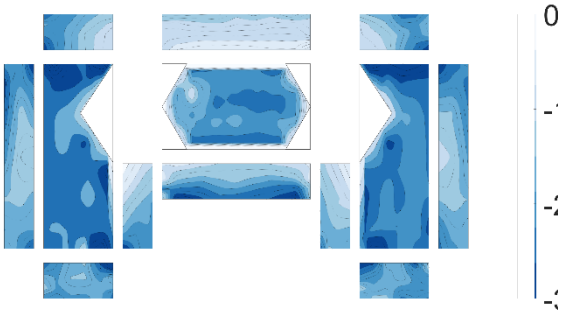

Figure 44. $C1_{gable\_2019}$ minimum $C_{p,\,critical}$

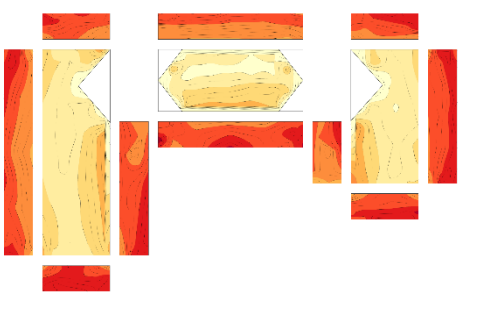

Figure 45. $C2_{gable\_2019}$ maximum $C_{p,\,critical}$

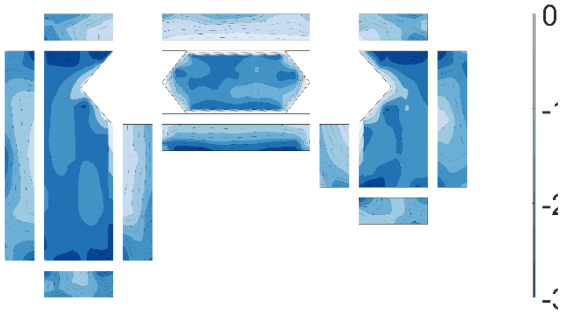

Figure 46. $C2_{gable\_2019}$ minimum $C_{p,\,critical}$

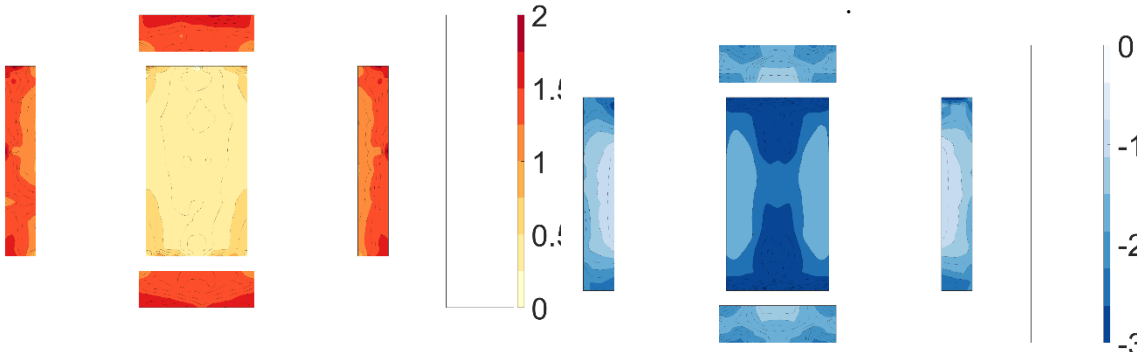

Figure 47. $R_{\_2019}$ maximum $C_{p,\ critical}$

Figure 48. $R_{\_2019}$ minimum $C_{p,\ critical}$

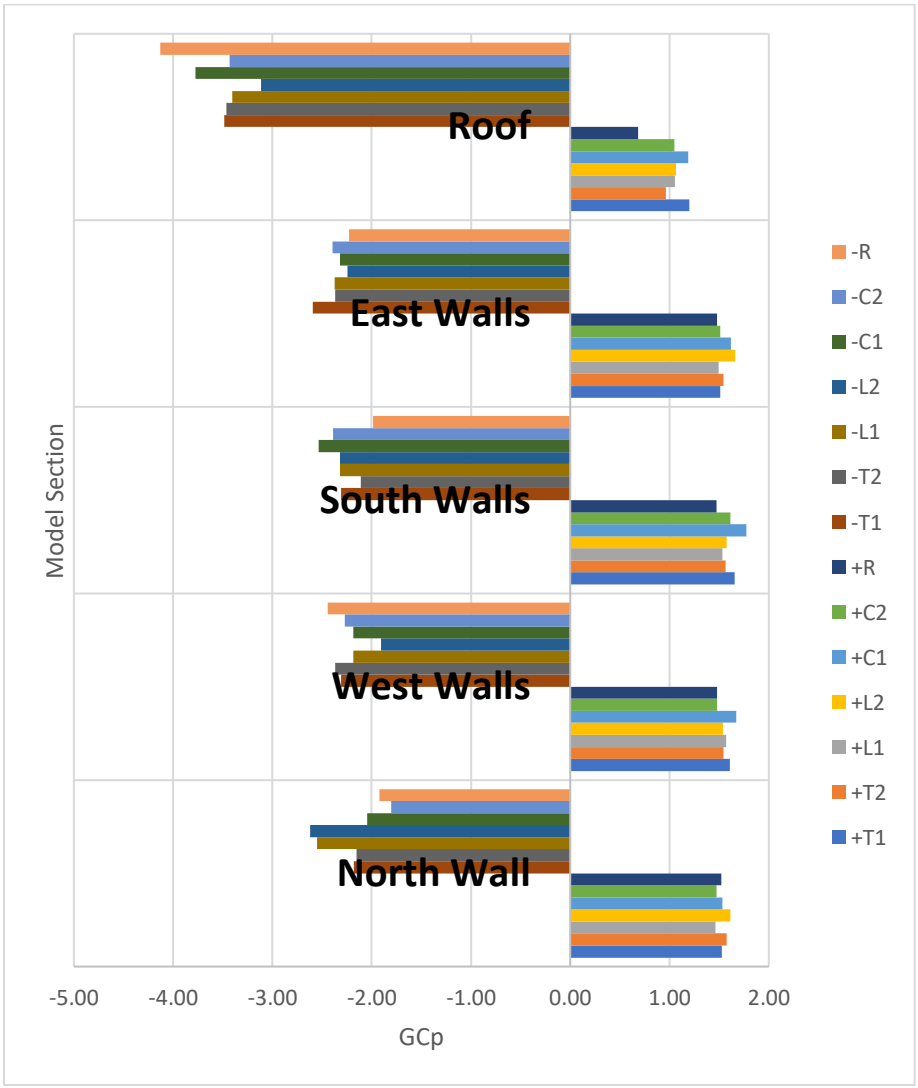

Figure 49. Wall and roof sections highest maximum vs minimum $C_{p,\ critical}$ values

Table 1. Wall and roof sections highest maximum vs minimum $C_{p,\,critical}$ variation percentages – 2019 experiments (gable roofs)

Model Section	T1 gable_2019		T2 gable_2019		L1 gable_2019		L2 gable_2019		C1 gable_2019		C2 gable_2019	
	MAX	MIN	MAX	MIN	MAX	MIN	MAX	MIN	MAX	MIN	MAX	MIN
North Wall	100 %	113 %	104 %	112 %	96 %	133 %	106 %	136 %	101 %	106 %	97 %	94 %
West Walls	109 %	95 %	104 %	97 %	106 %	89 %	104 %	78 %	113 %	89 %	100 %	93 %
South Walls	112 %	116 %	106 %	106 %	104 %	117 %	107 %	117 %	120 %	127 %	110 %	120 %
East Walls	102 %	116 %	104 %	106 %	101 %	106 %	112 %	101 %	109 %	104 %	102 %	107 %
Roof	175%	84 %	141 %	84 %	154%	82 %	156 %	76 %	173 %	91 %	154 %	83 %

Table 2. Overall walls sections highest maximum vs minimum $C_{p,critical}$ – 2019 experiments (gable roofs)

Model Section	T1 gable_2019		T2 gable_2019		L1 gable_2019		L2 gable_2019		C1 gable_2019		C2 gable_2019	
	MAX	MIN	MAX	MIN	MAX	MIN	MAX	MIN	MAX	MIN	MAX	MIN
Walls	109 %	106 %	104 %	97 %	103 %	104 %	109 %	107 %	117 %	104 %	106 %	98 %

4.4. DATA VALIDATION WITH AERODYNAMIC DATABASE

Due to the limited number of studies conducted on low-rise structures with non-standard floor plans, it becomes challenging to evaluate or juxtapose the experimental findings of this investigation with those of other researchers. To address this, a rectangular model was constructed and tested to serve as a reference point and means of comparison against other studies. Publicly accessible aerodynamic databases such as the ones provided by the National Institute of Standards and Technology (NIST) and Tokyo Polytechnic University (TPU) have been established for various applications. In this instance, the NIST and TPU databases were employed to compare the gathered experimental outcomes, thereby instilling confidence in the results derived from models with irregular configurations. In the NIST database, a model known as Test Model 3, scaled at 1:100, was chosen for the comparative assessment. The model's dimensions in full-scale measurements were 100x50x12 feet for its length, width, and height. This particular model was instrumented with 557 pressure sensors (also identified as pressure taps) strategically placed across its walls and roof segments, and its roof had a slope of 1:24 (Ho et al., 2003). In the case of the TPU model for comparison, a similarly scaled gable roof model was employed, with dimensions measuring 131.23x52.49x14.1 feet (in full-scale dimensions) for length, breadth, and height as well as a roof slope of 18 degrees. This model is identified as "g200218" in the research conducted by Tamura et al. (2005) and Tamura (2012). In contrast, the WOW model full-scale dimensions were 62.5x29.7x10 feet for length, width, and height as well as a 4:12 roof slope. This WOW model was instrumented with 354 pressure taps distributed throughout its walls and roof sections, featuring a roof slope of 4:12 (Figure 50).

For comparing outcomes from the three rectangular models, a dividing line was marked on the walls and roof sections of both models. Given the differing dimensions of the models, the placement of this dividing line was determined based on the locations of pressure taps that shared a comparable position ratio. To establish the location ratio for the wall sections, the tap height relative to the overall wall height (h/H) was taken into consideration. Regarding the roof section, this ratio was determined by the tap's position over half of the model's width (d/W/2), for the NIST, TPU and WOW models. Moreover, each pressure tap's location on both models underwent normalization by the total length/width of the relevant wall section, based on the direction of the dividing line. The same normalization procedure was applied to the pressure taps on the roof sections. This approach facilitated a meaningful comparison between models of differing sizes, mitigating the impact of dimensional variations (Figure 50). Please note a summary of the models' physical properties as well as the Reynolds number for each model are presented in Table 3. Please note each models Reynolds number, at the models' eave height, was estimated (using Equation 3) to see if any violation could be the reason for discrepancies when comparing the different models. However, and as observed in Table 3, all three models were above the minimum value suggested ($Re=10^4$) by Cermak et al., 1999.

$$R_{eH} = \frac{V_H H}{\nu} \qquad \textit{Equation 3}$$

Where V_H is the mean wind speed at the model eave height, H is the model eave height and ν is the kinematic viscosity of air.

To make a comparison, specific wind directions were selected: 0 degree and 45 degrees. Concerning the 0-degree wind direction, the northern walls of all the models were positioned on the sheltered side (leeward), whereas the southern walls were situated on the

wind-facing side. The results revealed a notable similarity in the progression of mean pressure coefficients between the walls, indicating the absence of systematic or procedural errors in the two tests. The values for $C_{p,min}$ also exhibited consistent agreement across the two models. However, a difference arose in the evolution of $C_{p,max}$ along the northern wall (facing the wind at 0 degree) of the TPU model (as shown in Figure 51). Similarly, for the same wind direction of 0 degree, the western and eastern walls (sidewalls) demonstrated a high level of concurrence upon comparison. The values of $C_{p,max}$, $C_{p,mean}$, and $C_{p,min}$ showed uniformity along the length of the sidewalls. A deviation was noticed on the NIST west and east walls, where a decrease in $C_{p,min}$ was observed, leading to slightly lower values than the TPU and WOW models, particularly near the edge of the separated flow (depicted in Figure 52). Regarding the roof sections, $C_{p,max}$ and $C_{p,mean}$ values displayed consistent alignment between all models (as shown in Figure 53).

Upon examining the outcomes acquired at an oblique angle of 45 degrees with respect to the wind direction, it became evident that there was a strong overall alignment in the trends of $C_{p,mean}$, indicating no procedural or systematic errors between the tests. Some deviations were apparent, particularly in the context of the $C_{p,max}$ values of the TPU model along the northern and eastern walls (as illustrated in Figure 54). In terms of the side walls (west and south walls), a notable level of agreement was observed between the trends of $C_{p,max}$, $C_{p,min}$ and $C_{p,mean}$. However, there was a small departure in the $C_{p,min}$ values, where the NIST model displayed slightly lesser negative values compared to those recorded in the TPU and WOW model (Figure 55). Likewise, the roof sections of all models demonstrated a strong concordance at this specific wind direction. Nevertheless, it was noted that the roof section of the NIST model generated slightly lower $C_{p,min}$ values,

particularly along the edges of the roof in proximity to leeward areas further away from the separation edge (Figure 56).

In general, it can be affirmed that the conclusions drawn from the rectangular models in the NIST, TPU and WOW scenarios demonstrate a significant degree of concurrence, even though minor deviations have been observed in some instances. These slight disparities could be attributed to differences in the calibration procedures of the wind tunnels in the two facilities, as well as variations in the criteria employed to identify peak values using the BLUE method. This tendency can be attributed to advancements in instrumentation, including higher sampling frequencies, improvements in wind tunnel methodologies, innovations in the materials and techniques used in model construction, and progress in theoretical insights. Furthermore, such variations are commonplace in wind tunnel studies conducted at different establishments (Li et al., 2020, Ho et al., 2003 – Phase I, Ho et al., 2003 – Phase II, Gierson et al., 2015, Uematsu et al., 1999, Duthinh et al., 2015, Duthinh et al., 2017, St. Pierre 2005, and Shelly et al., 2022, Azzi et al., 2020). For example, NIST conducted a comprehensive comparison of their experiments against results from the Tokyo Polytechnic University (TPU) Aerodynamic Database. Discrepancies were also found in peak pressure coefficients; however, the agreement in mean pressure coefficients indicated the absence of procedural errors during the experiments (Ho et al., 2003 – Phase I). Additionally, NIST proceeded with testing in a second phase (Phase II) and conducted a comparison between NIST Phase I and NIST Phase II. The outcomes of the two phases also revealed disparities in peak pressure coefficients (Ho et al., 2003 – Phase II).

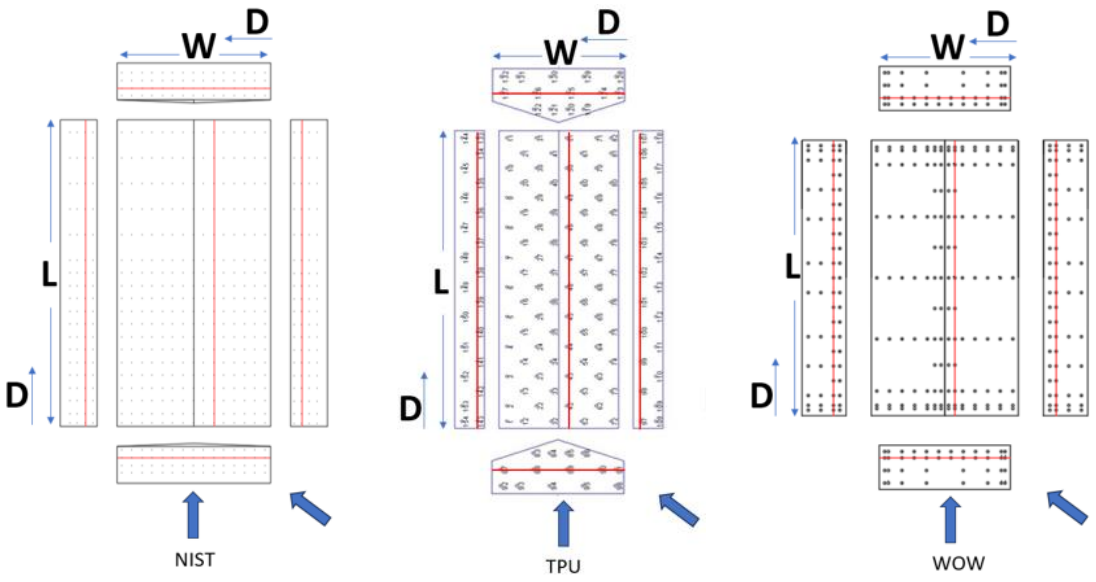

a) b) c)

Figure 50. Bisecting lines for a) NIST model, b) TPU model and c) R_{gable_2019} model (WOW)

Table 3. Models' dimensional properties and Reynolds number comparison – 2019 tests

Model	Scale	Eave height velocity V_H (mph)	Full Scale Eave Height (ft)	Full Scale Width (ft)	Full Scale Length (ft)	Roof Slope (degrees)	Reynolds Number R_H
NIST	100	20.4	12.0	50.0	100.0	2.4	2.24E+04
TPU	100	14.5	14.1	52.5	131.2	18.0	1.88E+04
WOW	50	28.3	10.0	31.2	62.5	20.0	5.18E+04

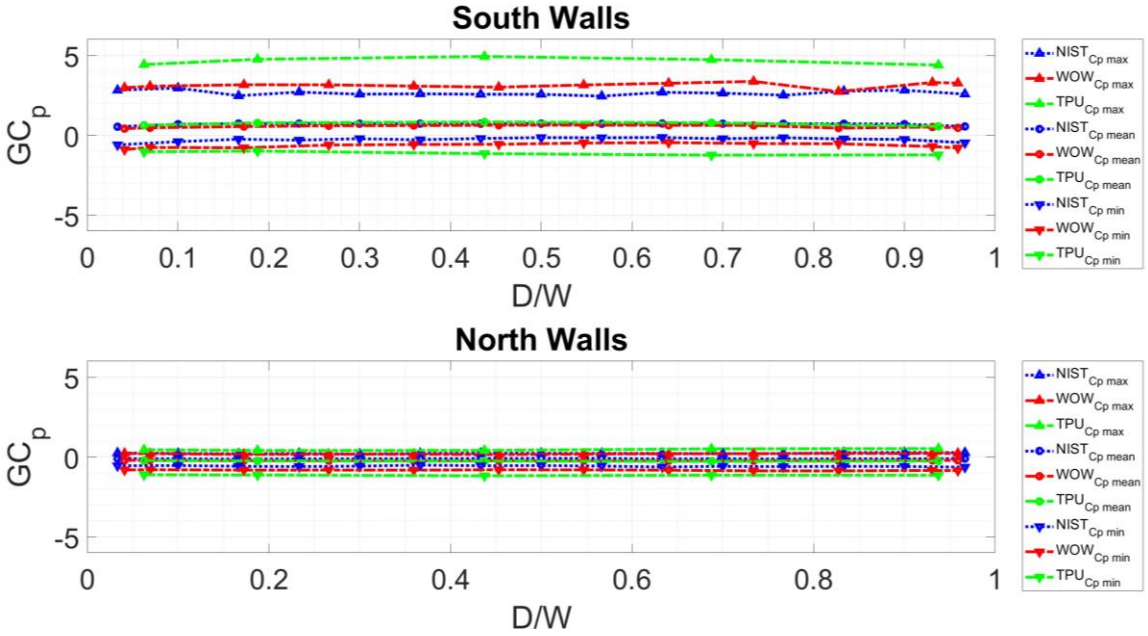

Figure 51. NIST vs WOW south and north walls - Cp max vs Cp mean vs Cp min - 0 degree.

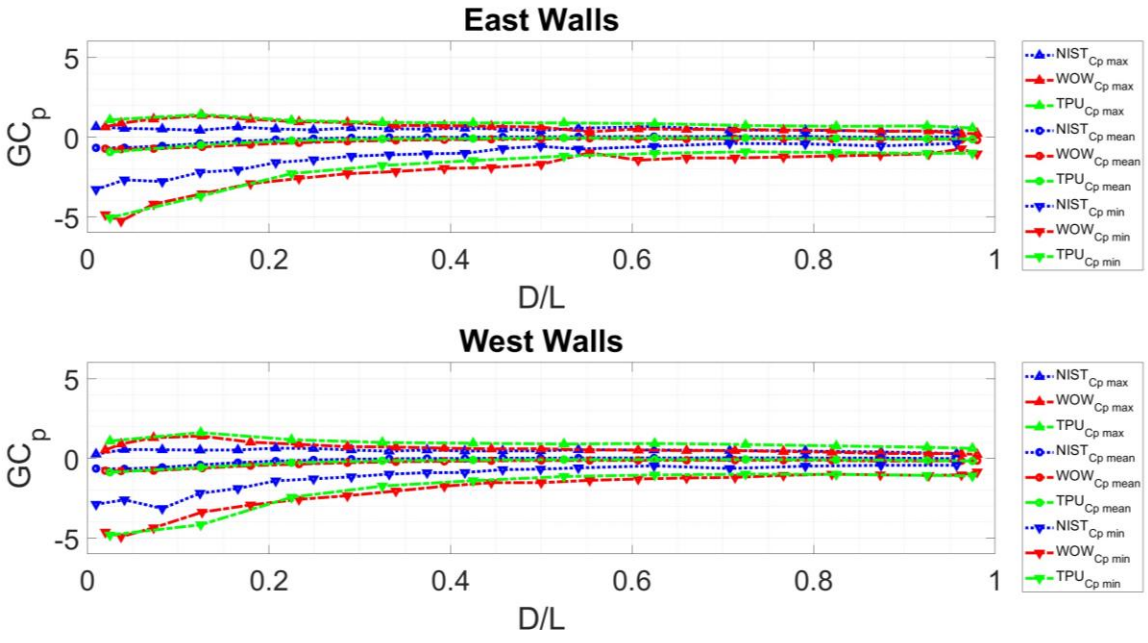

Figure 52. NIST vs WOW East and West walls - Cp max vs Cp mean vs Cp min - 0 degree.

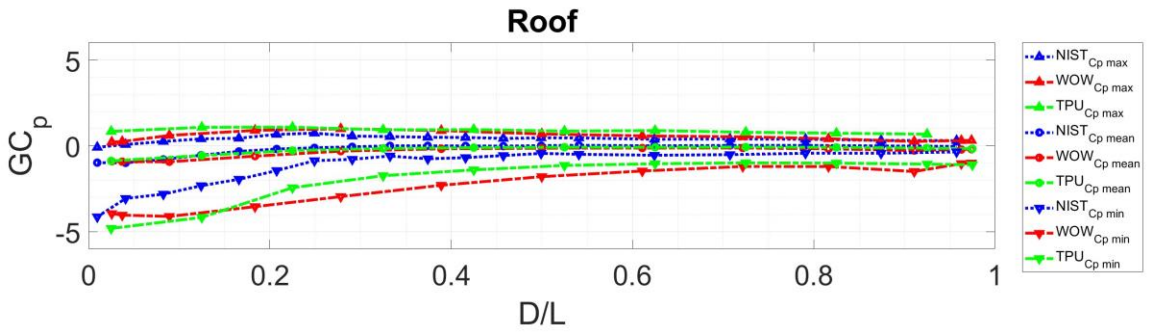

Figure 53. NIST vs WOW roofs - Cp max vs Cp mean vs Cp min - 0 degree.

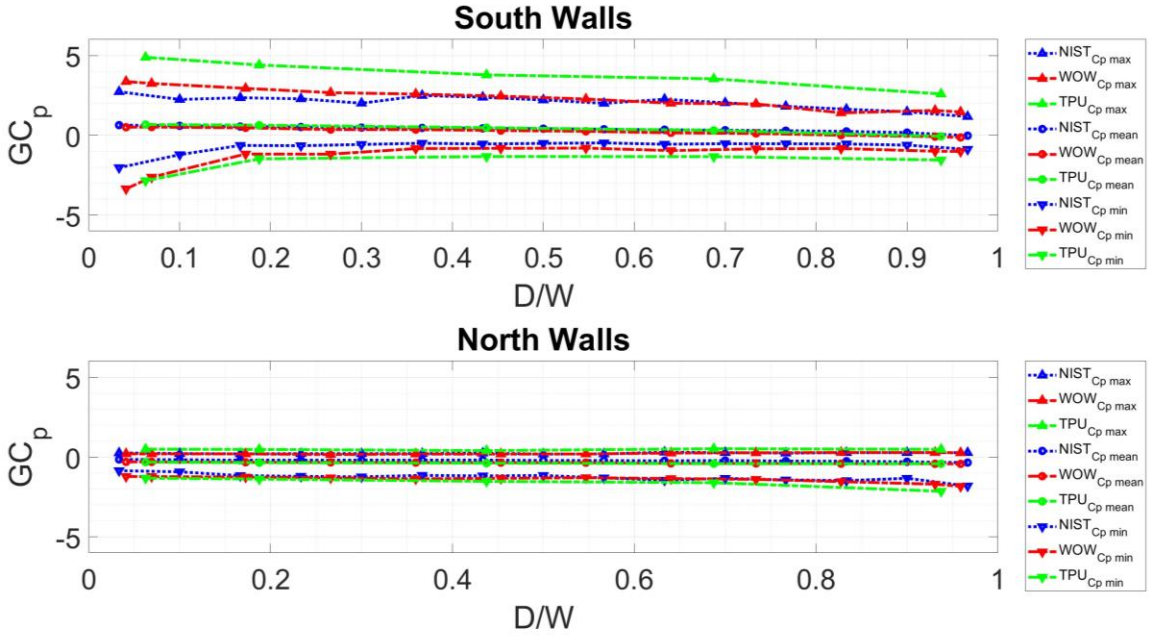

Figure 54. NIST vs WOW south and north walls - Cp max vs Cp mean vs Cp min - 45 degrees.

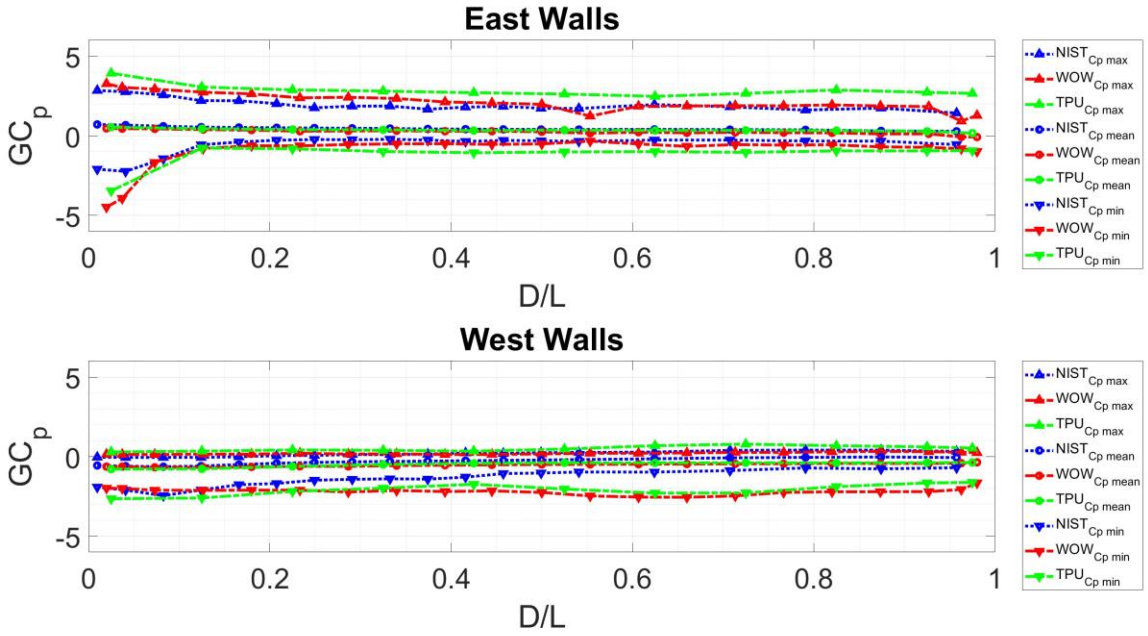

Figure 55. NIST vs WOW east and west walls - Cp max vs Cp mean vs Cp min - 45 degrees.

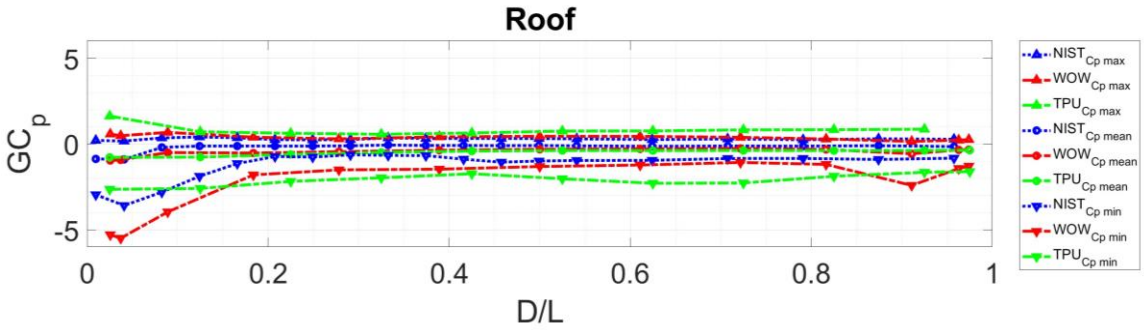

Figure 56. NIST vs WOW roofs - Cp max vs Cp mean vs Cp min - 45 degrees.

5. SMALL SCALE TESTING

5.1. ATMOSPHERIC BOUNDARY LAYER (ABL) WIND TUNNEL

5.1.1. INTRODUCTION

Wind tunnels serve as reliable tools for investigating the impact of wind loads on various structures. The dimensions of wind tunnels can differ, often directly correlating with operational expenses. Notably, at Florida International University (FIU), the Wall of Wind Experimental Facility (WOW EF) stands as a full-scale wind tunnel capable of

emulating Category 5 hurricanes, reaching speeds of 156+ mph. The wind tunnel test section measures 20 feet in width and 14 feet in height. While this size permits the testing of a diverse array of structures (Chowdhury et al., 2017), operational restrictions due to community electricity demand peaks prevent the use of the 12-fan Wall of Wind during such periods. The operation of such a facility proves immensely valuable when assessing large-scale models, particularly for dynamic analyses of entire structures or their components and potential failure modes. Nevertheless, there appeared to be a need for a more budget-friendly testing approach to accommodate a larger number of experiments.

Recognizing the value of expanding testing capabilities and accommodating the demand for experimentation with a larger number of models cost effectively, the notion of constructing a smaller Atmospheric Boundary Layer (ABL) wind tunnel emerged. This section presents an overview of the design, construction, and calibration process of a scaled-down Atmospheric Boundary Layer Wind Tunnel (ABLWT). The goal was to maximize the number of models subjected to assessment within this investigation. Through this initiative, enhanced versatility and cost-effective testing of reduced-scale models was realized.

Several design constraints were established for this wind tunnel project: 1) Space: The available space between the building walls measured 60 feet. 2) Existing Fans: Two 75 horsepower fans, with a diameter of 55 inches, were currently available for utilization. 3) Desired Test Section Dimensions: The target dimensions for the test section were 8 feet in width and 6 feet in height. 4) Fabrication Simplicity: The wind tunnel was going to be constructed by FIU students and staff, necessitating a straightforward fabrication process. 5) Mobility: The wind tunnel needed to be built in sections, for future expansion and/or

transport to another building and 6) Budget: The wind tunnel project was required to adhere to a limited available budget.

Considering all the design criteria described above, the most suitable choice for construction at the Wall of Wind Experimental Facility was determined to be an open-circuit (open jet) wind tunnel. Further details outlining the design of each component of the wind tunnel, as well as the procedures for calibration, are provided in the following sections.

5.1.2. LITERATURE REVIEW

Wind tunnels emerged as a valuable tool in the late 1800s, driven by the need to investigate the influence of fluid flow on human-made structures and components, such as wings. Prior to contemporary wind tunnels, engineers relied on mechanical whirling arms that generated a circular motion to induce flow around the object of interest. These centrifuge-like mechanical-arm devices offered valuable insights into the aerodynamic traits of various shapes under the influence of wind-induced forces at different orientations (Baals et al., 1981). Although these contraptions furnished a significant portion of aerodynamic data until the late 1880s, it became apparent that more effective methods were needed to simulate airflow.

In the late 1800s, the first wind tunnel made its appearance, and over time, its utility extended not only to the realm of aeronautics but also to civil engineering. In the domain of aeronautical wind tunnels, the focus laid on generating laminar flows characterized by minimal turbulence. Conversely, in civil engineering wind tunnels, the emphasis was on generating turbulent flows on the boundary layer of the Earth in proximity to the ground (Baals et al., 1981, Bradshaw et al., 1964).

Generally speaking, there are two types of wind tunnels. Open-circuit wind tunnels, also known as open jet wind tunnels, are characterized by drawing environmental air via an intake side and forcing it to flow through a contraction, diffuser and test section, in which models are placed, to then be expelled into the surrounding atmosphere via an exhaust end. On the other hand, closed-circuit, also known as closed-loop wind tunnels, are characterized by producing an airflow which is recirculated back into the system having the exhaust connected right back to the intake allowing almost no exchange of air with the exterior (Baals et al., 1981, Bradshaw et al., 1964, Cermak 2003). It must be noted that both wind tunnel types have pros and cons depending on factors like a) what the main purpose of the wind tunnel is, b) location of the wind tunnel, c) funding available, among others (Jimenez et al., 2020, Baals et al., 1981, Bradshaw et al., 1964, Cermak 2003, Barlow et al., 1999).

In addition, it is important to note that an open-circuit wind tunnel can be classified as either a "blow-down" or "suction" wind tunnel. In a "blow-down" configuration, the wind tunnel intakes fresh air on the intake side and channels it through interconnected components downstream of the fan housing, effectively generating high pressure. Conversely, a "suction" wind tunnel positions its fans at the exhaust side of the wind tunnel, creating a vacuum throughout the length of the tunnel to induce air flow through its components by generating low pressure (Hegade et al., 2020 - Figure 57). These wind tunnel configurations offer distinct methods of generating airflow for research purposes.

A table summarizing advantages and disadvantages of each wind tunnel type is presented below:

Table 4. Open-circuit vs closed-circuit wind tunnel advantages and disadvantages

Aspect	Open-Circuit Wind Tunnels	Closed-Circuit Wind Tunnels
Airflow Direction	One-way flow of air through test section	Continuous recirculation of air
Flow Control	Limited control on flow characteristics	Precise control on flow parameters
Turbulence	More susceptible to turbulence	Reduced turbulence due to controlled flow
Applicability	Suitable for low-speed testing	Well-suited for high-speed testing and detailed research
Complexity	Simpler design and construction	More complex design and higher costs
Test Section Size	Suitable for larger test sections	Limited to smaller test sections
Applications	Some natural airflow simulation	Controlled and specialized research
Cost	Generally lower construction and maintenance costs	Higher construction and maintenance costs
Flexibility	Less flexibility in controlling flow conditions	High flexibility in controlling various flow parameters
Power	Requires more energy to run	Requires less energy to run
Noise	Generally noisier	Generally quieter
Smoke Visualization	No purging required	Purging is required
PIV	Constant seeding during experiments	Reduced seeding due to recirculation

Multiple publications have been made available for the design of wind tunnels. It must be noted that all wind tunnels vary in size, flow conditions, number of fans, maximum wind speed, location of the wind tunnel within a building, among others. All these factors drastically influence the resulting wind tunnel design and therefore it was found that a "direct" or "step-by-step" procedure for the successful design of a wind tunnel is not possible. For this reason, a considerable number of publications on wind tunnel design were studied taken into consideration for the design of a small-scale atmospheric boundary layer wind tunnel at the Wall of Wind Experimental Facility (Mauro et al., 2017, Cattafesta et al., 2010, Van Dommelen 2013, Kulkarni et al., 2011, Carlson et al., 1967, Johnston et al., 1969, Mehta 1979, Reid 1953, Vogel 1968, Mehta et al., 1979, Bell et al., 1988, Marshall 1985, Chowdhury et al., 2017, Matus et al., 2021).

For this research, an open-circuit blow-down wind tunnel was selected as the best option considering all the constraints as well as the available funding. Having decided the type of wind tunnel to be designed and constructed, a list of all the wind tunnel components was generated to design them accordingly. An open-circuit blow-down wind tunnel consists of (from intake to exhaust):

a) "Fans" to generate air flow

b) "Diffuser" to generate a reservoir of air to achieve a constant flow

c) "Settling Chamber" to pre-treat flow and remove any induced effects from fans

d) "Contraction or Nozzle" to contract the flow and speed it up

e) "Fetch" to treat the flow and achieve naturally occurring properties

f) "Test Section" to house the models to be tested

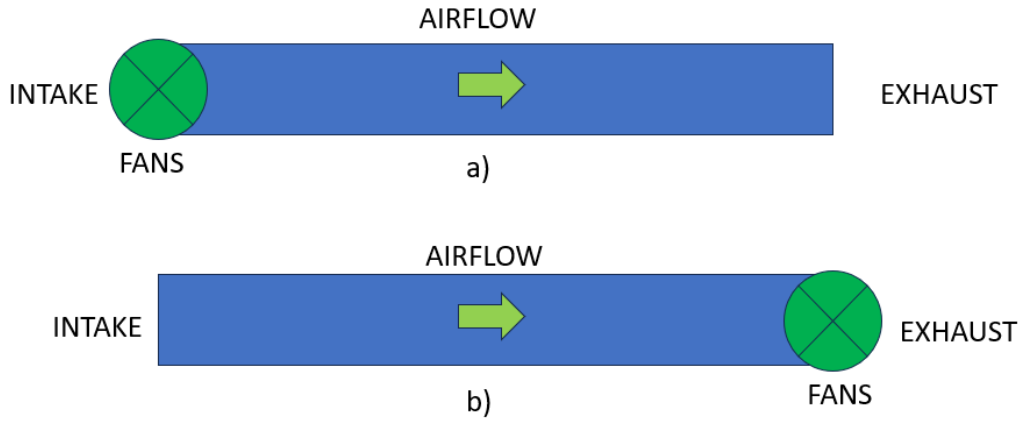

Figure 57. Open-circuit wind tunnels: a) blow-down vs b) suction wind tunnel

5.1.3. DESIGN CRITERIA

Atmospheric Boundary Layer (ABL) wind tunnels constitute a valuable resource for exploring the impacts of wind on civil infrastructure. These apparatuses encompass multiple components that enable the creation of wind and the characterization of its properties to replicate natural atmospheric conditions.

5.1.3.1. FANS

Typically, selecting a fan for a wind tunnel design is the last task as airflow, static pressure, and mounting and dimension restriction data are required before making the selection. In this case, primarily budget constraints forced the use of two existing vane-axial fans no longer used in another wind tunnel on site. The static pressure and airflow limits within a reasonable efficiency range for the fan are a design constraint for the tunnel design.

The specific model fan was an AVD-1400 / 578-10, which means it had a hub diameter, d = 22.75 in (578mm), housing diameter, D = 55.1 in (1400mm) and 10 impeller blades that could be manually set to any angle between 25 and 60 degrees. The higher the

angle the more energy will be imparted to the air for a given rotational speed. The rotational speed may be varied with a variable frequency control not to exceed 1553 RPM per the manufacturer's specifications. The performance of the fan at a given RPM was presented by the manufacturer as a graph of static or total pressure vs airflow for the range of blade angle and may also include power consumption. A performance curve was developed by the manufacturer by testing the fan with a downstream duct that varies between "free delivery" (outlet resistance is near zero) and completely blocked. Figure 60 shows the manufacturer's performance curve for the fan turning at 1120 RPM. A specific operating point is shown in red, with an airflow of 63,360 cfm, velocity pressure of 0.92 in. of water, and static pressure of 2.0 in. of water. For this airflow and total pressure, the blade angle would have to be set to 49°, the efficiency would result to be 80%, and the corresponding power consumption would reach 37 hp which must not be greater than the motor output power, 75 hp. Note that since there were two fans, all performance curves were applied to half the total wind tunnel load pressure and airflow.

The operating point described above was chosen for illustrative purposes based on a downstream duct size of 48 ft^2 with dimension 6 ft high and 8 ft wide, the desired test section dimensions, and an average velocity through the section of 44 ft/s (13.41 m/s) for a total airflow of 48 ft^2 x 44 ft/s x 60 s/m = 126,720 cfm driven by two fans or 63,360 cfm per fan. To determine a maximum airflow and corresponding static pressure that the fan could deliver based on the manufacturer's tested performance curve at 1120 RPM, a blade angle of 60° and airflow of 85,000 cfm would support a total pressure of 3.45 in of water of which 1.65 in of water is velocity pressure, and result in a power consumption of 65 hp. For the two fans, the total static pressure load would be 3.6 in of water. Any further airflow

increase would quickly reduce the static pressure supportable.

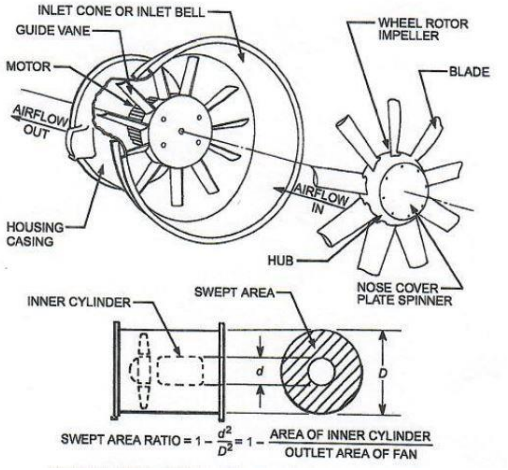

Figure 58. Vane-axial Schematic

Figure 59. Vane-axial existing fans

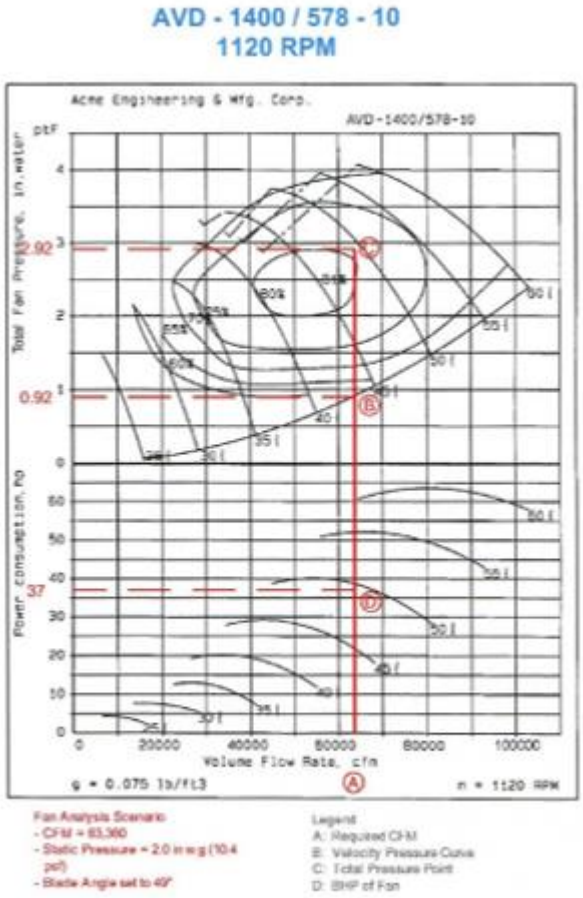

Figure 60. Fan power consumption

5.1.3.2. DIFFUSER

Taking into consideration the constrains in design, with respect to space and size, a conventional diffuser with a small diffuser angle ($2\theta < 6^{o}$) would be impractical. Here, the term "diffuser angle" (Mehta 1979), is the larger of the two cone angles with respect to the plan view and the elevation of the diffuser. Hence, a wide-angle diffuser ($2\theta < 6^{o}$ (Mehta 1979)) with additional devices for boundary layer control was adjudicated to be the best alternative. To design the diffuser, the size and shape requirements, as well as the angle of the diffuser and screens were taken into consideration. 1) Size and shape requirements: The total area of the fans (inlet area) was $A_1 = 36.19\ ft^2$, considering two fans of 4.8 ft diameter. The diffusers were required to be able to increase the cross-sectional area of flow to $A_2 = 96.00\ ft^2$ (8 ft × 12ft). Hence, the area ratio A of the diffuser was 2.65 (A_1/A_2). Since the length needed to be as short as possible, the diffuser angle also needed to be as large as possible. The plan dimensions of the diffuser would diverge from a width of 9.6 ft (4.8 ft × 2) of the fans to a width of 12 ft of the settling chamber. The height of the diffuser would diverge from 4.8 ft to 8 ft. Since the ratio of change in dimension was greater for the height ($\frac{h_2}{h_1} = 1.67$) it would govern the definition of the diffuser angle as well. The walls of the diffuser were straight, and the cross section was assumed to remain rectangular throughout. 2) Diffuser angle: A safe limit for the maximum diffuser angle was considered to be 55^{o} (Mehta 1979). This was based on several previously successful wind tunnels. 3) Screens as boundary layer control devices. Screens are a popular method of boundary layer control. Perforated metal or woven wire gauge screens may be considered for use here. It is recommended that the pressure drop coefficient, K for each screen be relatively low (1-2). Several screens placed at key locations are more effective than having a single screen with

a large K value. Screens are to be placed at the inlet, outlet, and any other location within the diffuser where the angle diverges. An empirically obtained limit for K_{sum} was recommended by Mehta 1979 (Equation 4), with K_{sum} resulting in a value of 1.45.

$$K_{sum} > \frac{(A-1)}{1.14} \qquad \textit{Equation 4}$$

A minimum of 2 screens (one at the outlet and one at the inlet) were considered, with each having a pressure drop coefficient of at least 1.0. Curved screens have been observed to perform better than straight screens and are preferred. The curved screens meet the diffuser walls at right angles.

To further ensure an unseparated flow, the diffuser angle can be diverged in two steps. In such a design (Figure 61), a screen would be needed at the inlet, the outlet and at the section where the angle diverges. The elevation and plan sections of the proposed diffuser are shown in Figure 61 and Figure 62 respectively.

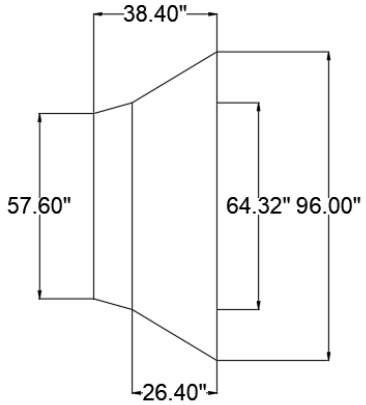

Figure 61. Diffuser with divergence in two steps (elevation view)

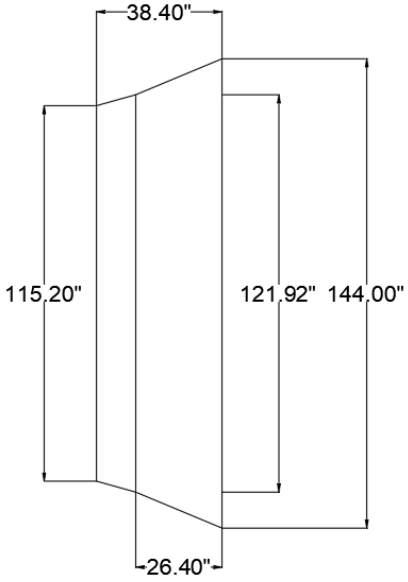

Figure 62. Diffuser with divergence in two steps (top view)

5.1.3.3. SETTLING CHAMBER

The Settling chamber is another very important component within an ABL wind tunnel, aiding in the preparation of the flow before it enters the fetch section. Typically, this chamber comprises two principal elements: a) honeycomb, and b) screens. Due to the rotational motion of the fan impeller blades, flow swirls may manifest. Additionally, diffusers with angles exceeding 10 degrees can induce flow separation that are carried to the flow. The primary objective of the settling chamber was to rectify any swirl and/or flow separation that may have arisen from the fans or within the diffuser. Empirical findings indicate that a honeycomb with three screens downstream significantly diminishes mean flow non-uniformity and turbulence intensities to acceptable thresholds (Kulkarni et al., 2011). It is noteworthy that the honeycomb aided in mitigating fluctuations perpendicular to the flow, while screens contributed to the breakdown of large-scale turbulence into smaller eddies, reducing axial velocity non-uniformity.

In the process of selecting the optimal honeycomb, the crucial dimensions to consider were the cell diameter and length. To minimize pressure loss, the honeycomb's diameter was recommended to be the Hydraulic Diameter of the settling chamber ($D_{sett\ chamber}$) divided by 150, which represents the optimal number of honeycomb cells per settling chamber diameter (Mehta et al., 1979, Barlow et al., 1999). The Hydraulic Diameter of the settling chamber was determined to be approximately 9.6 feet, resulting in a honeycomb cell diameter of around 0.75 inches (Equation 5). Furthermore, a cell diameter ratio of 8 to 10 was deemed optimal, effectively reducing turbulence intensity with minimal losses. For the selected honeycomb, based on the estimations and commercially available options, a hexagonal cell with a diameter of 0.75 inches and a length of 7.9 inches was chosen. The honeycomb's porosity should not fall below 80%.

$$D_{set\ chamber} = \frac{2WH}{W + H} \qquad \textit{Equation 5}$$

Where W and H are the width and height of the exit of the diffuser

In the design of this wind tunnel, the inclusion of three screens was proposed. Typically, screens are positioned downstream of the honeycomb, with the coarsest screen closest to the honeycomb and the finest screen just before the contraction section. Screen wire diameters of 1.5, 1.0, and 0.5 mm were selected for this wind tunnel.

To maintain appropriate spacing, a gap of about 10 in was maintained between the honeycomb and the first screen, with the same gap maintained between screens during the screen-to-screen separation (Kulkarni et al., 2011). Other references suggest that the distance between the first screen and the diffuser should be within the range of 0.1 to 0.2

times the settling chamber's hydraulic diameter (Van Dommelen 2013). A diagram depicting the arrangement of the honeycomb and screens provides an overall length requirement for the settling chamber to accommodate all the components (Figure 63).

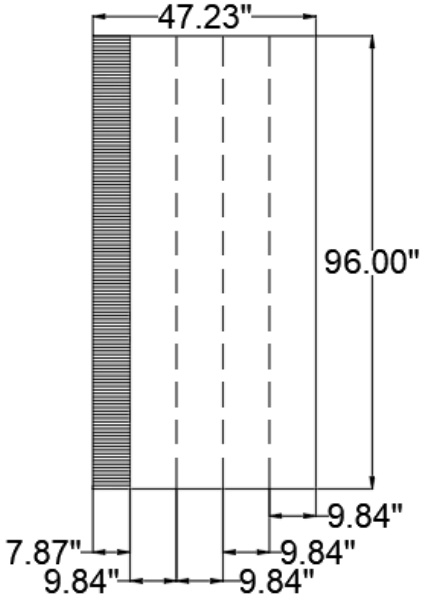

Figure 63. Settling chamber elevation view and positioning of honeycombs and screens

5.1.3.4. CONTRACTION

The primary objective of the contraction section, also referred to as the nozzle, is to accelerate the flow emerging from the settling chamber, generating a uniform flow velocity profile that is suitable for use in the test section (Mauro et al., 2017, Barlow et al., 1999). This uniform flow generation involves reducing both the mean and fluctuating velocity deviations to a smaller proportion of the average velocity (Mehta et al., 1979). The design of this section was of paramount importance due to its crucial role in ensuring flow uniformity for the testing chamber.

In the design for this wind tunnel, the target was to establish a test section with dimensions of 8 by 6 feet (width and height). The determination of the area ratio for the contraction section was based on two key considerations: 1) Ensuring a sufficiently ample

area to adhere to the 2:1 reservoir ratio for the fan openings, and 2) Choosing a width and height that would minimize the required length for the contraction section, mainly due to spatial limitations. As previously mentioned, the wind tunnel fans had a diameter of 58 inches, with a combined intake area of 37 square feet and a settling chamber area of 96 square feet, resulting in a fan-to-reservoir-area ratio of 2.6:1. For the contraction section, the inlet area matched that of the settling chamber (96 square feet), and the test section possessed an area of 48 square feet, yielding an area ratio of 2:1.

The shape of the contraction section holds significance as it necessitated a design that avoided flow separation (Mehta et al., 1979). Marshall (1985) proposed that the contraction profile can be represented using Equation 6, wherein 'x' denotes the distance measured from the nozzle inlet to the outlet, 'h' signifies the disparity in height between the nozzle's inlet and outlet, and 'L' stands for the total length of the contraction section. Figure 64 illustrates the profile of the contraction section, encompassing all the required dimensions.

$$Y(x) = -3h\left(1 - \frac{x}{L}\right)^4 + 4h\left(1 - \frac{x}{L}\right)^3 \qquad \text{Equation 6}$$

Parameters description shown in Figure 64

Considering the test section's desired dimensions of 8 by 6 feet (width and height) and factoring in the area ratio linking the fans' openings to the settling chamber, along with the crucial ratio between the inlet and outlet of the nozzle, the dimensions for the contraction section were approximated to be 12 by 10 feet at the inlet (outlet dimension of settling chamber) and 8 by 6 feet at the outlet (desired test section dimensions). For determining the value of 'L', Bell et al., 1988 offers an estimation wherein the ratio of the

inlet dimension to the length of the contraction zone should ideally approach 1, as denoted by Equation 7. To navigate space limitations, a decision was made to maintain a ratio of 0.83 (top view) and 1.25 (side view) for Equation 7. This decision was primarily driven by the need to design two profiles - the top view and side view profiles. The ultimate configuration of this section is visually depicted in Figure 65, while Figure 66 provides a 3D representation of the contraction section.

Figure 67 presents both the elevation and top view of the constructed atmospheric boundary layer wind tunnel. In Figure 68, the step-by-step assembly of various wind tunnel sections can be observed, including fans, diffusers, settling chambers, contractions/nozzles, and the fetch section. Furthermore, Figure 69 displays the components of the fetch section and the test section. For instance, figures a) to c) illustrate the installation process of the turntable, while figures d) and e) depict the elements used to set up the roughness features. It's important to note that metal sheets were affixed to the floor surface to enable the magnetic attachment of the roughness elements, streamlining the process of adjusting the exposure more efficiently and rapidly. Additionally, figure f) displays the spires and the baseboard situated at the interface between the end of the contraction section and the beginning of the fetch section.

$$\frac{L}{2Y} \cong 1 \qquad \textit{Equation 7}$$

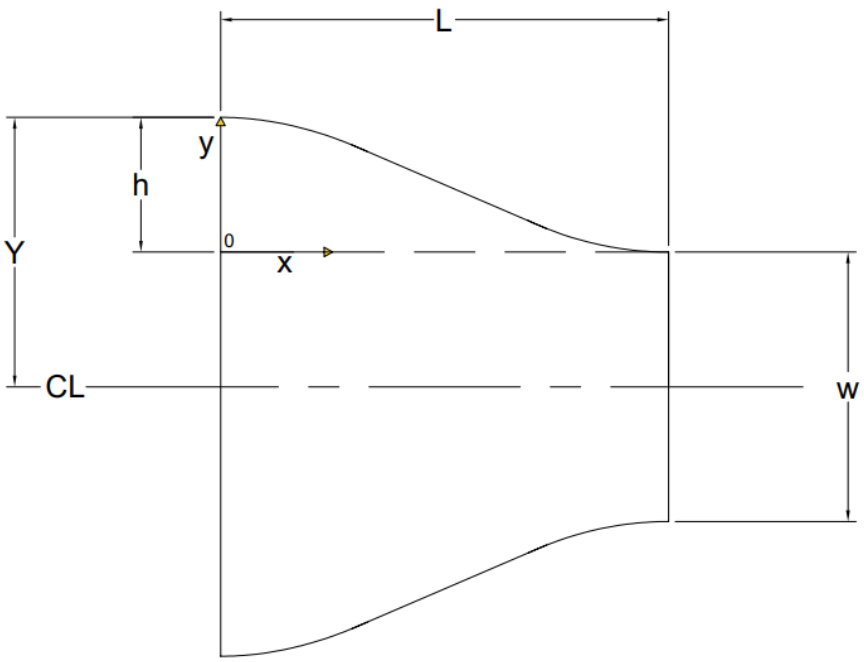

Figure 64. Contraction Profile (Marshall 1979)

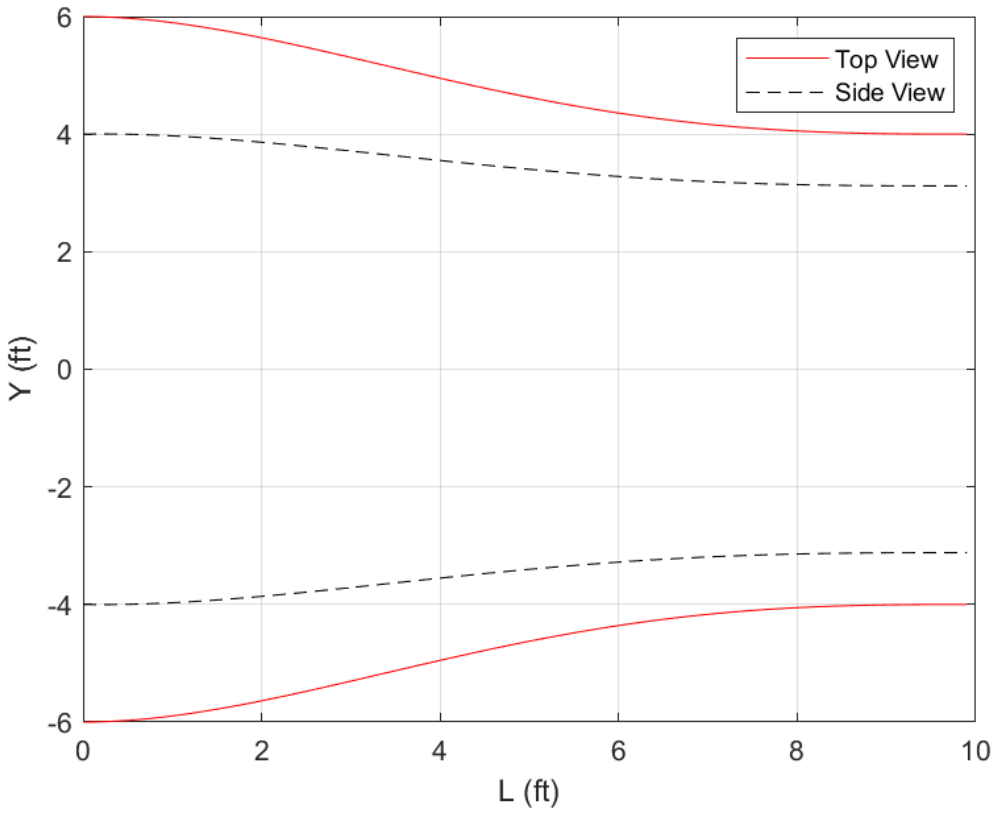

Figure 65. Contraction section profiles (top view vs side view)

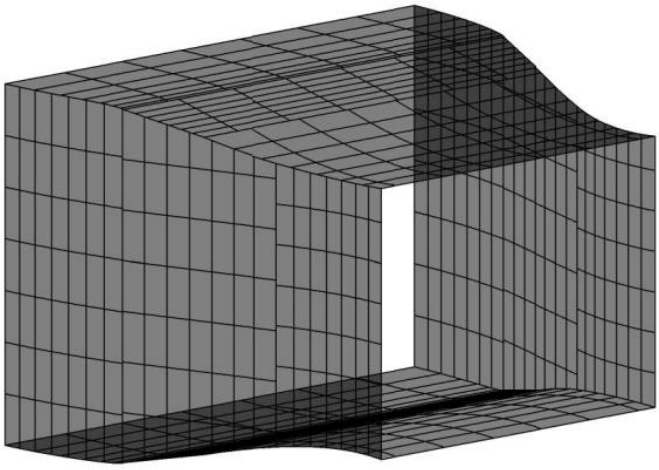

Figure 66. 3D drawing of contraction section

5.1.4. FINAL DESIGN

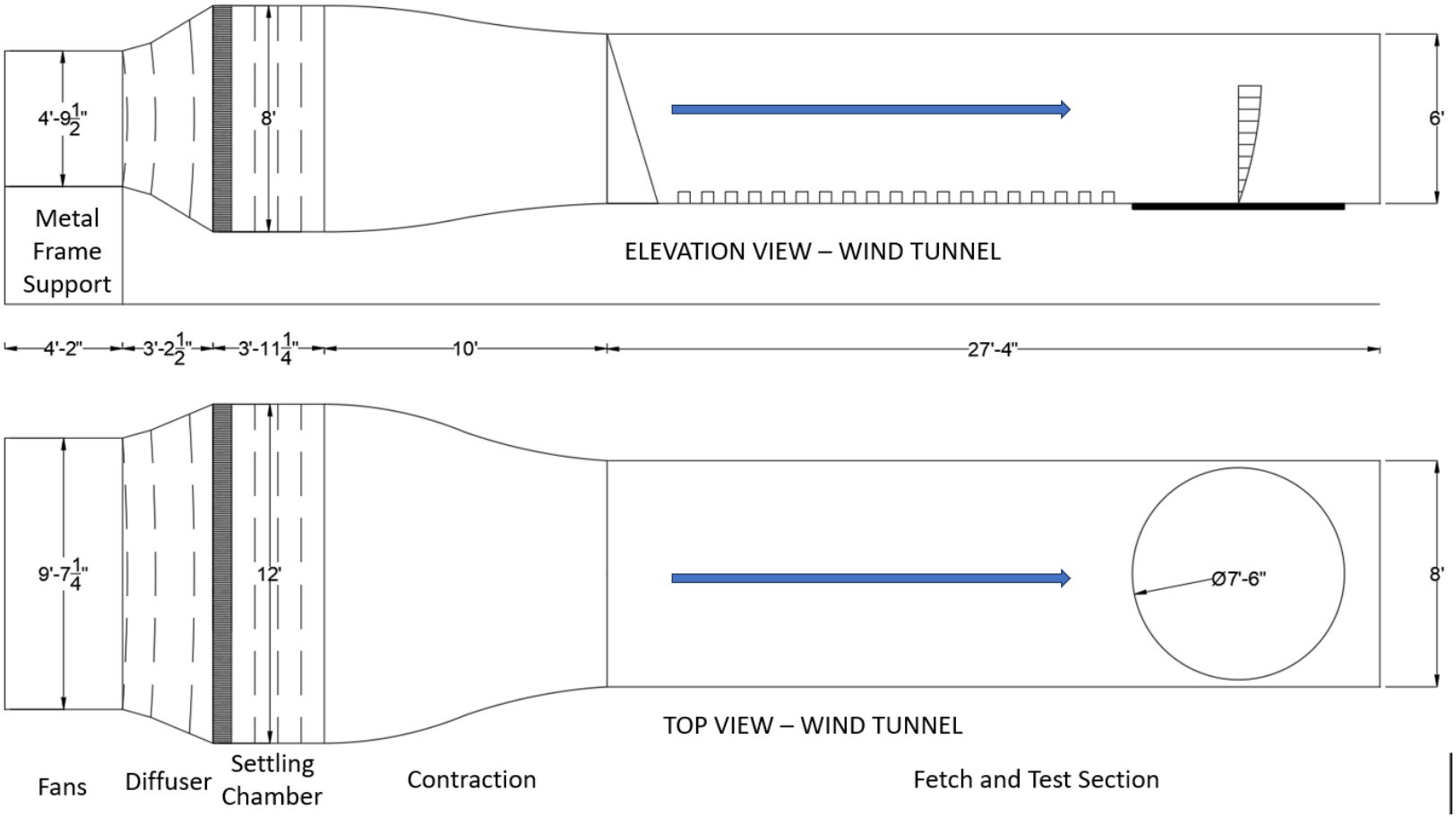

Figure 67. Atmospheric boundary layer wind tunnel: Elevation and Top views.

a)

b)

c)

d)

e)

f)

g)

h)

i)

Figure 68. Atmospheric boundary layer wind tunnel sections (progressive): a) Fans and Diffuser, b) Diffuser and Settling Chamber, c) Contraction (uncompleted), d) Contraction (uncompleted), e) Contraction (completed), f) Fetch (1 section), g) Fetch (2 sections), h) Fetch (2 sections), i) Wind Tunnel (completed).

a)

b)

c)

d)

e)

f)

Figure 69. Atmospheric boundary layer wind tunnel flow management and test section: a) Turntable (uncompleted), b) Turntable (mounting), c) Turntable (completed), d) Fetch with metal sheet, e) Fetch with magnetic roughness elements, f) Spires and Baseboard.

5.1.5. CALIBRATION

Subsequent to the design and construction of the wind tunnel, the initial phase involved conducting wind field measurements to assess the smoothness (or turbulence) of the generated flow in the absence of Settling Chamber screens and Honeycomb. At this juncture, only the wide-angle diffuser screens had been installed. In order to accomplish this, measurements were taken at five distinct points positioned in front of the turntable, with the fan operating at 50% throttle. A rake equipped with pitot tubes (connected to a Scanivalve DSA-3217-16Px pressure scanner) and cobra probes was employed to capture wind-related data. The pitot tubes were positioned at heights of 1, 2, 3, 5, 7, 9, 21, 26, 31, 36, 41, 46, 56, and 71 inches. Additionally, four Cobra Probes were set up at heights of 4, 18.5, 38.5, and 64.5 inches from the floor (as illustrated in Figure 70, Figure 71 and Figure 72).

Analysis of the mean wind speed findings revealed that the wind field generated by the wind tunnel, operating at 50% throttle, and solely equipped with diffuser screens, exhibited symmetry across horizontal locations. Vertically, the wind measurements obtained from the wind tunnel demonstrated strong agreement and minimal variation. Notably, the interaction with the floor influenced wind speed development up to a height of 4 inches, generating a wind field reaching approximately 11 m/s from the 5-inch mark to around 67 inches. Also, upon examining the turbulence intensity outcomes, it was observed that in the absence of honeycombs and Settling Chamber screens, the wind tunnel's turbulence intensity remained below 5% at heights above 4 inches. However, at and below the 4-inch mark, turbulence intensity was noted to increase to approximately 7.5%, primarily due to interactions with the floor (as depicted in Figure 73).

Upon the installation of the Settling Chamber screens and honeycomb, the wind tunnel initiated its calibration process. This calibration involved the design of two primary components: spires and floor roughness. Both the spires and roughness elements were designed following the methodology outlined in Irwin's 1981 work. It is worth highlighting that according to Irwin's recommendations, the length of the fetch section should be at least six times the height of the spires. However, due to this constraint, the wind tunnel faced challenges in achieving the anticipated wind field development through the spires and floor roughness design.

In pursuit of creating an open terrain wind tunnel exposure, the baseline design inspired by Irwin's 1981 guidelines underwent slight modifications, along with an iterative process. A baseboard was introduced at the base of the spires during the calibration process. This addition aimed to mitigate flow near the floor and enhance turbulence intensity, as demonstrated in prior research (Ghazal et al., 2019; Ghazal et al., 2020; Vita et al., 2018). Through multiple iterations, the calibration process led to the establishment of an open terrain configuration that exhibited reasonable wind speed (U) and turbulence intensity (Iu) profiles, as depicted in Figure 74. It is important to note that the wind tunnel was originally designed to test irregularly shaped models at a 1:100 scale, with a model height equivalent to 1.4 inches (representing 12 feet at full scale), as shown in Figure 74. In addition, the $1/\alpha$ value from the wind speed measurements was estimated to be 0.11, which agreed with the value provided by ASCE 7-22.

To assess the wind tunnel setup's capability to generate various eddy sizes, a Power Spectrum Density (PSD) profile was generated at the model height of approximately 1.4 inches (scaled at 1:100). Analyzing the results (Figure 75), it was apparent that the wind

tunnel possessed the capacity to reproduce the full range of turbulence content found in naturally occurring wind. This aspect holds significance, as encompassing all frequency components within the wind characteristics instills confidence in the simulation results. This comprehensive wind simulation approach ensures the generation of realistic loading, encompassing both low- and high-frequency responses.

Figure 70. Wind tunnel without screens, honeycombs, spires, roughness elements and baseboard

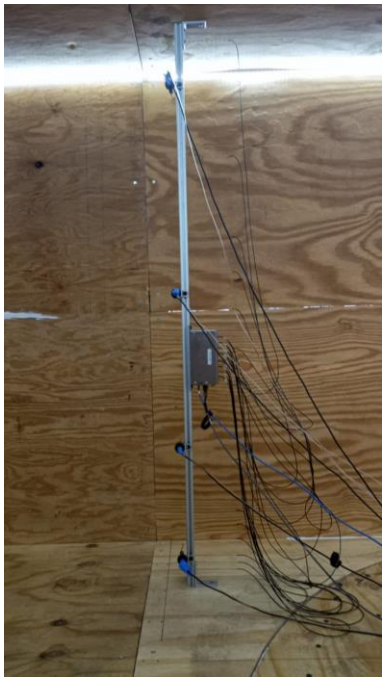

Figure 71. Wind field measurement rake

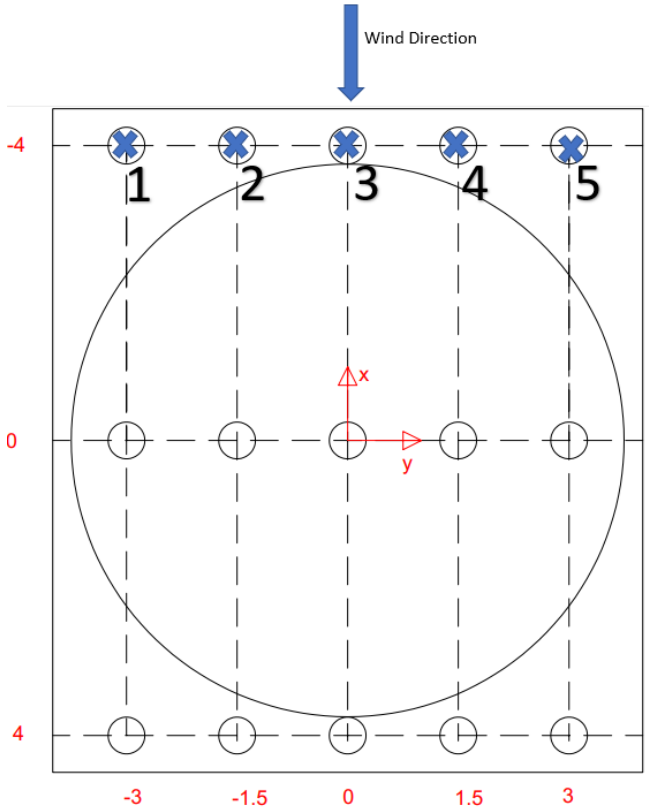

Figure 72. Measurement points

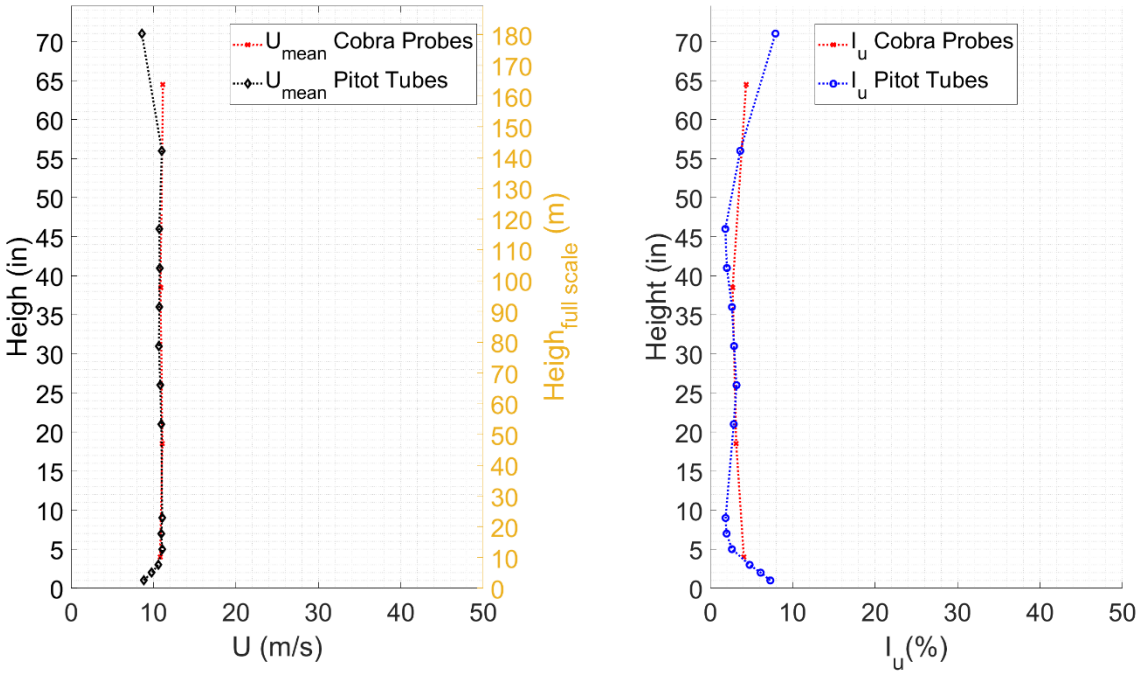

Figure 73. Wind speed and turbulence intensity profiles at location 3 (see Figure 72)

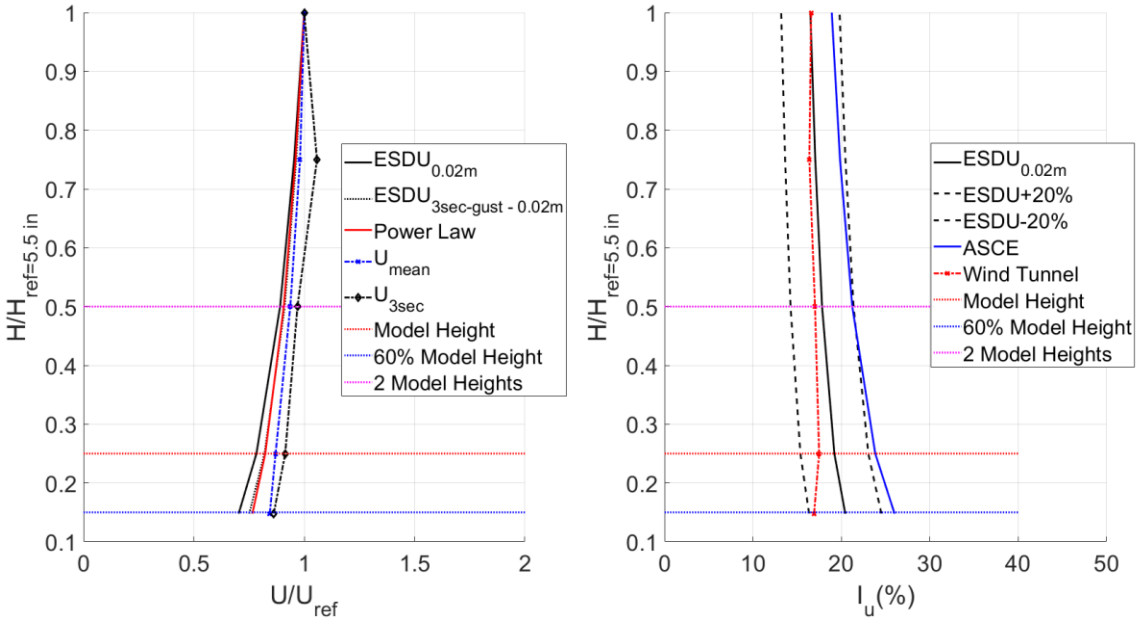

Figure 74. Wind speed and turbulence intensity profiles at turntable center – open terrain

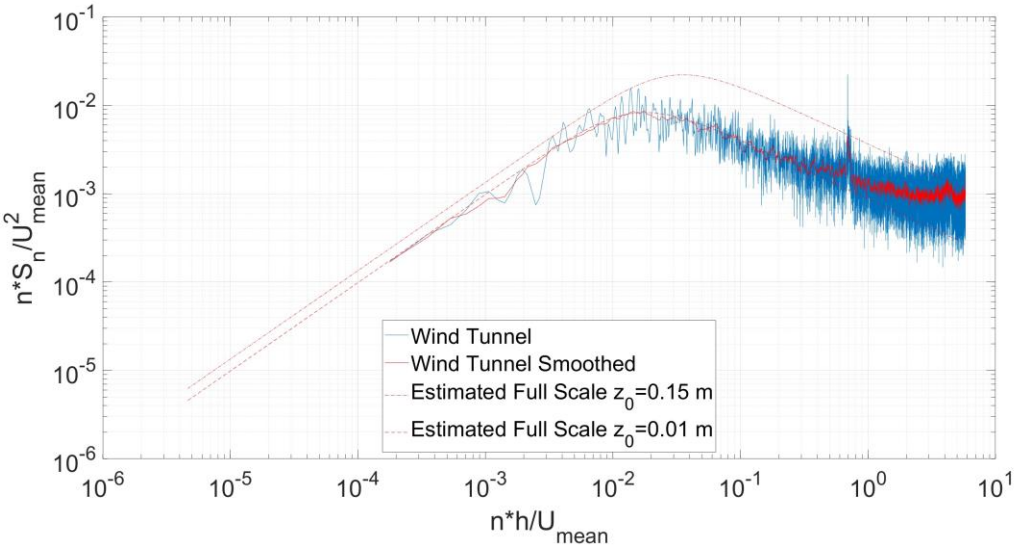

Figure 75. Power Spectrum Density (PSD) profile at H=1.375 inches (mean roof height)

5.2. MODELS

Drawing from previous insights derived from satellite imagery, several irregularly shaped models were fabricated, differing in their aspect ratios compared to the large-scale tests conducted in 2019 and 2020 (see Section 4). For the sake of simplicity, these models are denoted by the years of their testing, namely 2021 and 2023. The new models were

carefully crafted to reflect more lifelike aspect ratios, reducing the exaggeration in dimensions and protruding sections. Furthermore, the model areas adhered to a similar approach as seen in the design of the large-scale tests, targeting a full-scale area ranging between 1100 to 2000 square feet. In both phases (2021 and 2023), rectangular models were created to serve as the baseline for comparison and validation against publicly available aerodynamic databases, such as NIST (Ho et al., 2003 – Phase II). The dimensions for all five models are detailed in Figure 76 through Figure 80, with all measurements provided in inches and scaled down at a ratio of 1:100. Notably, all irregularly shaped models were produced using a Fused Deposition Modeling (FDM) 3D printer with Polylactic Acid (PLA) filament material, whereas the rectangular model was assembled using laser-cut plexiglass sheets.

In the context of the 2021 models (phase A), a comprehensive set of five models were conceptualized, fabricated, and subjected to testing. Among these, four took on irregular shapes, namely the T-, L-, C-, and a newly discovered common S-shape (as detailed in Figure 76 to Figure 79). Model $T1_{hip\_2021}$ was instrumented with 331 pressure taps meticulously positioned across all its walls and roof sections. This model represented a total full-scale area of 1200 square feet (as depicted in Figure 76). On a similar note, Model $L1_{hip\_2021}$ featured 333 pressure taps, with the overall full-scale area amounting to 1155 square feet (as indicated in Figure 77). The third model, $C1_{hip\_2021}$, was equipped with 363 pressure taps distributed across its walls and roof sections and represented a total full-scale area of 1610 square feet (as represented in Figure 78). Meanwhile, Model $S1_{hip\_2021}$, encompassing a total of 367 pressure taps thoughtfully distributed across all its walls and roof sections, exhibited a full-scale area of 1410 square feet (as illustrated in Figure 79). In

addition to these four diverse shapes, a rectangular model named R_{gable_2021} was also constructed. This model, designed to mirror the dimensions of the NIST model utilized for comparison within the large-scale section, was outfitted with 330 pressure taps positioned across all its walls and roof sections (as illustrated in Figure 80). All the irregular shaped models were conceptualized with hip roofs, while the rectangular model had gable ends only.

Concerning the 2023 models (phase B), a comprehensive set of ten models were conceptualized, fabricated, and subjected to testing. The series included eight low-rise irregularly shaped models and two rectangular models - one of each with a gable roof and the others with hip roof ends. The eight irregular shaped models encompassed four distinct shapes, four models featuring gable roofs and four models designed with hip roofs. The specific dimensions for each of these ten models can be observed in Figure 81 through Figure 90, all presented in inches and scaled down at a ratio of 1:100. In this iteration of tests, the models' dimensions were further fine-tuned to encapsulate various variations observed in real-world scenarios. For example, the C and S models in phase A were adjusted compared to their counterparts in phase B. Notably, the latter (phase B) featured unsymmetrical designs in their protruding sections (Figure 86 and Figure 88), differing from the layout of models $C1_{hip\text{-}2021}$ and $S1_{hip\_2021}$ (Figure 78 and Figure 79). Furthermore, the protruding sections in these models were intentionally less pronounced than those found in the models tested in the large-scale section (Figure 8 to Figure 13), as well as the models examined in the small-scale phase A (Figure 76 to Figure 79). Moving on to specifics, models $T1_{gable\_2023}$ and $T2_{hip\_2023}$ were equipped with 227 and 229 pressure taps, distributed across all walls and roof sections. These models represented a full-scale

structure with an area of 1410 square feet (depicted in Figure 81 and Figure 82). For models $L1_{gable\_2023}$ and $L2_{hip\_2023}$, pressure taps numbering 233 and 221, respectively, were incorporated. These two models featured a total full-scale area of 1410 square feet (as depicted in Figure 83 and Figure 84). Meanwhile, models $C1_{gable\_2023}$ and $C2_{hip\_2023}$ were outfitted with a total of 270 and 263 pressure taps, distributed across walls and roof sections, and exhibited a full-scale area of 1624 square feet (as illustrated in Figure 85 and Figure 86). As for models $S1_{gable\_2023}$ and $S2_{hip\_2023}$, these structures employed a total of 257 and 237 pressure taps on walls and roof sections, respectively. The full-scale representation of these models was an area of 1424 square feet (depicted in Figure 87 and Figure 88). Lastly, models $R1_{gable\_2023}$ and $R2_{hip\_2023}$ were equipped with 160 and 158 pressure taps, respectively (as shown in Figure 89 and Figure 90). All ten models were 3D printed with a Stereolithography (SLA) printer with a high temperature resistant and anti-deformation resin.

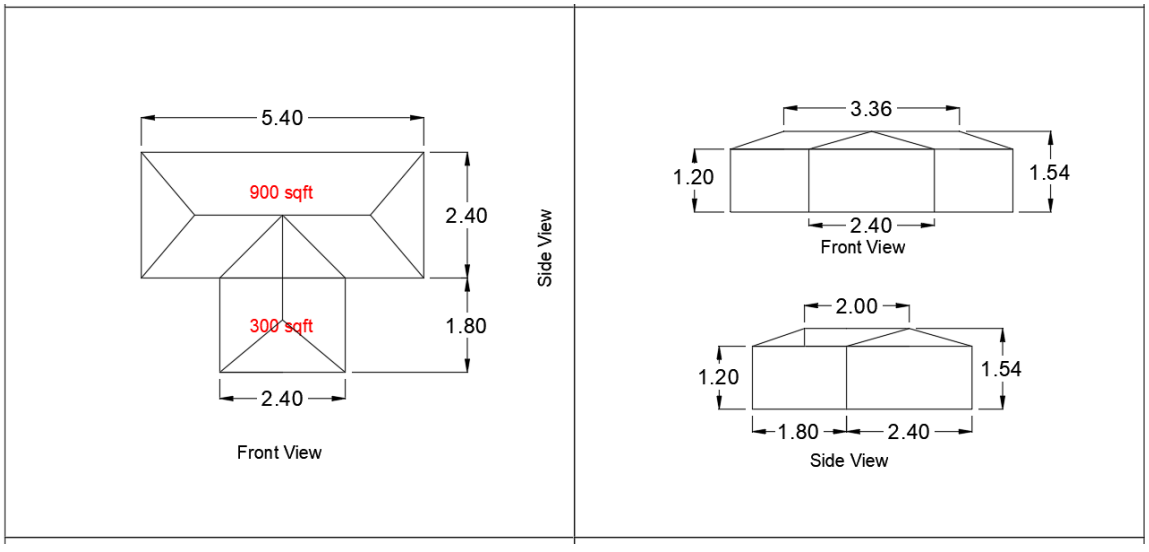

Figure 76. Model $T1_{hip\_2021}$ dimensions (top and elevation views)

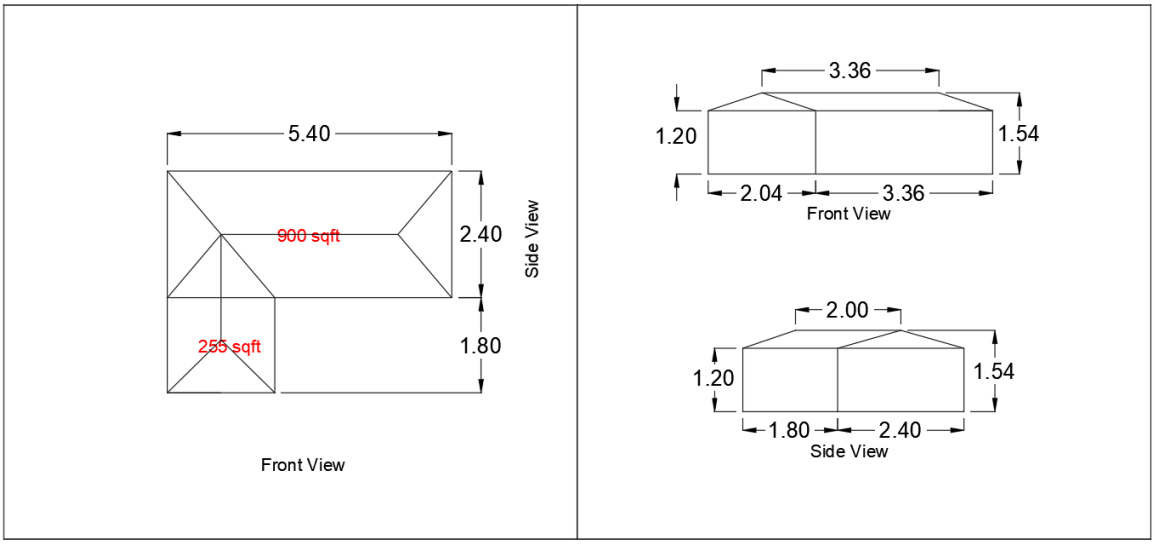

Figure 77. Model L1$_{hip_2021}$ dimensions (top and elevation views)

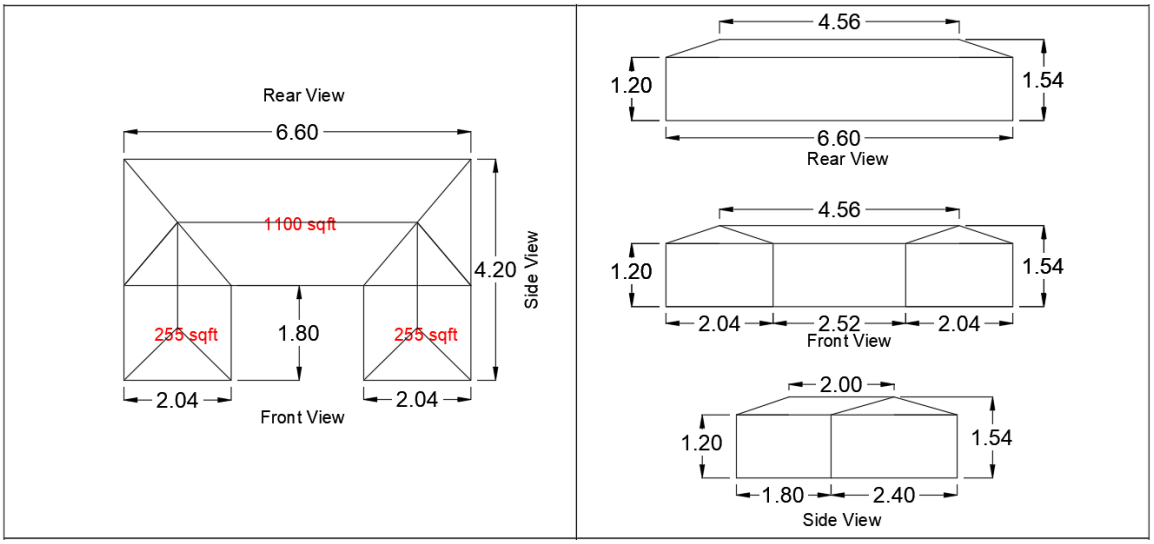

Figure 78.Model C1$_{hip_2021}$ dimensions (top and elevation views)

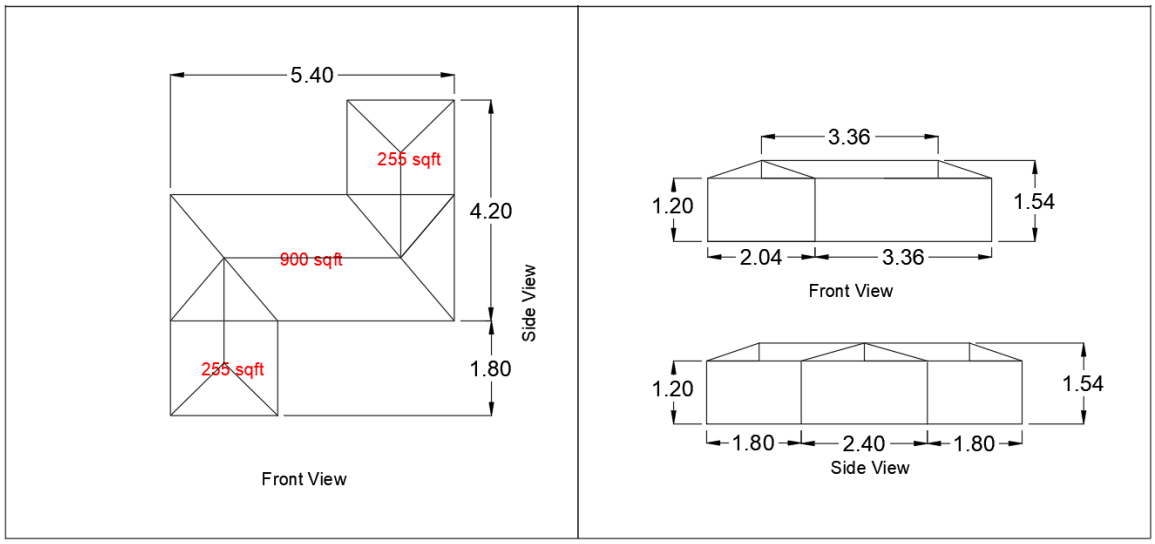

Figure 79. Model S1$_{hip_2021}$ dimensions (top and elevation views)

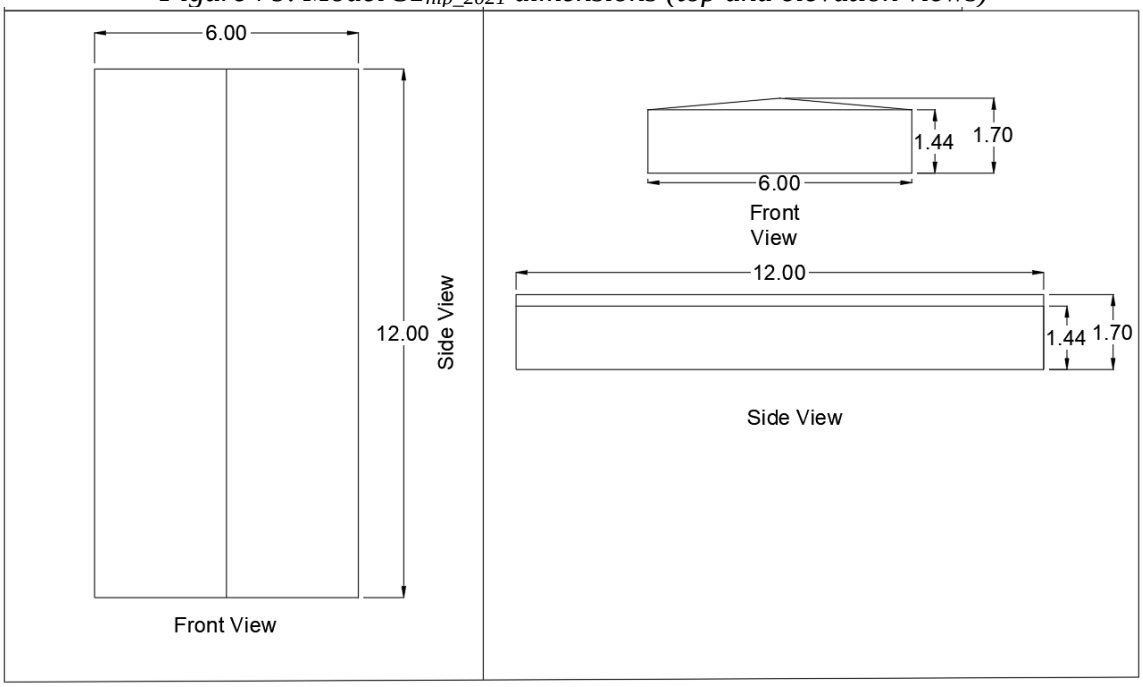

Figure 80. Model R$_{gable_2021}$ dimensions (top and elevation views)

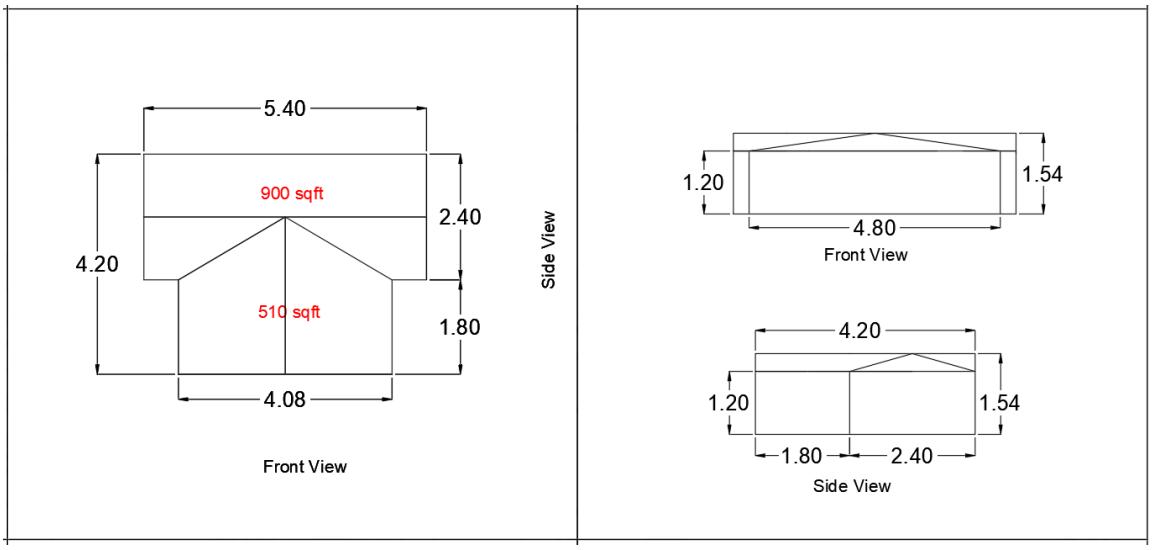

Figure 81. Model T1$_{gable_2023}$ dimensions (top and elevation views)

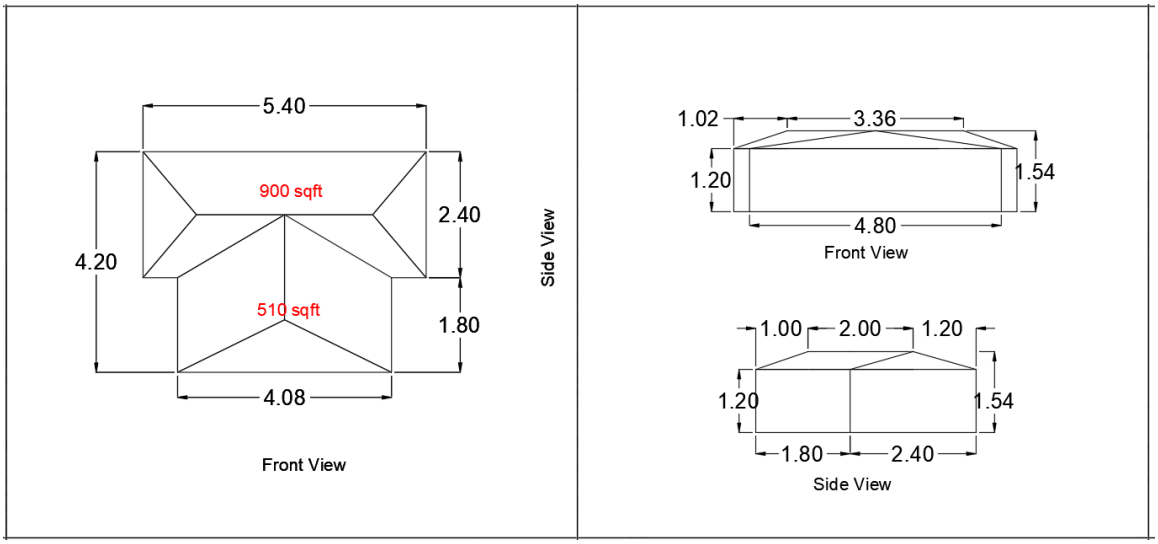

Figure 82. Model T2$_{hip_2023}$ dimensions (top and elevation views)

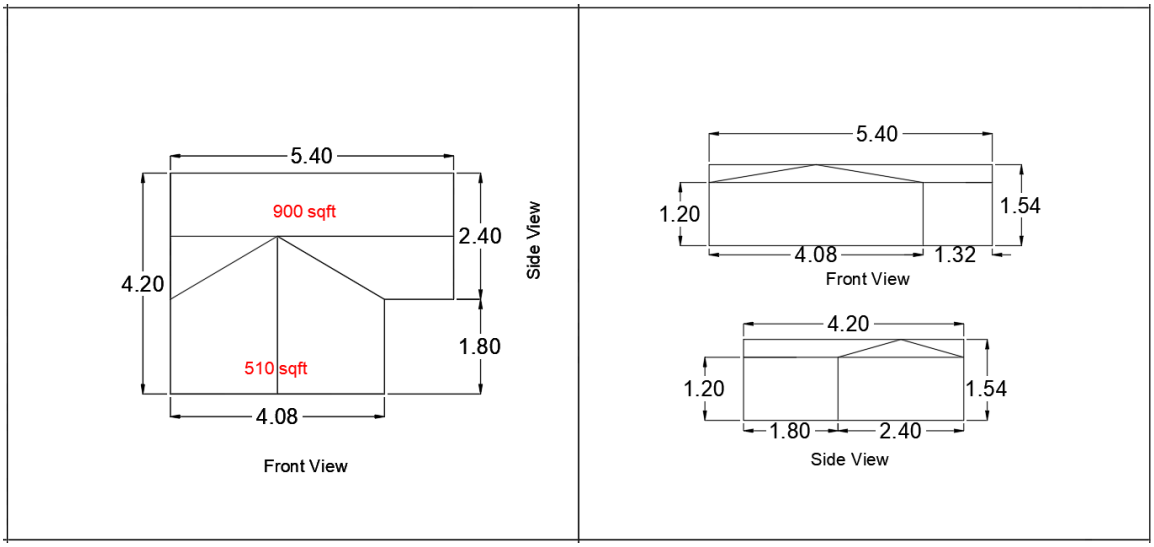

Figure 83. Model L1$_{gable_2023}$ dimensions (top and elevation views)

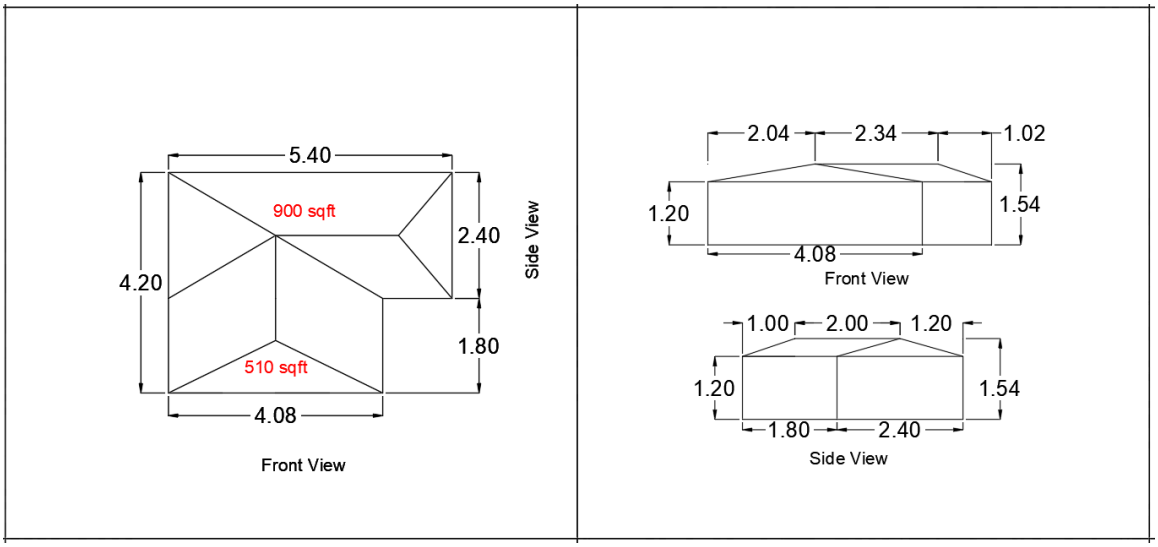

Figure 84. Model L2$_{hip_2023}$ dimensions (top and elevation views)

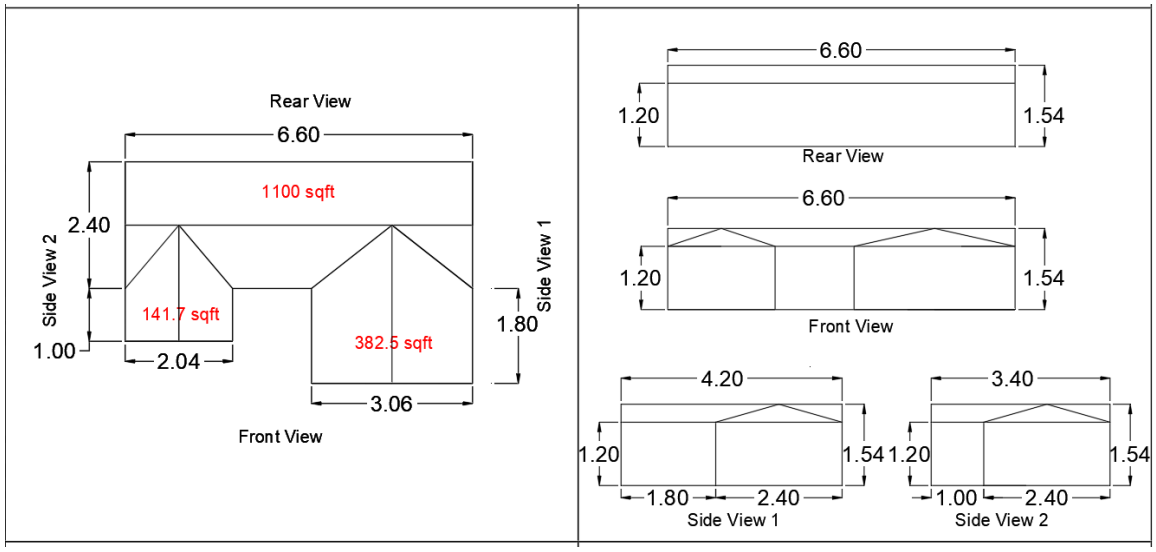

Figure 85. Model C1$_{gable_2023}$ dimensions (top and elevation views)

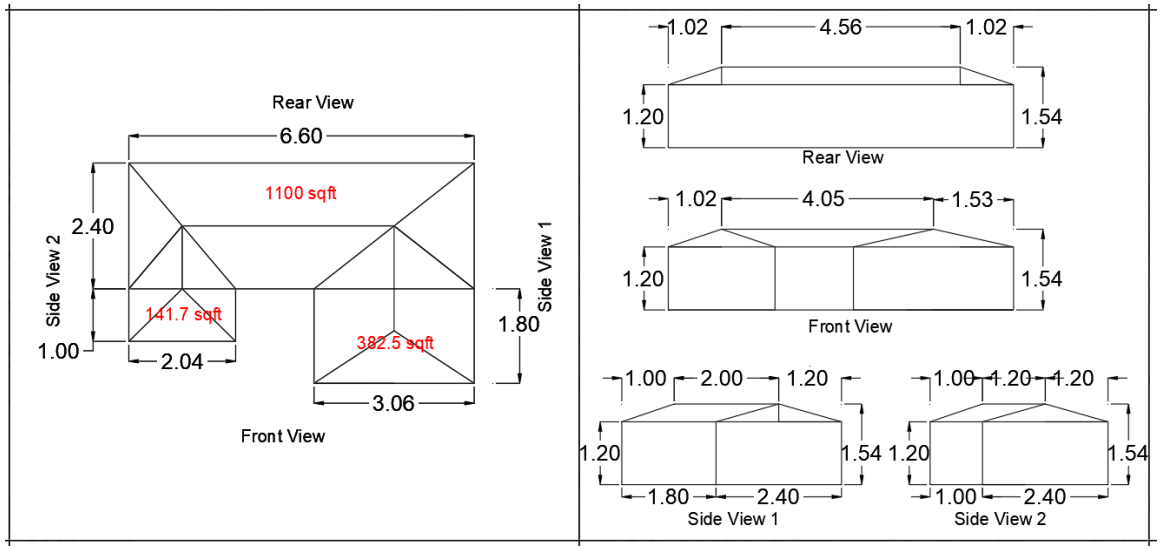

Figure 86. Model C2$_{hip_2023}$ dimensions (top and elevation views)

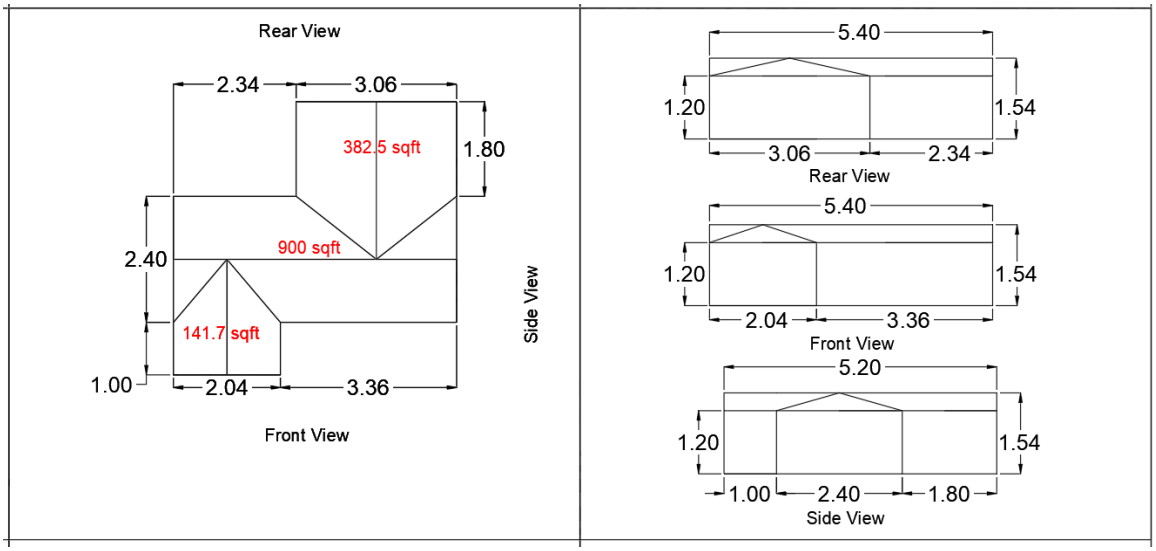

Figure 87. Model $S1_{gable\_2023}$ dimensions (top and elevation views)

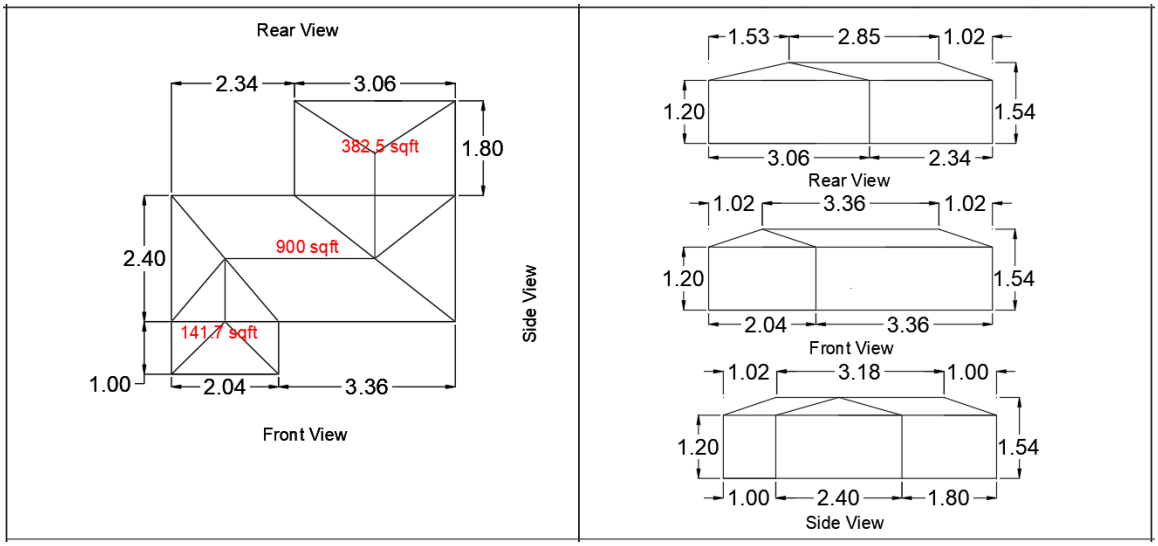

Figure 88. Model $S2_{hip\_2023}$ dimensions (top and elevation views)

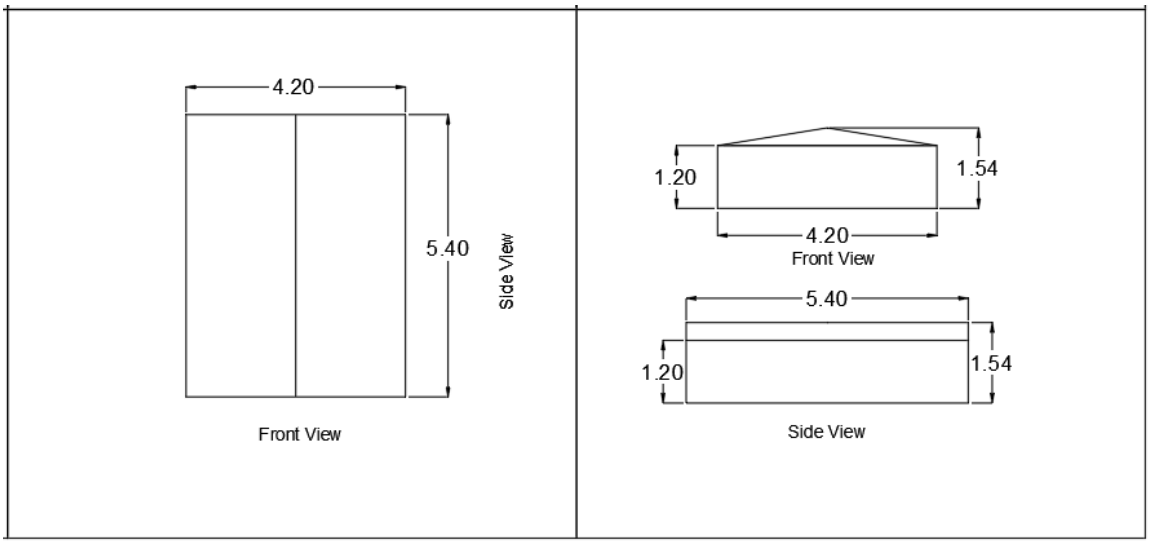

Figure 89. Model $R1_{gable\_2023}$ dimensions (top and elevation views)

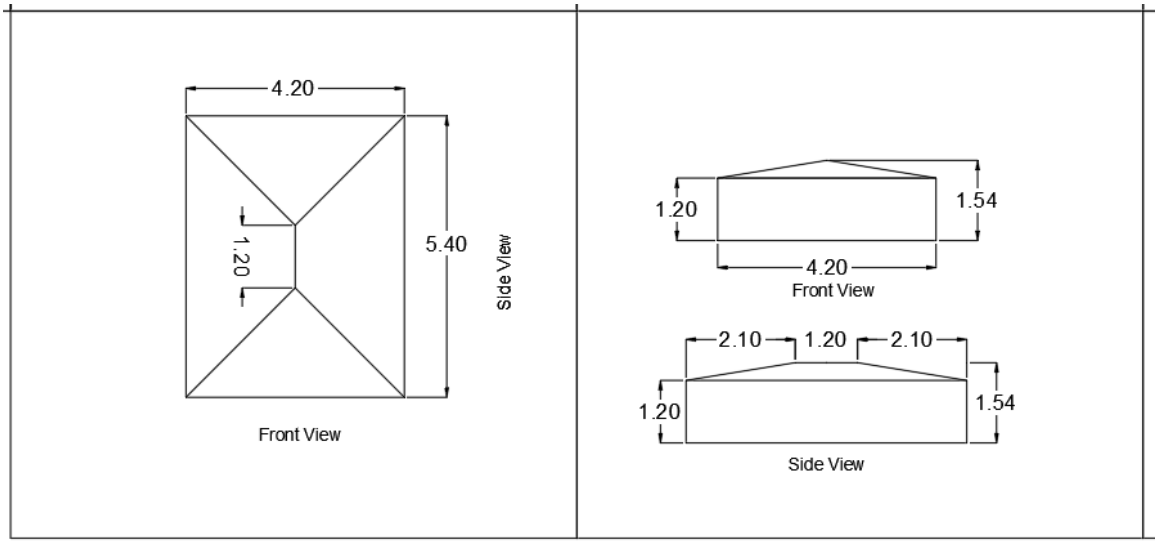

Figure 90. Model $R2_{hip\_2023}$ dimensions (top and elevation views)

5.3. METHODOLOGY

Wind tunnel testing is a widely adopted and effective tool for assessing the response of structures subjected to wind-induced loading, particularly in cases where the structure's shape is aerodynamically complex. All small-scale models, for this investigation, underwent testing in a small-scale Atmospheric Boundary Layer (ABL) wind tunnel designed and built at the Wall of Wind (WOW) Experimental Facility (EF) located at Florida International University in Miami, Florida, USA (see section 5.1). The aim for

building such wind tunnel was to achieve a cost-effective manner of testing a significant number of models as full/large scale testing requires significantly increased effort, scheduling time, and funds. As it has been stated before, the wind tunnel was designed to included multiple flow-management sections with adjustable components (spires, baseboard and floor roughness), enabling the modification of wind characteristics such as turbulence intensity and wind profiles in order to achieve an accurate simulation of wind properties ensuring accurate results (Uematsu et al., 1999, Stathopoulos, 1984, Holmes, et al., 1990, Akins et al., 1977, Bachlin et al., 1983, Stathopoulos et al., 1983, Tieleman 1992).

The scale of 1 to 100 was chosen for wind tunnel testing as it offered the capacity of 3D printing the models in one single piece as well as having the entirety of the wind frequency domain at the models mean roof height. The wind tunnel was previously calibrated to provide an open terrain exposure by means of spires, a baseboard and floor roughness elements to achieve the best possible alignment between wind speed (U) and turbulence intensity (I_u) profiles (Figure 91). To accurately measure the wind characteristics within the wind tunnel setup, five Turbulent Flow Instruments (TFI) Cobra Probes were strategically installed at the center of the turntable at various heights: 0.8125 inches, 1.375 inches, 2.75 inches, 4.125 inches, and 5.5 inches. It is worth noting that for models with irregular shaped plans, the mean roof height was 1.375 inches (for both phase A and B), while for the rectangular models of phase A, it was 1.57 inches and for both rectangular models of phase B, it was also 1.375 inches.

The wind speed and turbulence intensity profiles, as depicted in Figure 92, closely matched the Engineering Sciences Data Unit (ESDU) profiles for a simulated Open terrain (z0=0.02 m), confirming the validity of the setup and results obtained. Additionally, the

Power Spectrum Density profile in Figure 93 demonstrated the wind tunnel's capability to generate both high-frequency and low-frequency turbulence.

Subsequently, the models were placed at the center of the turntable and connected to three Thermal Control Units (TCU) via Zoc33/64Px, and data was sampled with a Scanivalve system, which consisted of a DSM4000 and an SPC4000 along with their corresponding hardware components. The system had the capability to accommodate a total of 384 pressure taps connected concurrently, with a sampling frequency of 520 Hz. The testing of all models was conducted across a range of wind directions, spanning from 0 to 345 degrees in 15-degree increments (clockwise direction) for 1-minute duration (Figure 22). The full-scale data sampling frequency and test time were obtained with Equation 1, where frequency and time attained values of 25.8 Hz and 20 minutes, assuming full-scale speed was equal to 84 mph. All data was then post-processed with a transfer function to compensate for any distortion caused by the urethane tubing length used to tap onto the models' pressure tap (Irwin et al., 1979).

a) b)

Figure 91. Wind tunnel a) spires and baseboard and b) floor roughness elements

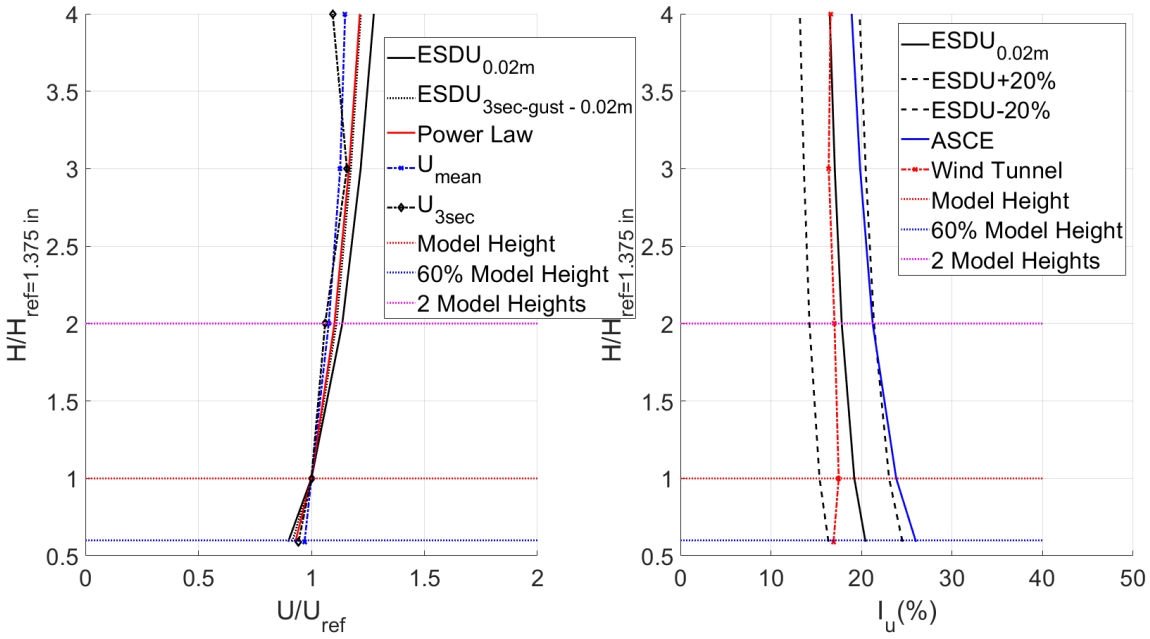

Figure 92. Wind speed (U) and turbulence intensity (I_u) profiles

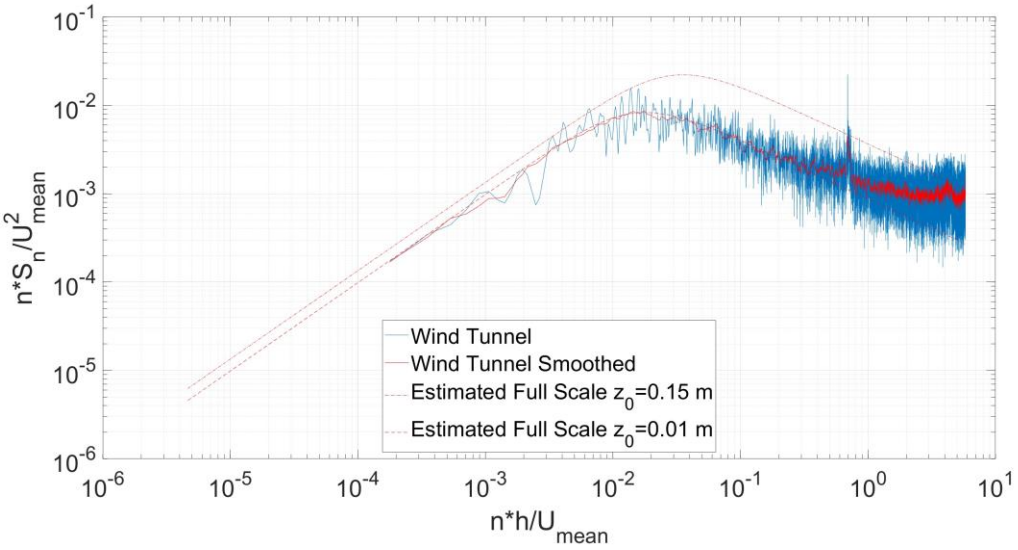

Figure 93. Power Spectrum Density profile at 1.375 inches height

5.4. RESULTS SMALL SCALE STUDY

5.4.1. PRESSURE COEFFICIENTS

Pressure coefficient estimates were determined utilizing the identical methodology outlined in the large-scale experiments, as elucidated in section 4.3.1.

5.4.1.1. MEAN PRESSURE COEFFICIENTS

All mean pressure coefficient contour plots of the models tested in the small-scale ABL wind tunnel are presented in this section. As it was previously stated, due to the significant number of contour plots generated for all the models at all wind directions, only the 0-degree wind direction mean Cp contour plots are presented and discussed. Mean pressure coefficients, for cornering angles, are presented in the Appendix.

The first five models presented below correspond to the experiments carried out in 2021 for models T- L-, C-, S-shape, and a rectangular model. All irregular shaped models had hip roof ends while the rectangular model has gable ends (Figure 94 to Figure 98).

The ten last models presented in this section correspond to the experiments carried out in 2023 for models $T1_{gable\_2023}$, $T2_{hip\_2023}$, $L1_{gable\_2023}$, $L2_{hip\_2023}$, $C1_{gable\_2023}$, $C2_{hip\_2023}$, $S1_{gable\_2023}$, $S2_{hip\_2023}$, $R1_{gable\_2023}$ and $R2_{hip\_2023}$. The difference between models 1 and 2 was the roof ends type (e.g., T1 gable ends – T2 hip ends). Please refer to section 5.2.

Please note the same wall sections definitions as that described in the large-scale section will be followed for consistency (see Figure 24 in section 4.3.1.1).

When examining the Cp mean results for model $T1_{hip\_2021}$ at a wind direction of 0 degree (Figure 94), a strong correlation with the outcomes from the previous tests was observed (Figure 25 and Figure 26). This alignment pertained to the overall pressure distribution patterns around the wall and roof sections. The "upwind windward wall" exhibited a maximum mean Cp of 0.59, while both "downwind windward walls" displayed lower values, reaching as high as 0.49, representing a 17% reduction. Moreover, due to the reduced length of the "downwind windward wall," a partial positive pressure bubble formed at the wall's edge, indicating that the development of the high positive pressure zone depended on the wall's length. Based on these observations, it was noted that the

stagnation point of a "downwind windward wall" begins to form approximately 10 feet from the 90-degree junction, with the center of this high positive pressure area expanding as the wall dimension increases. This extension of the high-pressure (positive) bubble was also observed in models $L1_{gable\_2019}$ and $L2_{gable\_2019}$ (Figure 27 and Figure 28). Additionally, it was observed that the length of the protruding section in the upwind direction had minimal impact on the formation of this phenomenon. When analyzing the pressure distribution on the "upwind sidewalls," it was observed that a more pronounced suction developed near the center of the wall (horizontally), adjacent to the roof edge (vertically). This behavior was also noted in model $T2_{gable\_2019}$ (Figure 26). The suction value observed on this wall reached -0.55, compared to a -0.84 noted on the "downwind sidewall," representing a significant 35% reduction for the “upwind sidewalls.” Comparing these results to the values generated on the rectangular model side walls, the irregularly shaped model experienced an approximate 10% increase in suction Cp mean, making it more susceptible to higher negative mean suction values on the walls than a rectangular model.

Turning our attention to the roof section, it was observed that most of the roof was subject to a suction bubble's influence. However, the roof edges were less prone to developing high suction values when compared to the rectangular model, measuring -1.04 versus close to -0.8 for models $R1_{gable\_2021}$ and $T1_{hip\_2021}$, respectively (Figure 94 and Figure 98). This is also attributed to the roof ends being hip type.

In the case of model $L1_{hip\_2021}$ (Figure 95), it was evident that the "upwind windward wall" continued to experience the highest positive pressures, with a mean Cp of 0.59. Conversely, the "downwind windward wall" underwent a 15% reduction in comparison to the "upwind windward wall," achieving a positive mean Cp value of 0.5.

Additionally, this "downwind windward wall" displayed a concentration of positive pressure values beginning roughly 10 feet from the 90-degree junction and extending along the wall's length. Regarding the side walls, the "upwind side wall" exhibited a suction of -0.11 near the top upwind edge of the wall, while the "downwind sidewall" experienced a more substantial suction of -0.8. Furthermore, consistent with observations in the large-scale section, the "upwind sidewall" transitioned from negative pressure near the upwind edge to positive pressure development near the 90-degree junction between the parallel and perpendicular-to-wind wall sections. Concerning the "leeward wall's" overall pressure development, it was noted that the side without a 90-degree joint (the left side of the leeward wall) tended to exhibit slightly increased mean Cp values (-0.41 compared to -0.36 on the right side), representing a 14% increase in Cp mean values.

As for the roof sections, they were primarily affected by a suction bubble, but elevated negative suctions were observed to concentrate at the roof edges, reaching values of approximately -1.23.

Figure 96 presents the Cp mean contour plot results for Model $C1_{hip\_2021}$. Similar to previous observations, the trend of the "upwind" versus "downwind windward wall" persisted, with the latter experiencing reduced pressure development. Interestingly, the "downwind windward wall," situated between two perpendicular side walls known as "inner side walls," might lead to the expectation of higher pressures compared to the "upwind" direction. However, the interaction of separated layers of wind introduced complexities that mitigated the effects of wind on the "downwind windward wall." The reduction between the "upwind windward wall" and the "downwind windward wall" was nearly 38%. In addition, the "inner sidewalls" experienced minimal suction forces and were

primarily exposed to positive pressures, exhibiting a clear increasing gradient from the upwind edge to the 90-degree joint edge, reaching a value of 0.35. This value represented 50% of the mean Cp observed on the "upwind windward wall." On the other hand, the "outer sidewalls" exhibited an overall pressure distribution similar to what is typically observed on the sidewalls of a rectangular model, and the same trend was noted for the leeward wall.

Upon examining the roof sections of this same $C1_{hip\_2021}$ model, it was evident that the roof edges facing the upwind direction tended to have higher mean Cp values. Additionally, a distinct suction bubble formed in the roof edge adjacent to the "downwind windward wall," achieving a mean Cp value of nearly -1.04. Furthermore, the areas of the roof near the 90-degree joint, specifically the roof corner situated between the "inner sidewall" and the "downwind windward wall," displayed increased negative mean Cp values compared to other roof areas.

In this round of testing, a novel S-shaped model (Figure 97) was introduced. It is worth mentioning that the data obtained at a 0-degree wind direction may have been compromised during the experiments. Therefore, we are presenting the results at a 180-degree wind direction since the model is symmetric (here, "upwind" and "downwind" are defined with reference to the walls closer to the wind source - Figure 24).

The results from this S-shaped model, at a 180-degree wind direction, closely resembled the overall pressure distribution observed in models with an L-shape on the entire upwind side (north/upper direction/side in the image). As previously observed in L-shaped models (such as $L1_{hip\_2021}$, $L1_{gable\_2019}$, and $L2_{gable\_2019}$), the "upwind windward wall" experienced more pronounced pressures than those on the "downwind windward

wall" (the wall located on the top left side facing north). The same was observed for the “downwind sidewalls” as well as “upwind sidewalls.” A noteworthy difference observed in this model was the development of higher suction pressures on the leeward walls, particularly on the walls forming a 90-degree joint between parallel-to-wind and perpendicular-to-wind walls.

Regarding the roof sections, they exhibited pressure development patterns similar to those observed in the $L1_{hip\_2021}$ model, with the highest suctions occurring on the edges adjacent to the "upwind and downwind windward walls" as well as the "upwind sidewalls."

When examining the outcomes produced by model $T1_{gable\_2023}$ (Figure 99), it became evident that the overall pressure distribution aligned with what was previously observed in prior experiments. Specifically, the "upwind windward wall" demonstrated higher positive mean C_p values compared to those observed on the "downwind windward wall." An intriguing finding pertains to the "downwind windward wall," where a distinctive "bubble" of considerably lower positive pressures emerged along the upper outer edge of the wall (the top corner adjacent to the "downwind sidewall"). The substantial reduction on development of positive pressures in the “downwind windward wall” is attributed to the length of this wall, which is 5.5 feet in full scale dimensions (less than the 10 feet length previously mentioned). Regarding the sidewalls, a noteworthy observation revolves around the reduced dimensions of the "downwind windward wall." In this context, the "upwind sidewall" developed values that closely resemble those of the "downwind side wall," with respective values of -0.77 and -0.797. This observation underscores an interdependence between the sidewalls and the length of the "downwind windward wall." It becomes apparent that the longer the "downwind windward wall," the more pronounced the

reduction in suction values along the windward edge of the "upwind sidewall" as well as on the "downwind sidewall."

Turning to the roof sections in model $T1_{gable\_2023}$, the windward leading edges exhibited suction, and the leeward side of the roof ridge also experienced suction, particularly on the outer edges when considering the crosswind direction. In comparison to the rectangular model $R1_{gable\_2023}$, the irregular shape model's roof section yielded somewhat lower values, as has been consistently observed in prior instances, -1 vs -1.12 (Figure 107).

When scrutinizing the data extracted from the irregular shape model $T2_{hip\_2023}$ (Figure 100), it became apparent that the same wall trends observed in model $T1_{gable\_2023}$ remained consistent. The primary distinction between these two models laid in the suction phenomena occurring on the roof. Specifically, the windward edge of the protruding section (the roof edge adjacent to the "upwind windward wall") exhibited higher suction values compared to those observed on the roof edge of model $T1_{gable\_2023}$ (Figure 99). Furthermore, akin to the observations made in the previous model, the region situated on the leeward side of the roof ridge (perpendicular to the direction of the wind) manifested higher suction pressures than those found along the roof ridge aligned with the wind direction.

When examining the outcomes derived from model $L1_{gable\_2023}$ (Figure 101), it became evident that the "upwind windward wall" consistently maintained high positive pressure values. An intriguing observation arose in connection with the "downwind windward wall," which extended a full-scale measurement of 11 feet from the junction of the 90-degree walls. This portion of the wall experienced higher pressures that aligned with

the hypothesis proposing the emergence of a positive pressure bubble at a distance of nearly 10 feet from the junction. Turning to the side walls in this model, it is noteworthy that the "upwind sidewall" underwent a significant reduction in the development of suction values, while the "downwind sidewall" exhibited the anticipated suction values. The observations drawn from models $T1_{gable\_2023}$ (Figure 99) and $L1_{gable\_2023}$ (Figure 101) validated the influence of the length of the "downwind windward wall" on the overall pressure distribution in neighboring wall sections. Furthermore, a slight increase in suction values was discernible on the "downwind side wall" in comparison to the standard side wall (located on the left side of the image), -1.09 vs 0.888, a 22% increase. When compared to model R1gable_2023 (-0.818 - Figure 107), an increase of ~33% was observed on the “downwind side wall” of model $L1_{gable\_2023}$. This increase could likely be attributed to the placement of the stagnation point, situated on the "downwind windward wall," near the upwind edge of the "downwind sidewall." This configuration created an area of air concentration capable of escaping over the roof and towards the "downwind side wall." The pressure patterns on the roof section exhibited heightened suctions near the leading edges of the roof and in the vicinity of the leeward side of the roof ridge, positioned in the crosswind direction.

When examining the results derived from model $L2_{hip\_2023}$ (Figure 102), the same observations made for model L1gable_2023 were reaffirmed. In fact, as previously mentioned, it was posited that a localized concentration of positive pressures, resulting from a stagnation point, would account for the elevated suction values on the "downwind side wall." The pressurization occurring near the periphery of the "downwind windward wall" led to the escape of air both over the roof edge and along the outer edge of the

"downwind windward wall." The contour plot further validated this hypothesis by depicting an augmentation of suction near the "localized stagnation point" on the roof. This served as concrete evidence supporting the notion that higher suction values were generated due to the presence of a localized stagnation point near the edge of a wall section due to a previously separated wind flow being shed on a windward section located downwind. When assessing the rise in suction magnitude on the "downwind side wall" in comparison to the side wall of model R2hip_2023 (Figure 108), there was a discernible increase of 34% (-0.703 versus -0.742).

Upon examining the contour plot generated for model $C1_{gable\_2023}$ under a 0-degree wind direction (Figure 103), it became evident that the overall pressure distribution across all wall sections closely mirrored what was observed in prior experiments conducted in 2019 and 2020 (as depicted in Figure 29, Figure 30, Figure 33, Figure 34, and Figure 96). Specifically, the "upwind windward walls" consistently exhibited higher positive values when compared to the "downwind windward wall," which was positioned at the model's center, flanked by two "inner side walls." Furthermore, the "inner side walls" registered positive pressures, albeit with reduced suctions emerging along their upwind edges adjacent to the edges of the "upwind windward wall." Of notable significance, and as previously mentioned, the roof edges situated near the joint of the 90-degree walls (forming an inverted U-shape) tended to manifest elevated suction values. This phenomenon could likely be attributed to the accumulation of pressure (pressurization) that can only escape over the roof section.

When analyzing model $C2_{hip\_2023}$ (Figure 104), similar findings to those observed in model $C1_{gable\_2023}$ were identified. In this context, the "upwind windward walls"

consistently exhibited the highest positive pressures, while the "downwind windward wall" experienced a reduction in the development of positive pressures. The "inner side walls" demonstrated a pattern where they tended to display negative pressures along their upwind edges, transitioning into positive pressures as they approach the 90-degree walls junction with the "downwind windward wall." Additionally, the "outer side walls" manifested the expected suction values, with readings reaching -0.703 on the west side and -0.844 on the east side. As observed in previous instances, the roof areas situated near the 90-degree wall junctions exhibited heightened suction values, peaking at a mean Cp of -0.85.

Models $S1_{gable\_2023}$ (Figure 105) and $S2_{hip\_2023}$ (Figure 106) exhibited consistent agreement with the outcomes observed in model $S1_{hip\_2021}$ (Figure 97). In these models, the "upwind windward wall" achieved values approaching 0.6, while the "downwind windward wall" attained its highest mean Cp value of approximately 0.5, 17% reduction. The overall pressure development on the "downwind windward wall" was significantly influenced by the presence of a protruding section in the upwind direction. In the cases of models $S1_{gable\_2023}$ and $S2_{hip\_2023}$, the reduction in mean Cp values between the "upwind" and "downwind windward walls" reached 28% and 15%, respectively. Conversely, the "upwind side walls" were profoundly affected by the presence of the "downwind windward wall," inducing a localized pressure buildup. This effect was manifested as a positive pressure gradient on the "upwind side wall." Although these walls would typically be expected to develop predominantly negative mean Cp values, they mostly exhibited positive mean Cp values and negligible suction mean Cp values. Side walls lacking perpendicular walls in the downwind direction (i.e., without the "downwind windward wall") were observed to generate the expected mean Cp values. Furthermore, somewhat

increased suction values tended to concentrate on the leeward side of the models. In this context, the walls forming a 90-degree joint experienced higher suction values than the wall located furthest downwind. The same observation was noted in model $S1_{hip\_2021}$ (Figure 97). Roof edges located on the windward side tended to manifest higher suction values. Notably, the model with gable ends displayed a greater tendency to develop increased negative mean Cp values on the roof edges, whereas the model with a hip roof tended to exhibit higher negative mean Cp values near the roof ridge perpendicular to the direction of the wind.

In general, buildings featuring non-standard shapes were found to induce intricate airflow patterns around their various protruding sections, whether in the upwind or crosswind directions. The intricate nature of separation bubbles intermingling with other localized flows resulted in unconventional pressure patterns in specific wall segments. Furthermore, the length of these aforementioned segments played a pivotal role in either reducing or augmenting positive and negative pressures on both wall and roof sections. This dynamic highlighted that buildings with complex shapes are more prone to experiencing atypical overall pressure distributions highlighting the need of more investigations to better understand their response under wind-induced loads.

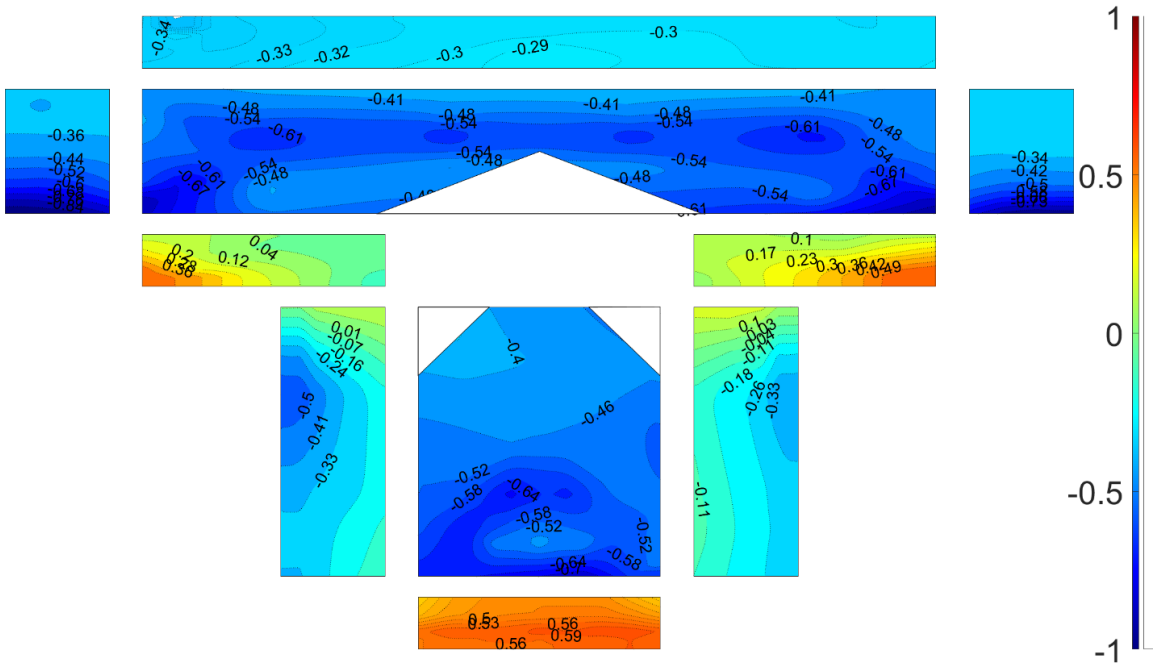

Figure 94. Model $T1_{hip\_2021}$ $C_{p,mean}$ – 0 degree.

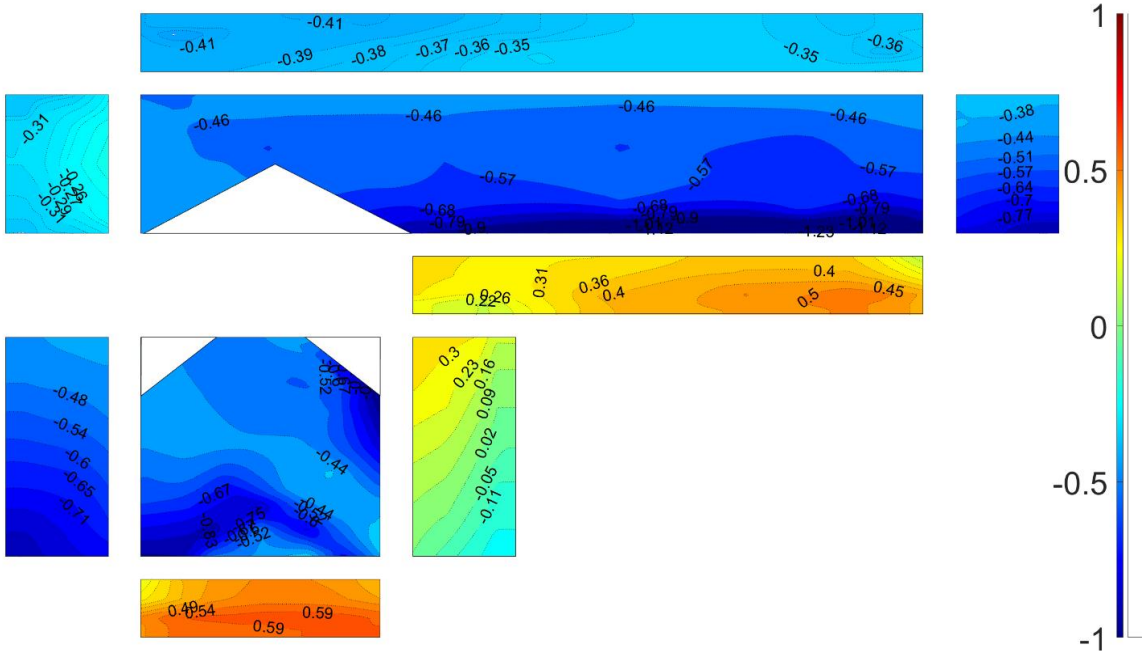

Figure 95. Model $L1_{hip\_2021}$ $C_{p,mean}$ – 0 degree.

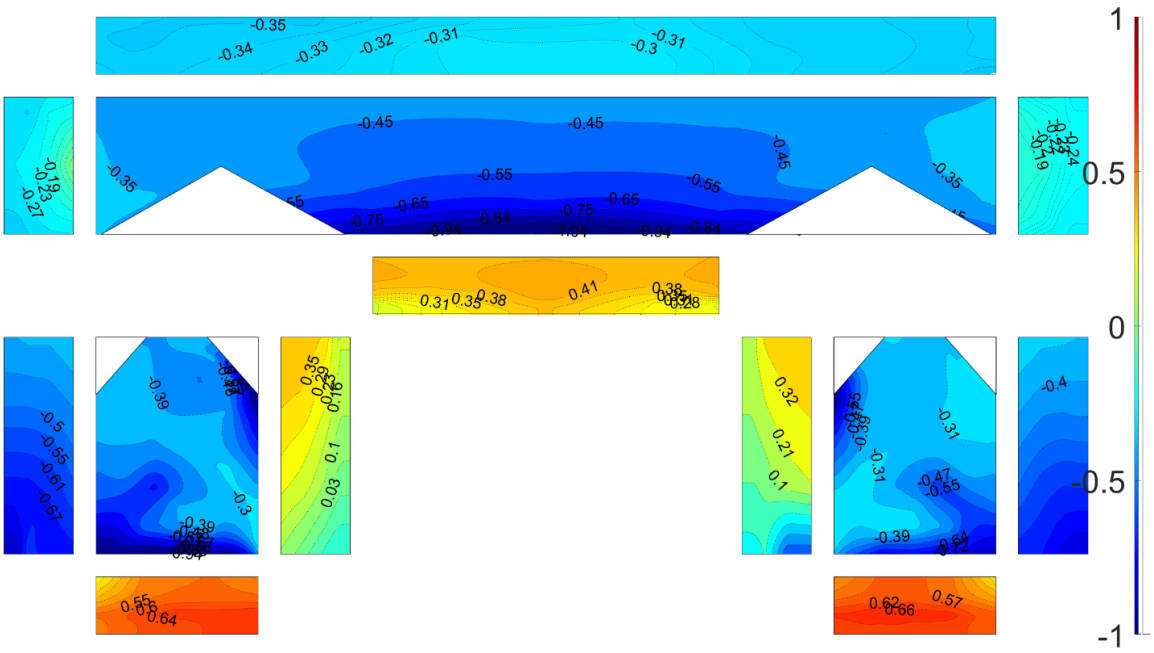

Figure 96. Model $C1_{hip\_2021}$ $C_{p,mean}$ – 0 degree.

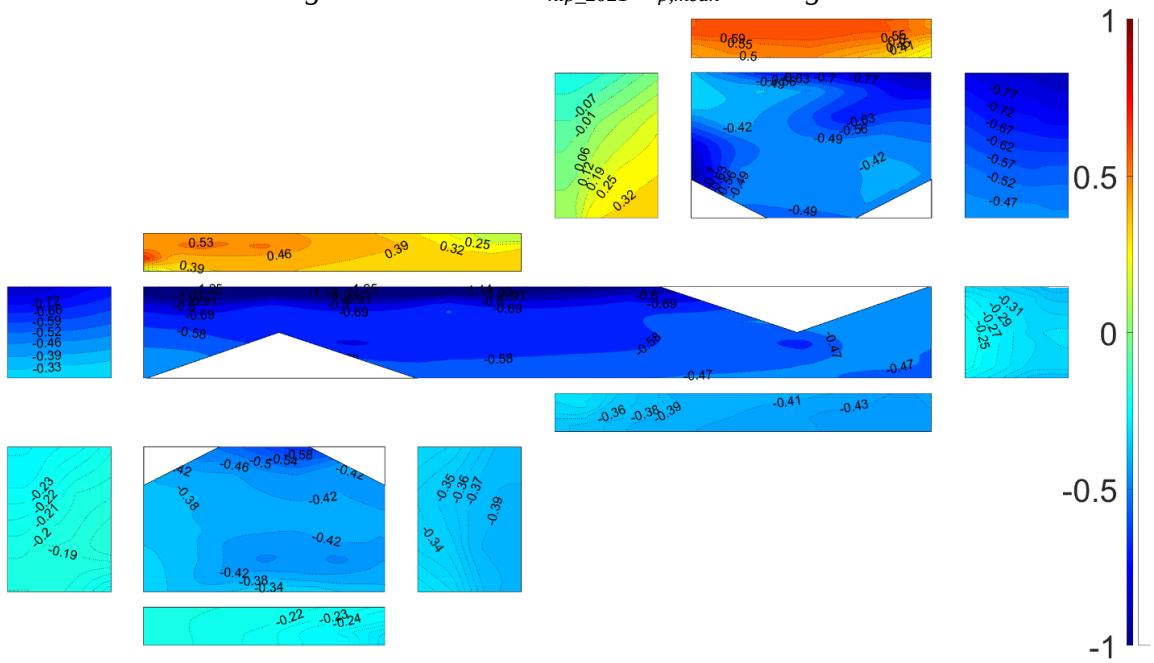

Figure 97. Model $S1_{hip\_2021}$ $C_{p,mean}$ – 180 degrees.

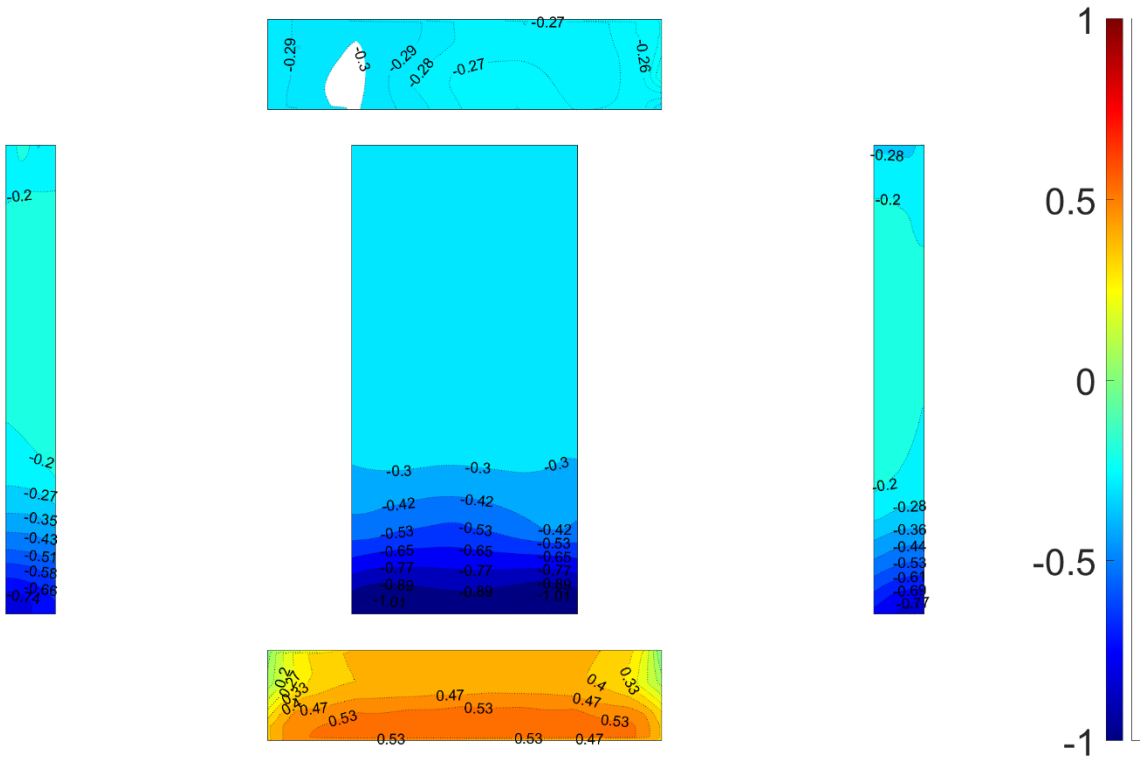

Figure 98. Model $R1_{gable\_2021}$ $C_{p,mean}$ – 0 degree.

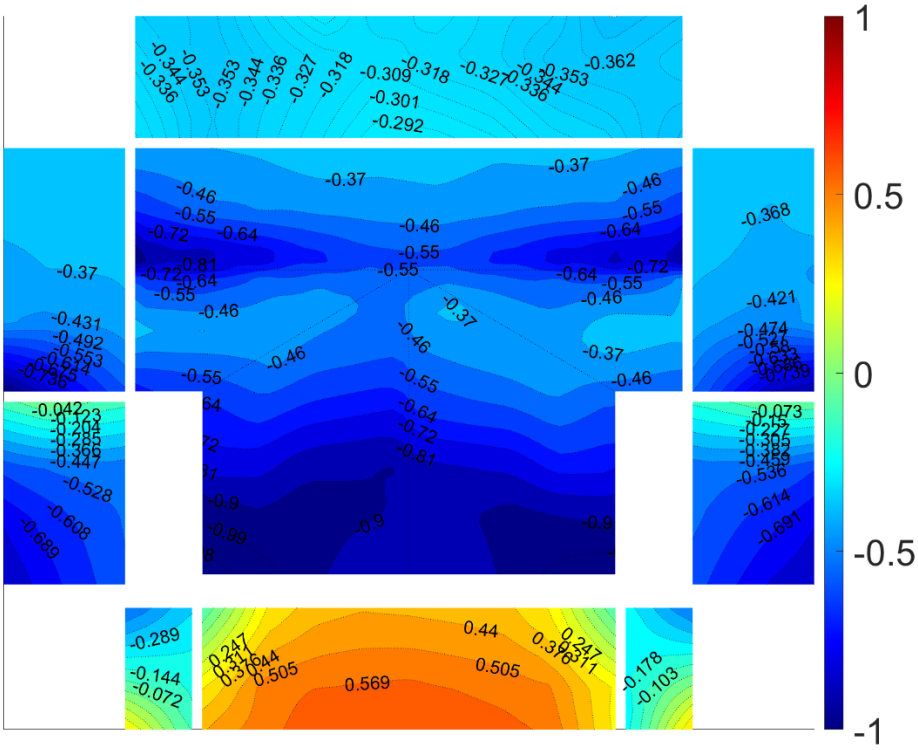

Figure 99. Model $T1_{gable\_2023}$ $C_{p,mean}$ - 0 degree.

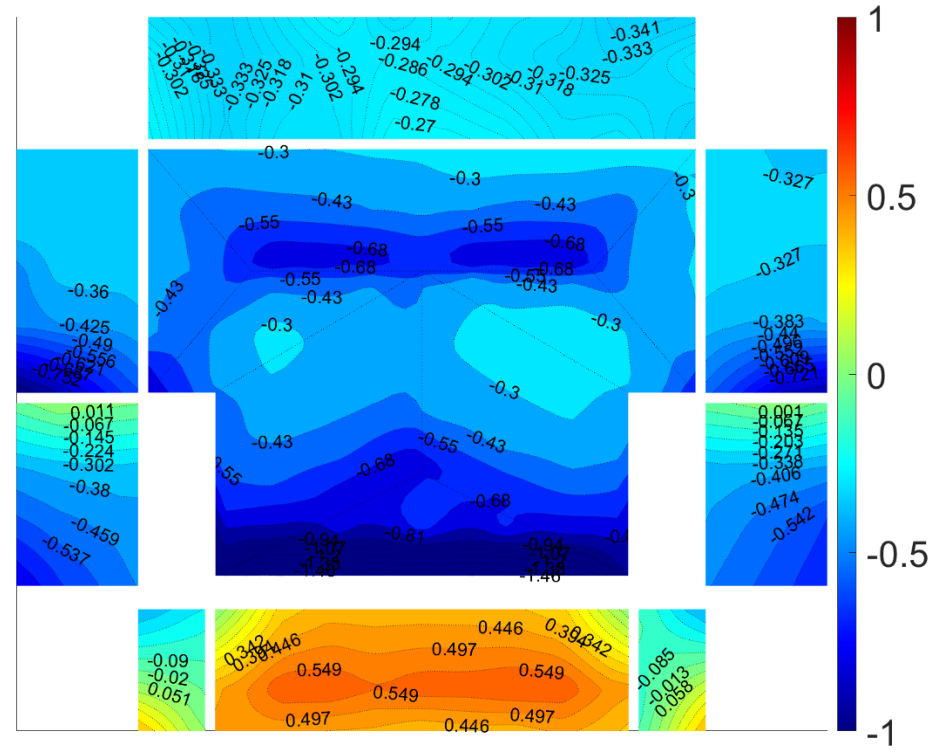

Figure 100. Model $T2_{hip\_2023}$ $C_{p,mean}$ - 0 degree.

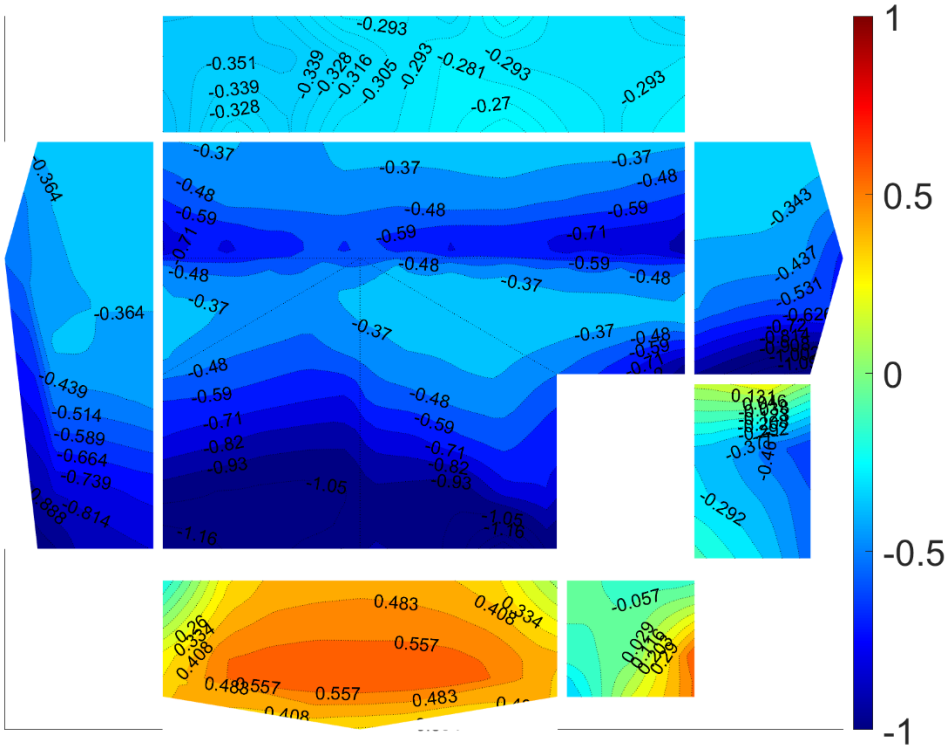

Figure 101. Model $L1_{gable\_2023}$ $C_{p,mean}$ - 0 degree.

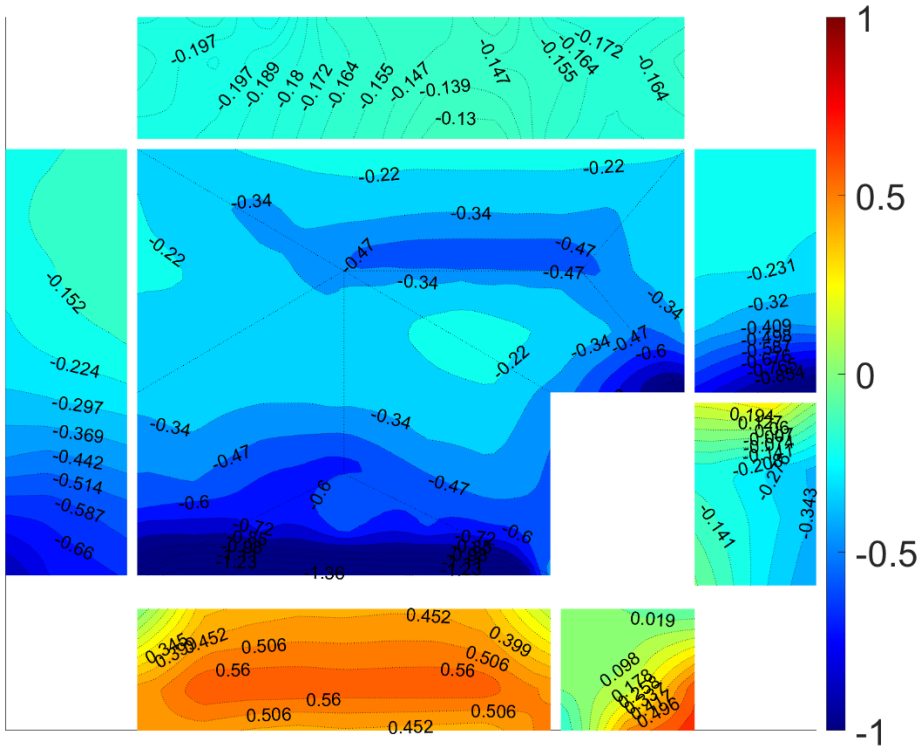

Figure 102. Model $L2_{hip\_2023}$ $C_{p,mean}$ - 0 degree.

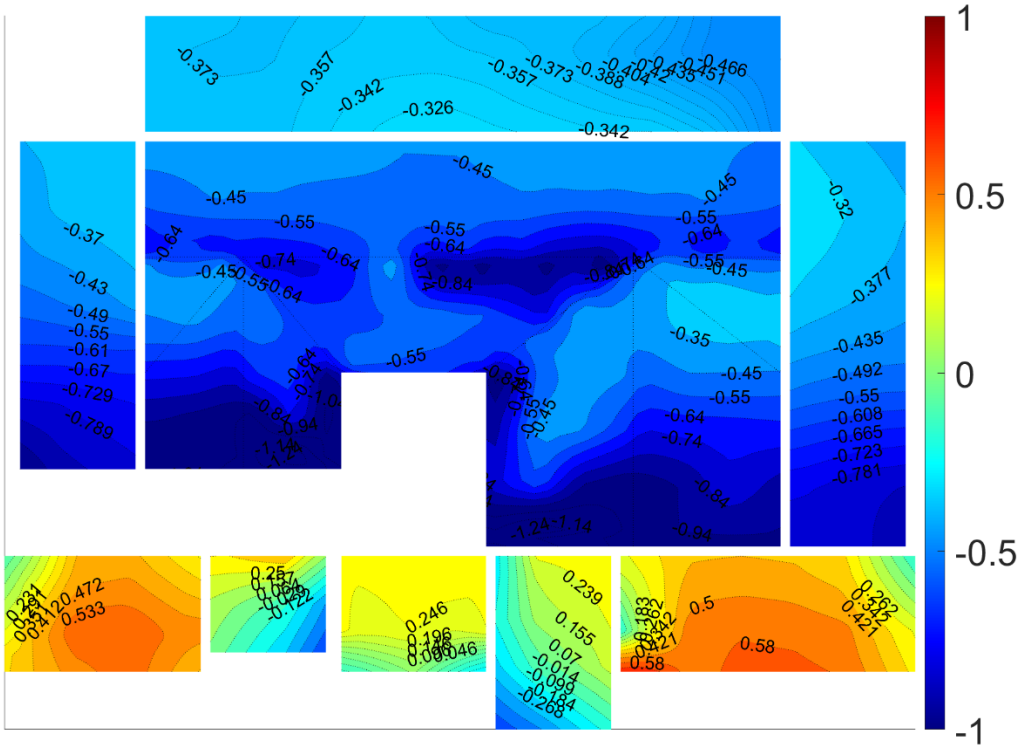

Figure 103. Model $C1_{gable\_2023}$ $C_{p,mean}$ - 0 degree.

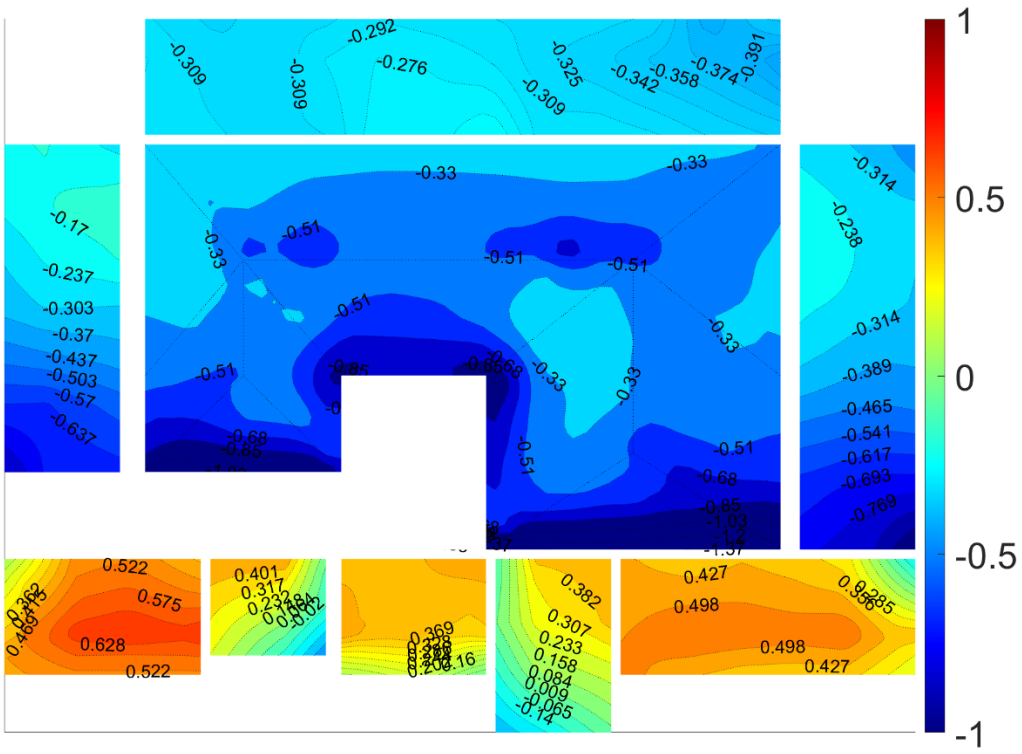

Figure 104. Model C2$_{hip_2023}$ $C_{p,mean}$ - 0 degree.

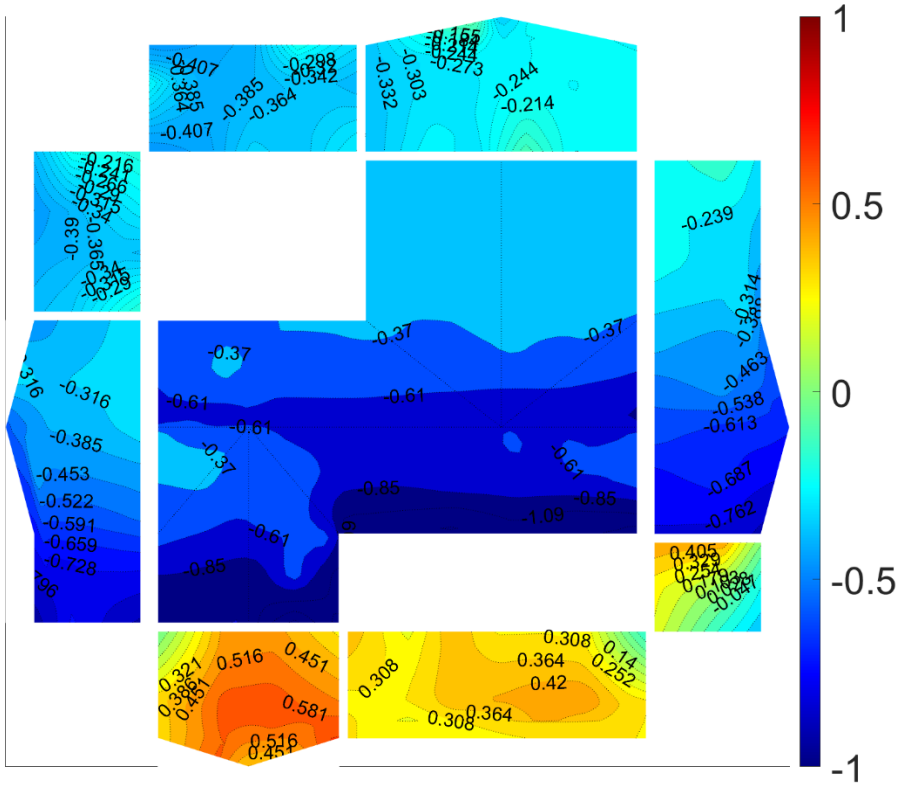

Figure 105. Model S1$_{gable_2023}$ $C_{p,mean}$ - 0 degree.

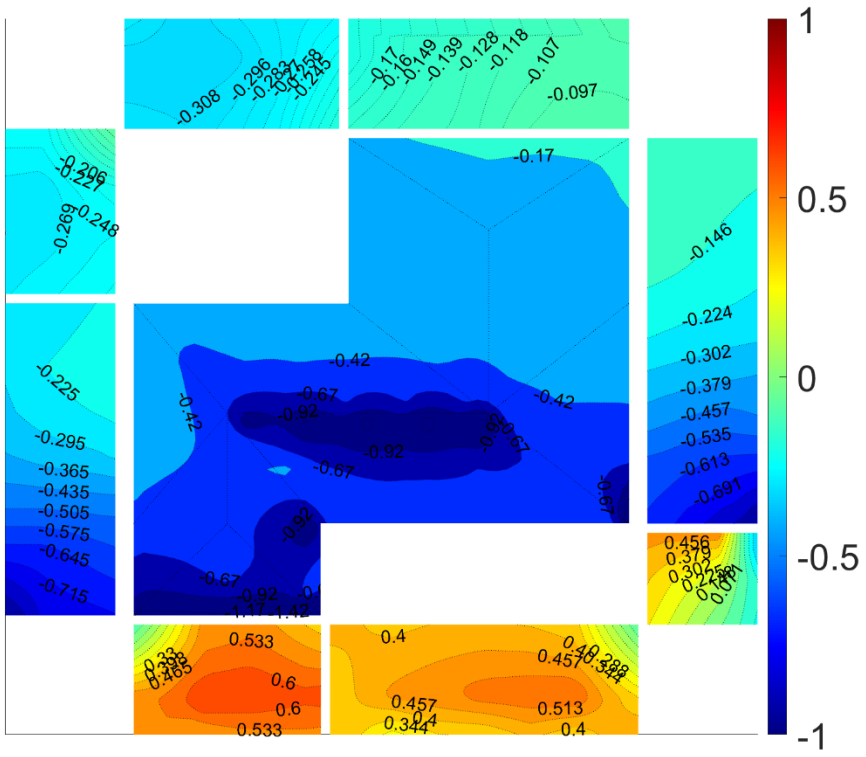

Figure 106. Model S2$_{hip_2023}$ $C_{p,mean}$ - 0 degree.

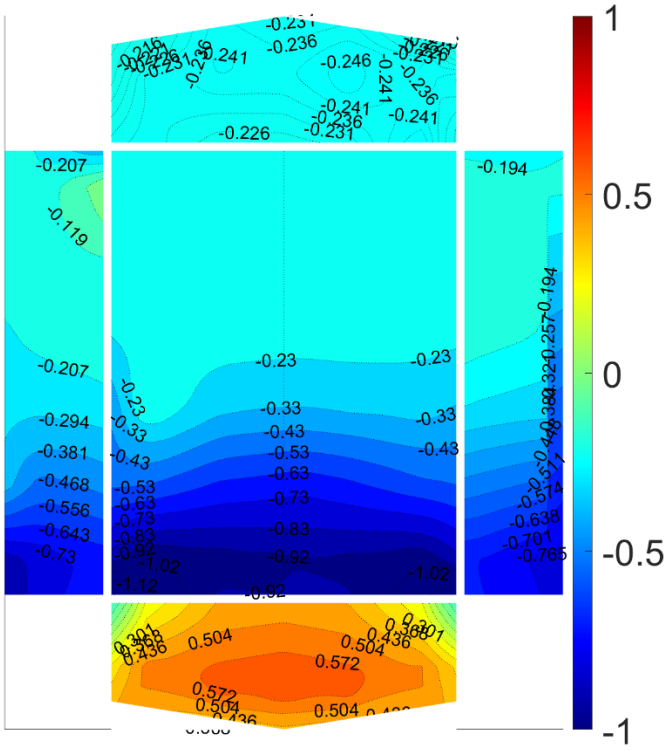

Figure 107. Model R1$_{gable_2023}$ $C_{p,mean}$ - 0 degree.

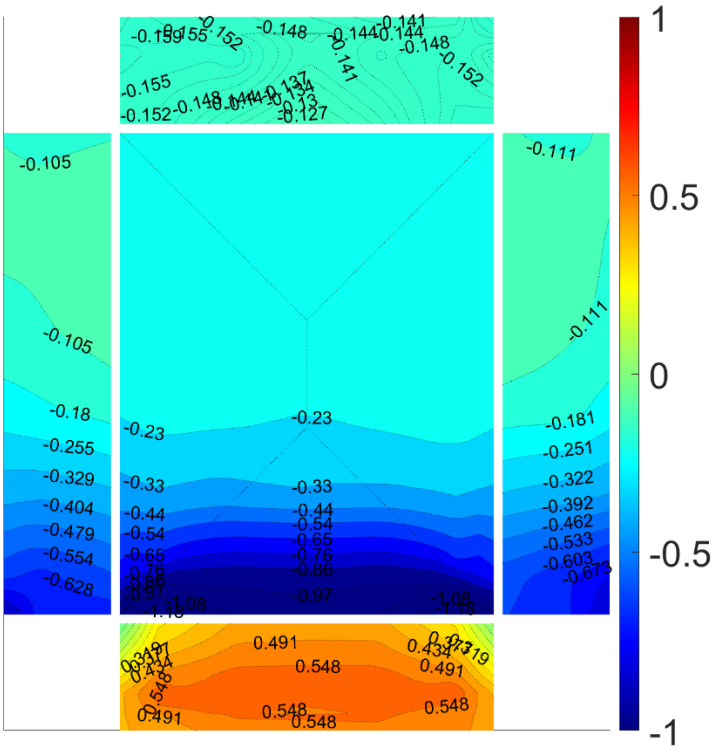

Figure 108. Model R2$_{hip_2023}$ $C_{p,mean}$ - 0 degree.

5.4.1.2. CRITICAL PRESSURE COEFFICIENTS

Contour plots were generated for each model with irregular shapes to illustrate the critical peak pressure coefficient ($C_{p,\ critical}$) and to provide a visual representation that encompasses the most challenging scenarios across all wind directions. (Figure 109 to Figure 136). As stated previously (section 4.3.1.2), these plots aimed to identify the specific regions within the models that are more susceptible to encountering the highest positive and negative forces.

The critical values (both maximum and negative) for each pressure tap were determined by choosing the highest peak Cp value among all wind directions, as well as the lowest peak Cp value among all wind directions.

To facilitate a straightforward comparison among the outcomes of models with irregular shapes, the walls were categorized based on their orientation: North, West, South,

and East. Here, North pertains to walls facing the upper portion of the page, West indicates walls oriented towards the left side, South refers to walls facing the bottom of the page, and East designates walls positioned along the right side.

The $C_{p,\ critical}$ values for model $T1_{hip\_2021}$ are depicted in Figure 109 and Figure 110. The results revealed that the highest maximum $C_{p,\ critical}$ values on all sections facing the North, West, South, East walls, and roof section reached 1.55, 1.79, 1.78, 1.57, and 0.61, respectively. When comparing these values to the rectangular model $R2_{hip\_2023}$ (Figure 135), it was observed that the wall sections experienced an increase in positive values, reaching up to a 17% upsurge, whereas the roof section exhibited a positive increase of up to 15%. Regarding suction values, certain wall sections displayed an increment of up to 23% (side walls). Most notably, the roof section experienced a significant 20% reduction in suction value development, when compared to the regular shaped model $R2_{hip\_2023}$ (Figure 136). Furthermore, adhering to the definitions of wall and roof sections outlined in Figure 24, the "upwind windward wall" manifested higher positive pressure values across the entire upper half of the wall. Conversely, the "downwind windward walls" tended to exhibit elevated positive pressure values near the outer edge of the wall and close to the 90-degree joint between the "upwind side wall" and "downwind windward wall." This same pattern was observed on the "upwind side wall," where there was a concentration of higher positive pressures near the upwind edge, possibly due to separation shedding from the "downwind side walls" at the 90-degree wind direction. As for the "downwind side walls" and the leeward wall, they displayed heightened positive values near the edges of the upper half of the wall. Notably, the roof sections exhibited increased pressure values near the 90-degree joints between the parallel and perpendicular wall sections when

compared to the results from the rectangular model. Regarding suction values, the "upwind windward wall" developed higher suction values near the wall's edges. Conversely, the "downwind windward walls" exhibited higher suction values at the top of the inner corner (at the 90-degree wall joint), and the same was observed on the "upwind side wall." The "downwind side walls" and the leeward wall of this model displayed the highest suction values near the edges. Interestingly, the roof edges near the 90-degree section joints tended to exhibit increased suction values compared to other parts of the roof.

Model $L1_{hip\_2021's}$ $C_{p,\ critical}$ values are depicted in Figure 111 and Figure 112. Upon analyzing the results, it was observed that the wall sections experienced a minor increase in the development of maximum $C_{p,\ critical}$ values, amounting to nearly 3%. In contrast, the highest value in the roof section exhibited a remarkable increase of 53% when compared to the values obtained from the rectangular model $R2_{hip\_2023}$ (Figure 135). Conversely, the minimum $C_{p,\ critical}$ value for the walls increased by 7%, while the highest minimum $C_{p,\ critical}$ value in the roof section decreased by 20% (Figure 136). For this model results, the "upwind windward wall" was observed to generate higher maximum $C_{p,\ critical}$ values near the wall's center and across the entire upper half of the wall. The "downwind windward wall" displayed higher maximum $C_{p,\ critical}$ values on one edge of the wall (starting from nearly 10 feet off the 90-degree wall joint), a result of the flow being shed off the "upwind windward wall." Additionally, a concentration of higher maximum $C_{p,\ critical}$ values was noted to develop at the 90-degree wall joint, progressively extending onto the "upwind side wall." Furthermore, the "upwind side wall" exhibited a similar overall maximum $C_{p,\ critical}$ pressure development as the "downwind windward wall." The remaining walls (such as the side wall, "downwind side wall," and leeward wall) demonstrated the expected maximum

$C_{p,\ critical}$ pressure development. Moreover, the roof edges near the 90-degree wall joints were observed to experience higher maximum $C_{p,\ critical}$ values than those observed in model $R2_{hip\_2023}$ (Figure 135). Regarding the minimum $C_{p,\ critical}$ values, it was observed that the "upwind side wall" and "downwind windward wall" tended to exhibit unconventional minimum $C_{p,\ critical}$ pressures. For instance, a concentration of suction values near the 90-degree wall joint was noted, reaching values of -1.75 and -1.56 on the "downwind windward wall" and "upwind side wall," in contrast to -1.48 and -1.15 on the opposite edges of these walls. Additionally, the roof edges along these walls (e.g., "upwind side wall" and "downwind windward wall") were noted to experience somewhat elevated suction values.

Figure 113 and Figure 114 display the maximum and minimum $C_{p,\ critical}$ values for model $C1_{hip\_2021}$. In this model, the wall sections (North, West, South, and East) experienced an increase of maximum $C_{p,\ critical}$ values of up to 11% in the highest single values observed on the walls (102%, 111%, 105%, and 107%) when compared to the rectangular model with the same roof ends type (e.g., hip ends). Furthermore, the roof section experienced a significant 56% increase in the highest observed maximum $C_{p,\ critical}$ value. In addition, most of the walls in this model showed an upsurge of nearly 2% in the development of minimum $C_{p,\ critical}$ values, while the roof demonstrated a 23% reduction. In general, the walls (excluding the "inner side walls" and the "downwind windward wall") displayed the expected maximum $C_{p,\ critical}$ pressure distribution, with higher pressure values concentrated in the upper half of the walls. Conversely, the "inner side walls" were noted for developing higher maximum $C_{p,\ critical}$ values near the upwind edge of the walls and at the joint between the "inner side wall" and the "downwind windward wall."

Additionally, the roof edges along these walls (e.g., "inner side walls" and "downwind windward wall") experienced somewhat higher maximum $C_{p,\ critical}$ values than those observed in model $R2_{hip\_2023}$. Concerning minimum $C_{p,\ critical}$ values (Figure 114), similar observations were made as with maximum $C_{p,\ critical}$ values. The "inner side walls" and the "downwind windward wall" exhibited unconventional or unexpected minimum $C_{p,\ critical}$ development. For example, the "inner side walls" displayed higher suction values near the upwind edge of the wall and at the 90-degree wall joint, a phenomenon observed in previous models. An intriguing minimum $C_{p,\ critical}$ pressure development was noticed on the "downwind windward wall," where two suction bubbles were observed to form at ¼ and ¾ of the wall's length. As seen in previous models, roof edges along these "inner side walls" and "downwind windward walls" tended to exhibit a small increase in minimum $C_{p,\ critical}$ values.

Regarding model $S1_{hip\_2021}$, similar observations to those made for model $C1_{hip\_2021}$ were noted. In the results presented in Figure 115 and Figure 116, it is evident that the walls experienced an increase in maximum $C_{p,\ critical}$ values, reaching an elevation of up to 16%. On the roof, this increase reached as high as 61%. In addition, the suction values (represented by the single highest minimum $C_{p,\ critical}$ values) increased by up to 8% on the wall sections and reached a reduction of 22% on the roof section when compared to the values observed on the rectangular model. Overall, most walls exhibited higher maximum $C_{p,\ critical}$ values across the top half of the wall, spanning from edge to edge. However, the "upwind side walls" and "downwind windward walls" (located at the north and south of the figure, corresponding to the top and bottom of the figure) displayed unconventional distributions of maximum $C_{p,\ critical}$ values. For instance, as previously described in other

models, the "downwind windward walls" tended to exhibit higher maximum $C_{p,\ critical}$ values starting approximately 10 feet away from the 90-degree wall joint and near the 90-degree wall joint itself. In addition, the "upwind side walls" demonstrated a concentration of high suction values near the edge of the wall, likely due to the separated flow being shed from the walls facing east and west of the page at wind directions of 90 and 270 degrees. Examining the results from the minimum $C_{p,\ critical}$ contour plot, it became apparent that the "upwind side walls" as well as the "downwind windward walls" exhibited somewhat unexpected distributions of overall minimum $C_{p,\ critical}$ values. For example, both walls were observed to generate concentrations of suction forces near the walls' 90-degree joint as well as at their outer edges. Interestingly, in both "downwind windward walls," the suction concentrations developed most likely due to complex flow interactions at wind directions of 0 and 180 degrees. Lastly, the roof edges near the "inner side walls" and "downwind windward walls" experienced somewhat increased suction values.

A table summarizing the percentage difference between irregular shaped models tested in 2021 is presented in Table 5. Please note that the worst positive and negative Cp, critical value, for all wall sections, was compared against the worst positive and negative Cp, critical value of a rectangular model. The increase, or decrease, in the critical pressure coefficient values are presented in Table 6. From the table, it was observed that wall sections, in some models, underwent an increase of positive critical pressure coefficients of up to 14%. Interestingly, negative critical pressure coefficients were also observed to increase up to 14% in one of the models with irregular shape.

The results for models tested in 2023 are presented from Figure 117 to Figure 136 in the form of maximum $C_{p,\ critical}$ and minimum $C_{p,\ critical}$ contour plots.

For model $T1_{gable\_2023}$ (Figure 117), most walls exhibited the expected maximum $C_{p,\ critical}$ development. However, the walls located near the 90-degree wall joint, specifically between the "upwind side wall" and "downwind windward wall," displayed deviations in results due to the complex flow interactions shedding off the upwind sections. In the case of the "upwind windward walls," there was a concentration of pressures extending from the center of the wall towards the upwind edge. On the other hand, the "downwind windward walls" exhibited the highest maximum $C_{p,\ critical}$ values near the outer top corner. Additionally, the roof section displayed increased maximum $C_{p,\ critical}$ values near the areas of the 90-degree wall joints. When compared to the results obtained from model $R1_{gable\_2023}$ (Figure 133), the highest single value observed on the entire roof of the irregular-shaped model was 42% higher than the highest single value observed on the rectangular model. In terms of minimum $C_{p,\ critical}$ values (Figure 118), it was noticed that the edges of the walls tended to develop higher minimum $C_{p,\ critical}$ values. Interestingly, only a slight deviation in minimum $C_{p,\ critical}$ values was observed on the "upwind side walls," possibly influenced by the overall length of the "downwind windward wall." Furthermore, the "downwind windward wall" exhibited the highest minimum $C_{p,\ critical}$ values on the top inner corner of the wall, contrary to the conventional expectation of suctions developing near the outer edges (model $R1_{gable\_2023}$ - Figure 133 and Figure 134). Regarding the roof's minimum $C_{p,\ critical}$ values, it was observed that most edges tended to experience significantly higher values than the areas near the center of the overall roof, reaching values similar to those in model $R1_{gable\_2023}$ (Figure 134).

Figure 119 displays the maximum $C_{p,\ critical}$ values for model T_{2hip_2023}. Similar comments to those made regarding the wall sections in model T_{1gable_2023} (Figure 117) can

be applied here. The main distinction lies in the development of higher maximum $C_{p,\ critical}$ values in model $T2_{hip\_2023}$, albeit over a smaller area adjacent to the 90-degree wall joint. Turning our attention to the minimum $C_{p,\ critical}$ (Figure 120) values on the walls, it was observed that the edges of the walls generally exhibited the highest minimum $C_{p,\ critical}$ values, with the exception of the "downwind windward wall" and the "upwind side wall." These two walls experienced an increase in minimum $C_{p,\ critical}$ values near the 90-degree wall joint. As for the roof, it demonstrated elevated values of minimum $C_{p,\ critical}$ values along the edges (Figure 115).

Contour plots illustrating model $L1_{gable\_2023}$ $C_{p,\ critical}$ values are depicted in Figure 121 and Figure 122. In general, the wall sections exhibited a conventional distribution of maximum and minimum $C_{p,\ critical}$ values (like those observed in model $R1_{gable\_2023}$ and model $R2_{hip\_2023}$ - Figure 133, Figure 134, Figure 135 and Figure 136), with the exception of the two walls located at the 90-degree wall joint, namely the "upwind side wall" and the "downwind windward wall." Concerning maximum $C_{p,\ critical}$ values, the "downwind windward wall" displayed elevated values near the top outer corner of the wall, a phenomenon attributed to the re-entrant flow shed off the "upwind windward wall" at the 0-degree wind direction. Additionally, a similar occurrence was observed on the "upwind side wall," attributed to re-entrant flow shed off the "downwind side wall" at the 90-degree wind direction. Along the wall sections forming the 90-degree wall joint, the roof edges were noted to develop increased maximum $C_{p,\ critical}$ values. Regarding the minimum $C_{p,\ critical}$ values on the wall sections, the same observations as those made for the maximum $C_{p,\ critical}$ values apply. However, the "upwind side wall" and the "downwind windward wall" exhibited unconventional minimum $C_{p,\ critical}$ values. For instance, as seen in previous

models, the inner edges of these walls showed an upsurge in minimum $C_{p,\ critical}$ values, contrary to the behavior observed in all other walls. Across the model, the roof edges consistently experienced higher minimum $C_{p,\ critical}$ values.

The findings in model $L2_{hip\_2023}$ parallel those of model $L1_{gable\_2023}$ when examining the maximum and minimum $C_{p,\ critical}$ values across the wall sections, as depicted in Figure 123 and Figure 124. These sections exhibit a similar pattern, suggesting a consistency in the pressure coefficient distribution on the walls. However, the noteworthy departure from this similarity arises when focusing on the results pertaining to the roof sections. In model $L2_{hip\_2023}$, there is a striking distinction, notably in the significant reduction in the extent of the suction bubble. This deviation from the patterns observed in model $L1_{gable\_2023}$ underscores the unique characteristics and behavior of the airflow around the roof sections in model $L2_{hip\_2023}$.

The results pertaining to maximum and minimum $C_{p,\ critical}$ values are displayed in Figure 125 and Figure 126 for model $C1_{gable\_2023}$, and Figure 127 and Figure 128 for model $C2_{hip\_2023}$. When examining the maximum $C_{p,\ critical}$ values in both models, it became evident that they generally exhibited a conventional distribution on most walls. However, the "inner side walls" and the "downwind windward wall" displayed unconventional patterns in pressure coefficient distribution. For instance, the "inner side walls" exhibited increased maximum $C_{p,\ critical}$ values near both 90-degree wall joints and along the upwind (outer) edge. Similarly, the "downwind windward wall" tended to exhibit heightened maximum $C_{p,\ critical}$ values near its edges. Moreover, with respect to the maximum $C_{p,\ critical}$ values, the roof sections in both models displayed elevated values near the roof edges adjacent to the 90-degree wall joints, as illustrated in Figure 120 and Figure 122. Turning

our attention to the minimum $C_{p,\,critical}$ values in both models ($C1_{gable\_2023}$ and $C2_{hip\_2023}$ - Figure 126 and Figure 128), a noteworthy trend emerges, particularly in the "inner side walls" and the "downwind windward walls." These sections demonstrated counterintuitive pressure distributions in the form of minimum $C_{p,\,critical}$ values. For instance, the two "inner side walls" tended to experience decreased minimum $C_{p,\,critical}$ values along their inner edges, which are adjacent to the 90-degree wall joints. Conversely, the "downwind windward wall" exhibited an increase in minimum $C_{p,\,critical}$ values near the top corner of the wall, adjacent to the largest protruding section. This unusual behavior can be attributed to complex flow interactions in this specific region.

The results regarding the maximum and minimum $C_{p,\,critical}$ values for models $S1_{gable\_2023}$ and $S2_{hip\_2023}$ are presented in Figure 129 through Figure 132. In general, the walls not positioned adjacent to a 90-degree wall joint exhibited expected maximum and minimum $C_{p,\,critical}$ values. However, a recurring trend observed in all models, spanning from 2019, 2021, to 2023, is the development of somewhat unconventional pressure values in walls adjacent to 90-degree wall joints. It is important to note that models S can be likened to two L models placed back-to-back. Therefore, the section definitions for the windward and leeward sides (Figure 24) apply similarly. For example, both "downwind windward walls" displayed increased maximum $C_{p,\,critical}$ values near the outer edge of the wall, while the "upwind side walls" exhibited similar behavior. These concentrations of maximum $C_{p,\,critical}$ values can be attributed to re-entrant flows being shed off the "upwind windward walls" at various wind directions (e.g., 0, 90, 180, and 270 degrees). Regarding the roof sections, the edges of the roof along the 90-degree wall joints demonstrated higher maximum $C_{p,\,critical}$ values for both models, as depicted in Figure 129 and Figure 131.

Interestingly, the roof edges adjacent to the widest "protruding section" of model $S2_{hip\_2023}$ (the protruding section facing north) also exhibited elevated maximum $C_{p,\ critical}$ values. For the minimum $C_{p,\ critical}$ values, the same observations that applied to the walls regarding overall maximum $C_{p,\ critical}$ values distribution can be extended. Specifically, the "upwind side walls" and the "downwind windward walls" displayed somewhat unique minimum $C_{p,\ critical}$ distributions, particularly in the inner top corners of the walls. Notably, there was a significant difference between the roof sections of the two models, with the roof of model $S2_{hip\_2023}$ being considerably more susceptible to developing higher suction values.

A summary of the difference between the single highest maximum and minimum Cp,critical values between North, West, South, East and Roof sections of irregular shaped model's vs regular shaped modes is presented in Table 7 and Table 8.

In order to obtain the difference between all the walls of the irregular shaped models against a rectangular model, the worst positive and negative critical pressure coefficient value (of all walls) was obtained and compared against the worst positive and negative value of all the walls of the rectangular model. From results, it was noted that walls on models with irregular shapes underwent an increase of positive critical pressure coefficients of up to 18% and 13% for models with gable and hip roof ends. On the other hand, the negative values developed on wall sections of models with irregular shapes were observed to experience a 26% and 14% on models with gable and hip roof ends (Table 9 and Table 10).

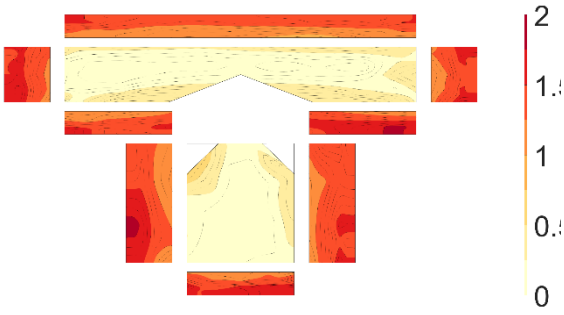

Figure 109. $T1_{hip\_2021}$ maximum $C_{p,\,critical}$

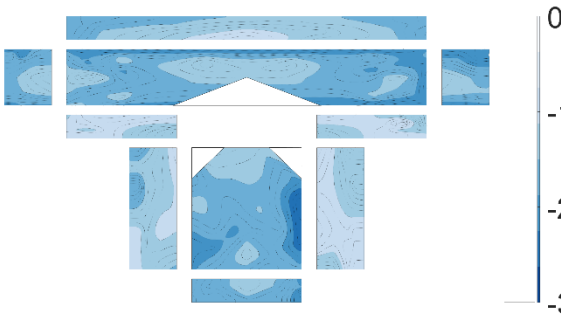

Figure 110. $T1_{hip\_2021}$ minimum $C_{p,\,critical}$

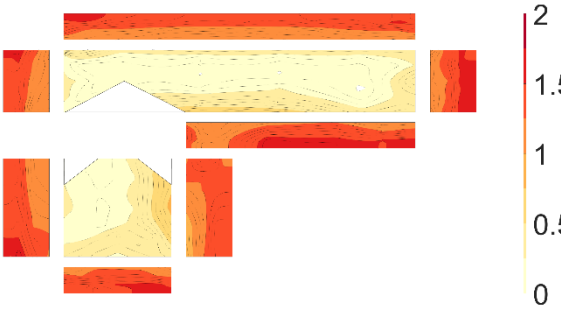

Figure 111. $L1_{hip\_2021}$ maximum $C_{p,\,critical}$

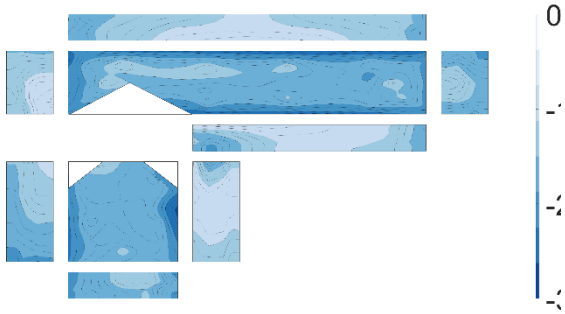

Figure 112. $L1_{hip\_2021}$ minimum $C_{p,\,critical}$

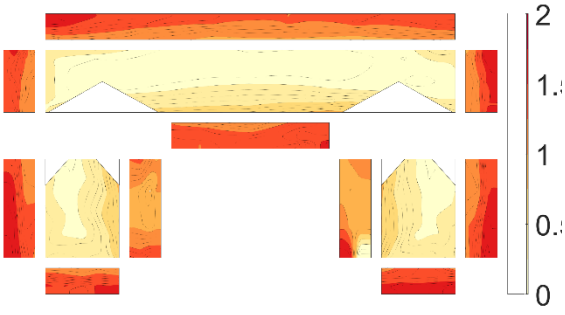

Figure 113. $C1_{hip\_2021}$ maximum $C_{p,\,critical}$

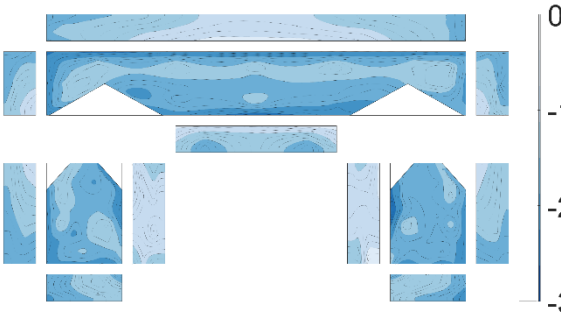

Figure 114. $C1_{hip\_2021}$ minimum $C_{p,\,critical}$

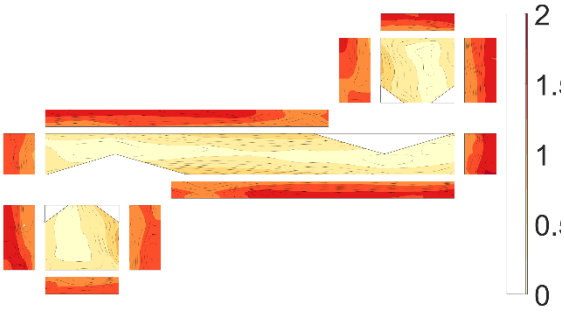

Figure 115. $S1_{hip\_2021}$ maximum $C_{p,\,critical}$

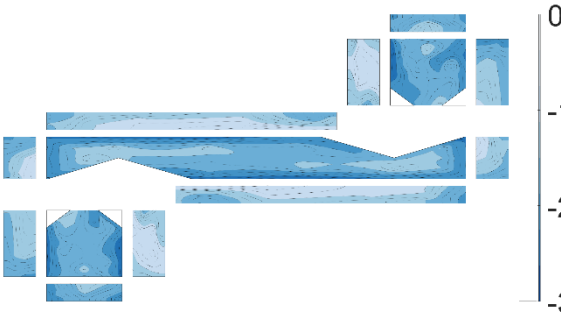

Figure 116. $S1_{hip\_2021}$ minimum $C_{p,\,critical}$

Table 5. Wall and roof sections highest maximum vs minimum $C_{p,\,critical}$ variation percentages – 2021 experiments (hip roofs)

SECTION	MODEL T1		MODEL L1		MODEL C1		MODEL S1	
	MAX	MIN	MAX	MIN	MAX	MIN	MAX	MIN
North	101%	96%	97%	100%	102%	91%	109%	102%
West	114%	110%	100%	107%	111%	99%	102%	104%
South	117%	111%	103%	102%	105%	100%	110%	108%
East	105%	123%	99%	103%	107%	102%	116%	108%
Roof	115%	80%	153%	80%	156%	77%	161%	78%

Table 6. Overall walls sections highest maximum vs minimum $C_{p,critical}$ – 2021 experiments (hip roofs)

SECTION	MODEL T1		MODEL L1		MODEL C1		MODEL S1	
	MAX	MIN	MAX	MIN	MAX	MIN	MAX	MIN
Walls	114%	114%	100%	102%	111%	100%	110%	108%

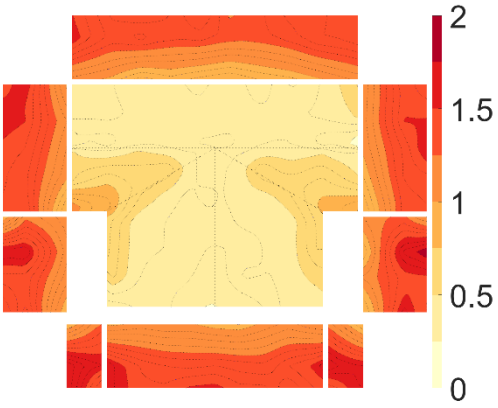

Figure 117. $T1_{gable\_2023}$ maximum $C_{p,\,critical}$

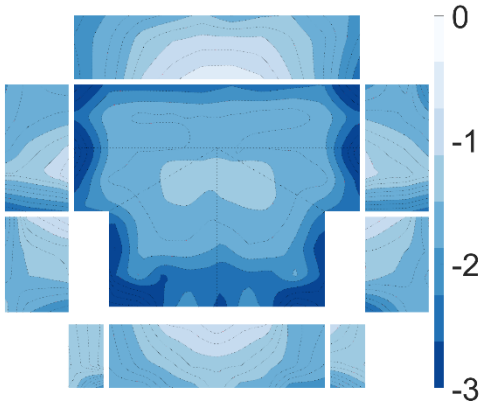

Figure 118. $T1_{gable\_2023}$ minimum $C_{p,\,critical}$

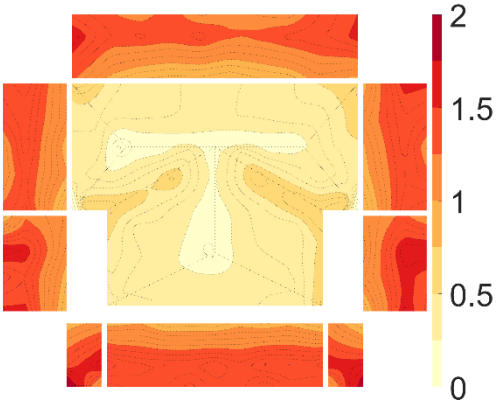

Figure 119. $T2_{hip\_2023}$ maximum $C_{p,\,critical}$

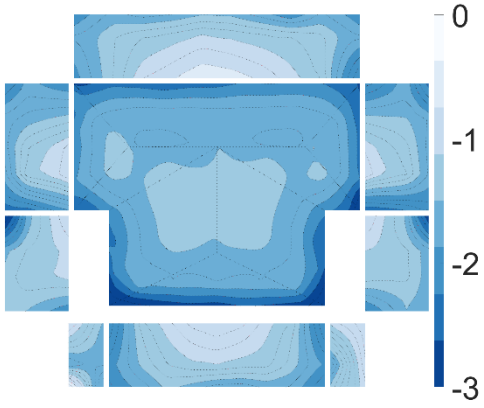

Figure 120. $T2_{hip\_2023}$ minimum $C_{p,\,critical}$

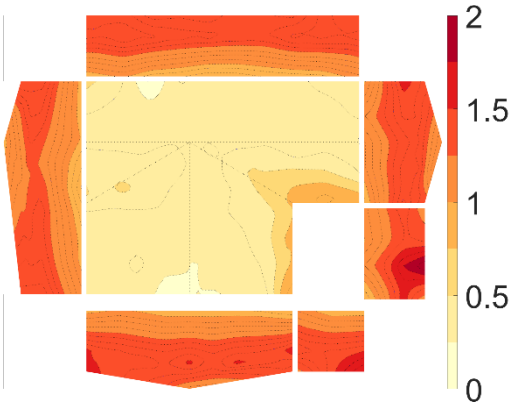

Figure 121. $L1_{gable\_2023}$ maximum $C_{p,\,critical}$

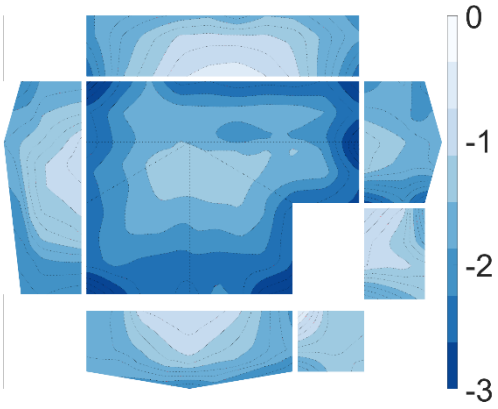

Figure 122. $L1_{gable\_2023}$ minimum $C_{p,\,critical}$

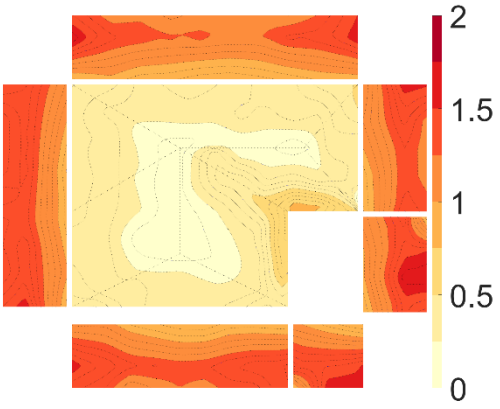

Figure 123. $L2_{hip\_2023}$ maximum $C_{p,\,critical}$

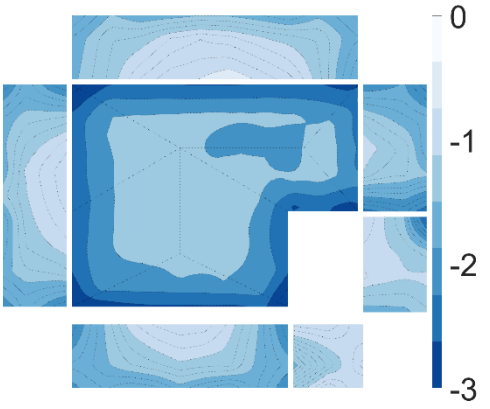

Figure 124. $L2_{hip\_2023}$ minimum $C_{p,\,critical}$

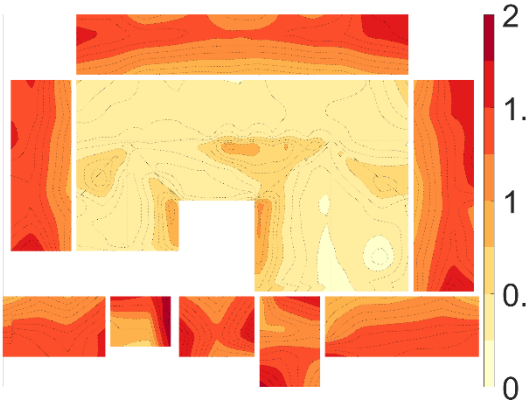

Figure 125. $C1_{gable\_2023}$ maximum $C_{p,\,critical}$

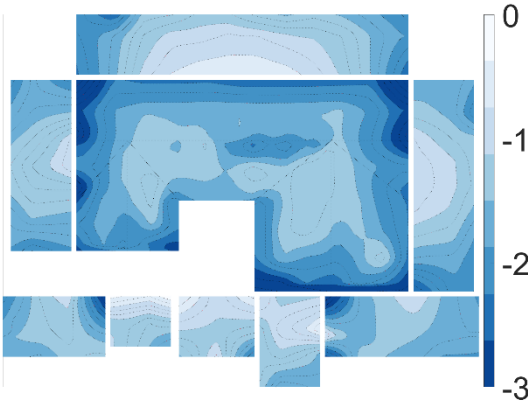

Figure 126. $C1_{gable\_2023}$ minimum $C_{p,\,critical}$

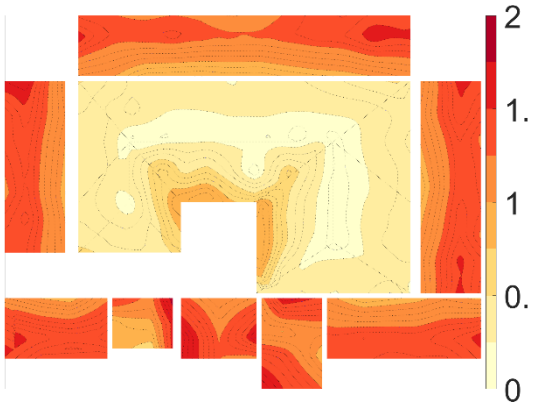

Figure 127. C2$_{hip_2023}$ maximum $C_{p,\ critical}$

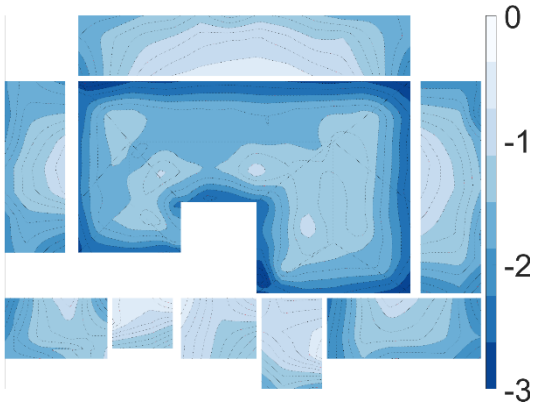

Figure 128. C2$_{hip_2023}$ minimum $C_{p,\ critical}$

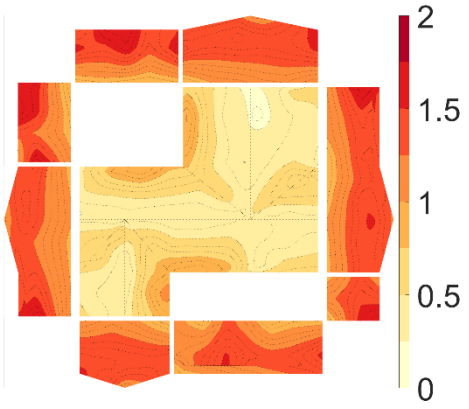

Figure 129. S1$_{gable_2023}$ maximum $C_{p,\ critical}$

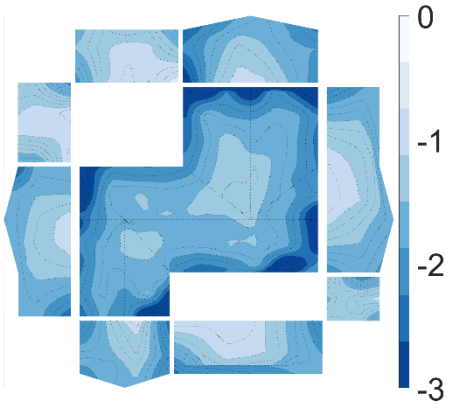

Figure 130. S1$_{gable_2023}$ minimum $C_{p,\ critical}$

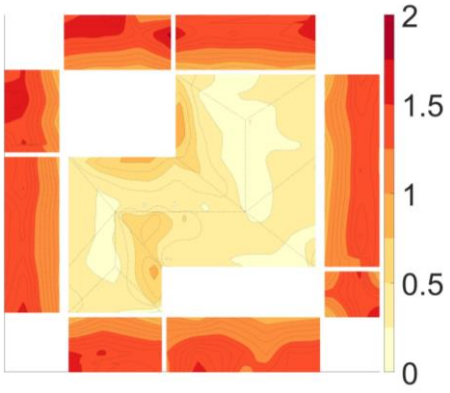

Figure 131. S2$_{hip_2023}$ maximum $C_{p,\ critical}$

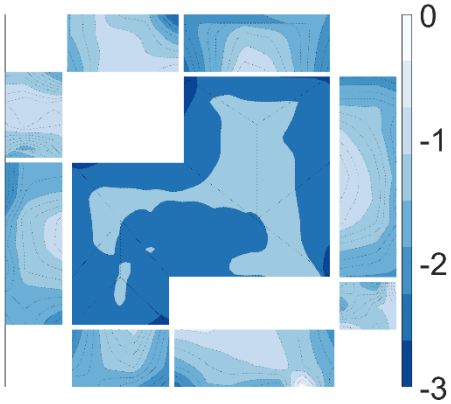

Figure 132. S2$_{hip_2023}$ minimum $C_{p,\ critical}$

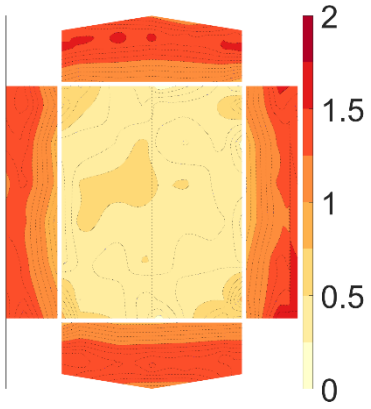

Figure 133. $R1_{gable\_2023}$ maximum $C_{p,\,critical}$

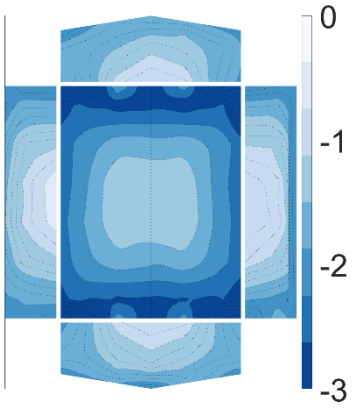

Figure 134. $R1_{gable\_2023}$ minimum $C_{p,\,critical}$

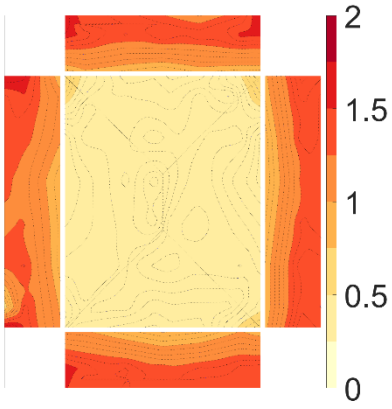

Figure 135. $R2_{hip\_2023}$ maximum $C_{p,\,critical}$

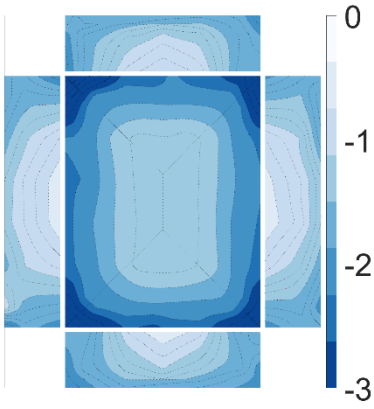

Figure 136. $R2_{hip\_2023}$ minimum $C_{p,\,critical}$

Table 7. Wall and roof sections highest maximum vs minimum $C_{p,\,critical}$ variation percentages – 2023 experiments (gable roofs)

Sections	T1gable_2023		L1gable_2023		C1gable_2023		S1gable_2023	
	MAX	MIN	MAX	MIN	MAX	MIN	MAX	MIN
North	96%	108%	97%	106%	100%	109%	106%	128%
West	112%	107%	124%	102%	112%	97%	110%	103%
South	115%	105%	109%	110%	109%	141%	109%	113%
East	113%	106%	99%	113%	111%	110%	104%	101%
Roof	142%	94%	135%	92%	157%	90%	161%	90%

Table 8. Wall and roof sections highest maximum vs minimum $C_{p,\,critical}$ variation percentages – 2023 experiments (hp roofs)

Sections	T2hip_2023		L2hip_2023		C2hip_2023		S2hip_2023	
	MAX	MIN	MAX	MIN	MAX	MIN	MAX	MIN
North	101%	107%	102%	91%	103%	100%	110%	116%
West	103%	121%	99%	103%	104%	109%	108%	112%
South	115%	102%	102%	95%	109%	111%	104%	103%
East	109%	114%	109%	113%	105%	109%	105%	109%
Roof	155%	96%	153%	99%	184%	104%	185%	104%

Table 9. Overall walls sections highest maximum vs minimum $C_{p,critical}$ – 2023 experiments (gable roofs)

Sections	T1gable_2023		L1gable_2023		C1gable_2023		S1gable_2023	
	MAX	MIN	MAX	MIN	MAX	MIN	MAX	MIN
Walls	112%	106%	118%	113%	110%	126%	106%	124%

Table 10. Overall walls sections highest maximum vs minimum $C_{p,critical}$ – 2023 experiments (hip roofs)

Sections	T2hip_2023		L2hip_2023		C2hip_2023		S2hip_2023	
	MAX	MIN	MAX	MIN	MAX	MIN	MAX	MIN
Walls	113%	114%	104%	106%	106%	111%	110%	111%

5.5. VALIDATION WITH AERODYNAMIC DATABASES

As outlined in section 4.4, there has been a limited focus on exploring the impact of plan irregularities in low-rise buildings on the overall pressure distribution. This scarcity of research makes it somewhat challenging to evaluate the outcomes derived from wind tunnel experiments. To address this issue, a rectangular model was constructed and tested as a "benchmark" during each phase of experiments (in 2019, 2021, and 2023). These wind tunnel results from the rectangular benchmark models were then compared to publicly available aerodynamic databases, such as the National Institute of Standards and Technology (NIST - Ho et al., 2005, NIST 2004) and Tokyo Polytechnic University (TPU

-, Tamura et al., 2005, Tamura 2012). This comparison allowed for a validation of the findings obtained through wind tunnel testing.

To facilitate a normalized comparison among the results from different models, various approaches were employed. When using the NIST model for comparison, a scaled gable roof model was utilized, featuring dimensions of 100x50x12 feet (in full-scale measurements) for length, breadth, and height. This specific model corresponds to Test 3 of Phase II in the NIST study (Ho et al., 2003 Phase I, Ho et al., 2003 Phase II, Ho et al., 2005, NIST 2004). In the case of the TPU model for comparison, a similarly scaled gable roof model was employed, with dimensions measuring 131.23x52.49x14.1 feet (in full-scale dimensions) for length, breadth, and height. This particular model is identified as "g200218" in the research conducted by Tamura et al. (2005) and Tamura (2012). For the rectangular model tested in the wind tunnel, a replica of the NIST mode was employed (Figure 80).

To evaluate the results across the three distinct structures, a dividing line was established on each wall segment and the roof sections, encompassing the North, West, South, East, and Roof sections. The positioning of these dividing lines was determined by considering the height of the pressure tap line in relation to the wall height (for the walls) and the distance from the roof ridge to the pressure tap line (for the roof sections). The ratios that most closely aligned with all the models, both for the walls and roof sections, were then chosen. Subsequently, these lines were generated for all three models, as illustrated in Figure 137. Please note each wall was identified as North, West, South and East walls and the direction of wind is shown with blue arrows in Figure 137. Please note the Reynolds number at each model eave height was estimated, as it was mentioned in

section 4.4, by using Equation 3. Models' properties and Reynolds number value for all models are presented in Table 11. Values show that Reynolds number for NIST, TPU and ABL were sufficient to obtain an accurate wind simulation, by meeting the criteria provided by Cermak et al., 1999 ($R_H=10^4$).

To verify the experimental results obtained for model R_{gable_2021} (Figure 80), a comparison was conducted between the mean, maximum, and minimum pressure coefficients across all three models. This validation process was carried out by plotting the pressure coefficient values for each pressure tap along the length of the bisecting line in each model. This involved creating plots for each wall section (North, West, East, and South), encompassing the mean, maximum, and minimum pressure coefficients of the pressure taps located along the bisecting line for NIST, TPU, and ABL results. Likewise, a similar plot was generated for the roof sections.

Based on the findings presented in Figure 138, it was evident that at a wind direction of 90 degrees, there was a noteworthy alignment in the mean and minimum Cp values between the east and west walls. Specifically, the east wall, acting as the windward wall, and the west wall, serving as the leeward wall, displayed consistent agreement in their mean and minimum Cp values across NIST, TPU, and ABL results. However, it was notable that TPU model exhibited somewhat higher positive peak values in comparison to those calculated for the ABL and NIST models. Similarly, the south and north walls, which functioned as side walls, exhibited reasonable congruence in the development of mean, maximum, and minimum Cp values when contrasting the ABL and TPU outcomes. A divergence was identified in the case of the TPU minimum Cp values when compared to the results obtained from the ABL and NIST datasets, as illustrated in Figure 139.

Furthermore, the results derived from the roof sections displayed strong agreement in mean, maximum, and minimum values, with the exception of the minimum values observed on the roof section of the ABL model resulting in somewhat higher values, as depicted in Figure 140.

When examining the outcomes at a cornering angle of 45 degrees (as illustrated in Figure 141 to Figure 143), it was apparent that there was a notable concurrence between the east and west walls of the TPU and ABL models. However, a small disparity in the development of maximum Cp values (on the east walls) and minimum Cp values (on the west walls) was discernible in the results from the TPU model, as shown in Figure 141. It is important to note that this difference primarily manifested at the upwind edge of the east and west walls, with the east wall experiencing higher suction pressures due to its shorter adjacent south wall. Moreover, the maximum, mean, and minimum pressure coefficient values for the south and north walls demonstrated reasonable agreement between the NIST, TPU, and ABL models. Nonetheless, as noted previously, the TPU model exhibited higher maximum Cp values on the south walls - Figure 142. Regarding the north walls, good agreement was observed across all three models for mean, maximum and minimum Cp values. At this cornering angle, some noteworthy discrepancies were observed along the roof leading edge, where the NIST model registered somewhat lower suction values, as shown in Figure 143.

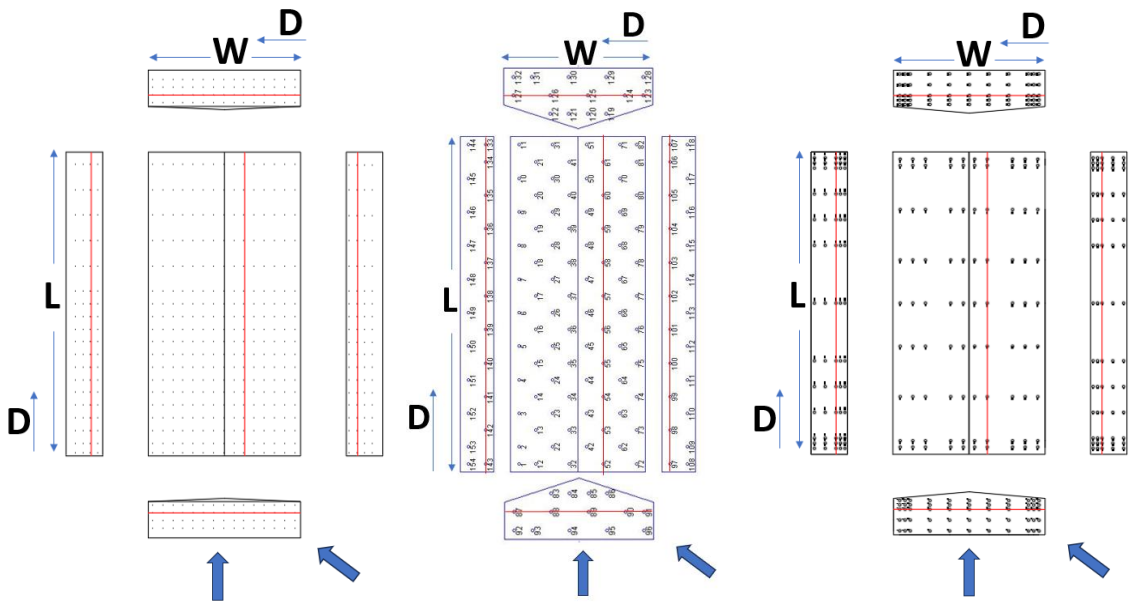

Figure 137. Bisecting lines for a) NIST model, b) TPU model and c) R_{gable_2021} model (ABL)

Table 11. Models' dimensional properties and Reynolds number comparison – 2021-2023 tests

Model	Scale	Eave height velocity V_H (mph)	Full Scale Eave Height (ft)	Full Scale Width (ft)	Full Scale Length (ft)	Roof Slope (degrees)	Reynolds Number R_H
NIST	100	20.4	12.0	50.0	100.0	2.4	2.24E+04
TPU	100	14.5	14.1	52.5	131.2	18.0	1.88E+04
ABLWT	100	18.1	12.0	50.0	100	20.0	1.99E+04

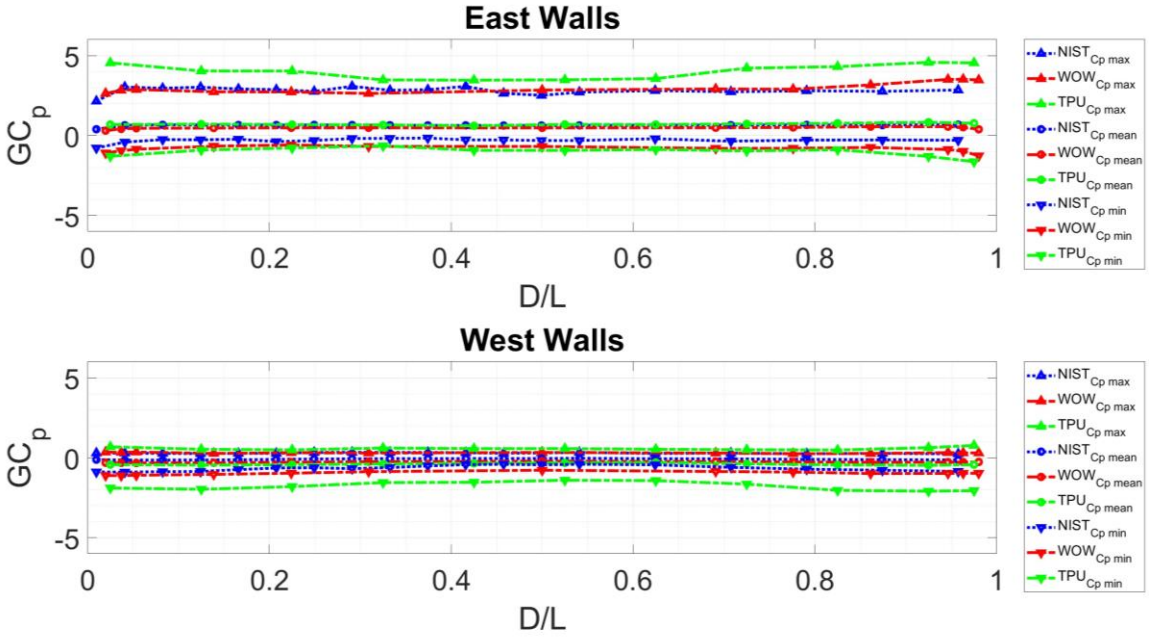

Figure 138. NIST vs TPU vs ABLWT_2021 validation – 90 degrees wind direction (East and West walls)

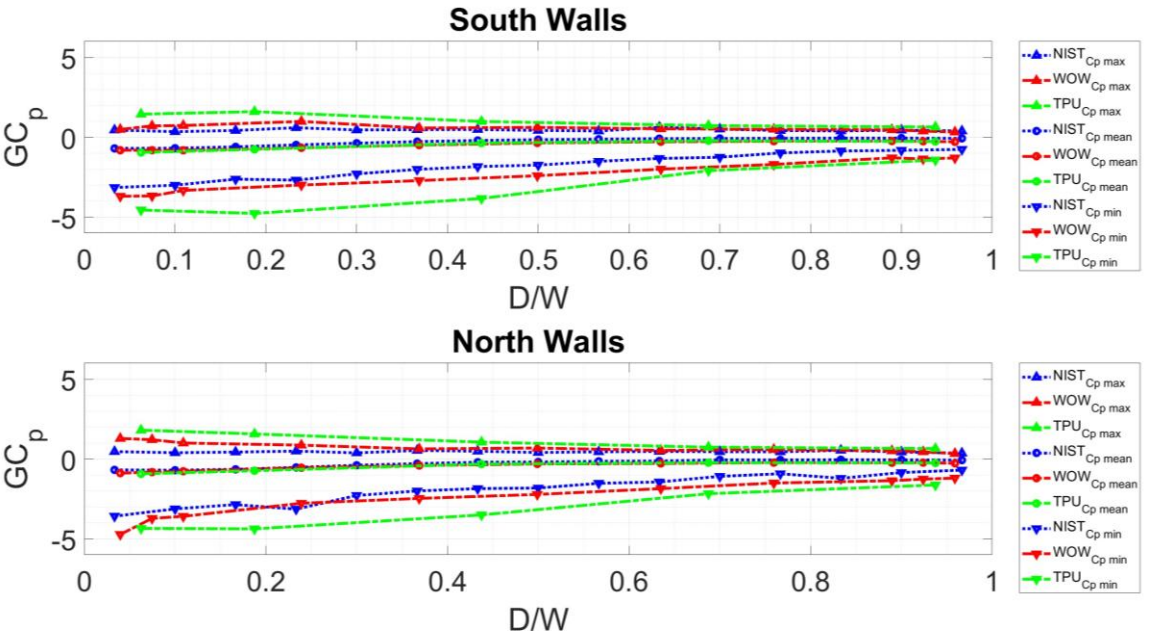

Figure 139. NIST vs TPU vs ABL_2021 validation – 90 degrees wind direction (South and North walls)

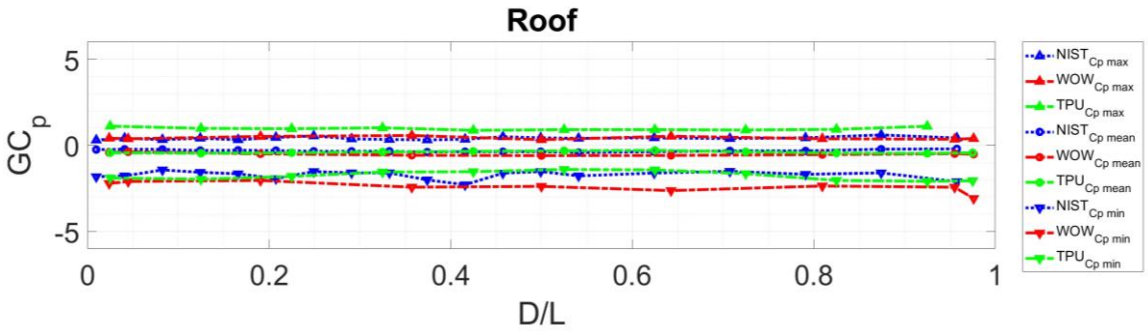

Figure 140. NIST vs TPU vs ABL_2021 validation – 90 degrees wind direction (Roof sections)

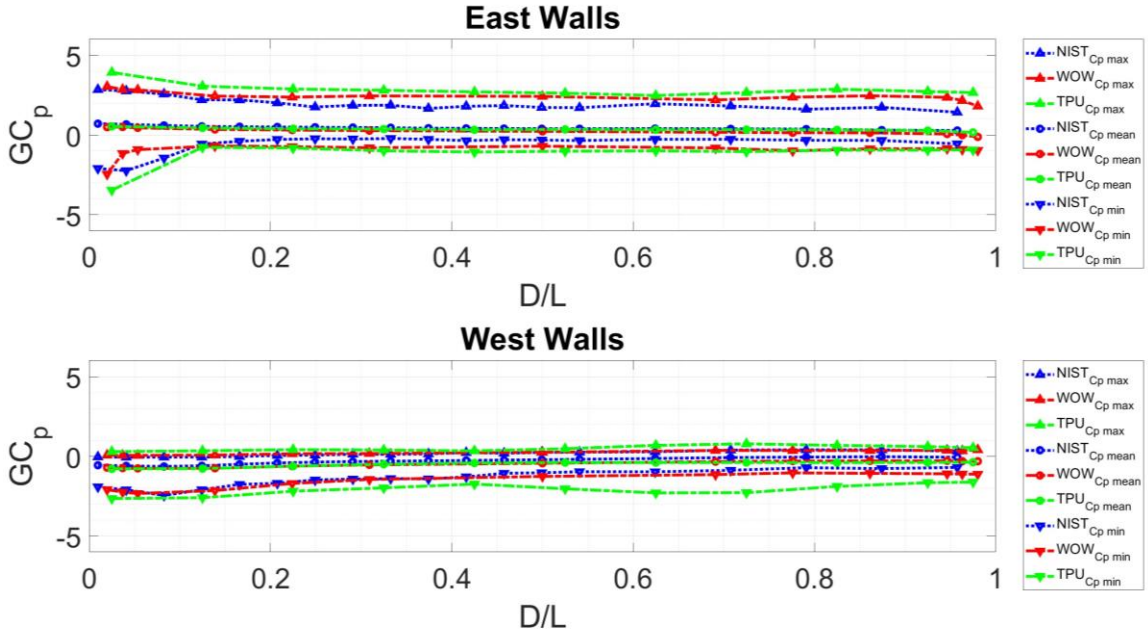

Figure 141. NIST vs TPU vs ABL_2021 validation – 45 degrees wind direction (East and West walls)

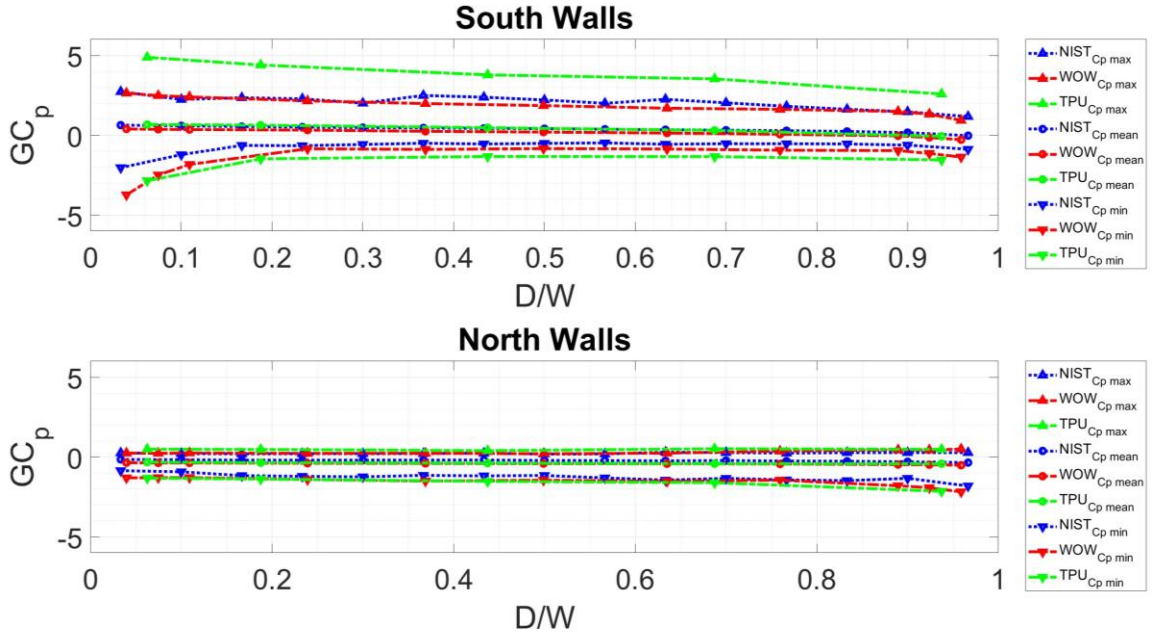

Figure 142. NIST vs TPU vs ABL_2021 validation – 45 degrees wind direction (South and North walls)

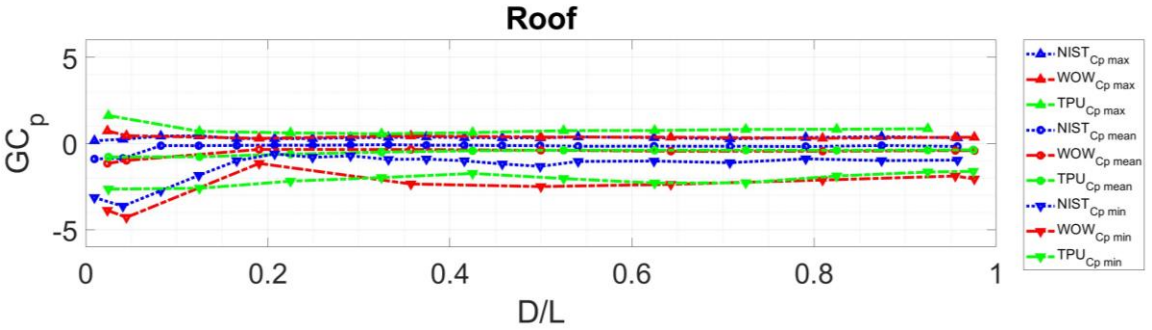

Figure 143. NIST vs TPU vs ABL_2021 validation – 45 degrees wind direction (Roof sections)

5.6. SMOKE VISUALIZATION

To gain a deeper understanding of the intricate airflow patterns surrounding low-rise buildings with irregular shapes, a smoke visualization study was conducted on select models tested in 2021. The primary objective of this study was to visually depict and comprehend the dynamics of airflow interactions, both within separated flows merging together and with other building sections extending beyond the main structure. To achieve this, three 2MegaPixel ELP high-speed cameras were strategically placed on the model:

one on the East side, one on the West side, and one on the Top side (refer to Figure 144). These cameras were synchronized to simultaneously capture video footage at 30 frames per second for a duration of 45 seconds. To generate the required smoke for visualization, a fog machine equipped with an extension rod was employed during the tests. It is essential to highlight that the wind tunnel conditions were adjusted to match the exposure settings used in the pressure measurement experiments and maintained at the same fan throttle position, specifically at 50% power or the 30Hz setting for the variable frequency drive. It should be noted that smoke visualization was conducted for all models tested in 2021 (T-, L-, C-, S-, and R-shape) spanning from 0 to 345 degrees, with increments of 15 degrees. Results for 0 and 90-degree orientations are provided for all models, while the 45-degree direction is exclusively presented for the rectangular model.

Upon scrutinizing the outcomes derived from model $T1_{hip\_2021}$ (Figure 145), an intriguing observation emerged. Specifically, when the wind direction was at 0 degree, it was observed that the airflow, which had separated from the "upwind windward wall," traveled downwind and collided with the outermost upper corner of the "downwind windward wall." This collision elucidates the formation of a pronounced concentration of high positive pressure at the juncture of these two crosswinds protruding sections, as depicted in the overlaid contour plots (refer to Figure a). The re-entrant flow, impacting the upper corner of the "downwind windward wall," also contributed to elevated mean Cp values of suction on the adjoining roof areas, as evidenced in Figure b. Furthermore, an intriguing phenomenon was witnessed—a recirculating bubble materialized due to the interaction between the separated flow originating from the "upwind windward wall" and the "downwind windward wall." This interaction notably influenced the pressure

distribution in proximity to the junction of the 90-degree walls. For instance, the "downwind windward wall" exhibited substantially lower mean Cp values (approaching 0) in the vicinity of the 90-degree wall juncture, a trend mirrored on the corresponding edge of the "upwind side wall." Additionally, the aggregation of negative pressures at the center top-edge of the "upwind side walls" may be attributed to the generation of recirculating flow in that corner. In the case of this same model but with a 90-degree wind direction (Figure 146), similar observations were noted. However, owing to the extended length (20% longer) of the new "downwind windward wall," a more conspicuous concentration of positive pressure became evident on this wall. This, in turn, exerted a more substantial influence on the neighboring "upwind side wall." Consequently, this configuration resulted in elevated mean Cp values of suction at the roof's corners compared to what was observed in the results obtained at a wind direction of 0 degree. Furthermore, a noteworthy observation pertained to the heightened suction values experienced on the "upwind leeward wall," which exhibited higher mean Cp values of suction than the farthest "downwind leeward wall."

Upon examining the findings from model $L1_{hip\_2023}$ (refer to Figure 147), it became evident that the flow impacting the "upwind windward wall" exhibited a distinct bifurcation into two separate streams: One stream led to the formation of a recirculation pattern along the "upwind side wall" and extended into a portion of the "downwind windward wall" in the vicinity of the 90-degree wall junction. The second stream comprised a mixture of the flow separated by the upwind windward wall (redirecting toward the outer edge of the "downwind windward wall") and the regular straight flow. This interplay resulted in a diminished impact on the development of positive pressures at

the point of stagnation, as illustrated in Figure a. Notably, there was a discernible increase in mean Cp values of suction along the roof edges adjacent to the "downwind windward wall." This phenomenon became particularly prominent from the 90-degree wall junction and extended outward to the edge of the roof, as depicted in Figure b. In the case of the same model but under a 90-degree wind direction (see Figure 148), it was observed that the impact of the separated flow generated by the "upwind windward wall" on the "downwind windward wall" was somewhat diminished due to the extended length of the protruding section in the upwind direction. Additionally, owing to the more pronounced length of the protruding section in the upwind direction, the "upwind side wall" exhibited a clearer progression of pressures, transitioning from positive (at the 90-degree walls junction) to negative (at the upwind edge of the "upwind side wall"). From the flow visualization, it was evident that a distinct recirculation bubble formed along the "upwind side wall." Furthermore, the roof section (as depicted in Figure b) displayed a reduced development of negative mean Cp values due to the decreased stagnation effect on the edge of the "downwind windward wall."

In the results obtained from model $C1_{hip\_2023}$ (at a wind direction of 0 degree - see Figure 149), an intriguing observation emerged concerning the three walls located centrally (comprising two "inner side walls" and the "downwind windward wall"). Upon inspecting the smoke visualization images, it became apparent that each of the "inner side walls" exhibited the formation of a recirculating flow bubble in the vicinity of the 90-degree wall junction area. Additionally, the "downwind windward wall" displayed a concentration of airflow at its central region. This observation aligns distinctly with the results portrayed in the contour plots, as depicted in Figure a. Moreover, the smoke traces depicted in this figure

revealed a flow pattern over the roof, concentrating along the valleys formed between the roof sections running parallel and perpendicular to the wind direction. Upon a closer examination of the results obtained from the roof section, it was noted that a heightened concentration of mean Cp values indicating suction was evident near the three locations corresponding to the recirculating bubbles, as illustrated in Figure b.

When examining the results under a 45-degree wind direction (as depicted in Figure 150), a notable presence of recirculating smoke traces became evident within the three walls forming a concave shape. This configuration, following the definition of the walls at 0-degree wind direction (comprising the two "inner side walls" and the "downwind windward wall"), engendered a complex interplay of flows. Consequently, the inner walls exhibited diverse pressure distributions, with the leftmost "inner side wall" and approximately half of the "downwind windward wall" manifesting positive pressures that subsequently transitioned into lower Cp values, ultimately reaching suction mean Cp values on the rightmost "inner side wall" (as illustrated in Figure a). This intricate flow recirculation had a discernible impact on the roof section adjacent to the leftmost "inner side wall." Here, the development of higher suction mean Cp values was observed compared to most of the roof, particularly along the roof valley in proximity to the 90-degree wall junction, area that exhibited elevated positive pressures forced to flow over the roof near the 90-degree wall junction, as depicted in Figure b.

Under a wind direction of 90 degrees, the C1hip_2021 model (as illustrated in Figure 151) also displayed the formation of a complex flow recirculation within the three walls that constituted a concave section. This flow recirculation, as discerned from the smoke traces, predominantly led to the walls experiencing mean Cp values indicative of

suction. It is important to mention that the leftmost "inner side wall" was subjected to a re-entrant flow, resulting in comparatively lower suction mean Cp values compared to the other two walls. When scrutinizing the roof section of this model under these wind conditions, it became evident that the flow recirculation had the effect of generating diminished mean Cp values indicative of suction near the roof's edge adjoining the leftmost "inner side wall" (as depicted in Figure b).

Finally, the results for model $S1_{hip\_2021}$ are presented for both 0-degree and 45-degree wind directions (see Figure 152 and Figure 153). In the case of the 0-degree wind direction (Figure 152), it was notable that the smoke traces displayed tendencies similar to those observed in model $L1_{hip\_2021}$ (Figure 142) for the sections situated in the upwind half (southern half). However, the other half of the model, positioned in the downwind direction, exhibited somewhat analogous outcomes to those witnessed in the $T1_{hip\_2021}$ model when oriented at a 90-degree wind direction (Figure 146). For instance, the resemblance to the L model was observed in terms of the separated flow generated by the "upwind windward wall" affecting both the "upwind side wall" and the "downwind windward wall." Furthermore, a similar pattern was noted in the upwind half of the roof, where the roof section tended to manifest more pronounced suction mean Cp values near the roof edges, particularly in proximity to the stagnation area on the "downwind windward wall." In contrast, the downwind half of the model, particularly the sections forming a 90-degree wall joint situated on the leeward side of the model, tended to exhibit values akin to those observed in the T model when oriented at a 90-degree wind direction. In this scenario, the two walls positioned on the leeward side of the model displayed varying suction values contingent on their specific location within the wall section. At a wind

direction of 90 degrees, the S model exhibited results resembling those obtained from the $L1_{hip\_2021}$ model at the same wind direction. Interestingly, this wind direction proved to be more critical in terms of the development of suction mean Cp values on the roof compared to those observed at a 0-degree wind direction, particularly evident at the 90-degree wall junction located on the south side of Figure 153 - b.

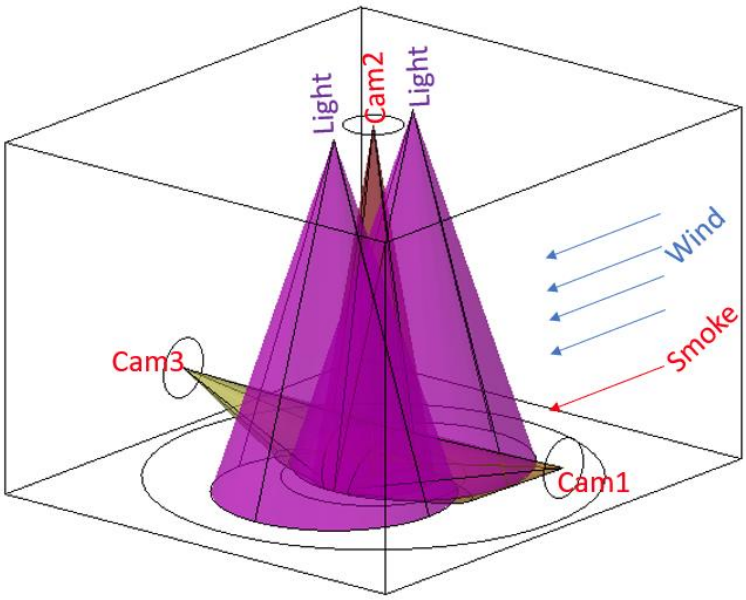

Figure 144. Camera setup for smoke visualization

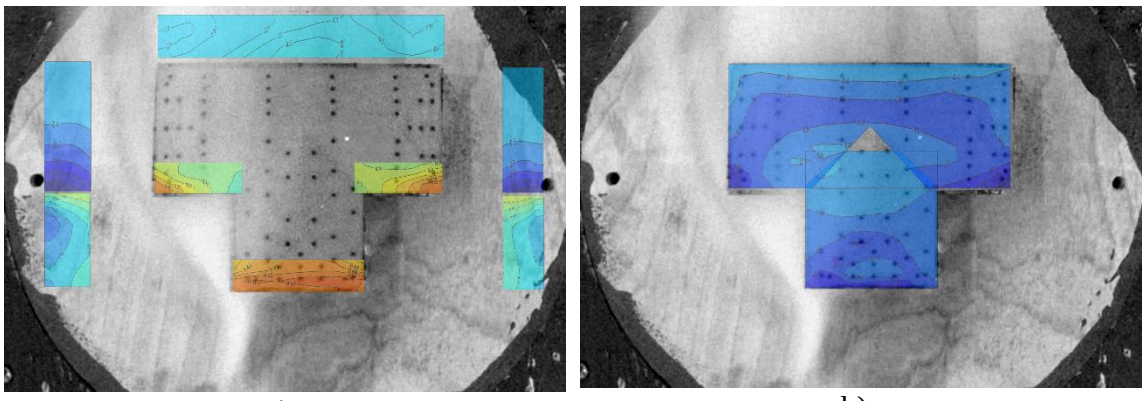

a) b)

Figure 145. Smoke visualization - model $T1_{hip\_2023}$ - 0 degree – a) walls, b) roof

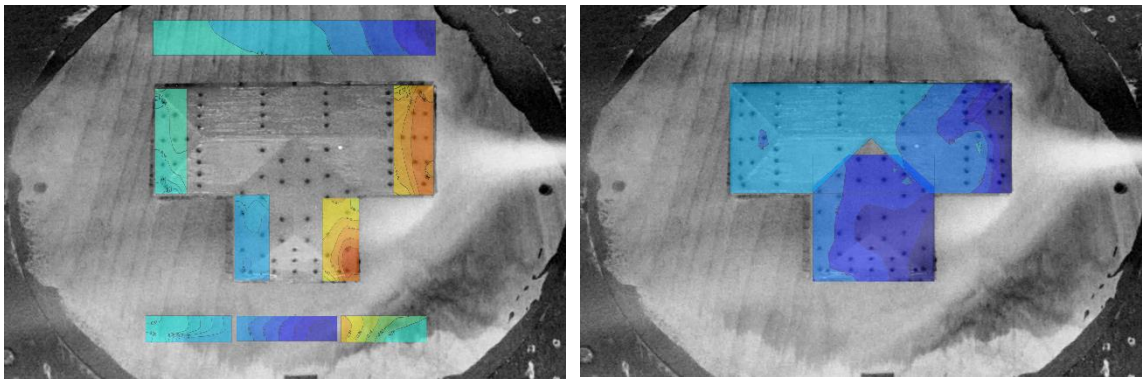

a) b)

Figure 146. Smoke visualization - model $T1_{hip\_2023}$ - 90 degrees – a) walls, b) roof

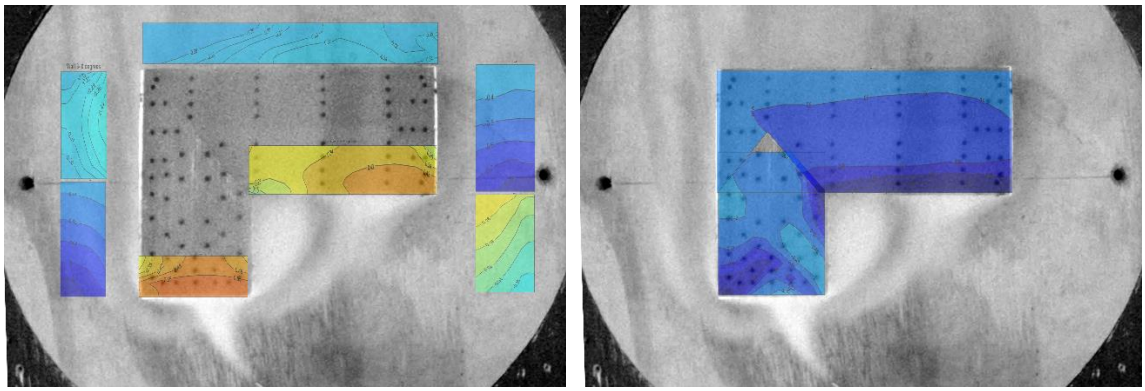

a) b)

Figure 147. Smoke visualization - model $L1_{hip\_2023}$ - 0 degree – a) walls, b) roof

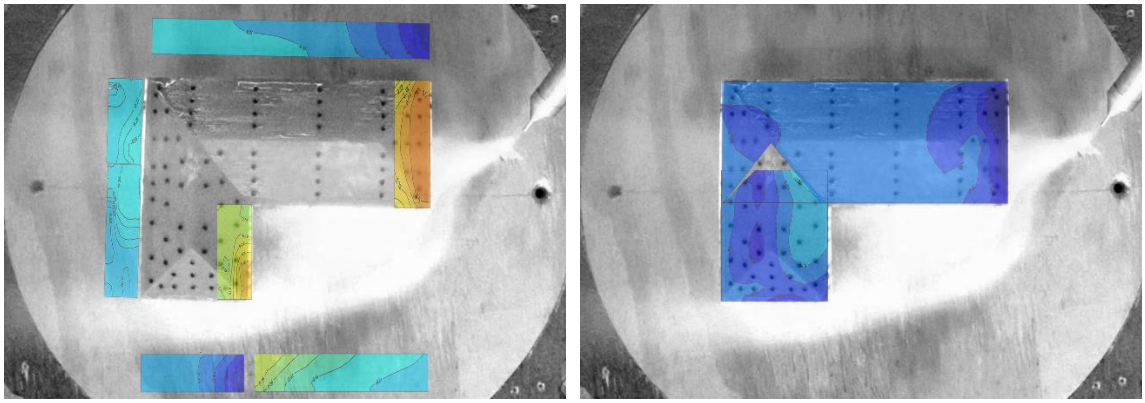

a) b)

Figure 148. Smoke visualization - model $L1_{hip\_2023}$ - 90 degrees – a) walls, b) roof

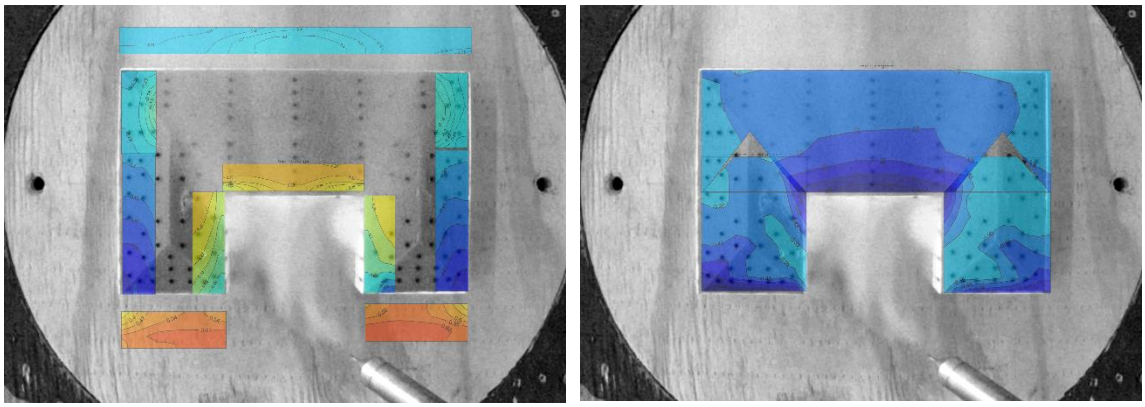

a) b)

Figure 149. Smoke visualization - model $C1_{hip\_2023}$ - 0 degree – a) walls, b) roof

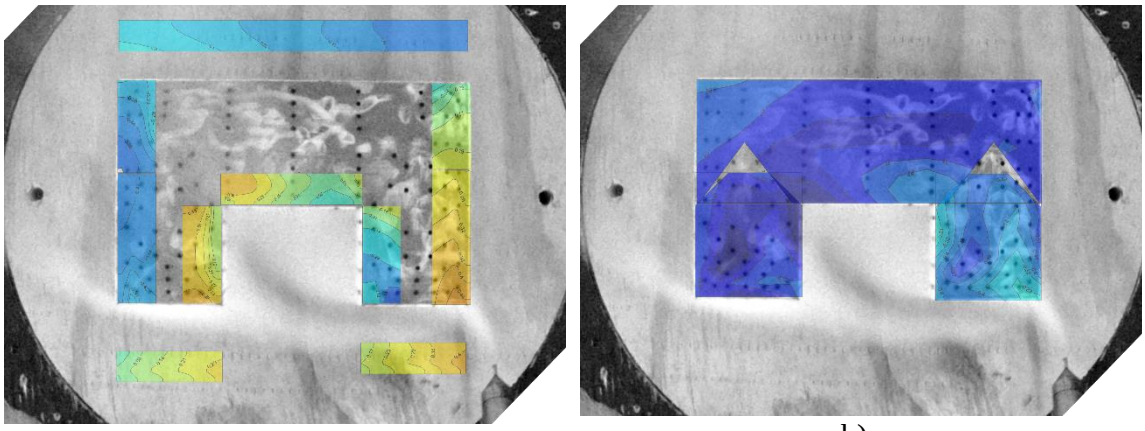

a) b)

Figure 150. Smoke visualization - model $C1_{hip\_2023}$ - 45 degrees – a) walls, b) roof

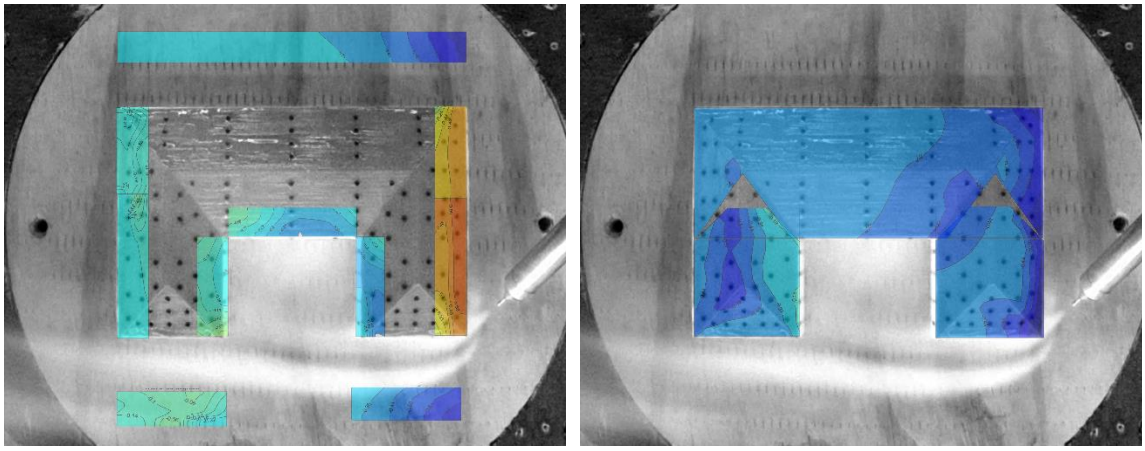

a) b)

Figure 151. Smoke visualization - model $C1_{hip\_2023}$ - 90 degrees – a) walls, b) roof

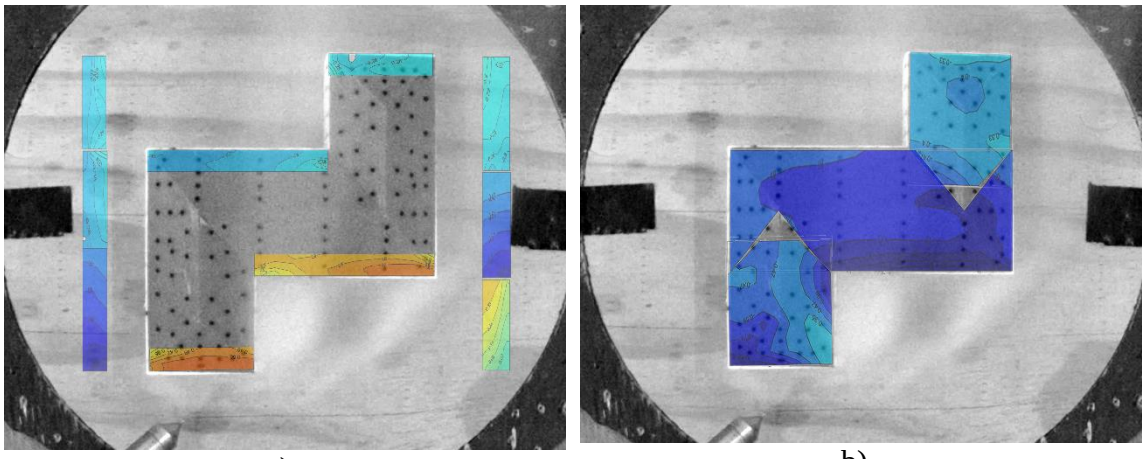

a) b)

Figure 152. Smoke visualization - model $S1_{hip\_2023}$ - 0 degree – a) walls, b) roof

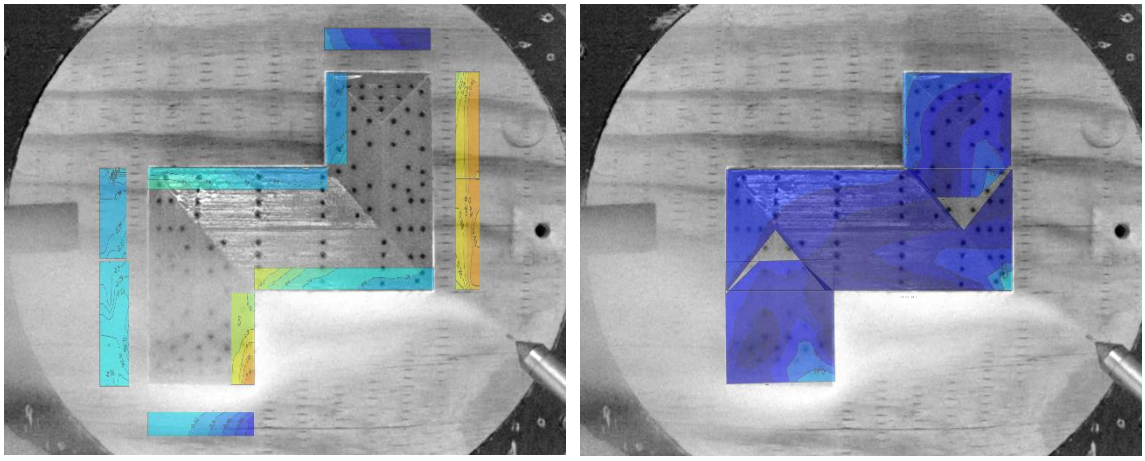

a) b)

Figure 153. Smoke visualization - model $S1_{hip\_2023}$ - 90 degrees – a) walls, b) roof

6. CODIFICATION

6.1. AREA AVERAGED PRESSURE COEFFICIENTS

Current building codes and wind standards (e.g., ASCE 7-22) offer a diverse array of methodologies for the design of low-rise structures. In this investigation, the primary emphasis was placed on the Components and Cladding (C&C) approach. The C&C

approach constitutes a specialized framework within the realm of structural engineering, specifically addressing the "elements of the structure or building envelope that do not fall under the purview of the Main Wind Force Resisting System (MWRF)" (as outlined in ASCE 7-22).

Within the context of this study, ASCE 7-22 holds a pivotal position as a principal point of reference. It provides a comprehensive set of guidelines, complete with envelope curves that are tailor-made for roof and wall sections. These envelope curves serve an indispensable function by furnishing crucial insights into the expected pressure levels that a particular section or cladding component is likely to encounter under the influence of wind forces. It is worth noting that these predictions are contingent upon the surface area of the specific building element in question.

To further enhance the precision of wind load analysis and facilitate meticulous structural design, the sections of walls and roofs are categorized into well-defined zones (Figure 154 and Figure 155). This zoning methodology has been meticulously formulated with the overarching goal of accurately identifying and appropriately configuring the areas of the structure that exhibit heightened vulnerability to increased suction forces, particularly those areas that are situated along the edges of the roof. Please note the zones distance from the edges depend on the value of a, which is defined as: 10% of the least horizontal dimension or 0.4h, whichever is smaller, but not less than either 4% of the least horizontal dimension or 3 feet. Please note h refers to the mean roof height of the building.

As visually represented in the accompanying figures, the zoning system systematically categorizes roof sections into zones 1, 2, and 3, following the guidelines set forth in ASCE 7-22. Similarly, wall sections are methodically divided into zones 4 and 5,

all in accordance with the same established standard (Figure 156 and Figure 157). This zoning framework assumes a pivotal role in ensuring that structural elements are meticulously designed to withstand the precise wind pressures they are anticipated to encounter. In turn, this contributes substantially to the overall safety and structural integrity of low-rise buildings.

It is crucial to emphasize that the development of these envelope curves relies heavily on a vast repository of empirical data derived from rigorous wind tunnel testing conducted on structures exhibiting consistent regular-shape geometrical configurations. This extensive dataset, which spans over a four-decade period, stands as a collective achievement stemming from the collaborative efforts of multiple researchers and research studies (Davenport et al., 1977, 1978; Ho et al., 2005, St. Pierre et al., 2005, Kopp et al., 2014, Vickery et al., 2011, Gavanski et al., 2013). These research endeavors have collectively laid a robust foundation upon which the envelope curves have been meticulously crafted for buildings with regular plans. However, it is evident that a lack of emphasis on investigating low-rise structures with complex plans has created a discernible absence of significant emphasis on the investigation of low-rise structures characterized by intricate, non-standard floor plans.

In the commentary of chapter 30 (ASCE 7-22), a figure and paragraph have been aimed for the design of buildings with shape irregularities, showing that although little information is provided, awareness on the subject is present. The guidance provided is a collective “judgment” of the Wind Load Committee (ASCE 7-22). The first step is to enclose the entirety of the irregularly shaped building into a rectangle (Holmes et al., 1990), to then estimate the value of ‘a’ to then apply the required zoning (Figure 158). When an

outward corner protrudes a distance less than 'a' from the wall, neither Zone 3 nor Zone 5 requirements are applicable. On the other hand, when the outward protrusion exceeds 'a,' both Zone 3 and Zone 5 requirements come into play. Reentrant (interior) corners, by their nature, do not necessitate the implementation of Zones 3 or 5. Similarly, corners with an included interior angle greater than 135 degrees also do not require compliance with Zone 3 or Zone 5 requirements. The expected loads on wall and roof sections are then estimated based on the GCp graphs provided for rectangular models. Another approach to design low-rise structures with irregular shapes is to divide the building into multiple rectangular sections and design then accordingly (ASCE 7-02), however, the estimation of loads would also be based on results obtained for regular shaped structures.

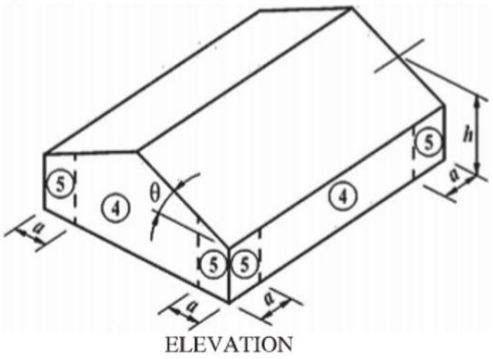

Figure 154. C&C – walls zoning (ASCE 7-22)

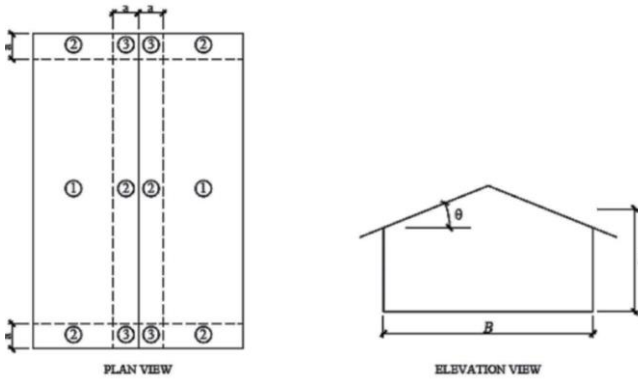

Figure 155. C&C – roof zoning (ASCE 7-22)

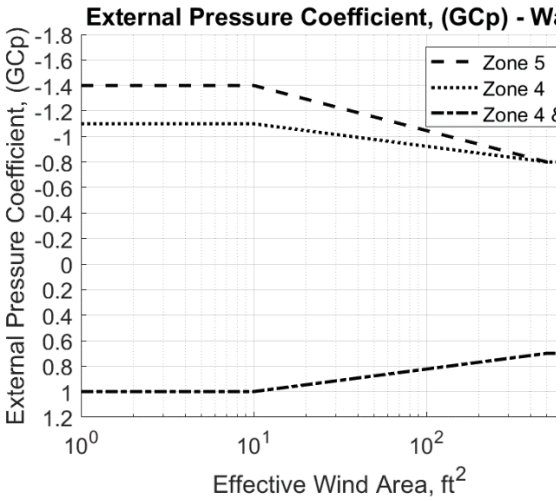

Figure 156. C&C external pressure coefficients (GCp) – walls (ASCE 7-22)

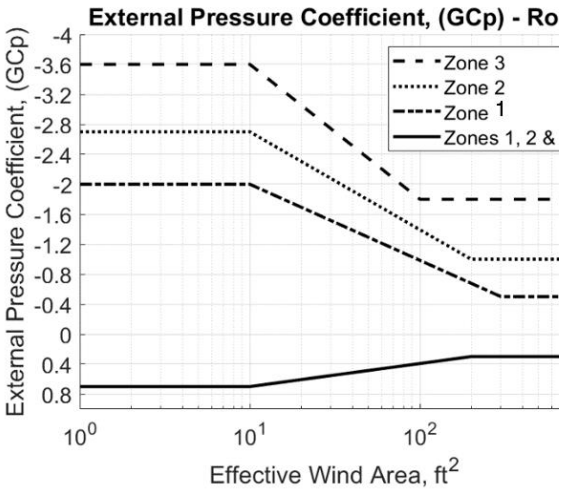

Figure 157. C&C external pressure coefficients (GCp) – roof (ASCE 7-22)

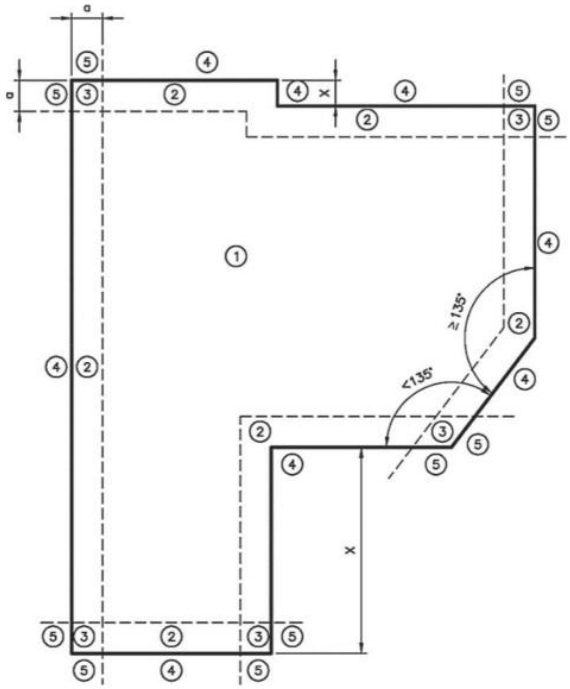

Figure 158. C&C irregular shaped buildings zoning (ASCE 7-22)

6.2. ASCE 7 COMPONENT AND CLADDING ASSESSMENT

The main objective of the current study was to conduct a systematic analysis and comparison of experimental data with existing design criteria. To achieve this, area

averaged GCp were computed for various combinations of pressure taps on walls and roof sections of the non-regular models. Multiple combinations of adjacent pressure-tap tributary areas, ranging from a single pressure tap to several pressure taps, were generated for each of the model zones (Zones 1 to 5). Subsequently, the Cp time history for each pressure tap was multiplied by its corresponding tributary area and used as input in Equation 8 for each wind direction. This approach enabled the generation of an area averaged GCp time histories for each area combination and wind direction tested.

These area-averaged time histories were then processed using the BLUE (Best Linear Unbiased Estimation) method to obtain statistical peaks, as discussed in Section 4.3.1. The worst result, among all wind directions, was selected for each area combination based on the obtained peaks, and scatter plots were generated. The area averaged GCp were then calculated for both walls and roofs sections and were plotted against the summation of the area for all different building shapes (Figure 159 to Figure 162). As expected, the area averaging had a reduction impact as the surface area increased, following the approach proposed by Stathopoulos 1984. Once the results for all non-regular models were obtained, they were plotted against the ASCE 7-22 C&C (Components and Cladding) curves for comparison.

When analyzing the results of experiments conducted on irregularly shaped models for roof sections, specifically referring to Figure 159 and Figure 160, it became clear that the experimental suction values in zone 1 exceeded the design curve outlined in ASCE 7-22. As the effective wind area increased, these experimental values tended to worsen, diverging even more significantly from the GCp values presented in the ASCE 7-22 design curve (represented by a dashed black line). A similar trend was observed in zone 2, where

there was a less significant deviation from the ASCE 7-22 values (indicated by the red dotted line). Furthermore, suction values in zone 3 fell within the recommended range provided by ASCE 7-22, as denoted by the blue dashed line.

For positive GCp values on the roof, it was observed that some results differed somewhat from those outlined in ASCE 7-22. However, the values specified in the current wind provisions were generally deemed sufficient.

When examining the data pertaining to wall sections extracted from models featuring irregular shapes (as depicted in Figure 161 and Figure 162), a conspicuous elevation in values was observed for both negative and positive data points. To illustrate, the experimental values significantly exceeded the recommended design GCp values outlined by ASCE 7-22 (as denoted by the red dashed line) across the entire range of wind effective area values. Moreover, concerning the negative values observed within zone 4 of the models, it was evident that they displayed a tendency to surpass the provided design values as the wind effective area decreased, although this trend diminished as the wind effective area increased (represented by the black dotted line). Additionally, there was a notable increase in the positive GCp values obtained through experimentation, and they were consistently observed to surpass the design parameters stipulated by ASCE 7-22 for all wind effective area values (indicated by the black dashed line).

Graphs showing the independent zone area averaging results (separately) were generated and shown in Figure 163 and Figure 164. From the figures, it was clearly noted that roof zone 1 and 2 was exceeded (for negative GCp values) by the experimental data as the wind effective area is increased. Also, the wall sections, for zones 4 and 5 were clearly exceeded for both positive and negative GCp values, when compared to ASCE 7-22.

$$C_{p,area,avg}(t) = \frac{\sum(C_{p,i}(t) * A_i)}{\sum A_i}$$ *Equation 8*

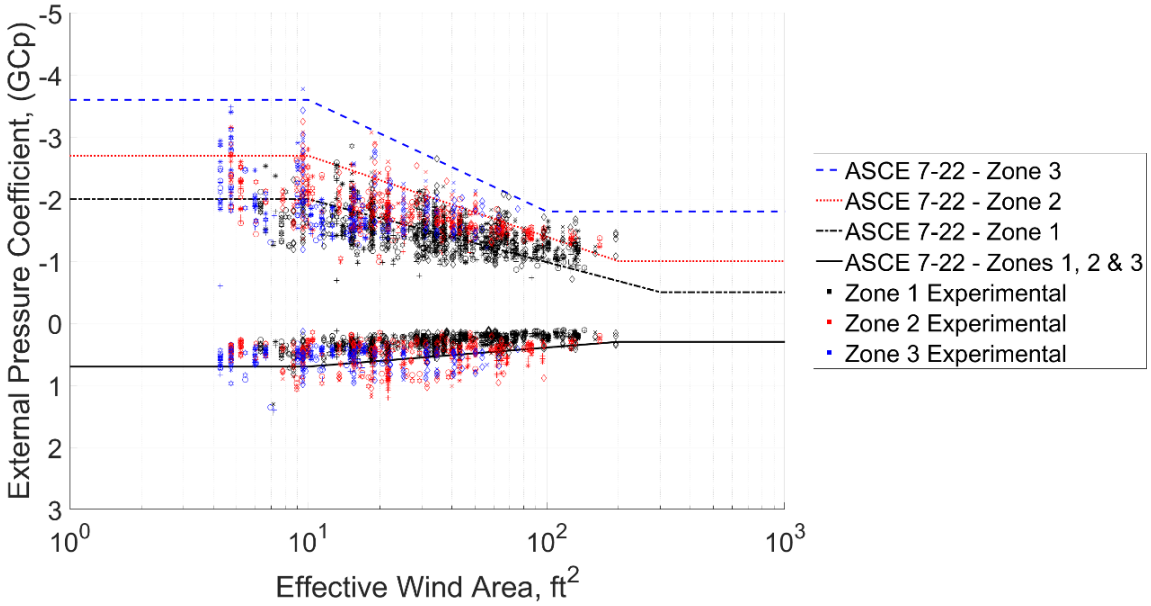

Figure 159. Experimental area-averaged graph – roof (large-scale results)

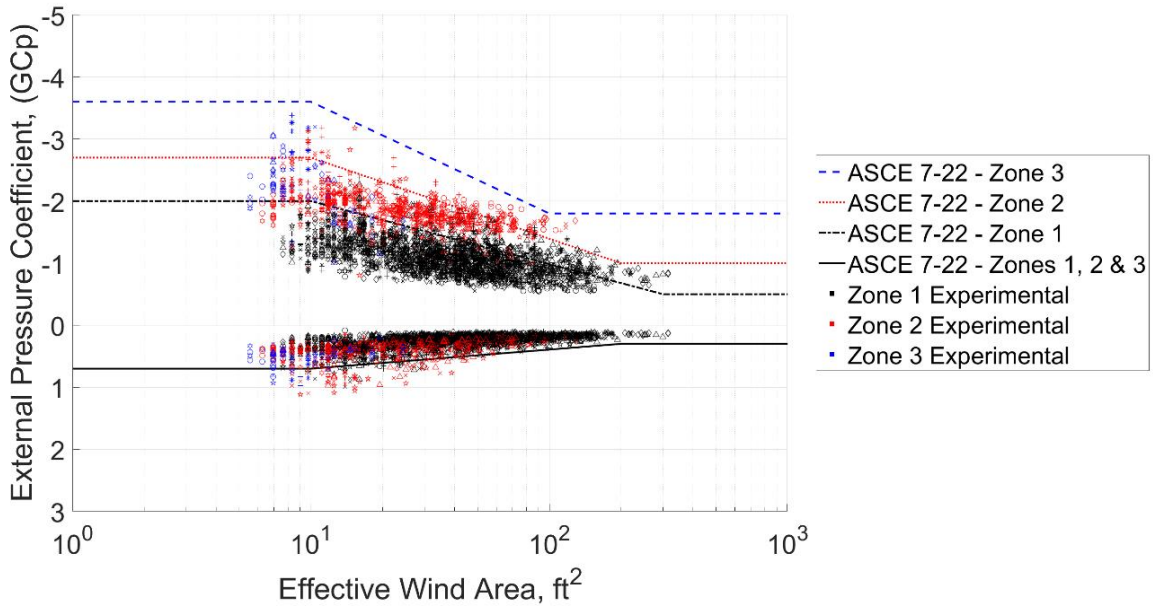

Figure 160. Experimental area-averaged graph – roof (small-scale results)

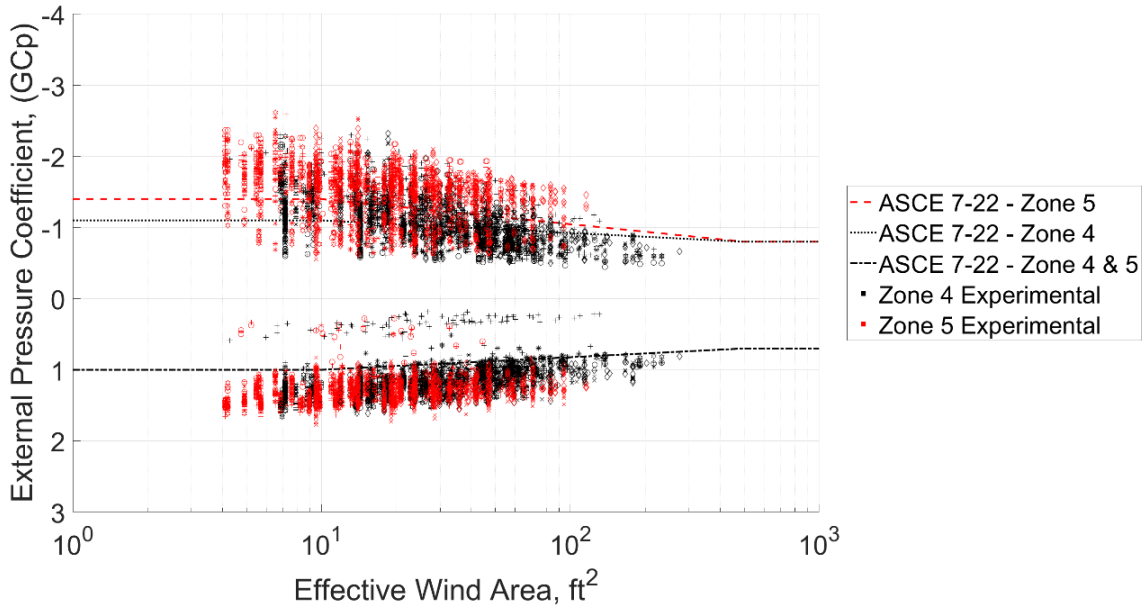

Figure 161. Experimental area-averaged graph – walls (large-scale results)

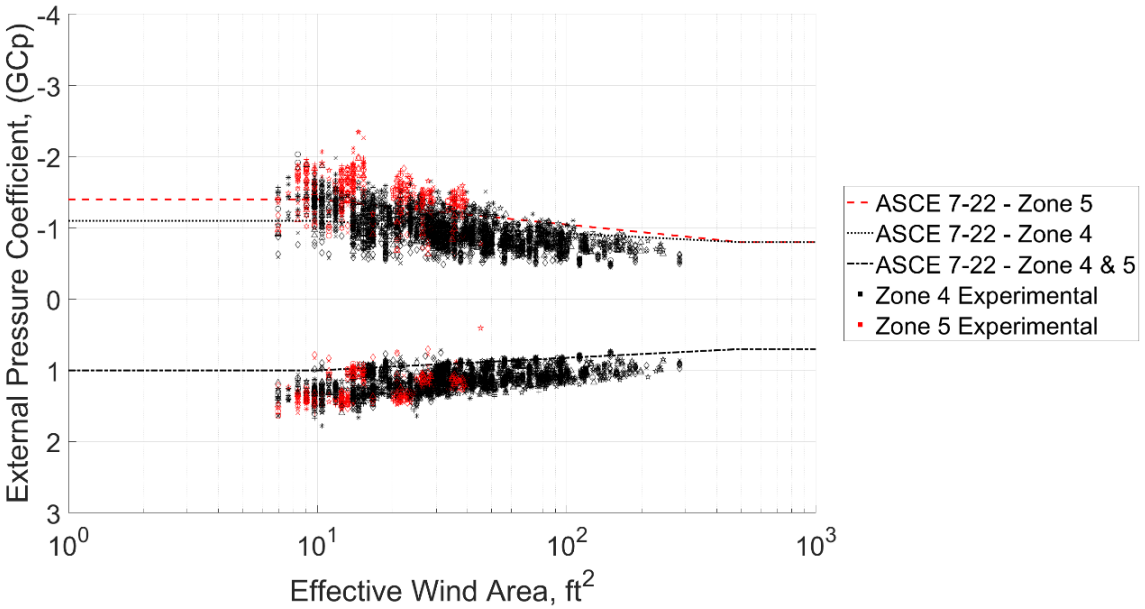

Figure 162. Experimental area-averaged graph – walls (small-scale results)

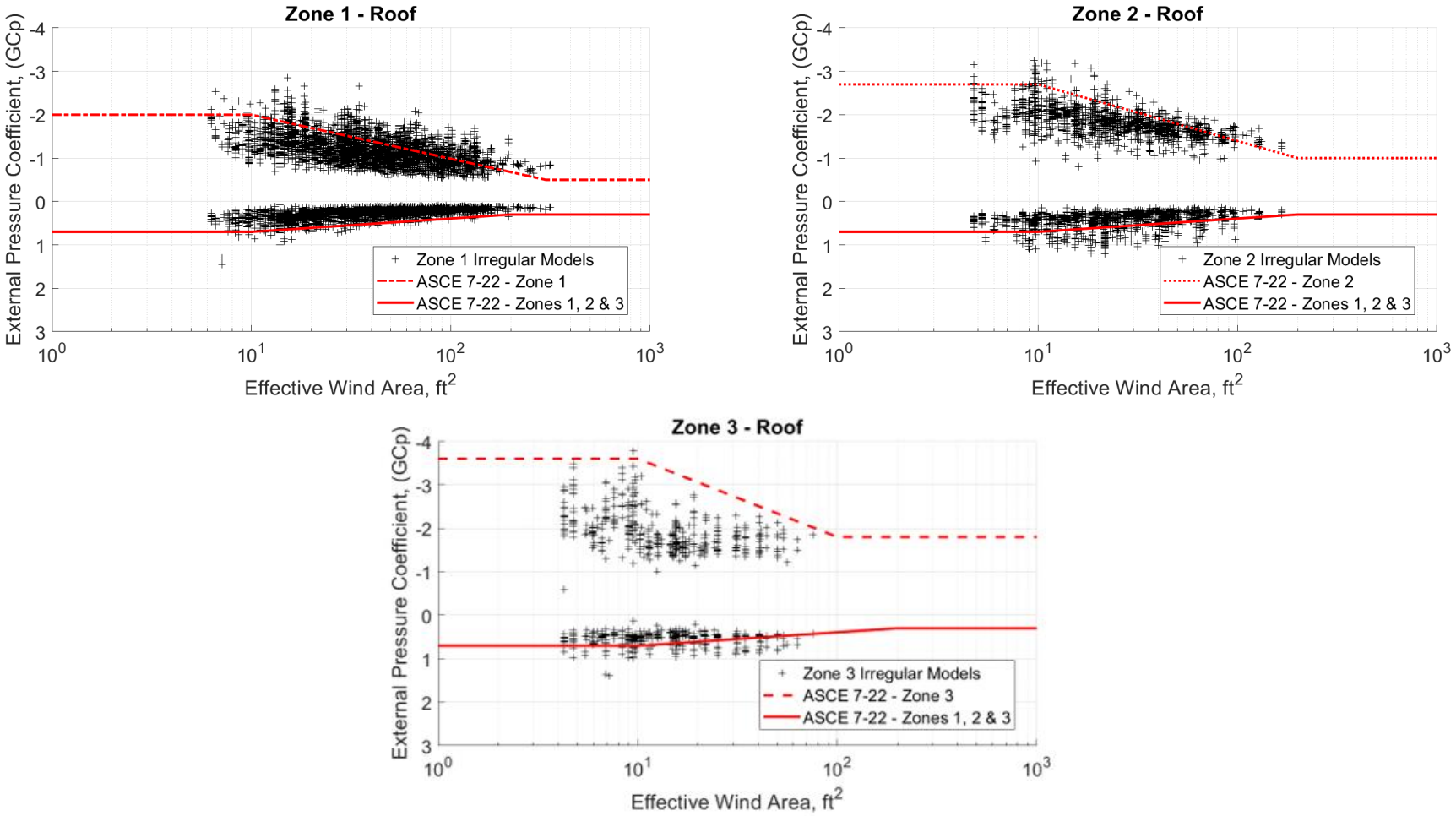

Figure 163. Experimental area-averaged graph by zone– roofs (irregular shaped models)

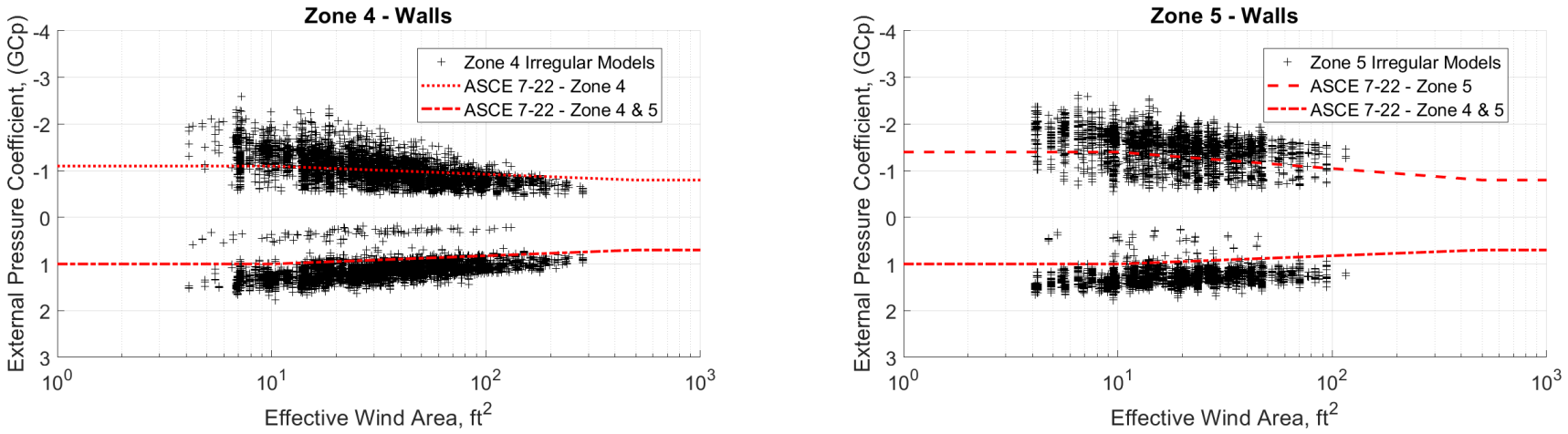

Figure 164. Experimental area-averaged graph by zone– walls (irregular shaped models)

7. CONCLUSIONS

Significant damage to low-rise residential buildings due to the impact of extreme wind events has been extensively documented and recognized as a pressing concern. In response to this, wind load regulations have been rigorously developed and implemented to guarantee the safe design and construction of these structures. However, it is crucial to acknowledge that modern architectural designs have progressively evolved, deviating significantly from the traditional rectangular forms that initially informed the foundation of current wind load regulations. As a consequence, the existing body of research has predominantly concentrated its efforts on irregularly shaped and non-rectangular structures, with a primary focus on mid- to high-rise buildings, thereby inadvertently leaving the unique vulnerabilities of low-rise structures somewhat overlooked and/or underexplored.

In this investigation, a comprehensive series of wind tunnel tests were planned and executed, featuring an array of both large- and small-scale models. This extensive collection included four meticulously crafted rectangular models alongside an impressive ensemble of eighteen irregularly shaped, non-rectangular models, each possessing distinct aspect ratios and shapes, such as T-, L-, C-, and S-shape. The experimental trials covered an exhaustive spectrum of wind directions, ranging from 0 to 345 degrees, meticulously sampled at 15-degree intervals, all within an open terrain configuration.

The construction of these models displayed a rigorous attention to detail, utilizing materials such as 3/8” plexiglass and employing advanced 3D printing techniques. The design process drew upon high-resolution aerial satellite imagery sourced from South Floridian residential areas to faithfully recreate the intricacies of real-world building shapes. Each of these models was carefully outfitted with over 300 precision-placed pressure sensors, meticulously distributed across their

wall and roof sections. This elaborate instrumentation ensured the collection of comprehensive and precise data throughout the experimental investigations.

The results of the study revealed notable differences in pressure distribution when compared to traditional rectangular buildings. The observed difference is primarily linked to the greater prevalence of corners and concave characteristics, whose varying intensity becomes evident as the wind direction changes. Mean and peak pressure coefficients (Cp) were computed for each pressure sensor across all wind directions. The critical Cp value (for each model) was identified for each pressure tap from all wind directions. These critical Cp values (obtained by an extreme value analysis) were then utilized to generate area-averaged graphs, which were subsequently compared to the existing ASCE 7-22 Components and Cladding (C&C) envelope curves.

The following conclusions can be drawn from the results:

- Low-rise buildings with irregularly shaped floor plans exhibit distinctive mean pressure distributions on roof and wall sections. These distributions differ significantly from those observed in rectangular buildings.
- When the wind direction is 0 degree, and a separated flow occurs from a windward wall located upwind of a protruded section in the crosswind direction, forming an L-shape (a 90-degree joint), the re-entrant flow reattaches to the downwind windward wall approximately 10 feet from the inner corner of the L-shape. This reattachment alters the location of the stagnation point and results in the development of complex and turbulent air recirculation at less than 10 feet. This, in turn, leads to non-standard pressure patterns near the 90-degree joint for both walls forming the L-shape.
- At a wind direction of 0 degree, when a windward wall and a side wall form an L-shape, the suction pressures on the side wall decrease significantly. These pressures exhibit a gradient,

transitioning from positive values near the 90-degree joint to negative values near the upwind edge.

- Buildings with irregular shapes tend to generate higher positive critical pressure coefficients on the roof sections, especially in areas where walls form a concave shape (a 90-degree joint).
- Irregularly shaped buildings generally experience a reduction in the development of negative critical pressure coefficients on the roof sections compared to rectangular buildings. However, the highest peak suction values develop mostly along the eave edges of the buildings. In addition, in some instances the separation bubble may extend further into the central areas of the roof.
- Suction pressure coefficients on the roof sections generally align well with the GCp values provided by ASCE 7-22, with the exception of zones 1 and 2. In contrast, positive pressure coefficients on the roof sections consistently exceed the GCp values provided by ASCE 7-22.
- Suction pressure coefficients on the wall sections tend to be higher than the values specified in ASCE 7-22, especially for zone 5. Furthermore, positive pressure coefficients on the wall sections of irregularly shaped buildings consistently exceed the values in ASCE 7-22 for both zones 4 and 5.

8. FUTURE WORK & DEVELOPMENTS

Continuing and intensifying the research endeavors is of paramount importance. Future research should direct the focus towards a more extensive set of non-standard, non-rectangular architectural structures, each characterized by its unique shapes, proportions, roof inclinations, number of floors and other pertinent variables. This strategic approach is essential in the quest to acquire pinpoint accurate results, enabling researchers to capture a much more inclusive spectrum

of building configurations that closely mirror the diverse realities of the real world. This research will not only refine the overall understanding but also contribute significantly to the practical applicability of the findings in the field of engineering, architecture and construction. In addition, a greater number of investigations on models with a significant number of intricate shapes could potentially lead to refined results that can encompass the great majority of shape variations found in the field.

Abdelfatah, N., Elawady, A., Irwin, P., Chowdhury, A. (2020). A study of aerodynamic pressures on elevated houses. Wind and Structures, Vol. 31, No. 4, p.p. 335-350. https://doi.org/10.12989/was.2020.31.4.335.

Ahmed, K.M., Mohammadi, F.G., Matus, M., Shenavarmasouleh, F., Pereira, L.M., Zisis, I., Amini, M.H. (2016). Towards Real-Time House Detection in Aerial Images Using Faster Region-Based Convolutional Neural Network. Available at SSRN: https://ssrn.com/abstract=3994191 or http://dx.doi.org/10.2139/ssrn.3994191.

Ahmed, K.M., Mohammadi, F.G., Matus, M., Shenavarmasouleh, F., Pereira, L.M., Zisis, I., Amini, M.H. (2023). Towards Real-time House Detection in Aerial Imagery Using Faster Region-based Convolutional Neural Network, IPSI Transactions on Internet Research, vol. 19(2), pp. 46-54, 2023. https://doi.org/10.58245/ipsi.tir.2302.06.

Akins, R.E., Peterka, J.A., Cermak, J.E. (1977). Mean force and moment coefficients for buildings in turbulent boundary layers. Journal of Wind Engineering and Industrial Aerodynamics, volume 2, issue 3, pages 1995-209. https://doi.org/10.1016/0167-6105(77)90022-8.

ASCE 7-02. (American Society of Civil Engineers). (2002). Minimum design loads for buildings and other structures.

ASCE 7-22 (American Society of Civil Engineers). (2022). Minimum design loads and associated criteria for buildings and other structures.

Azzi, Z., Habte, F., Elawady, A., Chowdhury, A.G., Moravej, M. (2020). Aerodynamic Mitigation of Wind Uplift on Low-Rise Building Roof Using Large-Scale Testing, Frontiers in Built Environment, Wind Engineering and Science, Vol. 5. https://doi.org/10.3389/fbuil.2019.00149.

Baals, D.D., Corlis, W.R. (1981). Wind tunnels of NASA. National Aeronautics and Space Administration (NASA) – SP-440. Scientific and technical information branch. Washington D.C.

Bachlin, W., Plate, E.J., Kamarga, A. (1983). Influence of the ratio of building height to boundary layer thickness and of the approach flow velocity profile on the roof pressure distribution of cubical buildings. Journal of Wind Engineering and Industrial Aerodynamics, volume 11, issues 1-3, pages 63-74. https://doi.org/10.1016/0167-6105(83)90090-9.

Barlow, J.B., Rae, W.H., Pope, A. (1999). Low-speed wind tunnel testing, 3rd Edition. Wiley-Interscience Publication, John Wiley & Sons,INC. Canada.

Bassas, E.C., Patterson, J., Phillip J. (2020). A review of the evolution of green residential architecture, Renewable and Sustainable Energy Reviews, Volume 125, 109796, ISSN 1364-0321, https://doi.org/10.1016/j.rser.2020.109796.

Bell, J.H., Mehta, R.D. (1988). Contraction design for small low-speed wind tunnels. National Aeronautics and Space Administration Contractor Report No. 177488 (Standford University).

Bradshaw, P., & Pankhurst, R. C. (1964). The design of low-speed wind tunnels. Progress in Aerospace Sciences, 5, 1–69. https://doi.org/10.1016/0376-0421(64)90003-X.

Carlson, J.J., Johnston, J.P., Sagi, C.J. (1967). Effects of wall shape on flow regimes and performance in straight, two-dimensional diffusers. Journal of Fluids Engineering. Volume 89, Issue 1, pp. 151-159. https://doi.org/10.1115/1.3609545.

Cattafesta, L., Bahr, C., Mathew, J. (2010). Fundamentals of wind-tunnel design. Encyclopedia of Aerospace Engineering, Fluid Dynamics and Aerothermodunamics. https://doi.org/10.1002/9780470686652.eae532.

Cermak, J.E. (2003). Wind-tunnel development and trends in applications to civil engineering. Journal of Wind Engineering and Industrial Aerodynamics. Volume 91, pg. 355-370. https://doi.org/10.1016/S0167-6105(02)00396-3.

Cermak, J.E., Davenport, A.G., Durgin, F.H., Irwin, PA., Isyumov, N., Peterka, J.A., Ramsay, S.R., Reinhol, T.A., Scanlan, R.H., Stathopoulos, T., Steckley, A.C., Tieleman, H., Vickery, P.J. (1999). Wind tunnel studies of buildings and structures. ASCE Manuals and Reports on Engineering Practice No. 67.

Chowdhury, A.G., Zisis, I., Irwin, P.A., Bitsuamlak, G., Pinelli, J.-P., Hajra, B., Moravej, M. (2017). Large-scale experimentation using the 12-fan wall of wind to assess and mitigate hurricane wind and rain impacts on buildings and infrastructure systems. Journal of Structural Engineering, volume 143, issue 7. https://doi.org/10.1061/(ASCE)ST.1943-541X.0001785.

Daemei, A.B., Khotbehsara, E.M., Nobarani, E.M., Bahrami, P. (2019). Study on wind aerodynamic and flow characteristics of triangular-shaped tall buildings and CFD simulation in order to assess drag coefficient. Ain Shams Engineering Journal, Vol. 10, p.p. 541-548, https://doi.org/10.1016/j.asej.2018.08.008.

Davenport, A.G., Surry, D., and Stathopoulos, T. (1977). Wind loading on low-rise buildings: final report on phases I and II. University of Western Ontario, Eng. Sci. Res. Rep., BLWT-SS8-1977.

Davenport, A.G., Surry, D., and Stathopoulos, T. (1978). Wind loads on low-rise buildings.” In Final report on phase III. London: University of Western Ontario.

Duthinh, D., Main, J.A., Gierson, M.L., Phillips, B.M. (2017). Analysis of wind pressure data on components and cladding of low-rise buildings. ASCE-ASME Journal of Risk and Uncertainty in Engineering Systems, Part A: Civil Engineering, Volume 4, Issue 1. https://doi.org/10.1061/AJRUA6.0000936.

Duthinh, D., Main, J.A., Phillips, M.B. (2015). Methodology to analyze wind pressure data on components and cladding of low-rise buildings. National Institute of Standards and Technology. http://dx.doi.org/10.6028/NIST.TN.1903

FEMA. FEMA National Risk Index. https://hazards.fema.gov/nri/map.

Friedman, A. (1995). The Evolution of Design Characteristics during the Post-Second World War Housing Boom: The US Experience. Journal of Design History, 8(2), 131–146. http://www.jstor.org/stable/1315979.

Fu, T.C., Aly, A.M., Chowdhury, A.G., Bitsuamlak, G., Yeo, D.H., Simiu, E. (2012). A proposed technique for determining aerodynamic pressure son residential homes. Wind and Structures, Vol. 15. No. 1. (2012) 27-41. ISSN: 1226-6116.

Gavanski, E.B., Kordi, B., Kopp, G.A., Vickery, P.J. (2013). Wind loads on roof sheathing of houses. Journal of Wind Engineering and Industrial Aerodynamics, Vol. 114, p.p. 106-121. https://doi.org/10.1016/j.jweia.2012.12.011.

Ghazal, T., Aboutabikh, M., Aboshosha, H. (2019). "Flow-conditioning of the wind tunnel at Ruerson university to model boundary layer flows." Canadian Society for Civil Engineering Annual Conference, Laval (Montereal), June 12-15, 2019.

Ghazal, T., Chen, J., Aboutabikh, M., Aboshosha, H., Elgamal, S. (2020). "Flow-conditioning of a subsonic wind tunnel to model boundary layer flows." Wind and Structures, vol. 30, No. 4, pp. 339-366. http://doi.org/10.12989/was.2020.30.4.339.

Gierson, M.L., Phillips, B.M., Duthinh, D. (2015). Evaluation of ASCE 7-10 wind velocity pressure coefficients on the components and cladding of low-rise buildings using recent wind tunnel testing data. 6th Int. Conference on Advances in Experimental Structural Engineering.

Gomez, M.G., Rodriguez, A.M., Mendez, P. (2005). Experimental and numerical study of wind pressures on irregular-plan shapes. Journal of Wind Engineering and Industrial Aerodynamics, volume 93, issue 10, pages 741-756. https://doi.org/10.1016/j.jweia.2005.08.008.

Hegade, K.P.N., Natalia, R., Wehba, B., Mittal, A., Bhat, R.B., Packirisamy, M. (2020). Design and study of mini wind tunnel for microsystems fluid interaction under low reynolds number flows. Springer Nature Applied Sciences Journal. https://doi.org/10.1007/s42452-020-2602-x.

Ho, T.C.E., Surry, D., Morrish, D. (2003). NIST/TTU cooperative agreement – windstorm mitigation initiative: Wind tunnel experiments on geleric low buildings. The University of Western Ontario, Faculty of Engineering, May 2003 – Report 1.

Ho, T.C.E., Surry, D., Morrish, D., Kopp, G.A. (2005). The UWO contribution to the NIST aerodynamic database for wind loads on low buildings: Part 1. Archiving format and basic aerodynamic data. Journal of Wind Engineering and Industrial Aerodynamics. Volume 93, Issue 1, pages 1-30. https://doi.org/10.1016/j.jweia.2004.07.006.

Ho, T.C.E., Surry, D., Nywening, M. (2003). NIST/TTU cooperative agreement – windstorm mitigation initiative: Further experiments on generic low buildings. The University of Western Ontario, Faculty of Engineering, September 2003 – Report 2.

Holmes, J.D., Carpenter, P. (1990). The effect of Jensen number variations on the wind loads on a low-rise building. Journal of Wind Engineering and Industrial Aerodynamics, volume 36, part 2, pages 1279-1288. https://doi.org/10.1016/0167-6105(90)90124-U.

Iglesias, V., Braswell, A. E., Rossi, M. W., Joseph, M. B., McShane, C., Cattau, M., Travis, W. R. (2021). Risky development: Increasing exposure to natural hazards in the United States. Earth's future, 9(7), e2020EF001795. https://doi.org/10.1029/2020ef001795.

Irwin, P., Cooper, K.R., and Girard, R. (1979). Correction of distortion effects caused by tubing systems in measurements of fluctuating pressures. Journal of Wind Engineering and Industrial Aerodynamics, Volume 5, Issues 1–2, October 1979, Pages 93-107. https://doi.org/10.1016/0167-6105(79)90026-6.

Irwin, P.A. (2009). Wind engineering challenges the new generation of super-tall buildings. Journal of Wind Engineering and Industrial Aerodynamics, Vol. 97, p.p.328-334, https://doi.org/10.1016/j.jweia.2009.05.001.

Jacobs, J. A. (2006). Social and Spatial Change in the Postwar Family Room. Perspectives in Vernacular Architecture, 13(1), 70–85. http://www.jstor.org/stable/20355369.

Jimenez-P. M., Chiapponi, L., Clavero, M., Losada, M.A. (2020). Air flow quality analysis of an open-circuit boundary layer wind tunnel and comparison with a closed-circuit wind tunnel. Physics of Fluids. https://doi.org/10.1063/5.0031613.

Johnston, J.P., Powars, C.A. (1969). Some effects of inlet blockage and aspect ratio on diffuser performance. Journal of Fluids Engineering, volume 91, Issue 3, pp. 551-553. Some Effects of Inlet Blockage and Aspect Ratio on Diffuser Performance. https://doi.org/10.1063/5.0031613.

Kim, Y.C., Bandi, E.K., Yoshida, A., Tamura, Y. (2015). Response characteristics of super-tall buildigs – effects of number of sides and helical angle. Journal of Wind Engineering and Industrial Aerodynamics, Vol. 145, p.p. 252-262. http://dx.doi.org/10.1016/j.jweia.2015.07.001.

Kim, Y.C., Tamura, Y. Tanaka, H., Ohtake, K., Bandi, E.K., Yoshida, A. (2014). Wind-induced responses of super-tall buildings with various atypical building shapes. Journal of Wind Engineering and Industrial Aerodynamics, Vol. 133, p.p. 191-199. http://dx.doi.org/10.1016/j.jweia.2014.06.004.

Konior, T. (2022). Shaping place in architecture – Diversity and harmony. ORCID: 0000-0002-2195-2620. http://dx.doi.org/10.23817/2022.defarch.3-9.

Kopp, G.A., Morrison, M.J. (2014). Component and cladding pressures and zones for the roofs of low-rise buildings. In Boundary layer wind tunnel report. London: University of Western Ontario.

Kourakis, I. (2005). Structural systems and tuned mass dampers of super-tall buildings: case study of Taipei 101. Aristotle University of Thessaloniki, thesis.

Kulkarni, V., Sahoo, N., Chavan, S.D. (2011). Simulation of honeycomb-screen combinations for turbulence management in a subsonic wind tunnel. Journal of Wind Engineering and Industrial Aerodynamics. Volume 99, pp. 37-45. https://doi.org/10.1016/j.jweia.2010.10.006.

Lee, Y.T., Boo, S.L., Lim, H.C., Misutani, K. (2016). Pressure distribution on rectangular buildings with changes in aspect ratio and wind direction. Wind and Structures, volume 23, number 5, pages 465-483. https://doi.org/10.12989/was.2016.23.5.465.

Lehman, M.L. (2011). How sensory design brings value to buildings and their occupants. Intelligent Buildings International, 3:1, 46-54, http://dx.doi.org/10.3763/inbi.2010.0011.

Li, S.H., Kilpatrick, J., Browne, M.T.L., Yakymyk, W., Refan, M. (2020). Uncertainties in prediction of local peak wind pressures on mid- and high-rise buildings by considering gumbel distributed pressure coefficients. Journal of Wind Engineering and Industrial Aerodynamics, vol. 206. https://doi.org/10.1016/j.jweia.2020.104364.

Lieblein, J. (1974) Efficient Methods of Extreme Value Methodology. NBSIR 74-602, National Bureau of Standards, Washington, DC 20234.

Marshall, R.D. (1985), Performance requirements and preliminary design of a boundary layer wind tunnel facility. National Institute of Standards and Technology, Gaithersburg, MD. https://doi.org/10.6028/NBS.IR.85-3168.

Mashalkar, B.S., Patil, G.R., Jadhav, A.S. (2015). Effect of plan shapes on the response of buildings subjected to wind vibrations. IOSR Journal of Mechanical and Civil Engineering (IOSR-JMCE). e-ISSN: 2278-1684, p-ISSN: 2320-334X.

Matus, M.A., Mostafa, K., Dev Sarma, H., Schwartz, B., Zisis, I. (2021). Design and development of a new boundary layer wind tunnel at Florida International University. 6th American Association for Wind Engineering Workshop.

Mauro, S., Brusca, S., Lanzafame, R., Famoso, F., Galvagno, A., Messina, M. (2017). Small-scale open-circuit wind tunnel: design criteria, construction and calibration. International Journal of Applied Engineering Research. Volume 12, N. 12, pp. 13649-12662.

Mehta, R.D. (1979). The aerodynamic design of blower tunnels with wide-angle diffusers. Progress in Aerospace Sciences. Volume 18, pp. 59-120. https://doi.org/10.1016/0376-0421(77)90003-3.

Mooneghi, M.A., Irwin, P., Chowdhury, A.G. (2014) Large-scale testing on wind uplift of roof pavers. Journal of Wind Engineering and Industrial Aerodynamics. Volume 128, pages 22-36. https://doi.org/10.1016/j.jweia.2014.03.001.

Mooneghi, M.A., Irwin, P., Chowdhury, A.G. (2016). Partial turbulence simulation method for predicting peak wind loads on small structures and building appurtenances. Journal of Wind

Engineering and Industrial Aerodynamics. Volume 157, pages 47-62. https://doi.org/10.1016/j.jweia.2016.08.003.

Moravej, M. (2018). Investigating scale effects on analytical methods of predicting peak wind loads on buildings. Florida International University Electronic Theses and Dissertations. https://dx.doi.org/10.25148/etd.FIDC006834.

Nagar, S.K., Raj, R., Dev, N. (2020). Experimental study of wind-induced pressures on tall buildings of different shapes. Wind and Structures, Vol. 31, No. 5, p.p. 441-453. https://doi.org/10.12989/was.2020.31.5.441.

NIST (National Institute for Standards and Technology). (2004). Extreme winds and wind effects structures. https://itl.nist.gov/div898/winds/homepage.htm.

NOAA (2021). National Centers for Environmental Information (NCEI) U.S. Billion-Dollar Weather and Climate Disasters (2021). https://www.ncdc.noaa.gov/billions/. https://doi.org/10.25921/stkw-7w73.

NOAA (2023). National Centers for Environmental Information (NCEI) U.S. Billion-Dollar Weather and Climate Disasters (2023). https://www.ncei.noaa.gov/access/billions/.

NOAA. (2013). National Coastal Population Report - Population Trends from 1970 to 2020. https://aambpublicoceanservice.blob.core.windows.net/oceanserviceprod/facts/coastal-population-report.pdf

Parackal, K.I., Humpthreys, M.T., Ginger, J.D., Henderson, D.J. Wind loads on contemporary Australian housing. Australian Journal of Structural Engineering, Volume 17, N. 2, 136-150. https://doi.org/10.1080/13287982.2016.1229375.

Paterson, D.A., Holmes, J.D. (1992). Computation of wind pressures on low-rise structures. Journal of wind engineering and industrial aerodynamics, 41-44, 1629-1640.

Potter, Brian. (2020). Every Building in America - an Analysis of the US Building Stock. Construction Physics, a newsletter about the forces shaping the construction industry. https://www.construction-physics.com/p/every-building-in-america-an-analysis?utm_campaign=post&utm_medium=web.

Rajabi, E., Sadaghi, H., Hashemi, M.R. (2022). Wind effect on buildings with y-shaped plan. Asian Journal of Civil Engineering 23. 141-151. https://doi.org/10.1007/s42107-022-00417-z.

Rajdip, P., Sujit, K.D. (2016). Wind effects on 'Z' plan-shaped tall building: a case study. International Journal Advanced Structural Engineering 8, 319–335. https://doi.org/10.1007/s40091-016-0134-9.

Reid, E.G. (1953). Performance characteristics of plane-wall two-dimensional diffusers. National Advisory Committee for Aeronautics, Technical Note 2888, Standford University, Washington.

Reyna, J., Wilson, E., Parker, A., Satre-Meloy, A., Egerter, A., Biachi, C., Praprost, M., Speake, A., Liu, L., Horsey, R., Dahlhauen, M., CaraDonna, C., Rothgeb, S. (2022). U.S. Building Stock Characterization Study: A National Typology for Decarbonizing U.S. Buildings. Golden, CO: National Renewable Energy Laboratory. NREL/TP-5500-83063. https://www.nrel.gov/docs/fy22osti/83063.pdf.

Russell, B., Torralba, A., Murphy, K., Freeman, W.T. (2007). LabelMe: a database and web-based tool for image annotation International Journal of Computer Vision.

Sarma, H.D., Zisis, I., Matus, M. 2023. Effect of roof shape on wind vulnerability of roof sheathing panels. Structural Safety, Volume 100, 102283. https://doi.org/10.1016/j.strusafe.2022.102283.

Shao, S., Stathopoulos, T., Yang, Q., Tian, Y. (2018). Wind pressures on 4:12-sloped hip roofs of L- and T-shaped low-rise buildings. American Society of Civil Engineers, Journal of Structural Engineering, Vol. 144, No. 7. https://doi.org/10.1061/(ASCE)ST.1943-541X.0002077.

Shao, S., Tian, T., Yang, Q.S., Stathopoulos, T. (2019). Wind-induced cladding and structural loads on low-rise buildings with 4:12-slopped hip roofs. Journal of Wind Engineering and Industrial Aerodynamics, volume 193, 103948. https://doi.org/10.1016/j.jweia.2019.103948.

Sharma, A., Mittal, H., Gairola, A. (2018). Mitigation of wind load on tall buildings through aerodynamic modifications: review. Journal of Building Engineering. https://doi.org/10.1016/j.jobe.2018.03.005.

Sharma, D., Pal, S., Raj, R. (2023). Numerical prediction of the proximity effects on wind loads of low-rise buildings with cylindrical roofs. Wind and Structures, Vol. 36, No. 4, 277-292. https://doi.org/10.12989/was.2023.36.4.277.

Shelly, E., Hubbard, E., Zhang, W. (2023). Comparison and uncertainty quantification of roof pressure measurements using the NIST and TPU aerodynamic databases. Journal of Wind Engineering and Industrial Aerodynamics, 232, 105246. https://doi.org/10.1016/j.jweia.2022.105246.

Simiu, E., Yeo, D.H. (2019). Wind Effects on Structure – 4th edition. Wiley Blackwell. ISBN 978-1-119-37588-3. www.wiley.com/go/construction.

Smith, Adam B. (2020). U.S. Billion-dollar Weather and Climate Disasters, 1980 - present (NCEI Accession 0209268). [indicate subset used]. NOAA National Centers for Environmental Information. Dataset. https://doi.org/10.25921/stkw-7w73.

Souvik, C., Sujut, K.D., Ashok, K.A. (2014). Wind load on irregular plan shaped tall building – a case study. Wind and Structures, volume 19, number 1, pages 59-73. https://doi.org/10.12989/was.2014.19.1.059.

St. Pierre, L.M., Kopp, G.A., Surry, D., Ho, T.C.E. (2005). The UWO contribution to the NIST aerodynamic database for wind loads on low buildings: part 2. Comparison of data with wind load provisions. Journal of Wind Engineering and Industrial Aerodynamics, volume 93, issue 1, pages 31-59. https://doi.org/10.1016/j.jweia.2004.07.007.

Stathopoulos, T. (1979). Turbulent wind action on low-rise buildings. Ph.D. Thesis. The University of Western Ontario, London, Canada.

Stathopoulos, T. (1984). Wind loads on low-rise buildings: a review of the state of the art. Engineering Structures, volume 6, issue 2, pages 119-135. https://doi.org/10.1016/0141-0296(84)90005-1.

Stathopoulos, T., Surry, D. (1983). Scale effects in wind tunnel testing of low buildings. Journal of Wind Engineering and Industrial Aerodynamics, volume 13, issues 1-3, pages 313-326. https://doi.org/10.1016/0167-6105(83)90152-6.

Stathopoulos, T., Zhou, Y.S. (1993). Computation of wind pressures on L-shaped buildings. Journal of Engineering Mechanics, volume 119, issue 8. https://doi.org/10.1061/(ASCE)0733-9399(1993)119:8(1526).

Tamura, Y. (2012). Aerodynamic database for low-rise buildings. http://www.wind.arch.t-kougei.ac.jp/info_center/windpressure/lowrise/mainpage.html.

Tamura, Y., Kareem, A., Solari, G., Kwok, K., Holmes, J.D., and Melbourne, W.H. (2005). Aspects of the dynamic wind-induced response of structures and codification. Wind Structures. 8 (4): 251–268. https://doi.org/10.12989/was.2005.8.4.251.

Tamura, Y., Xu, Z. Tanaka, H., Kim, Y.C., Yoshida, A., Yang, Q. (2017). Aerodynamic and pedestrian-level wind characteristics of super-tall buildings with various configurations. 10th International Conference on Structural Dynamics, EURODYN 2017. https://doi.org/10.1016/j.proeng.2017.09.146.

Tieleman, H.W. (1992). Problems associated with flow modelling procedures for low-rise structures. Journal of Wind Engineering and Industrial Aerodynamics. Volume 42, Issues 1-3, pages 923-934. https://doi.org/10.1016/0167-6105(92)90099-V.

Uematsu, Y., Isyumov, N. (1999). Wind pressure acting on low-rise buildings. Journal of Wind Engineering and Industrial Aerodynamics, volume 82, issues 1-3, pages 1-25. https://doi.org/10.1016/S0167-6105(99)00036-7.

Uematsu, Y., Tambe, T., Yamamoto, A. (2022). Wind loading of photovoltaic panels installed on hip roofs of rectangular and l-shaped low-rise buildings. Wind loads on buildings and structures, Wind 2022, 2(2), 288-304. https://doi.org/10.3390/wind2020016.

Van Dommelen, Rinka. (2013). Design of an atmospheric boundary layer wind tunnel. Thesis. Technische Universiteit Eindhoven, Eindhoven, Netherlands, 2013.

Verma, A., Meena, R.K., Raj, R., Ahuja, A. (2022). Experimental investigation of wind induced pressure on various types of low-rise structure. Asian Journal of Civil Engineering 23, 1251–1265. https://doi.org/10.1007/s42107-022-00480-6.

Vickery, P.J., Kopp, G.A., Twisdale Jr., L.A., (2011). Component and cladding wind pressures on hip and gable roofs: Comparisons to the U.S. wind loading provisions. In Proc., 13th Int. Conf. on Wind Engineering. Amsterdam, Netherlands.

Vita, Giulio., Hemida, H., Andrianne, T., Baniotopoulos, C.C. (2018). "Generating atmospheric turbulence using passive grids in an expansion test section of a wind tunnel." Journal of Wind Engineering and Industrial Aerodynamics, vol 178, pp. 91-104. https://doi.org/10.1016/j.jweia.2018.02.007.

Vogel, W.M. (1968). General description and calibration of the McGill 30-inch diameter blower cascade wind tunnel. Technical Note 68-1. Mechanical Engineering Research Laboratories, McGill University.

Wang.L., Zhang, W. (2023). The influence of chamfered and rounded corners on vortex-induced vibration of super-tall buildings. Applied Sciences, 13, 1049. https://doi.org/10.3390/app13021049.

Wilson, Steven G., Fischetti, Thomas R. (2010). Coastline Population Trends in the UNITED States: 1960 to 2008.

Xie, J. (2012). Aerodynamic optimization on super-tall building designs. The seventh international colloquium on bluff body aerodynamics and its applications (BBAA7). Shanghai, China, September 2-6.

Xie, J. (2014). Aerodynamic optimization of super-tall buildings and its effectiveness assessment. Journal of Wind Engineering and Industrial Aerodynamics, Vol. 130, p.p. 88-98. https://doi.org/10.1016/j.jweia.2014.04.004.

Xu, X., Yang, Q., Yoshida, A., Tamura, Y. (2017). Characteristics of pedestrian-level wind around super-tall buildings with various configurations. Journal of Wind Engineering and Industrial Aerodynamics, Vol. 166, p.p. 61-73. http://dx.doi.org/10.1016/j.jweia.2017.03.013.

Yan, B., Li, Q.S. (2016). Wind tunnel study of interference effects between twin super-tall buildings with aerodynamic modifications. Journal of Wind Engineering and Industrial Aerodynamics, Vol. 156, p.p. 129-145. http://dx.doi.org/10.1016/j.jweia.2016.08.001.

Yi, J., Li, Q.S. (2015). Wind tunnel and full-scale study of wind effects on a super-tall building. Journal of Fluids and Structures, Vol. 58, p.p. 236-253. http://dx.doi.org/10.1016/j.jfluidstructs.2015.08.005.

Yi, L., Duan, R.B., Li, Q.S., Li, T.G., Li, C. (2020). Research on the characteristics of wind pressures on L-shaped tall buildings. Advances in Structural Engineering. https://doi.org/10.1177/1369433220906934.

Yi, L., Li, Q.S. (2016). Wind-induced response based optimal design of irregular shaped tall building. Journal of Wind Engineering and Industrial Aerodynamics, volume 155, pages 197-207. https://doi.org/10.1016/j.jweia.2016.06.001.

Yi, L., Li, Q.S., Chen, F. (2017). Wind tunnel study of wind-induced torque on L-shaped tall buildings. Journal of Wind Engineering and Industrial Aerodynamics, volume 167, pages 41-50. https://doi.org/10.1016/j.jweia.2017.04.013.

Zhang, Z., Elsharawy, M., Stathopoulos, T. (2014). Aerodynamic torsional loads on L-shaped low-rise buildings. Advances in Civil, Environmental and Materials Research. The 2014 world congress. Busan, Korea, August 24-28.

Zhang., X., Weerasuriya, A.U., Zhang, X., Tse, K.Y., Lu, B., Li, C.Y. (2020). Pedestrian wind comfort near a super-tall building with various configurations in an urban-like setting. Building Simulation, 13, 1385-1408. https://doi.org/10.1007/s12273-020-0658-6.

Zhao, D.X., He, B.J. (2017). Effects of architectural shapes on surface wind pressure distribution: Case studies of oval-shaped tall buildings. Journal of Building Engineering, volume 12, pages 219-228. https://doi.org/10.1016/j.jobe.2017.06.009.

Zulian, M., (2022). Most Americans live in natural hazard hot spots, Temblor, http://doi.org/10.32858/temblor.229.

APPENDIX

Contour Plots of mean Cp values for large-scale models in 2019, specifically for cornering wind directions (from 45 to 345 degrees):

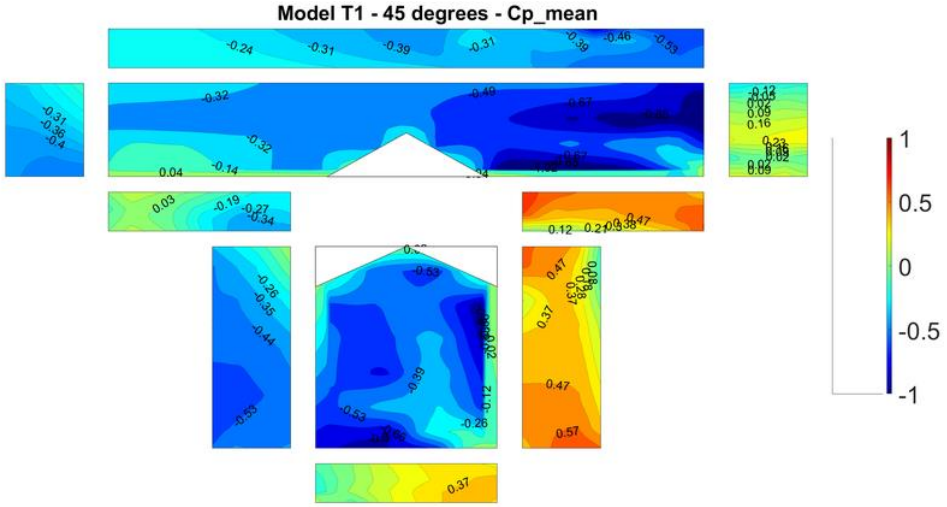

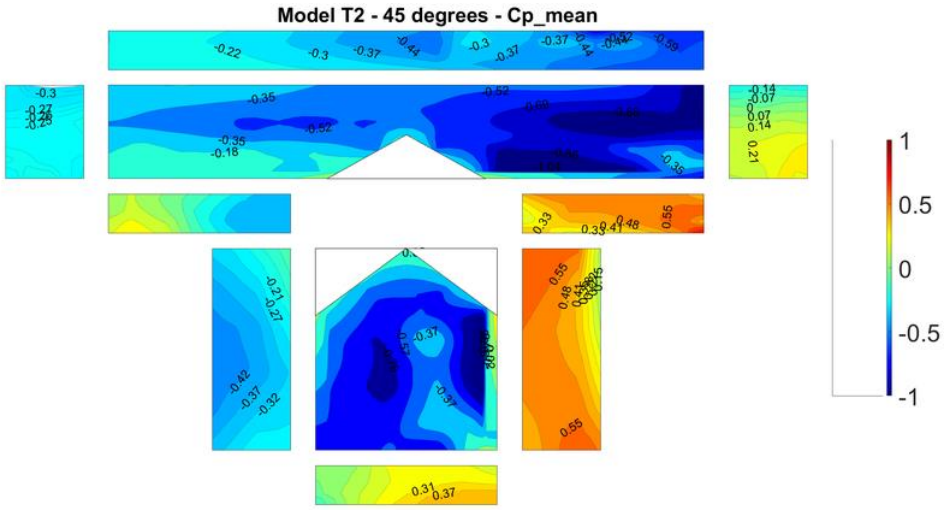

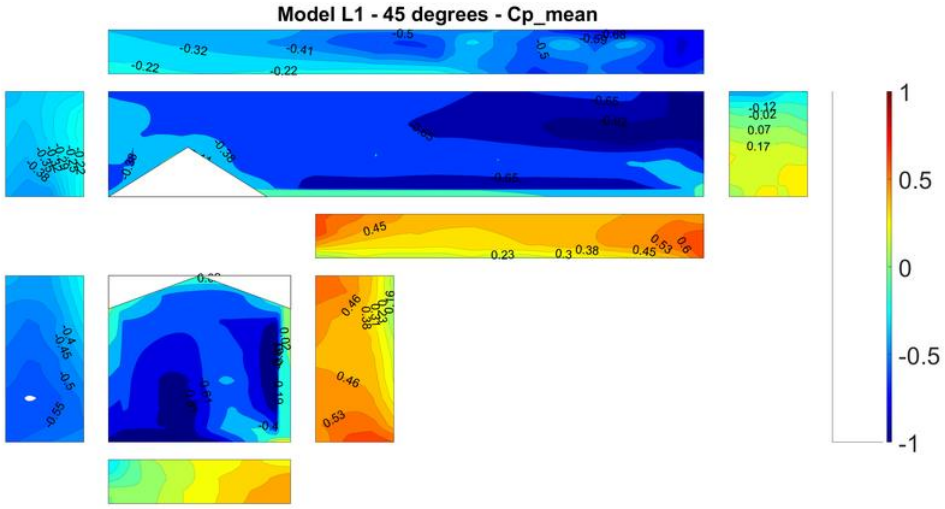
Model L1 - 45 degrees - Cp_mean
1
0.5
0
-0.5
-1

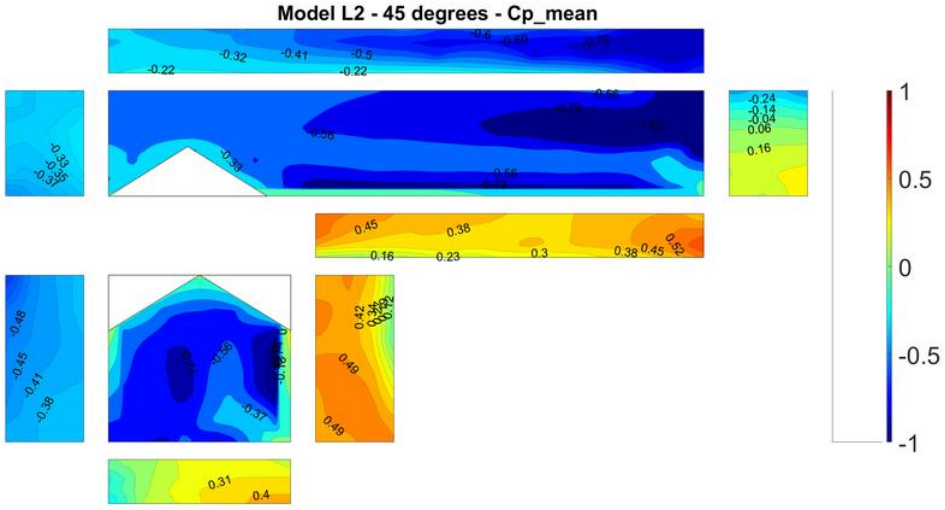
Model L2 - 45 degrees - Cp_mean
1
0.5
0
-0.5
-1

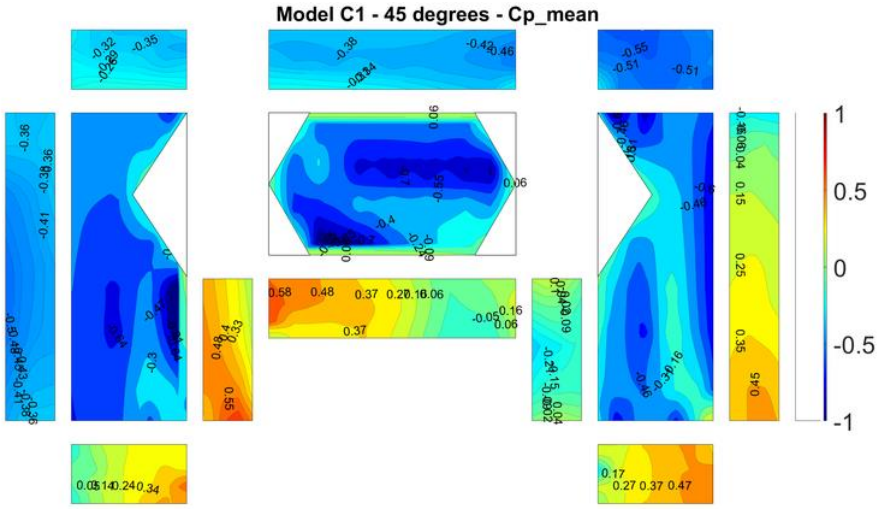
Model C1 - 45 degrees - Cp_mean
1
0.5
0
-0.5
-1

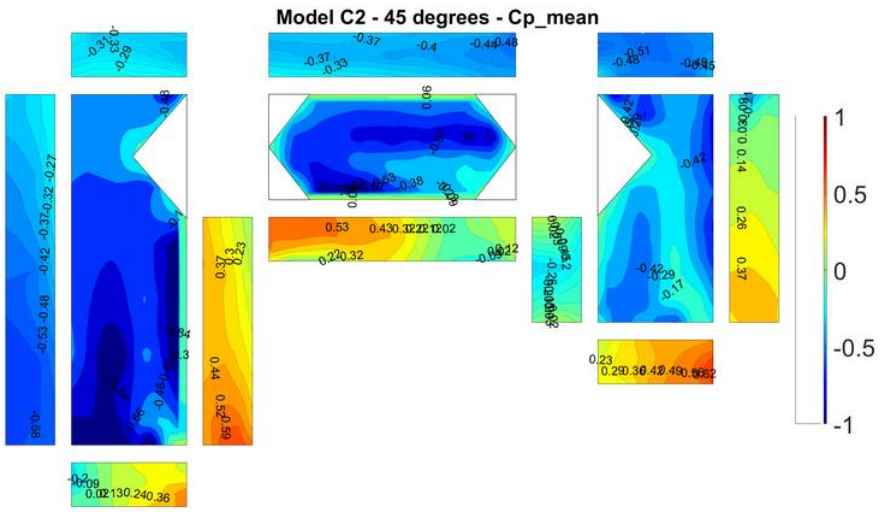
Model C2 - 45 degrees - Cp_mean
1
0.5
0
-0.5
-1

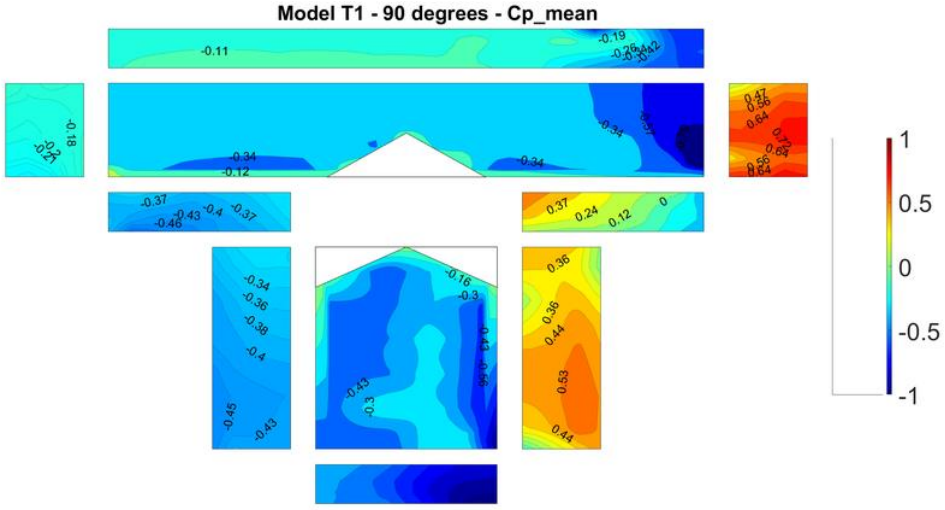
Model T1 - 90 degrees - Cp_mean
1
0.5
0
-0.5
-1

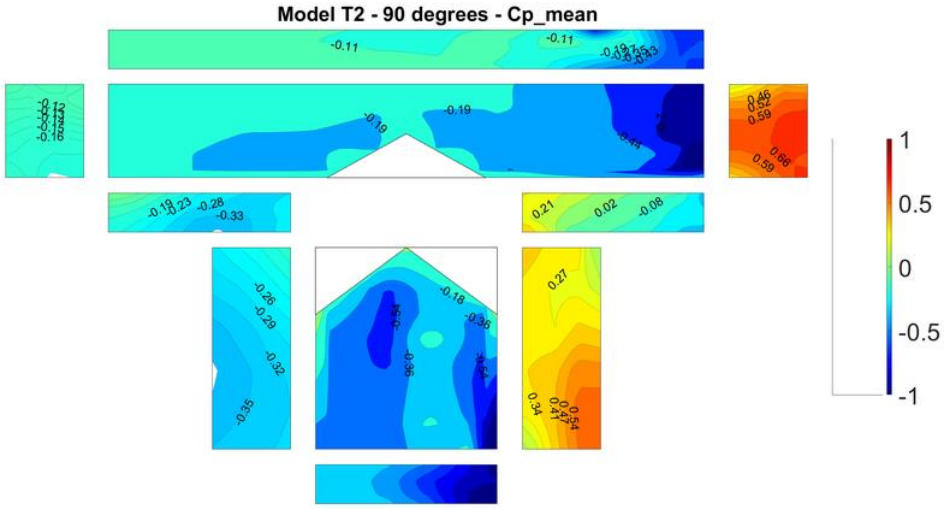
Model T2 - 90 degrees - Cp_mean
1
0.5
0
-0.5
-1

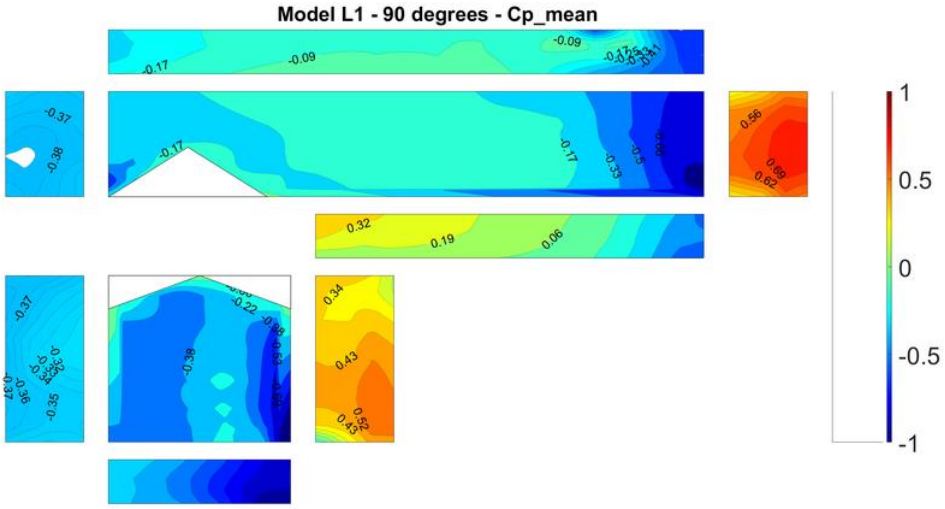
Model L1 - 90 degrees - Cp_mean
1
0.5
0
-0.5
-1

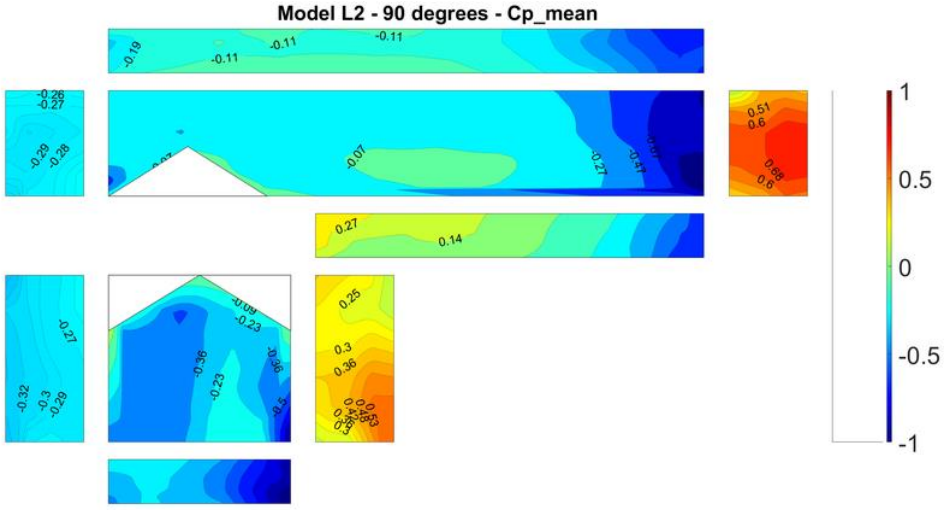
Model L2 - 90 degrees - Cp_mean
1
0.5
0
-0.5
-1

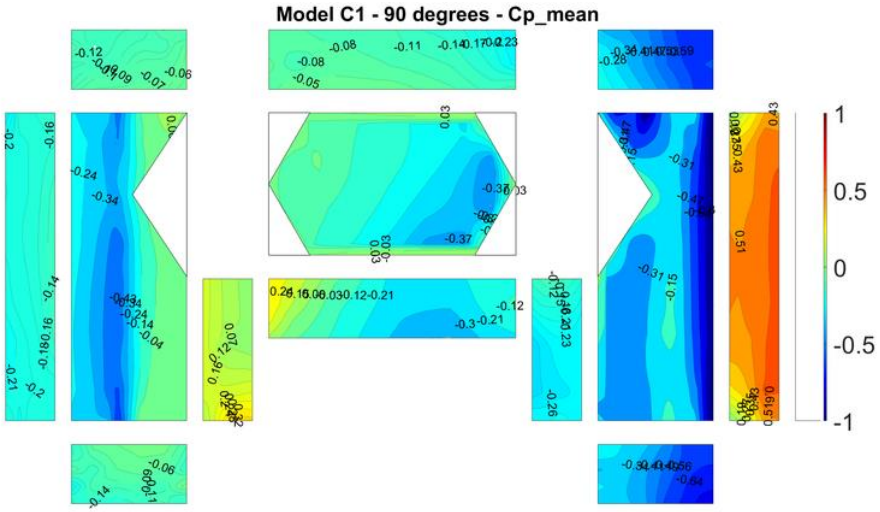
Model C1 - 90 degrees - Cp_mean
1
0.5
0
-0.5
-1

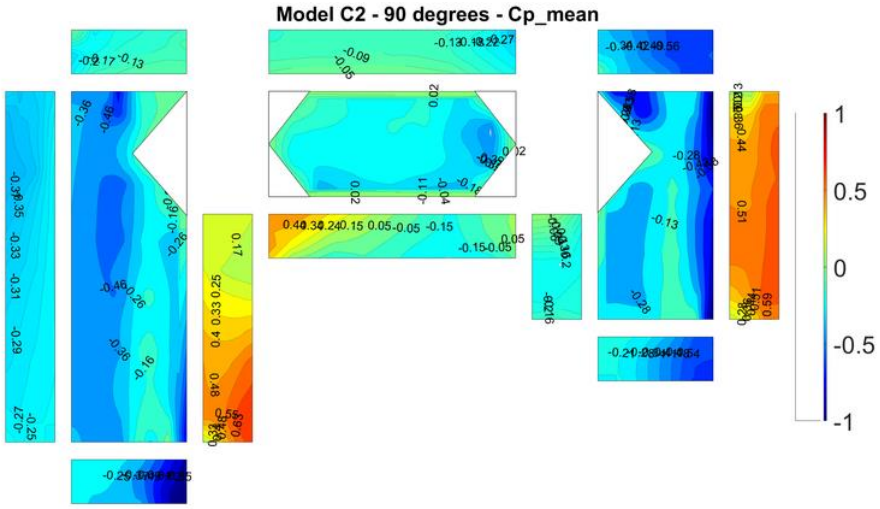
Model C2 - 90 degrees - Cp_mean
1
0.5
0
-0.5
-1

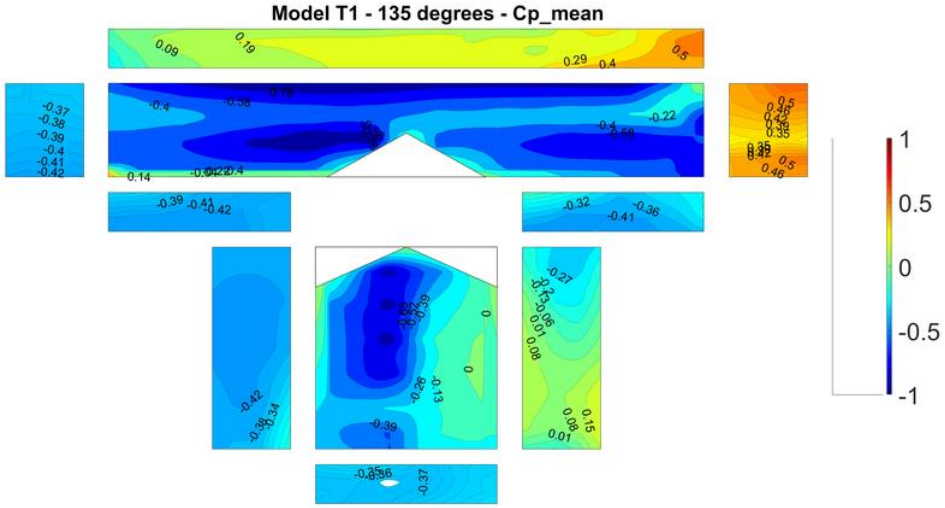
Model T1 - 135 degrees - Cp_mean
1
0.5
0
-0.5
-1

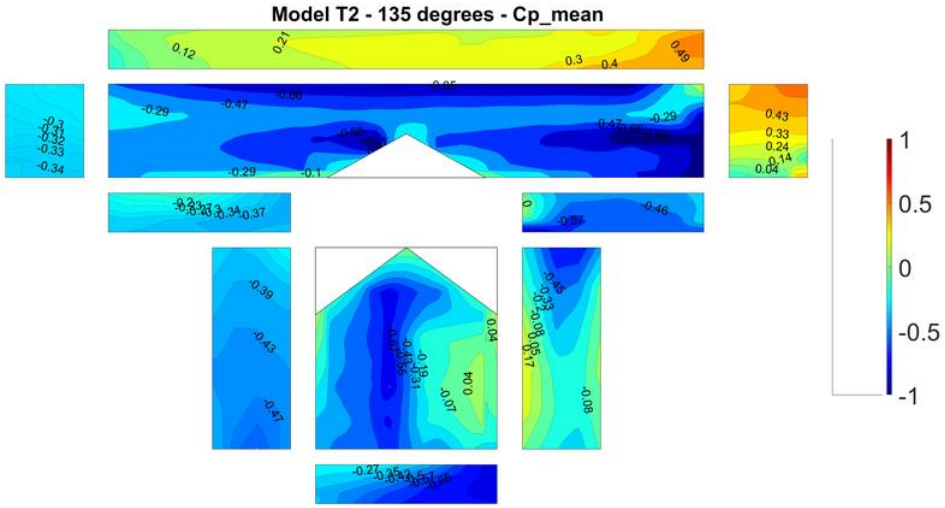
Model T2 - 135 degrees - Cp_mean
1
0.5
0
-0.5
-1

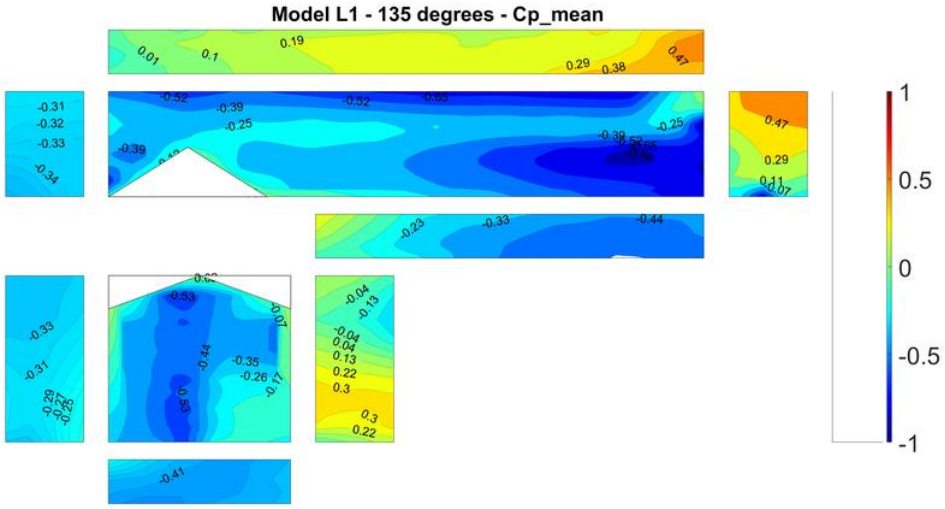
Model L1 - 135 degrees - Cp_mean
1
0.5
0
-0.5
-1

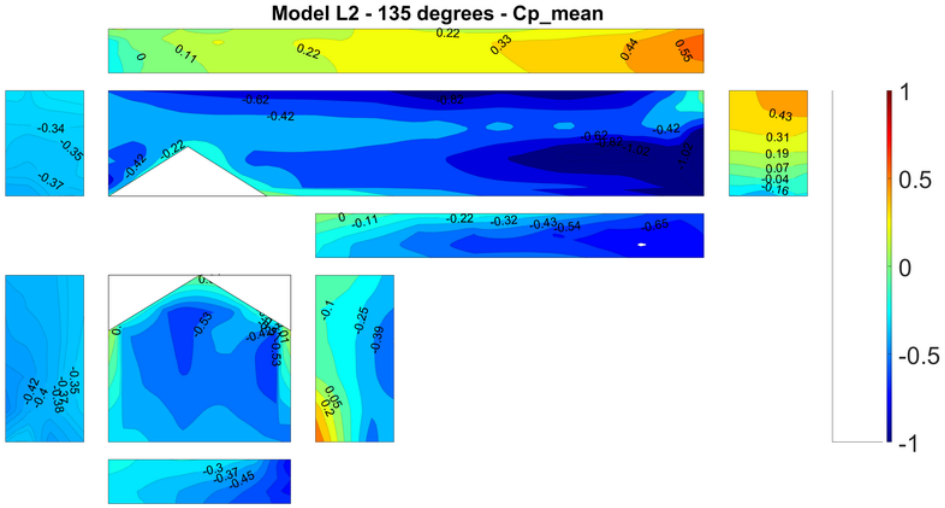
Model L2 - 135 degrees - Cp_mean
1
0.5
0
-0.5
-1

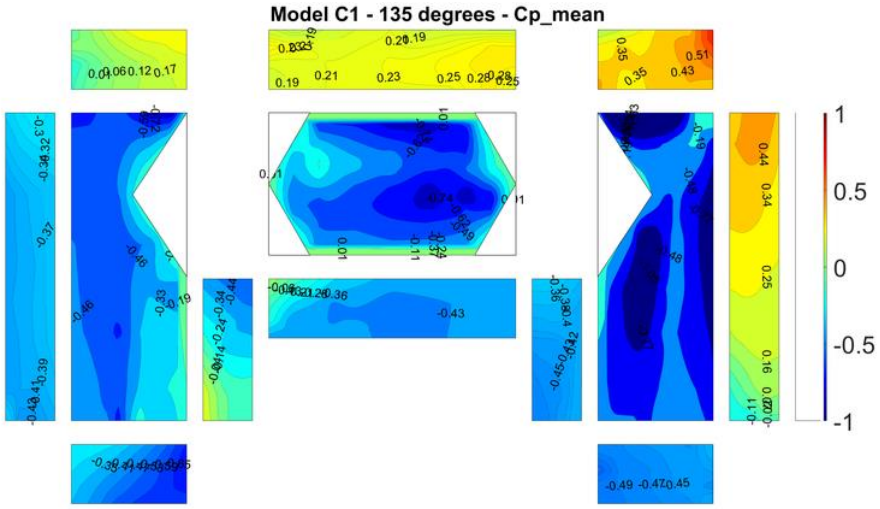
Model C1 - 135 degrees - Cp_mean
1
0.5
0
-0.5
-1

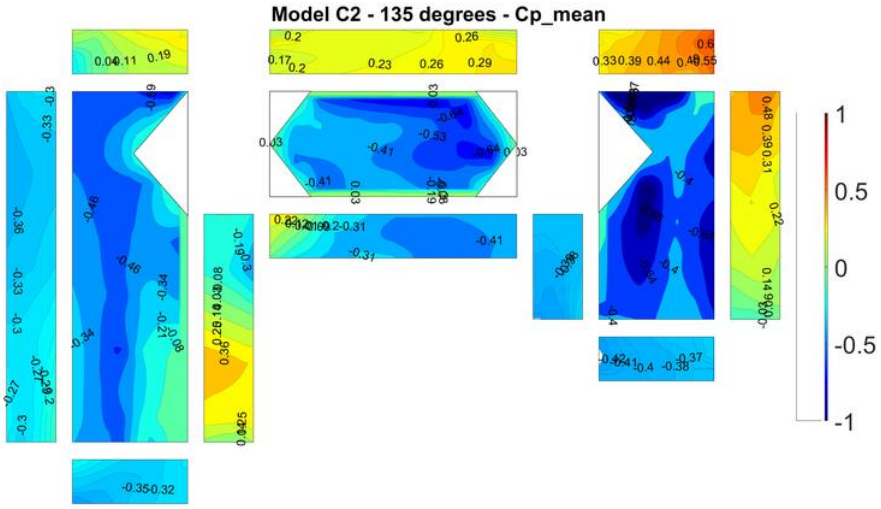
Model C2 - 135 degrees - Cp_mean
1
0.5
0
-0.5
-1

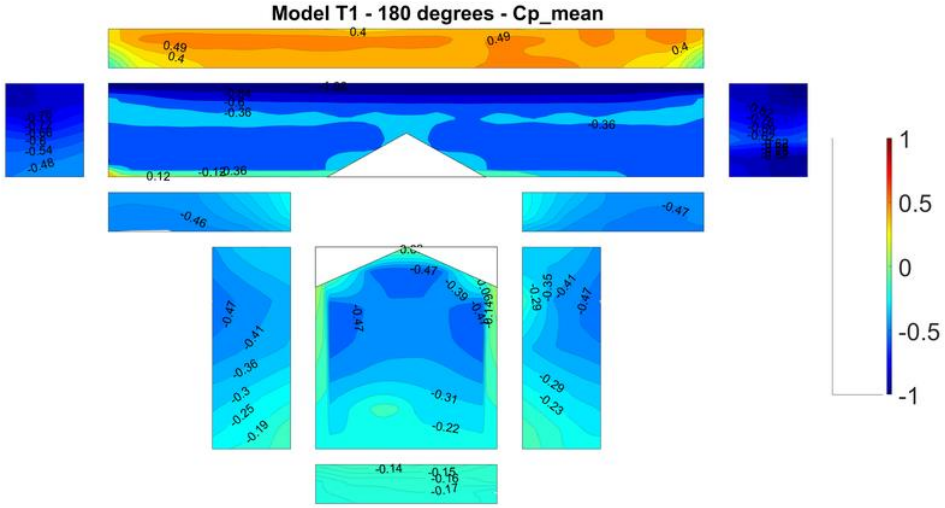
Model T1 - 180 degrees - Cp_mean
1
0.5
0
-0.5
-1

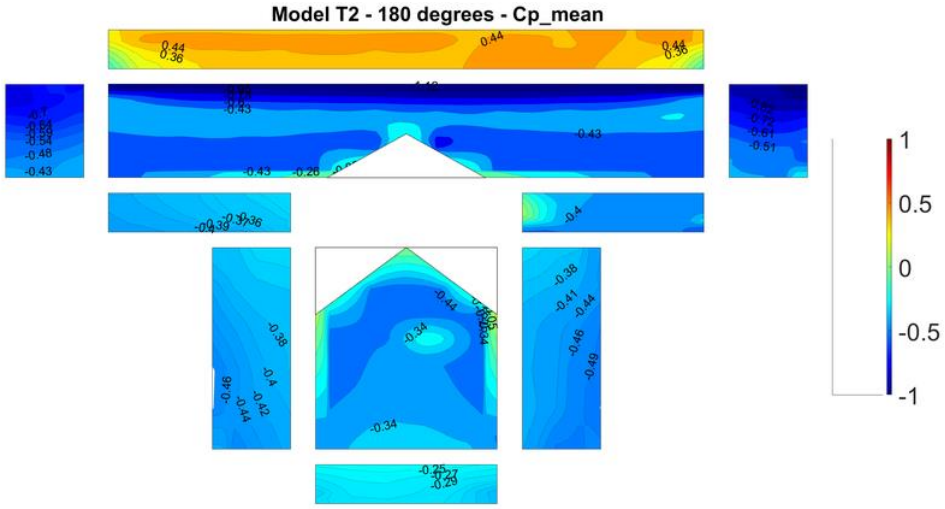
Model T2 - 180 degrees - Cp_mean
1
0.5
0
-0.5
-1

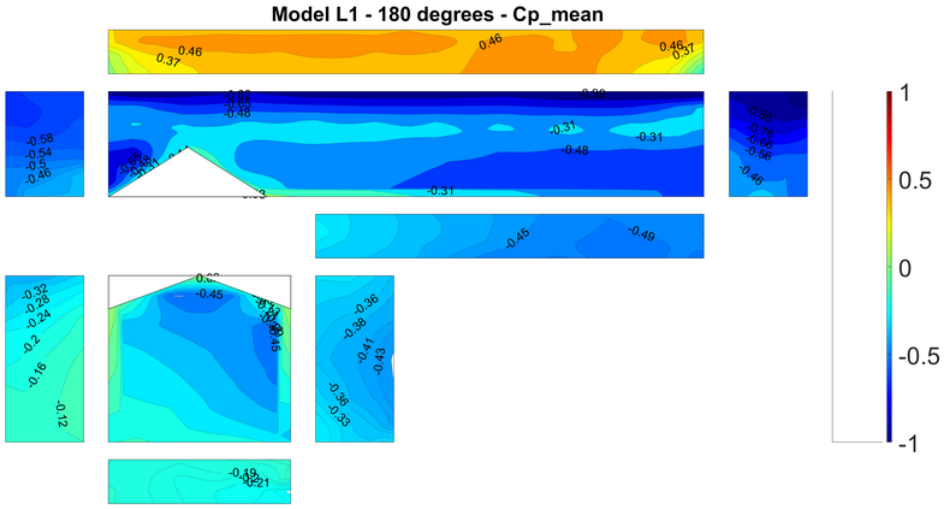
Model L1 - 180 degrees - Cp_mean
1
0.5
0
-0.5
-1

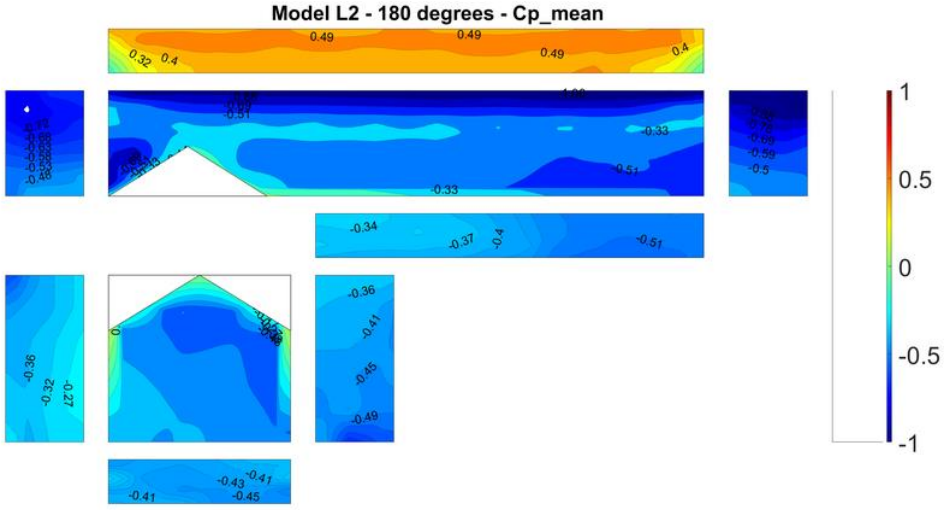
Model L2 - 180 degrees - Cp_mean
1
0.5
0
-0.5
-1

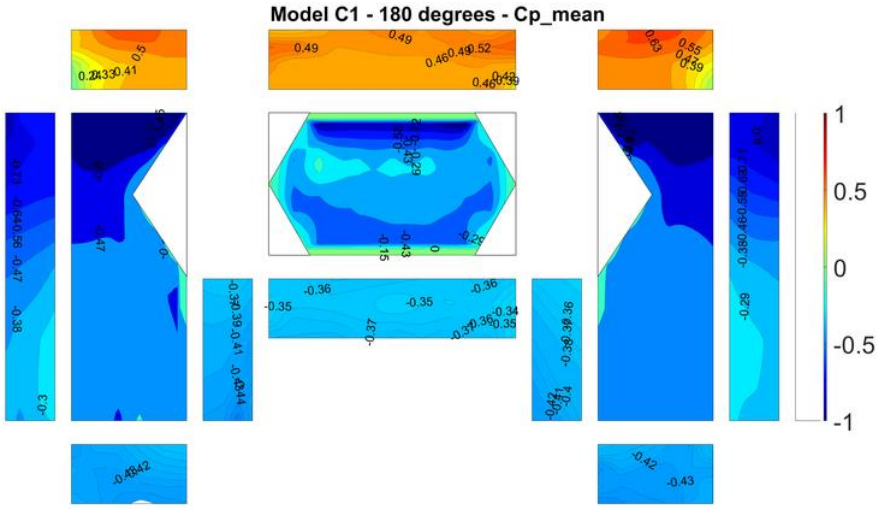
Model C1 - 180 degrees - Cp_mean
1
0.5
0
-0.5
-1

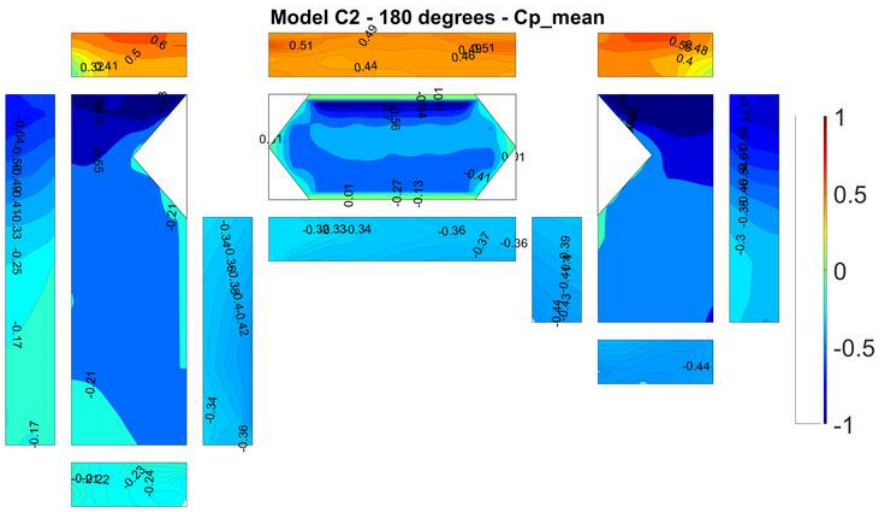
Model C2 - 180 degrees - Cp_mean
1
0.5
0
-0.5
-1

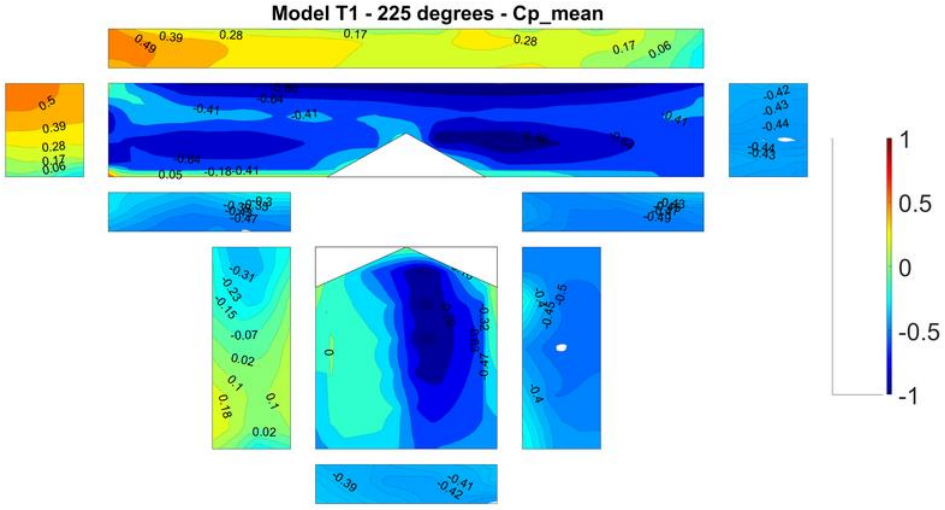
Model T1 - 225 degrees - Cp_mean
1
0.5
0
-0.5
-1

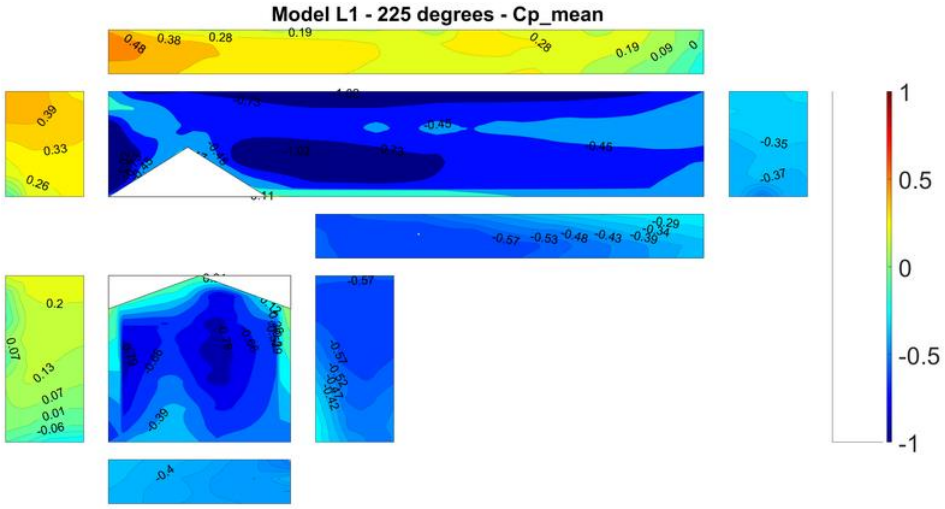
Model L1 - 225 degrees - Cp_mean
1
0.5
0
-0.5
-1

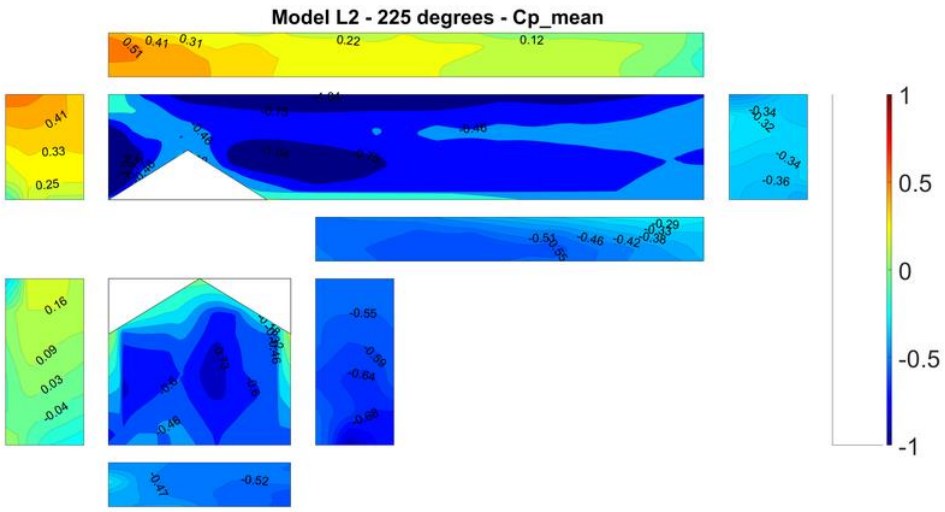
Model L2 - 225 degrees - Cp_mean
1
0.5
0
-0.5
-1

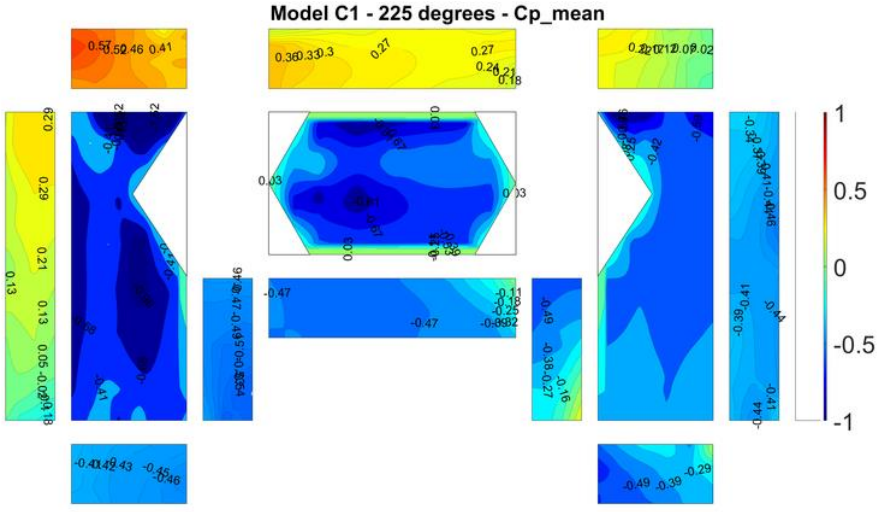
Model C1 - 225 degrees - Cp_mean
1
0.5
0
-0.5
-1

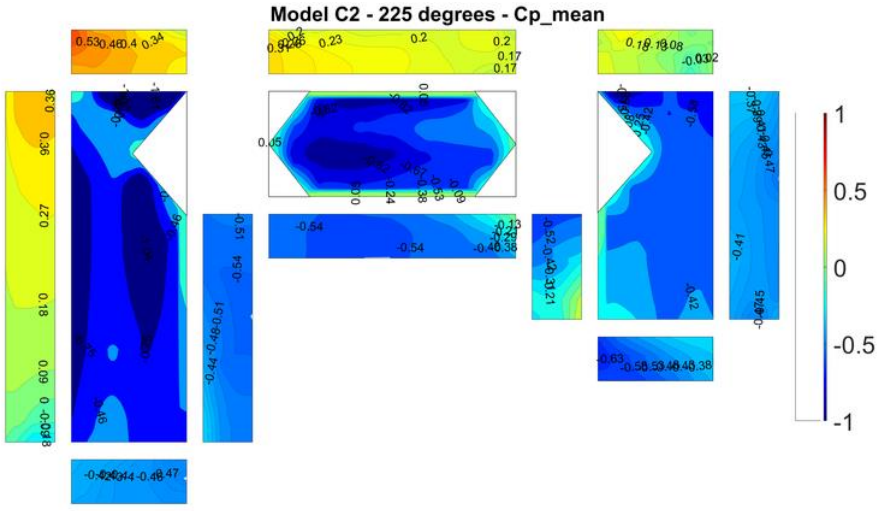
Model C2 - 225 degrees - Cp_mean
1
0.5
0
-0.5
-1

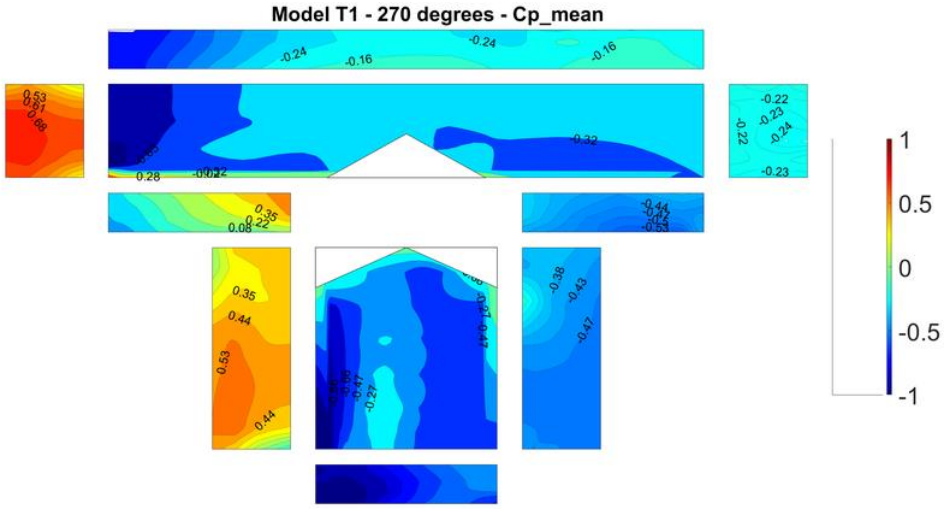
Model T1 - 270 degrees - Cp_mean
1
0.5
0
-0.5
-1

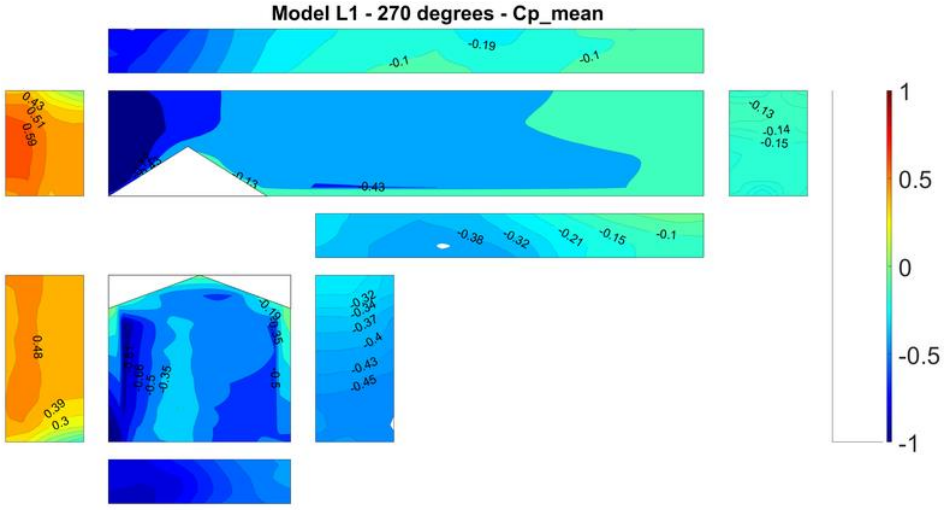
Model L1 - 270 degrees - Cp_mean
1
0.5
0
-0.5
-1

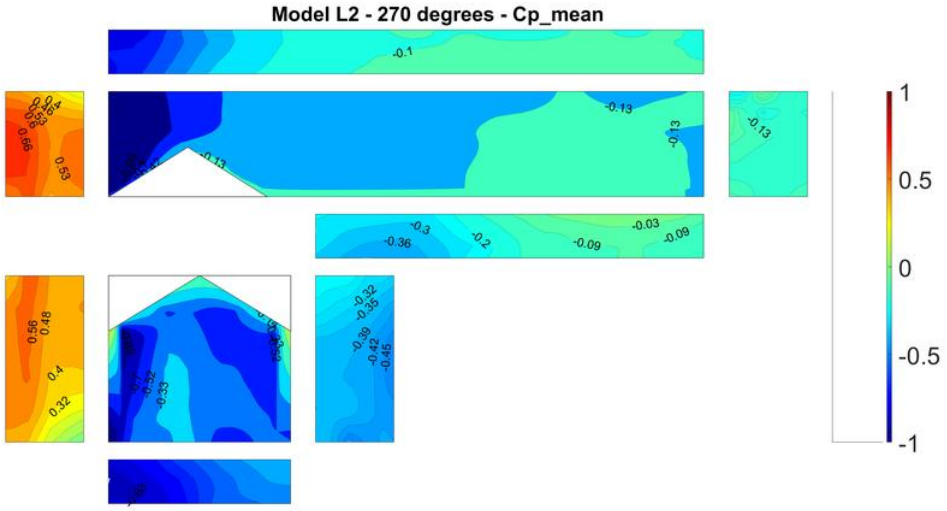
Model L2 - 270 degrees - Cp_mean
1
0.5
0
-0.5
-1

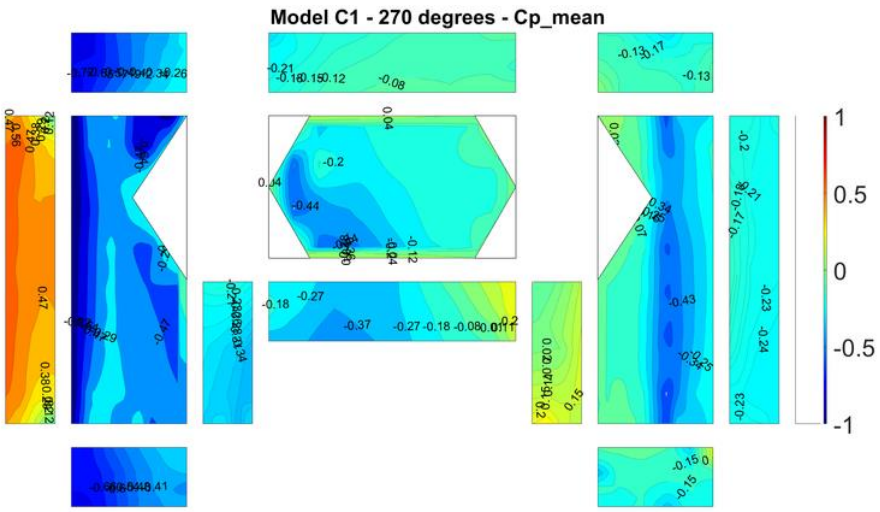
Model C1 - 270 degrees - Cp_mean
1
0.5
0
-0.5
-1

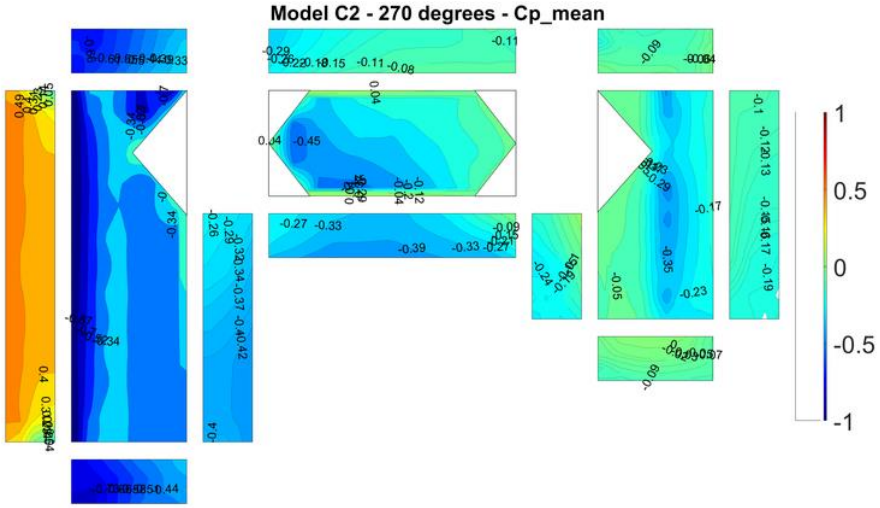
Model C2 - 270 degrees - Cp_mean
1
0.5
0
-0.5
-1

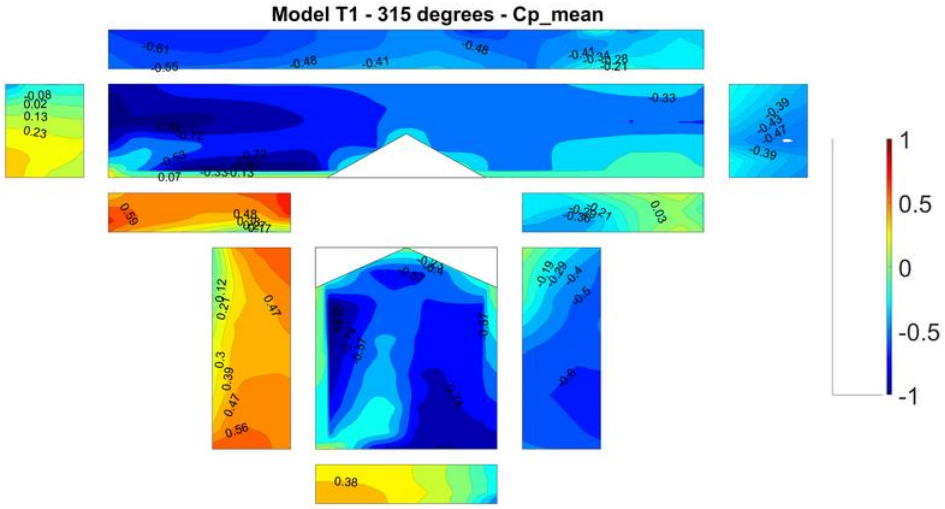
Model T1 - 315 degrees - Cp_mean
1
0.5
0
-0.5
-1

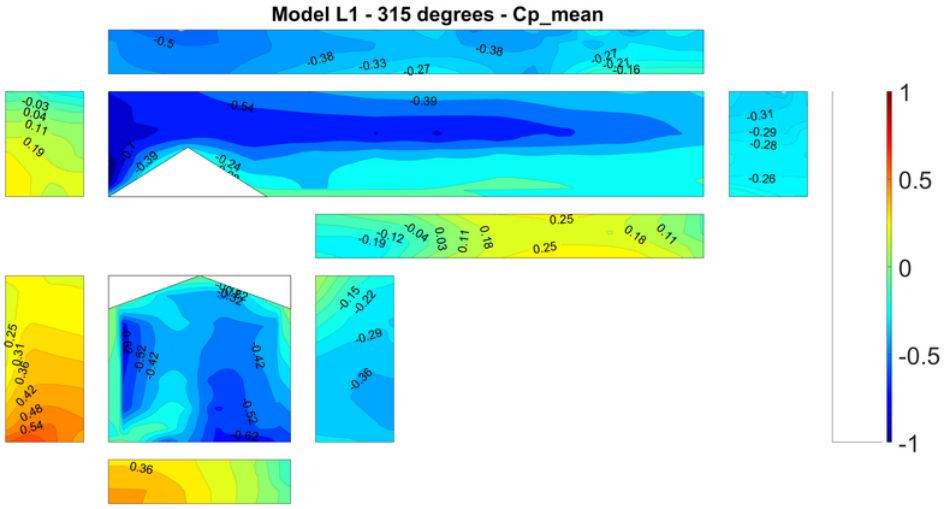
Model L1 - 315 degrees - Cp_mean
1
0.5
0
-0.5
-1

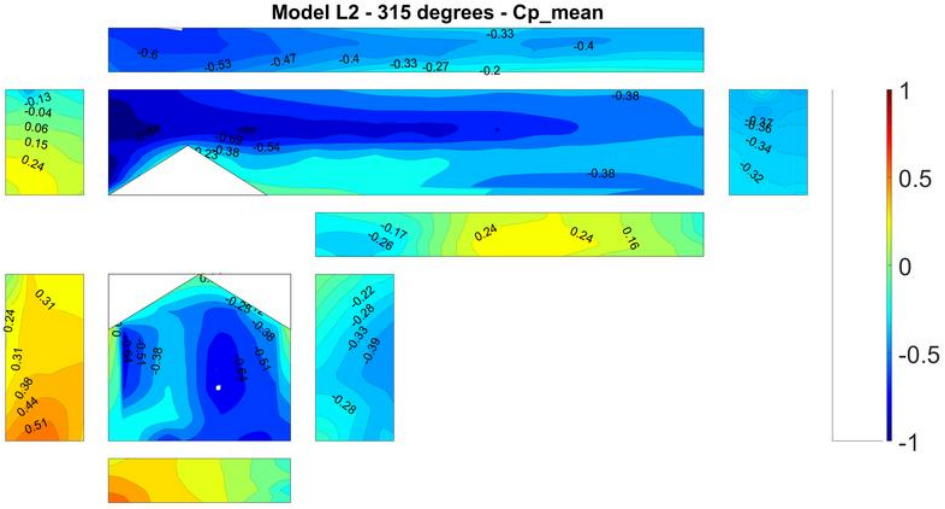
Model L2 - 315 degrees - Cp_mean
1
0.5
0
-0.5
-1

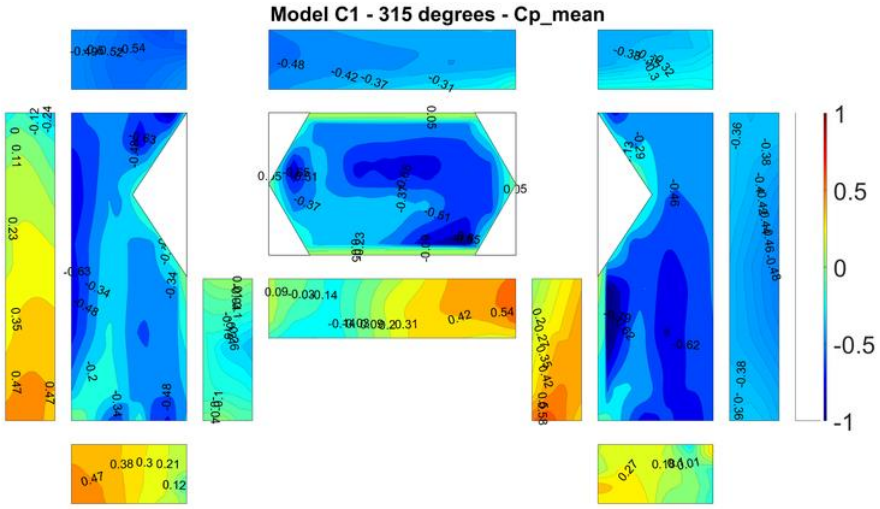
Model C1 - 315 degrees - Cp_mean
1
0.5
0
-0.5
-1

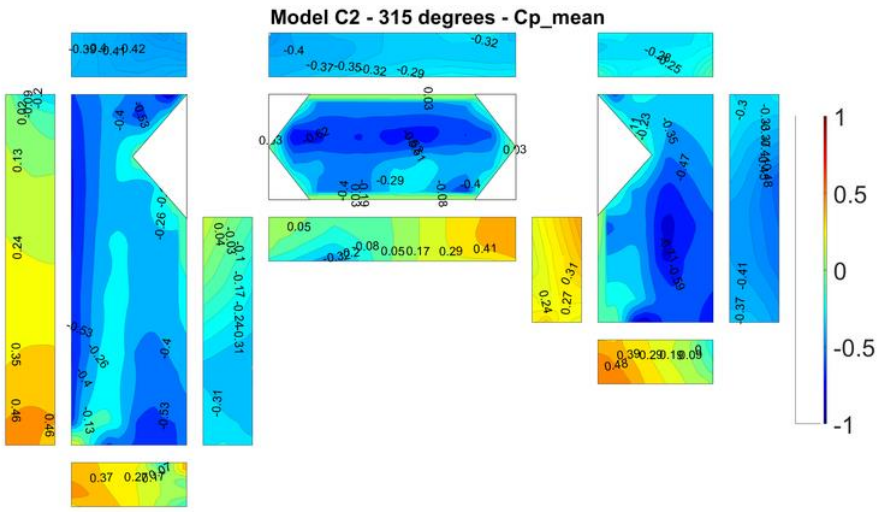

Contour plots of mean Cp values for small-scale models in 2021, specifically for cornering wind directions (from 45 degrees to 345 degrees):

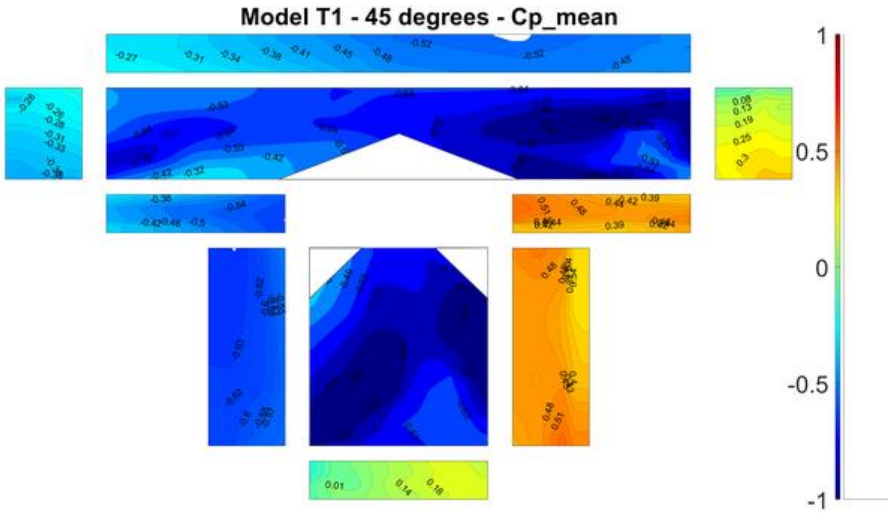

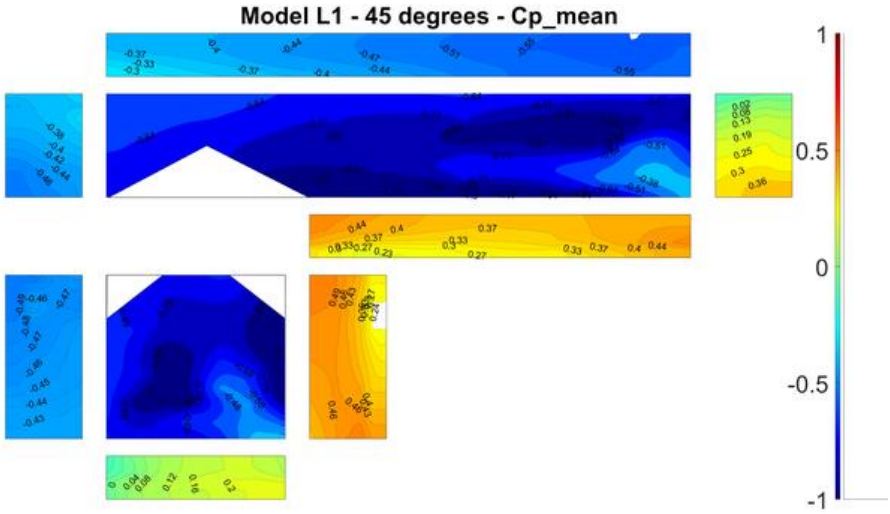
Model L1 - 45 degrees - Cp_mean
1
0.5
0
-0.5
-1

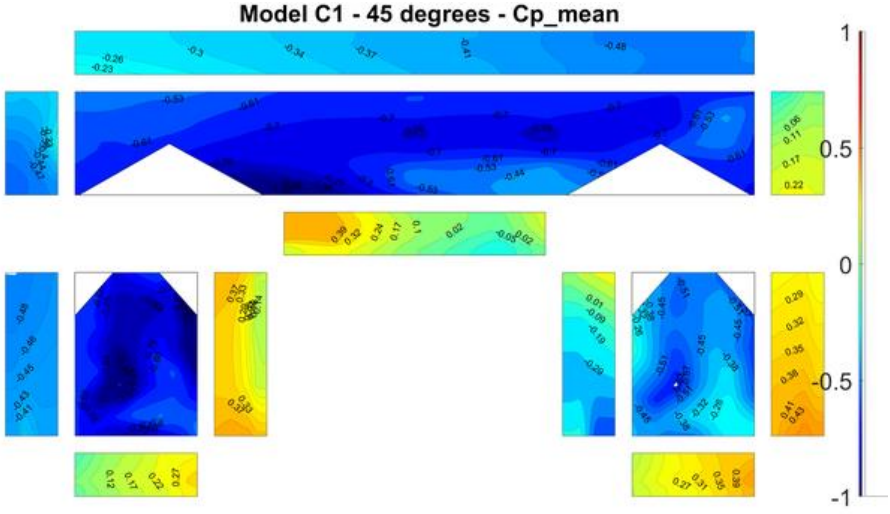
Model C1 - 45 degrees - Cp_mean
1
0.5
0
-0.5
-1

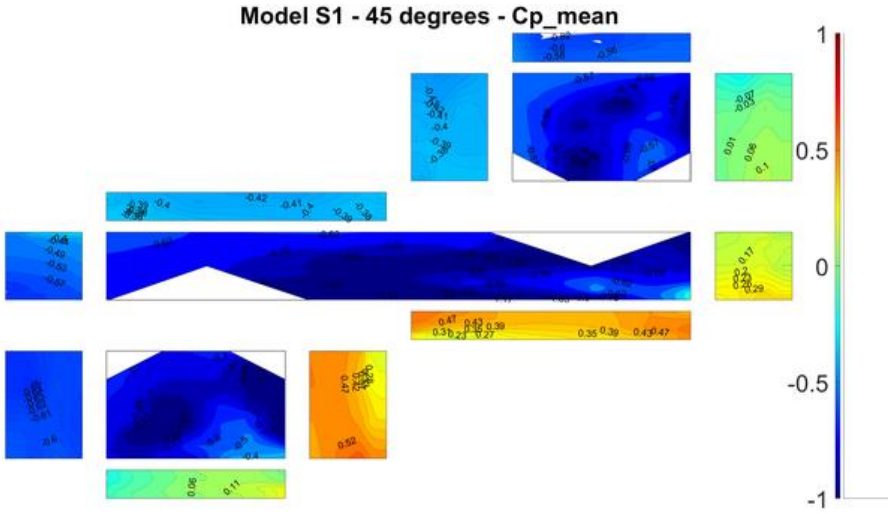
Model S1 - 45 degrees - Cp_mean
1
0.5
0
-0.5
-1

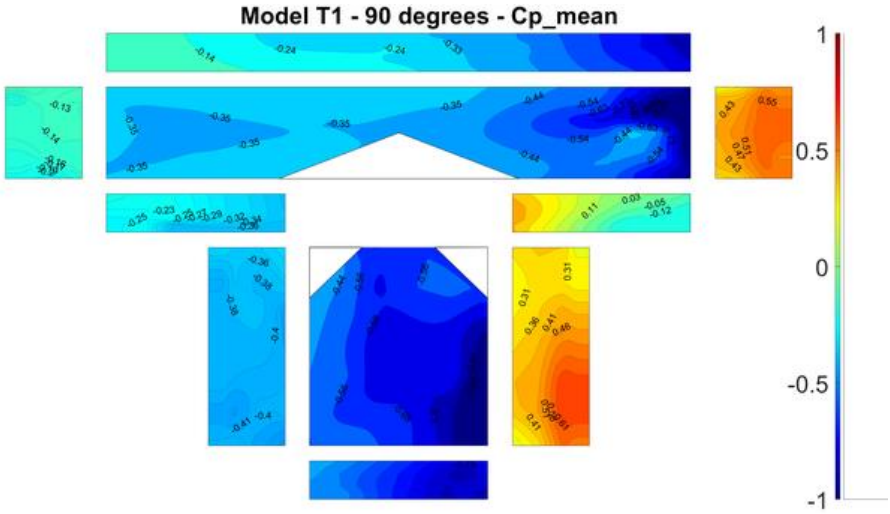
Model T1 - 90 degrees - Cp_mean
1
0.5
0
-0.5
-1

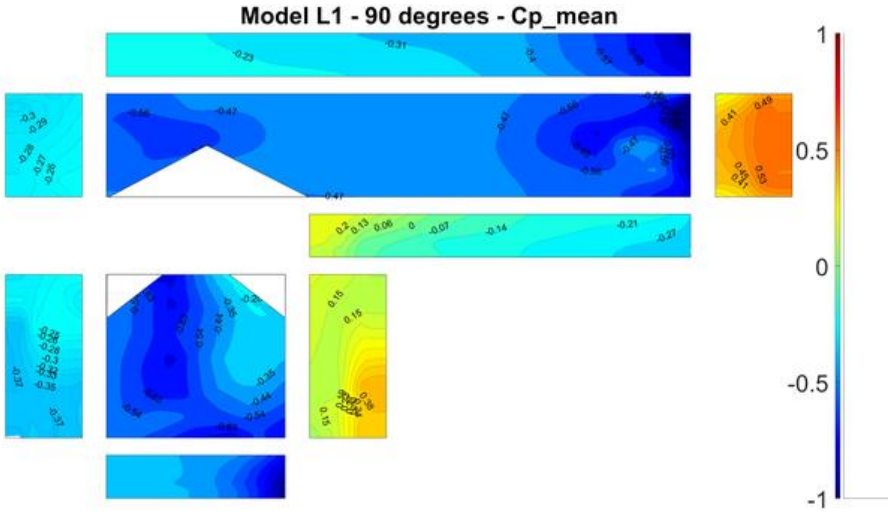
Model L1 - 90 degrees - Cp_mean
1
0.5
0
-0.5
-1

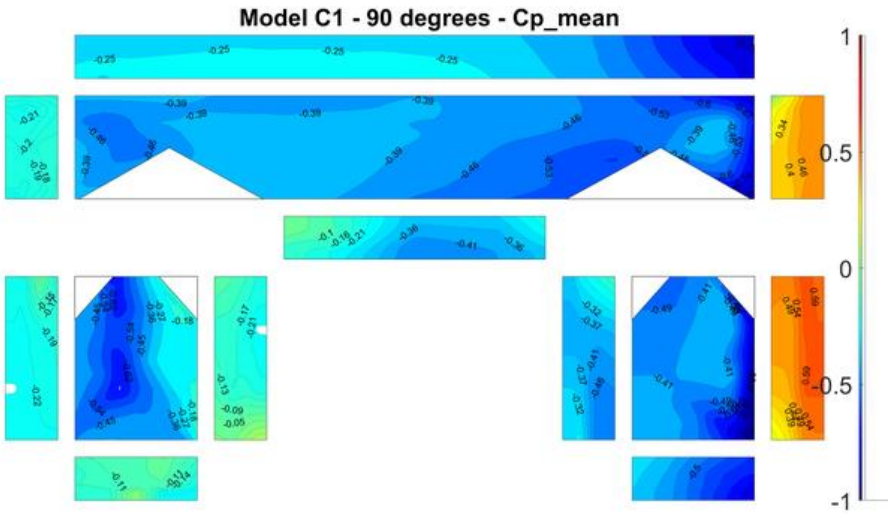
Model C1 - 90 degrees - Cp_mean
1
0.5
0
-0.5
-1

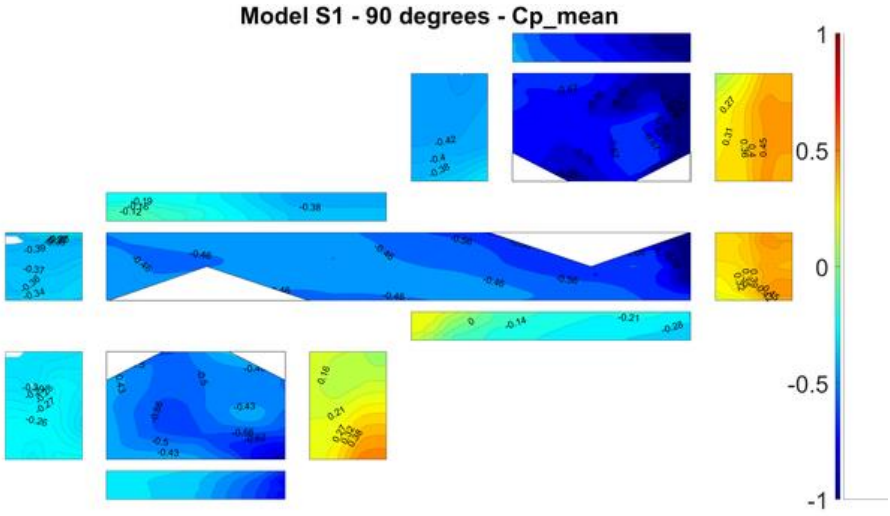
Model S1 - 90 degrees - Cp_mean
1
0.5
0
-0.5
-1

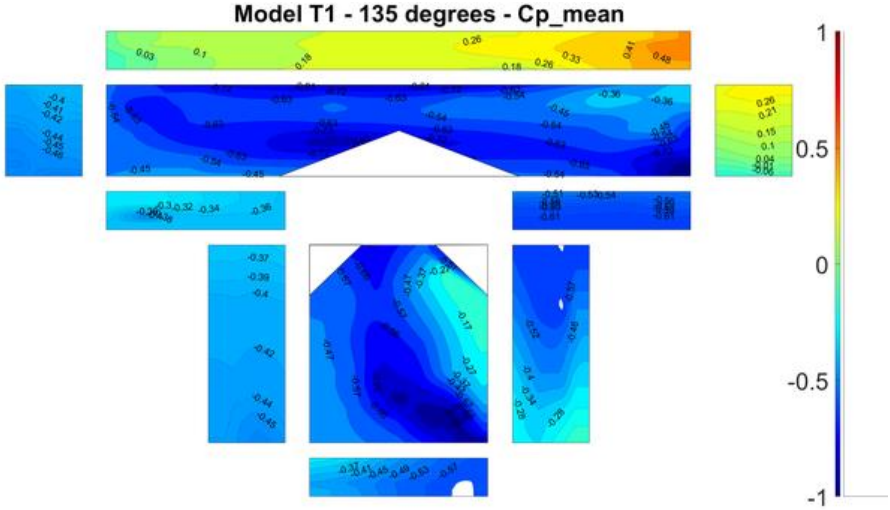
Model T1 - 135 degrees - Cp_mean
1
0.5
0
-0.5
-1

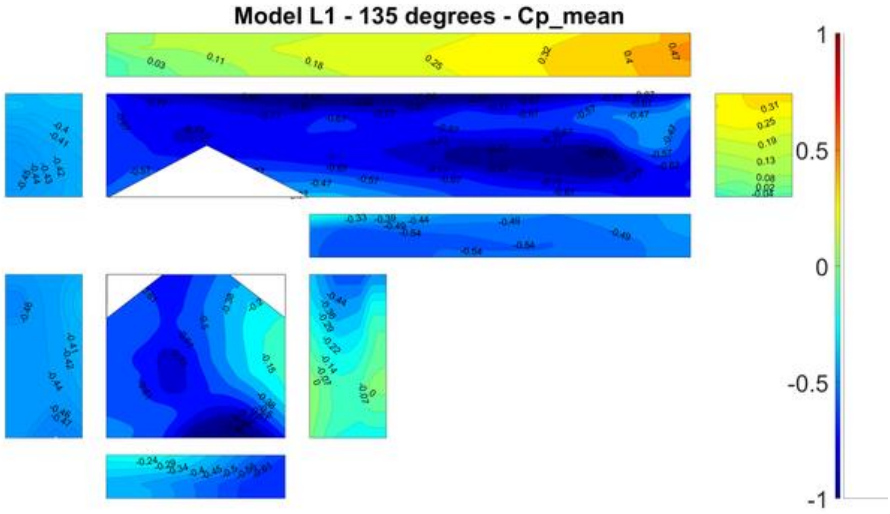
Model L1 - 135 degrees - Cp_mean
1
0.5
0
-0.5
-1

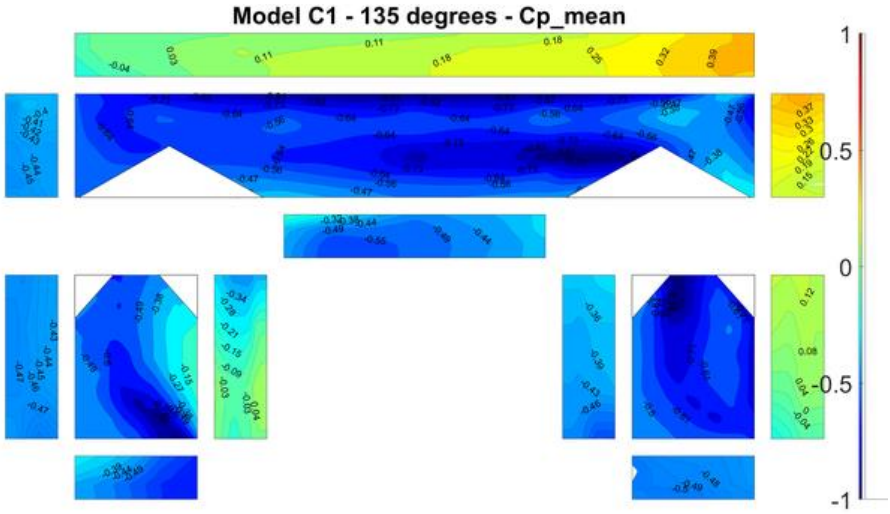
Model C1 - 135 degrees - Cp_mean
1
0.5
0
-0.5
-1

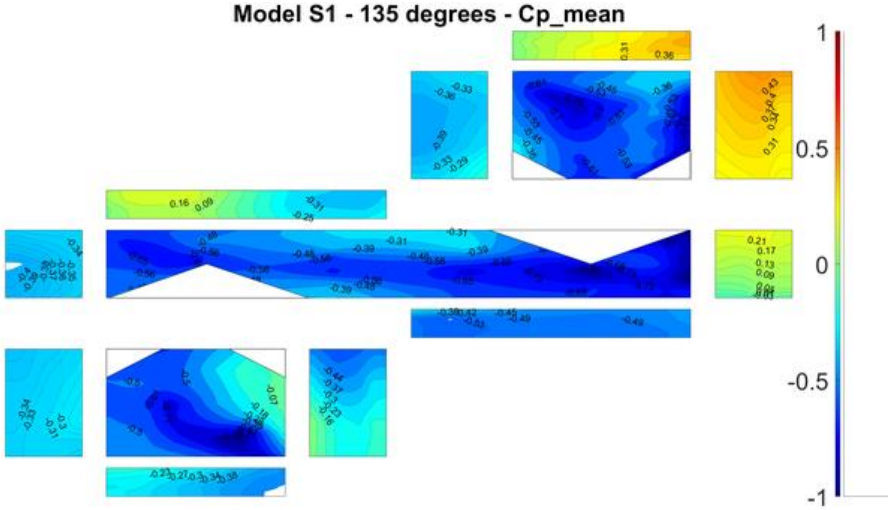
Model S1 - 135 degrees - Cp_mean
1
0.5
0
-0.5
-1

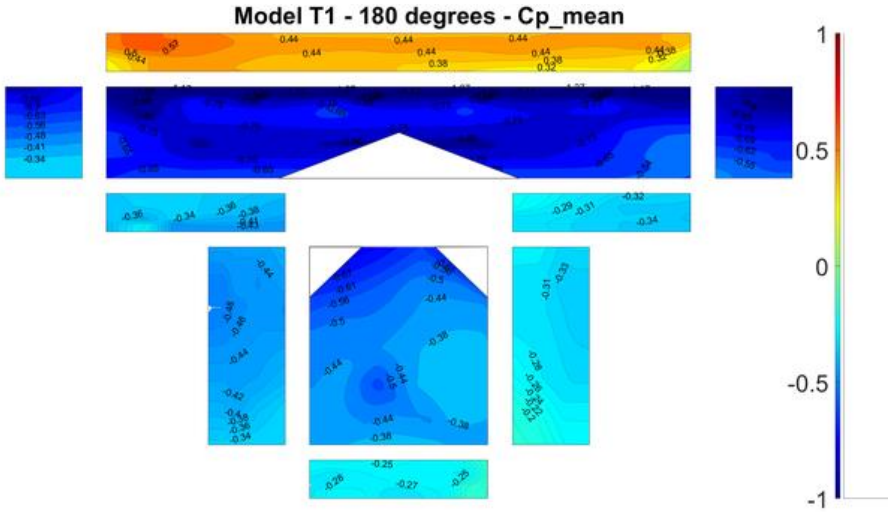
Model T1 - 180 degrees - Cp_mean
1
0.5
0
-0.5
-1

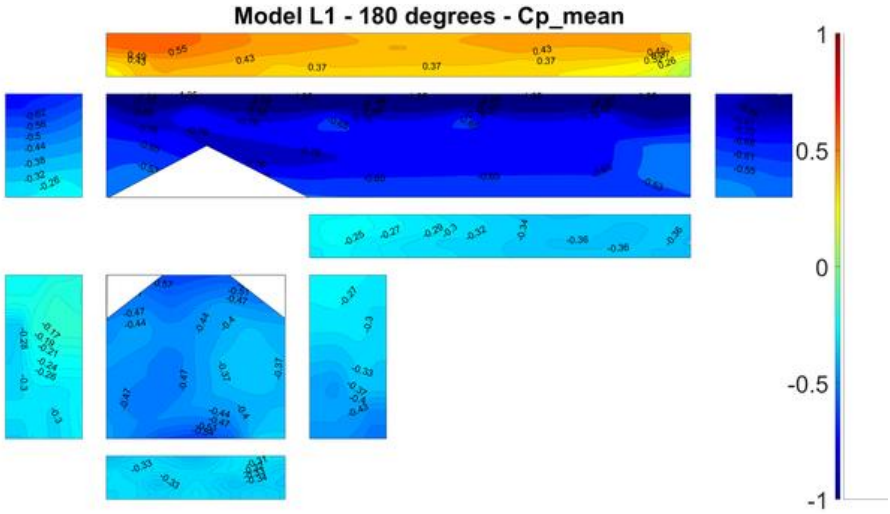
Model L1 - 180 degrees - Cp_mean
1
0.5
0
-0.5
-1

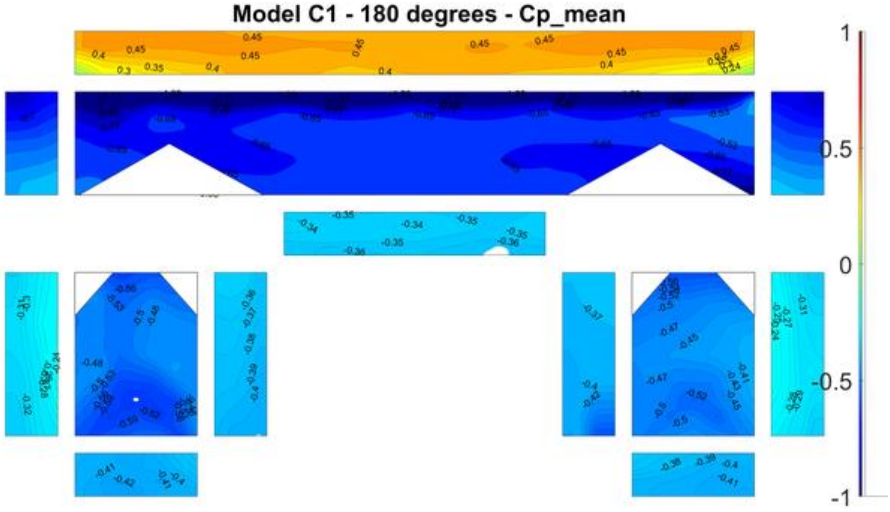
Model C1 - 180 degrees - Cp_mean
1
0.5
0
-0.5
-1

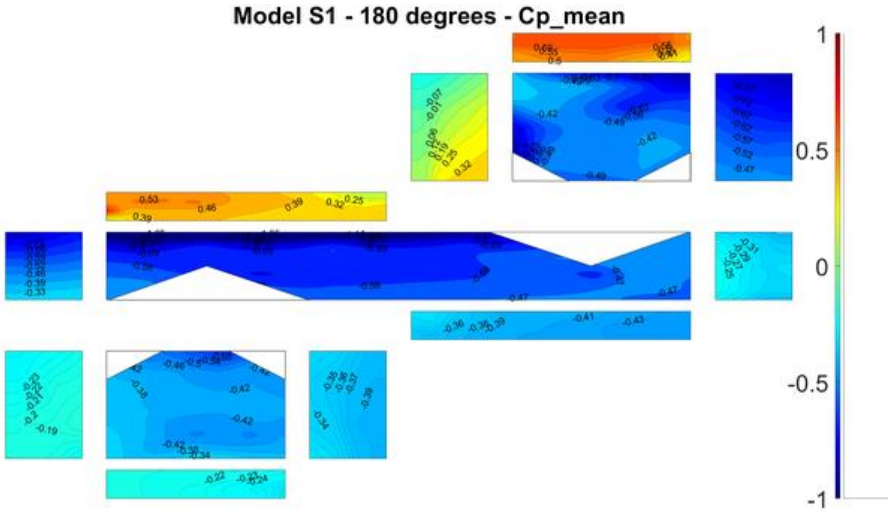
Model S1 - 180 degrees - Cp_mean
1
0.5
0
-0.5
-1

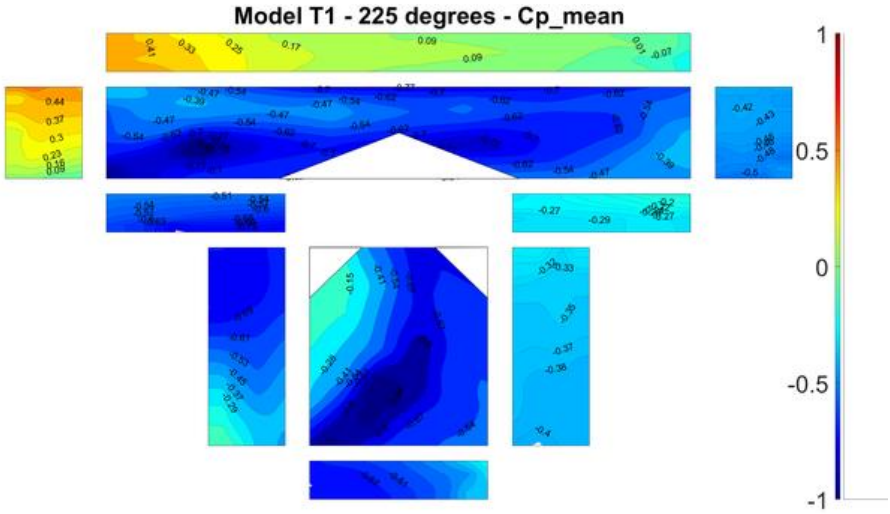
Model T1 - 225 degrees - Cp_mean
1
0.5
0
-0.5
-1

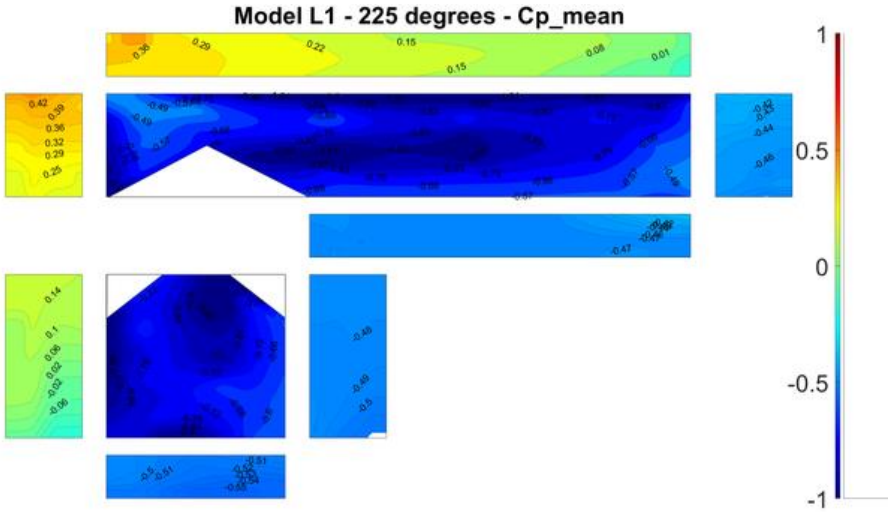
Model L1 - 225 degrees - Cp_mean
1
0.5
0
-0.5
-1

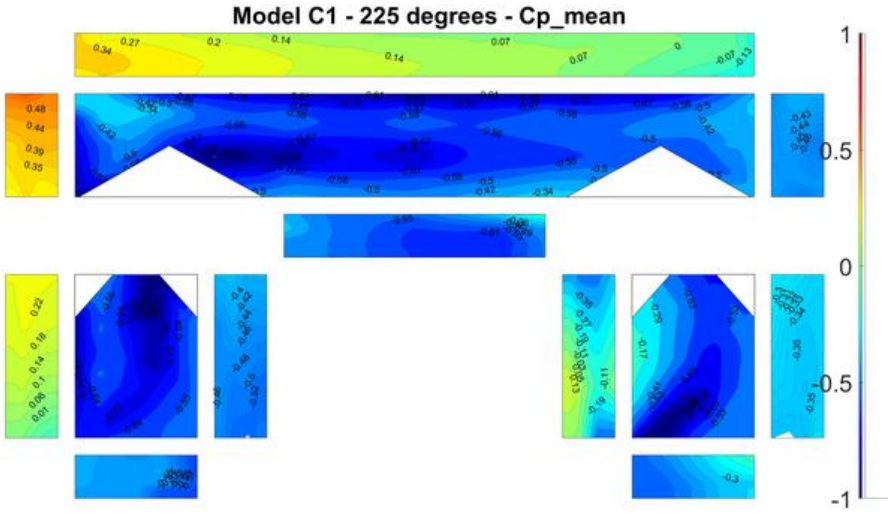
Model C1 - 225 degrees - Cp_mean
1
0.5
0
-0.5
-1

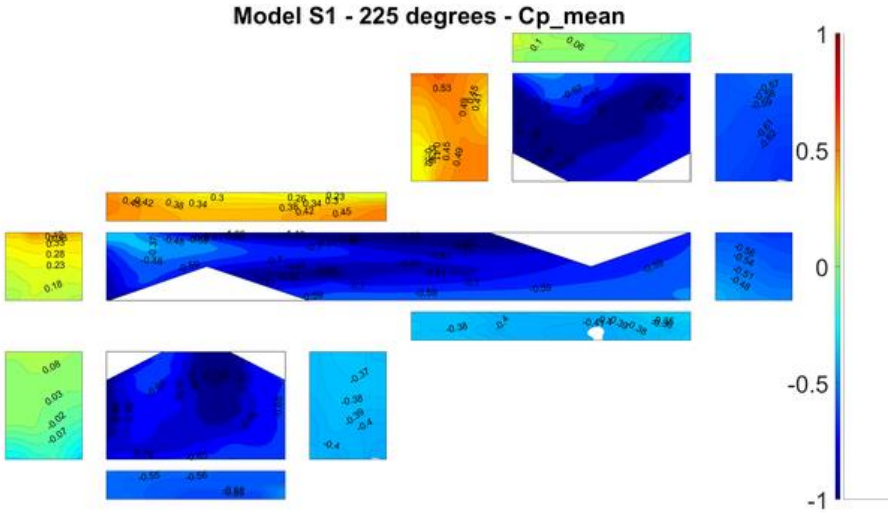
Model S1 - 225 degrees - Cp_mean
1
0.5
0
-0.5
-1

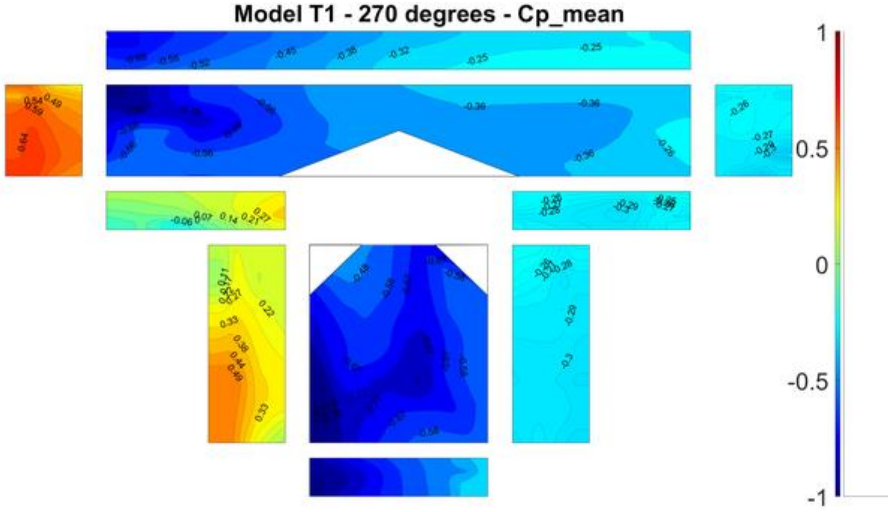
Model T1 - 270 degrees - Cp_mean
1
0.5
0
-0.5
-1

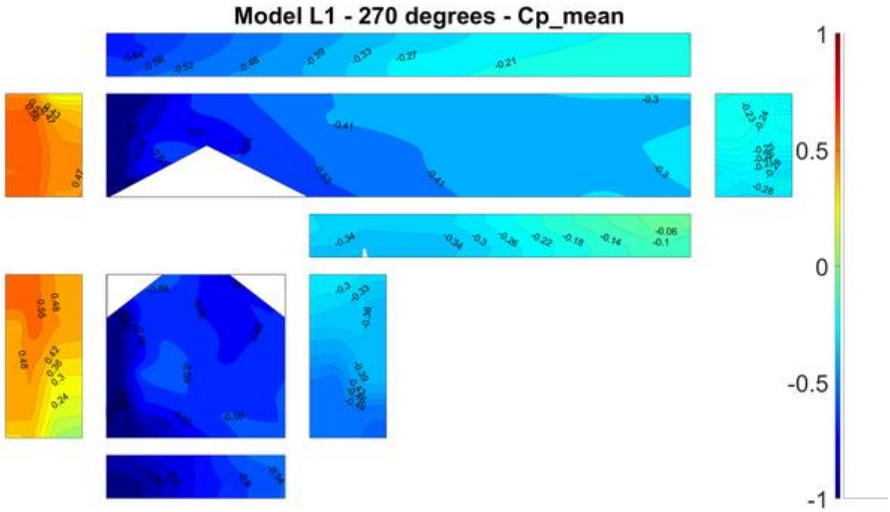
Model L1 - 270 degrees - Cp_mean
1
0.5
0
-0.5
-1

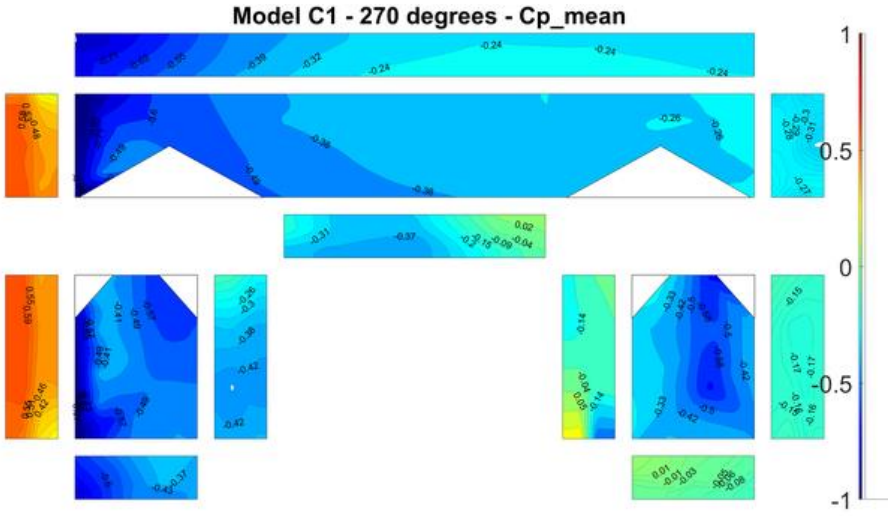
Model C1 - 270 degrees - Cp_mean
1
0.5
0
-0.5
-1

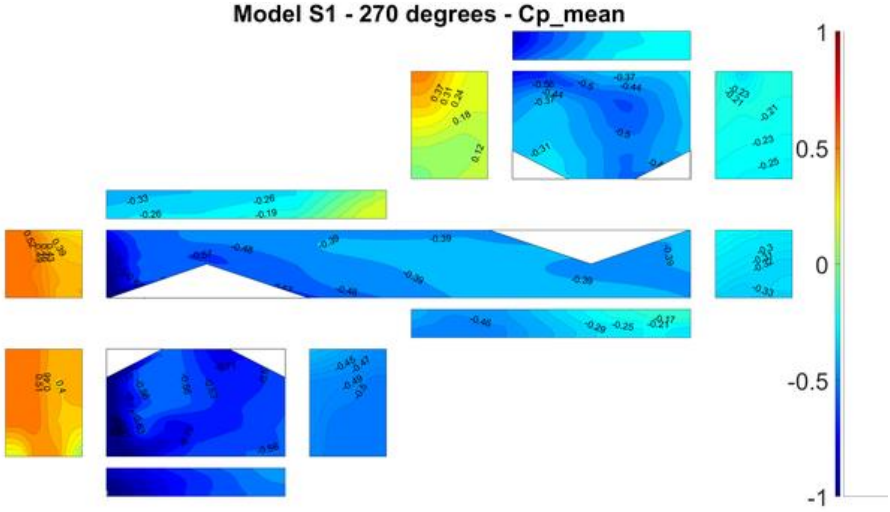
Model S1 - 270 degrees - Cp_mean
1
0.5
0
-0.5
-1

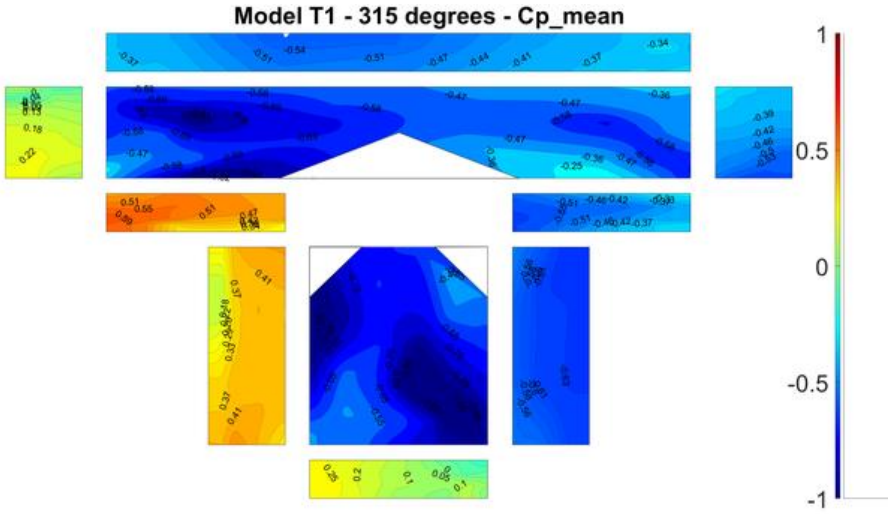
Model T1 - 315 degrees - Cp_mean
1
0.5
0
-0.5
-1

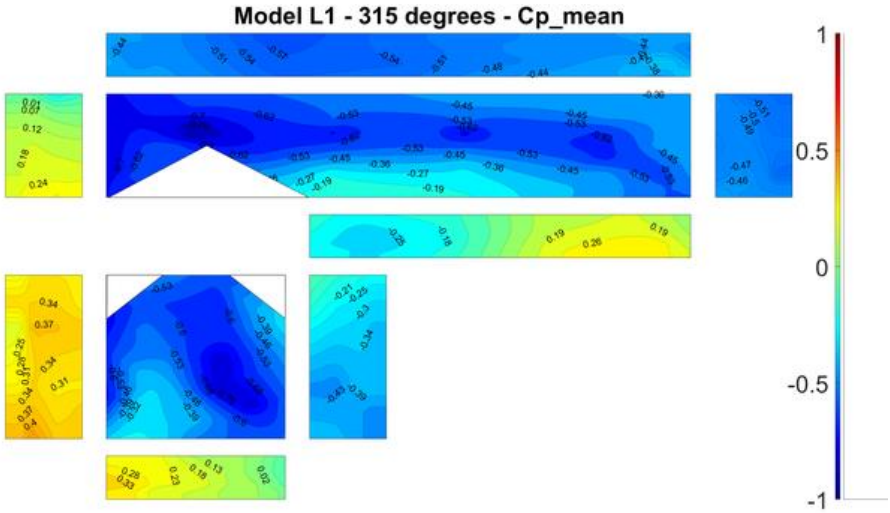
Model L1 - 315 degrees - Cp_mean
1
0.5
0
-0.5
-1

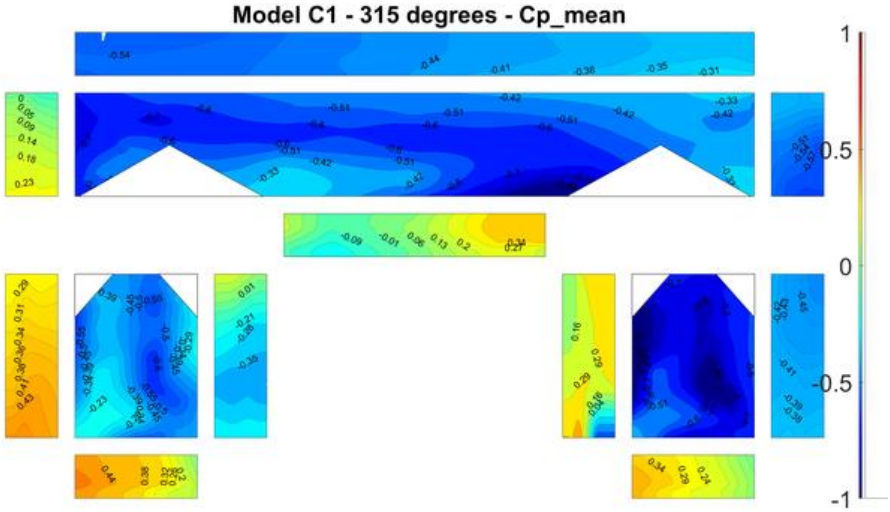
Model C1 - 315 degrees - Cp_mean
1
0.5
0
-0.5
-1

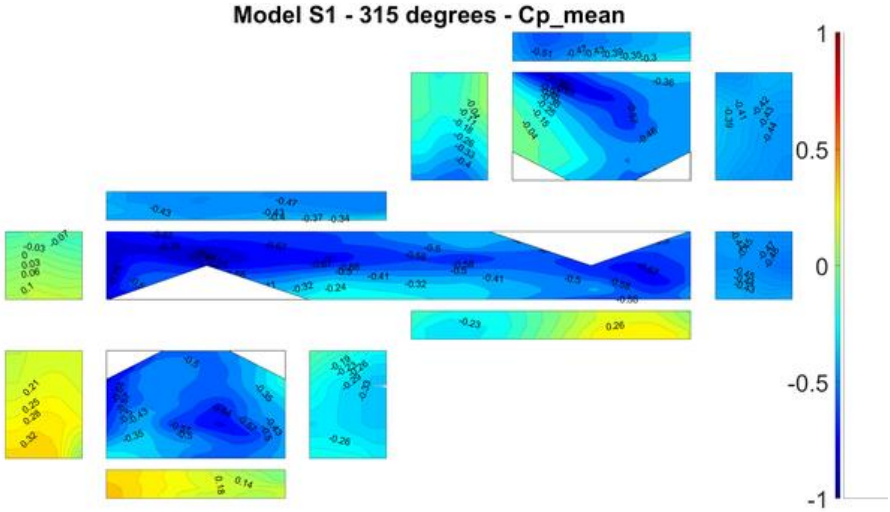
Model S1 - 315 degrees - Cp_mean
1
0.5
0
-0.5
-1

Contour Plots of mean Cp values for small-scale models in 2023, specifically for cornering wind directions (from 45 to 345 degrees):

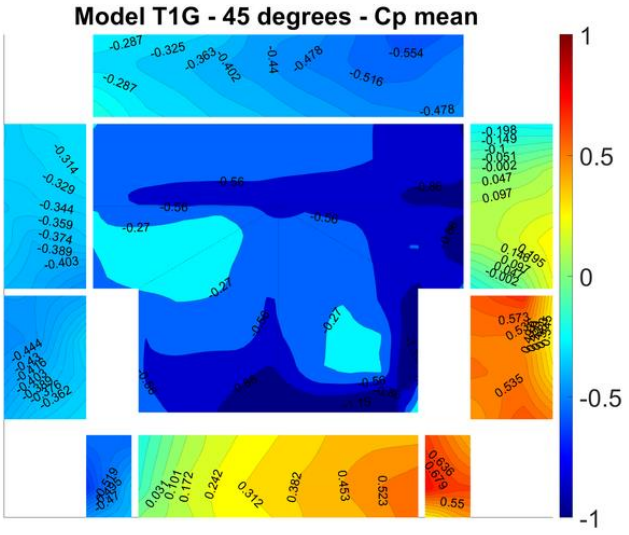

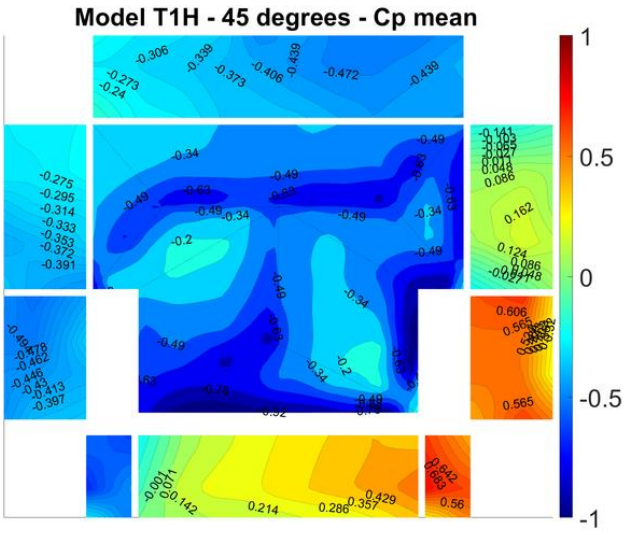

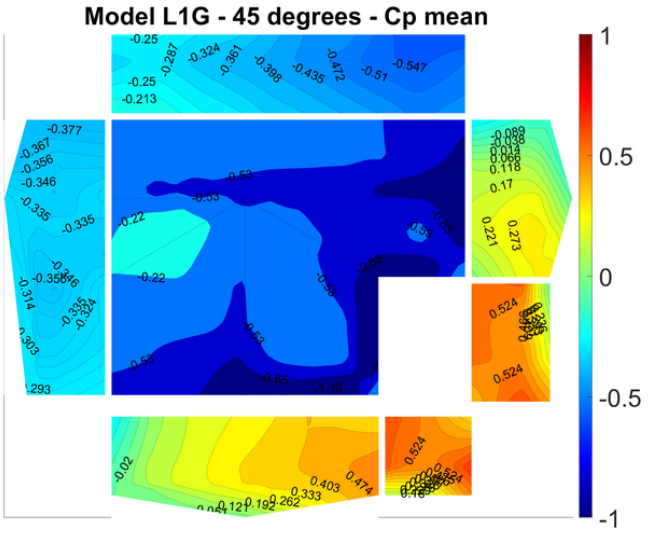
Model L1G - 45 degrees - Cp mean
1
0.5
0
-0.5
-1

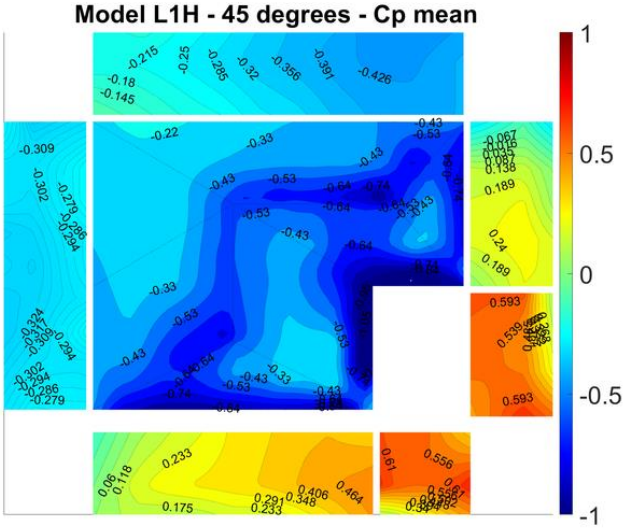
Model L1H - 45 degrees - Cp mean
1
0.5
0
-0.5
-1

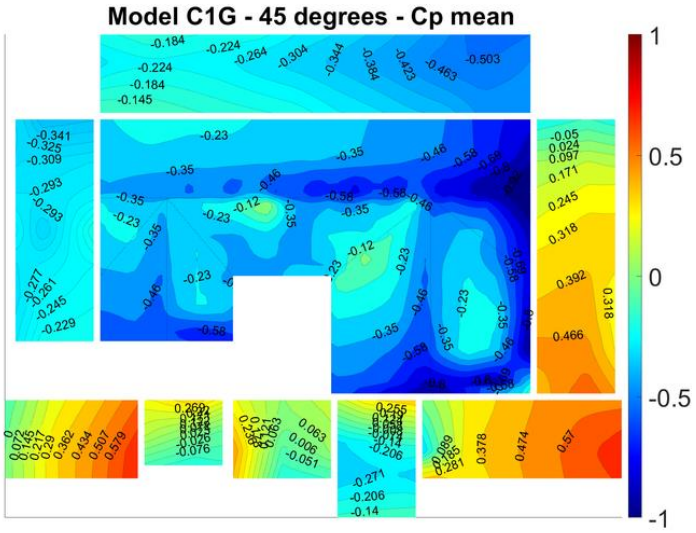
Model C1G - 45 degrees - Cp mean
1
0.5
0
-0.5
-1

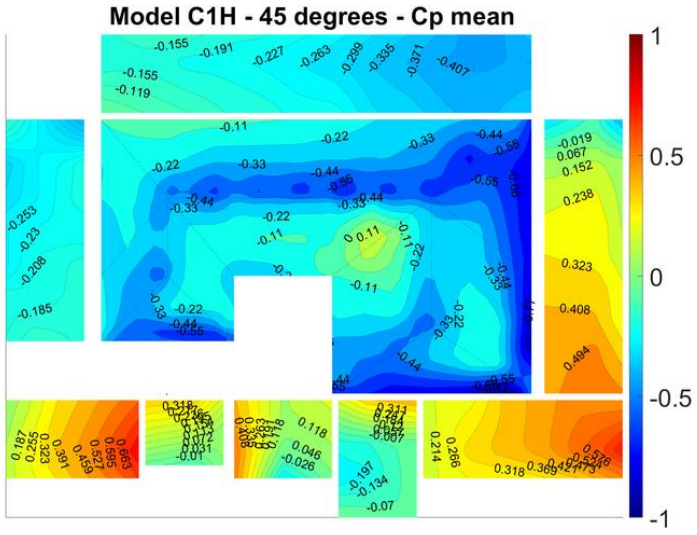
Model C1H - 45 degrees - Cp mean
1
0.5
0
-0.5
-1

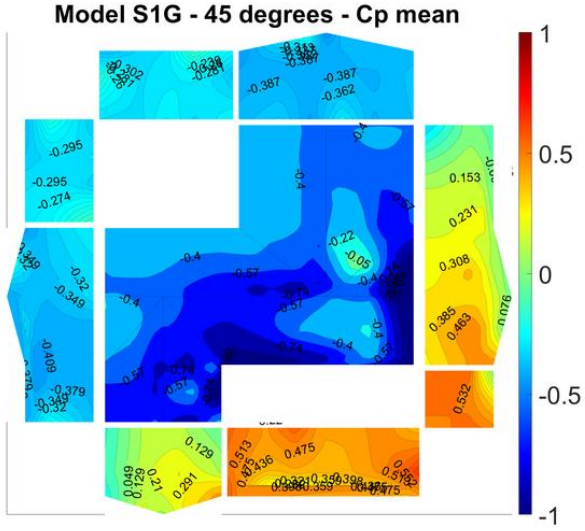
Model S1G - 45 degrees - Cp mean
1
0.5
0
-0.5
-1

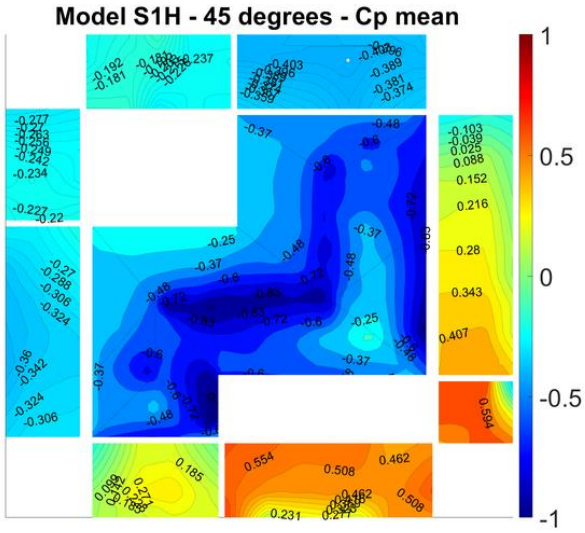
Model S1H - 45 degrees - Cp mean
1
0.5
0
-0.5
-1

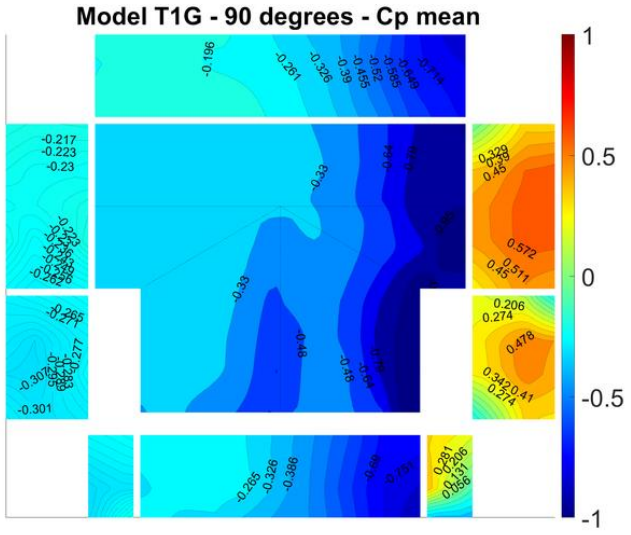
Model T1G - 90 degrees - Cp mean
1
0.5
0
-0.5
-1

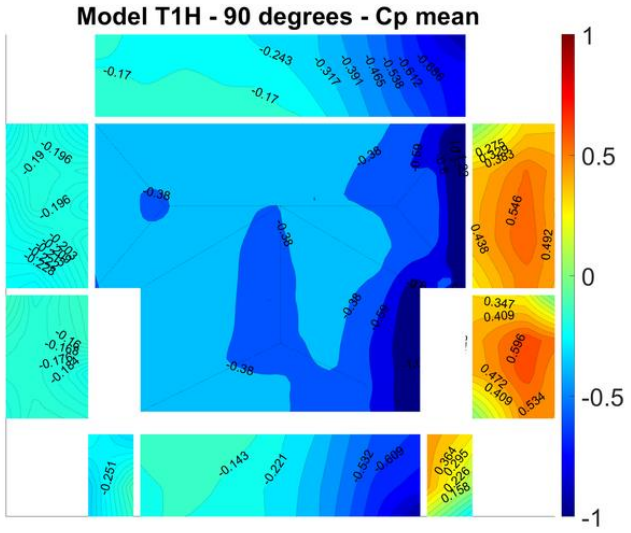
Model T1H - 90 degrees - Cp mean
1
0.5
0
-0.5
-1

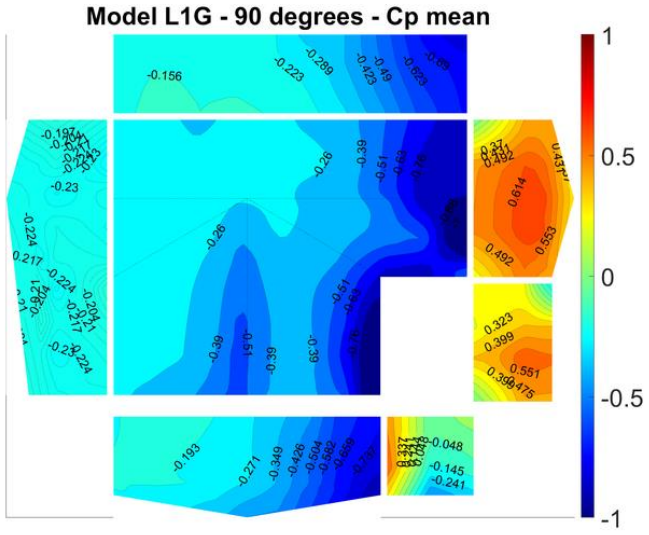
Model L1G - 90 degrees - Cp mean
1
0.5
0
-0.5
-1

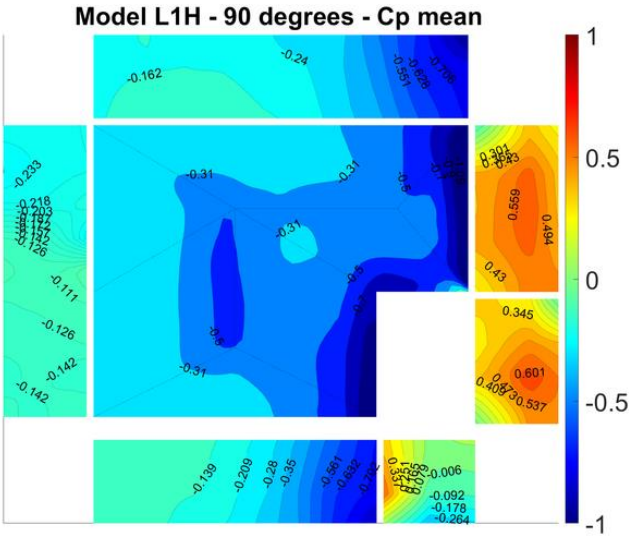
Model L1H - 90 degrees - Cp mean
1
0.5
0
-0.5
-1

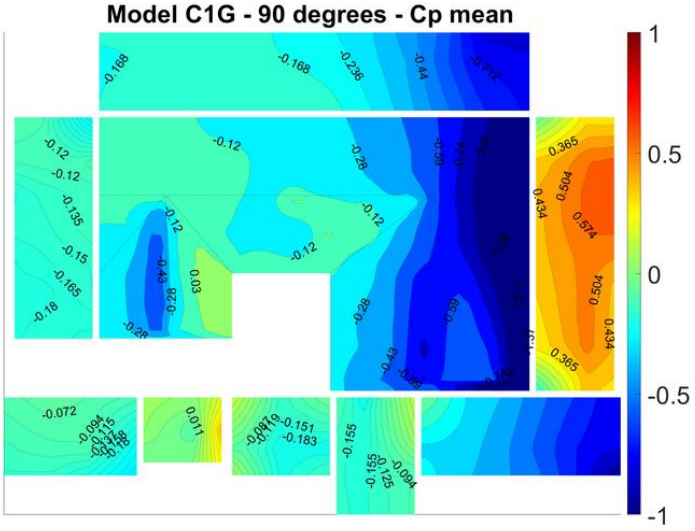
Model C1G - 90 degrees - Cp mean
1
0.5
0
-0.5
-1

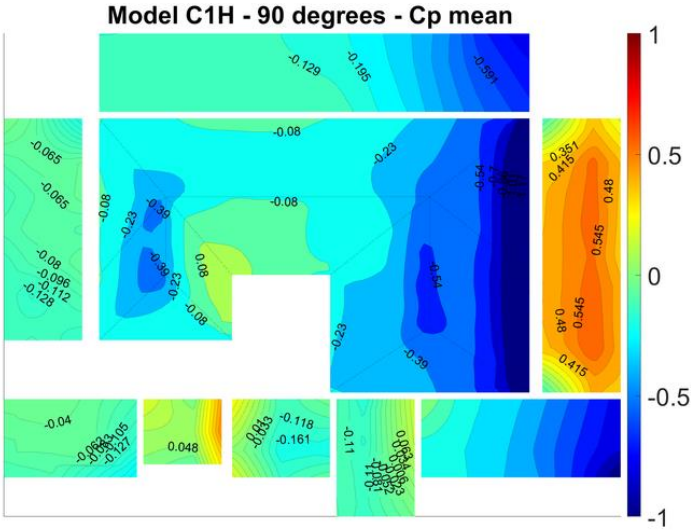
Model C1H - 90 degrees - Cp mean
1
0.5
0
-0.5
-1

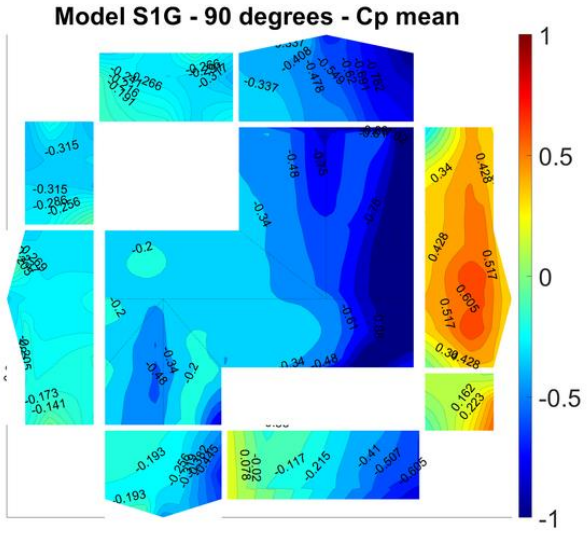
Model S1G - 90 degrees - Cp mean
1
0.5
0
-0.5
-1

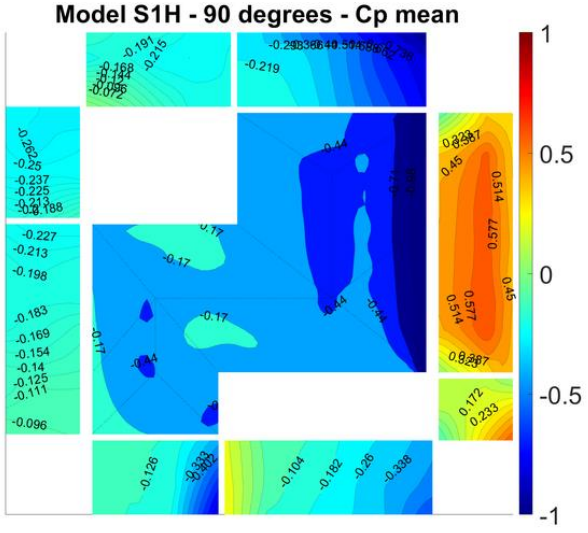
Model S1H - 90 degrees - Cp mean
1
0.5
0
-0.5
-1

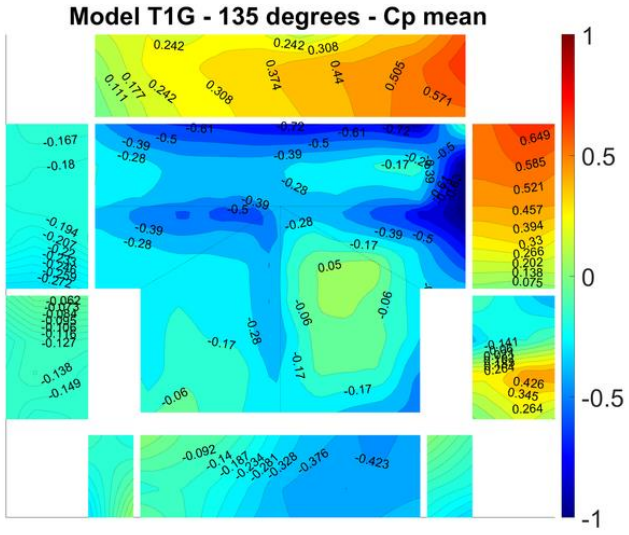
Model T1G - 135 degrees - Cp mean
1
0.5
0
-0.5
-1

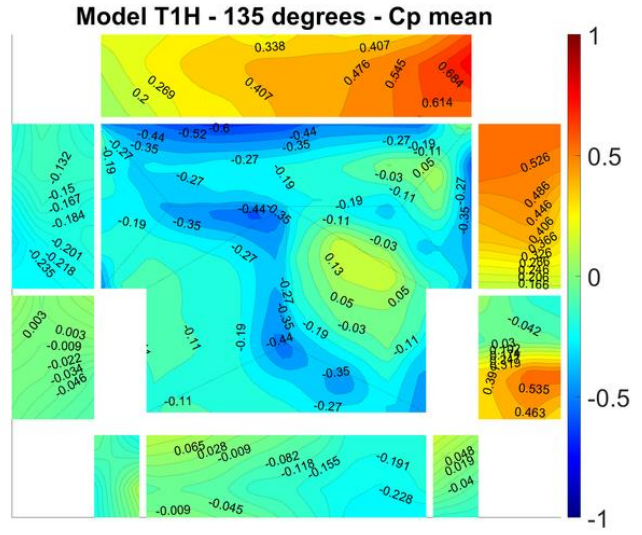
Model T1H - 135 degrees - Cp mean
1
0.5
0
-0.5
-1

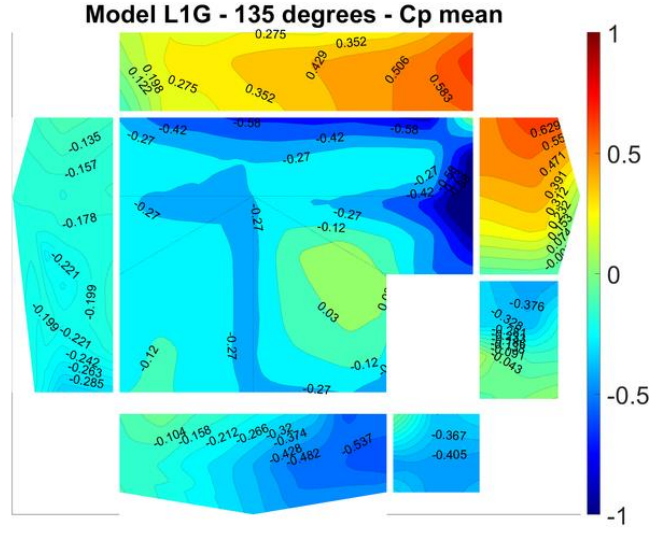
Model L1G - 135 degrees - Cp mean
1
0.5
0
-0.5
-1

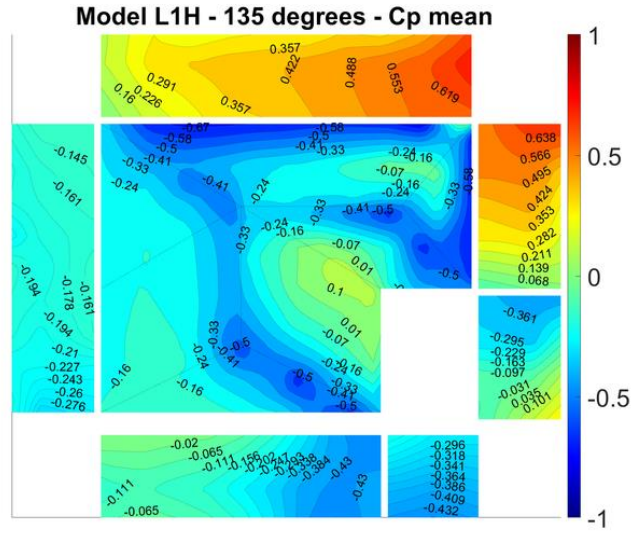
Model L1H - 135 degrees - Cp mean
1
0.5
0
-0.5
-1

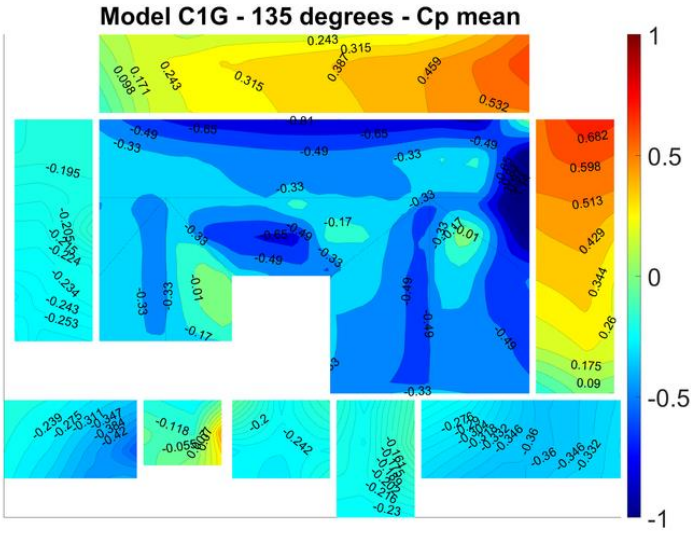
Model C1G - 135 degrees - Cp mean
1
0.5
0
-0.5
-1

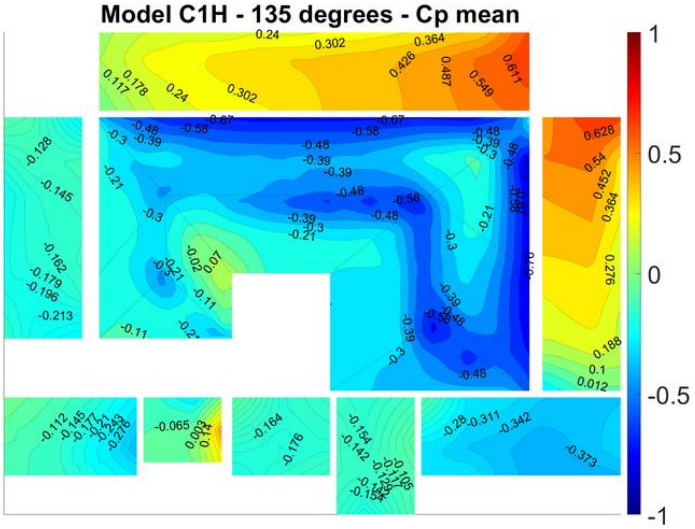
Model C1H - 135 degrees - Cp mean
1
0.5
0
-0.5
-1

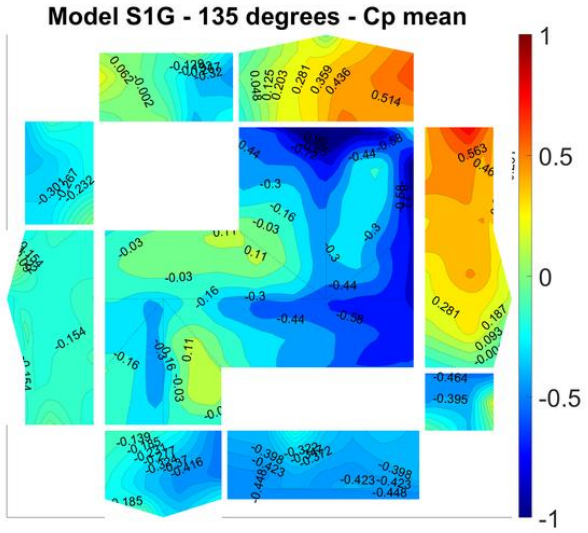
Model S1G - 135 degrees - Cp mean
1
0.5
0
-0.5
-1

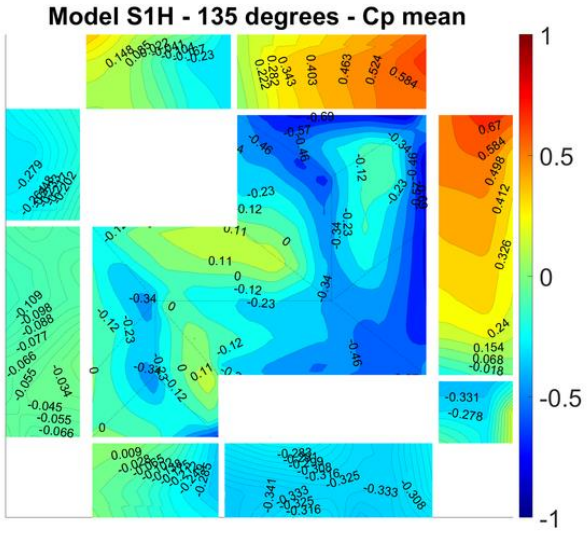
Model S1H - 135 degrees - Cp mean
1
0.5
0
-0.5
-1

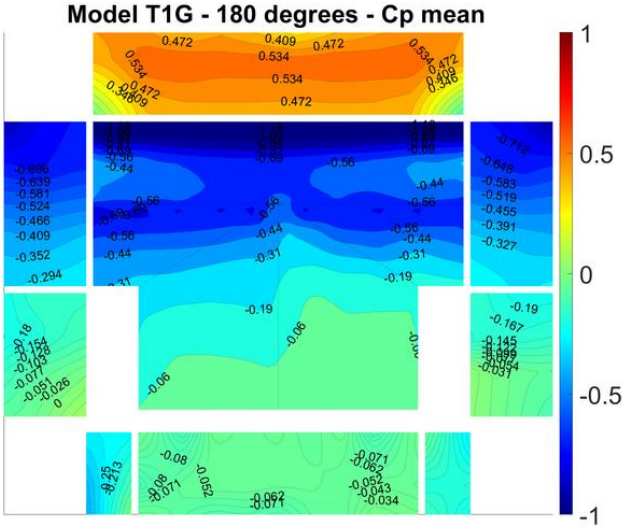
Model T1G - 180 degrees - Cp mean
1
0.5
0
-0.5
-1

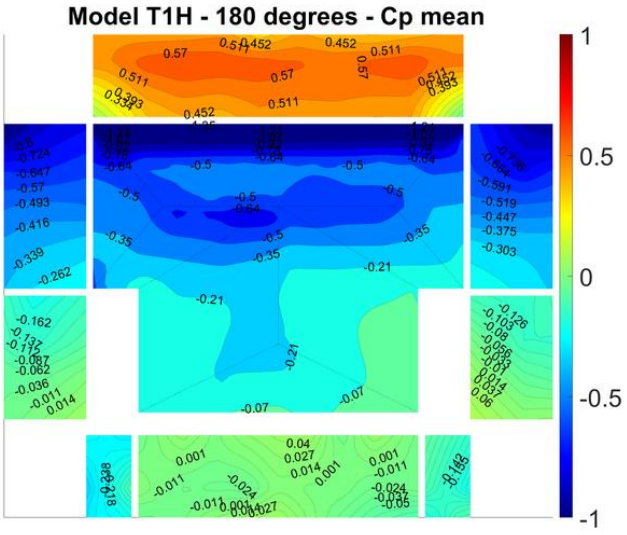
Model T1H - 180 degrees - Cp mean
1
0.5
0
-0.5
-1

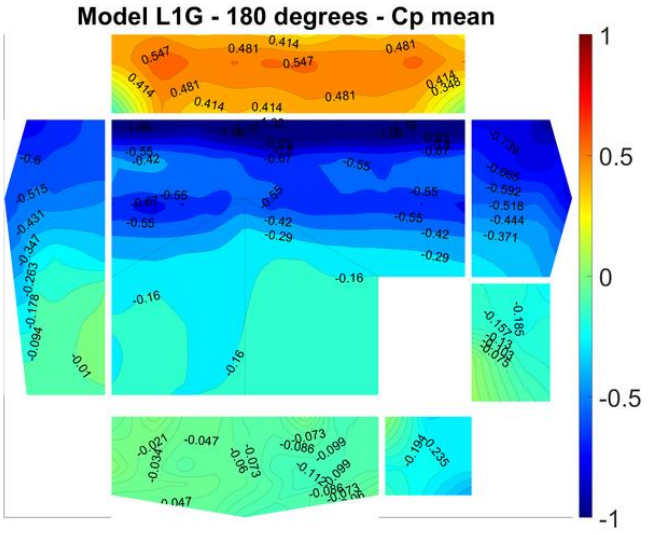
Model L1G - 180 degrees - Cp mean
1
0.5
0
-0.5
-1

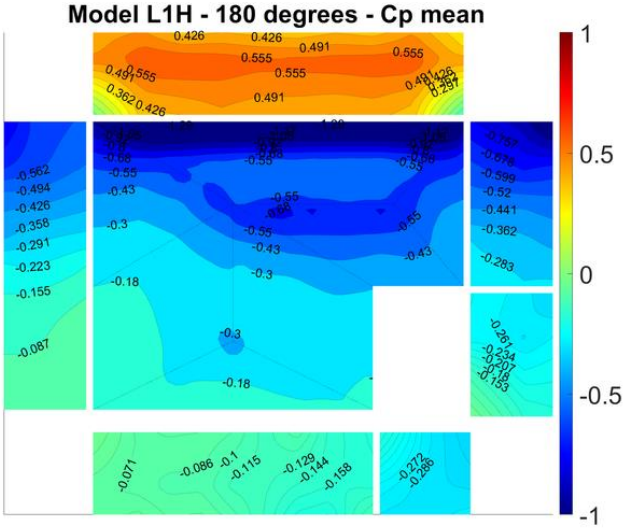
Model L1H - 180 degrees - Cp mean
1
0.5
0
-0.5
-1

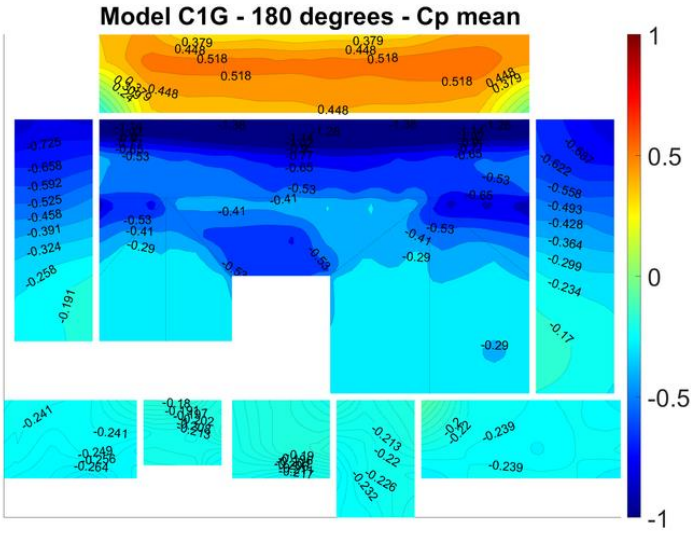
Model C1G - 180 degrees - Cp mean
1
0.5
0
-0.5
-1

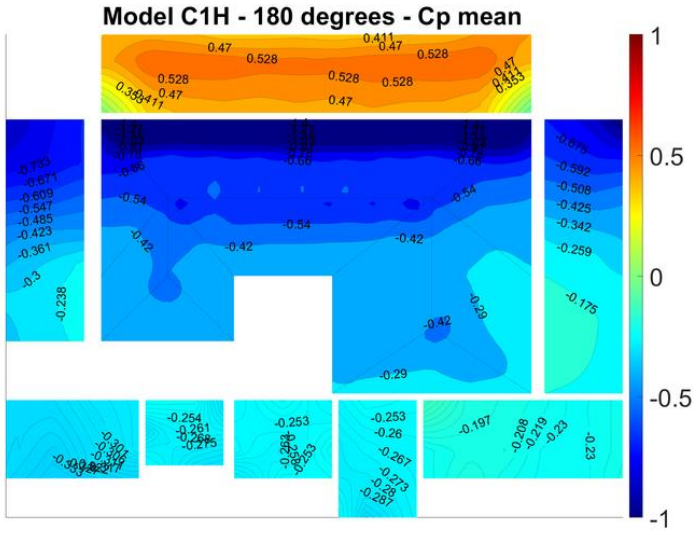
Model C1H - 180 degrees - Cp mean
1
0.5
0
-0.5
-1

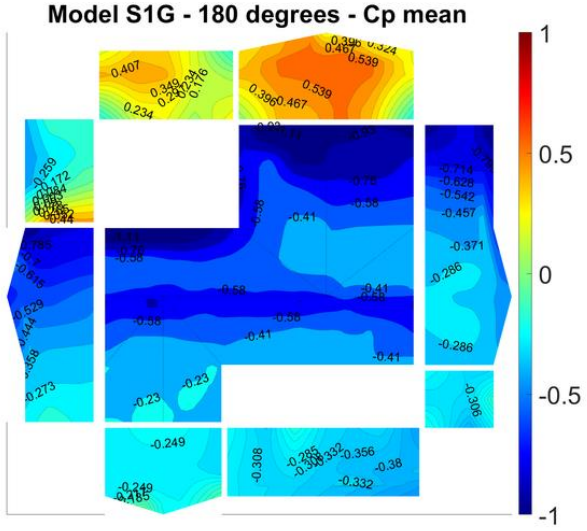
Model S1G - 180 degrees - Cp mean
1
0.5
0
-0.5
-1

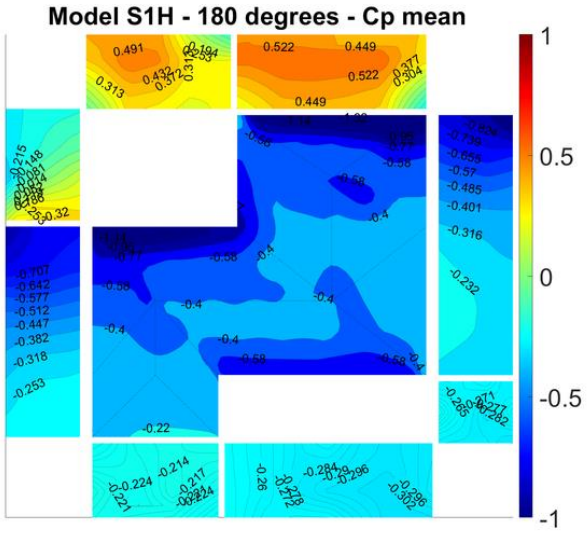
Model S1H - 180 degrees - Cp mean
1
0.5
0
-0.5
-1

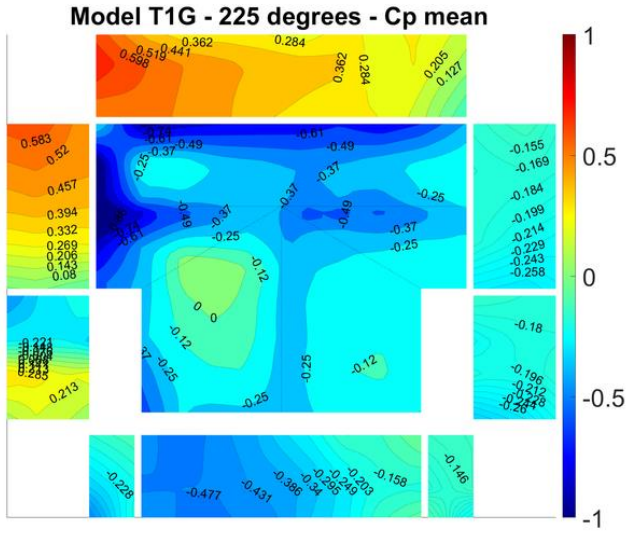
Model T1G - 225 degrees - Cp mean
1
0.5
0
-0.5
-1

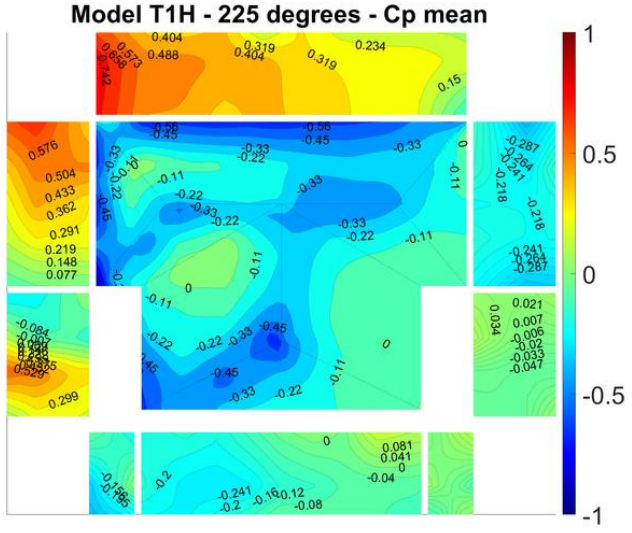
Model T1H - 225 degrees - Cp mean
1
0.5
0
-0.5
-1

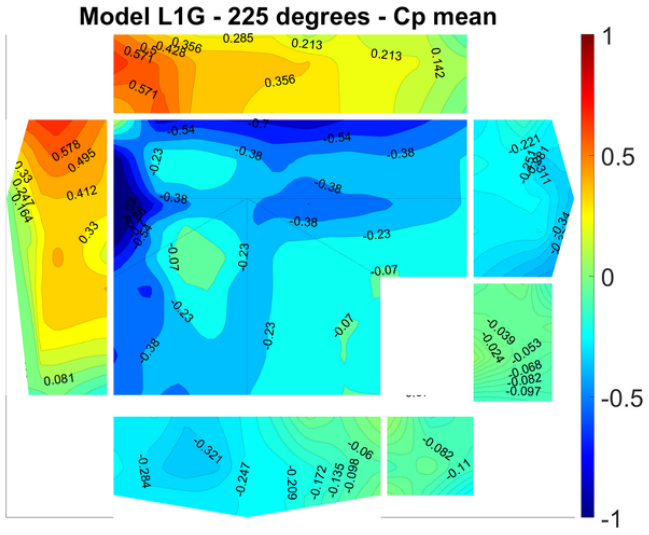
Model L1G - 225 degrees - Cp mean
1
0.5
0
-0.5
-1

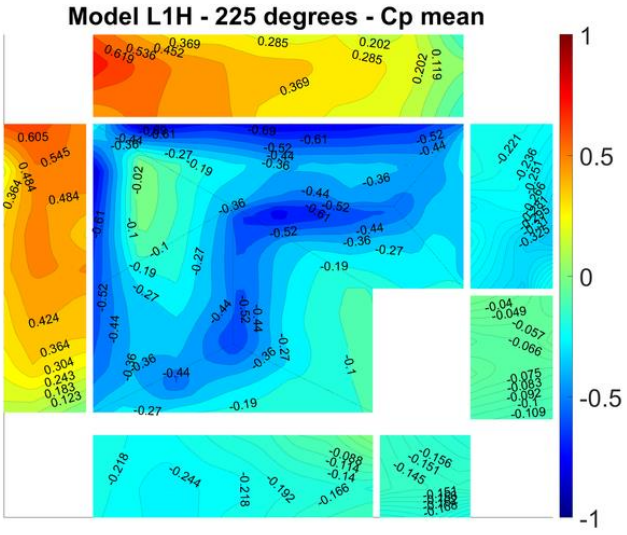
Model L1H - 225 degrees - Cp mean
1
0.5
0
-0.5
-1

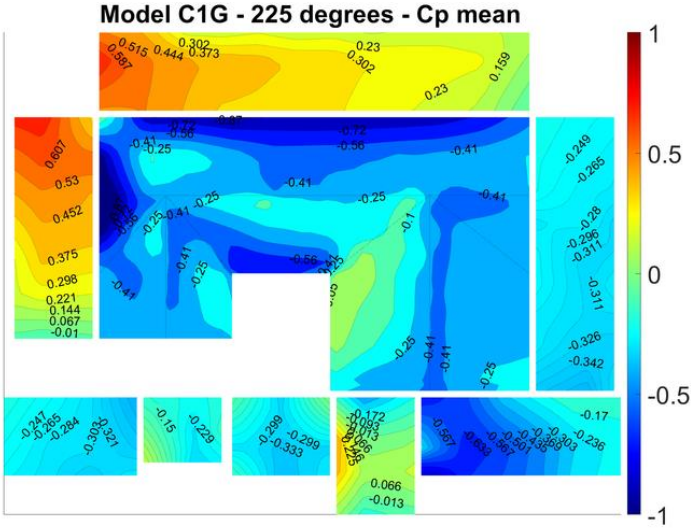
Model C1G - 225 degrees - Cp mean
1
0.5
0
-0.5
-1

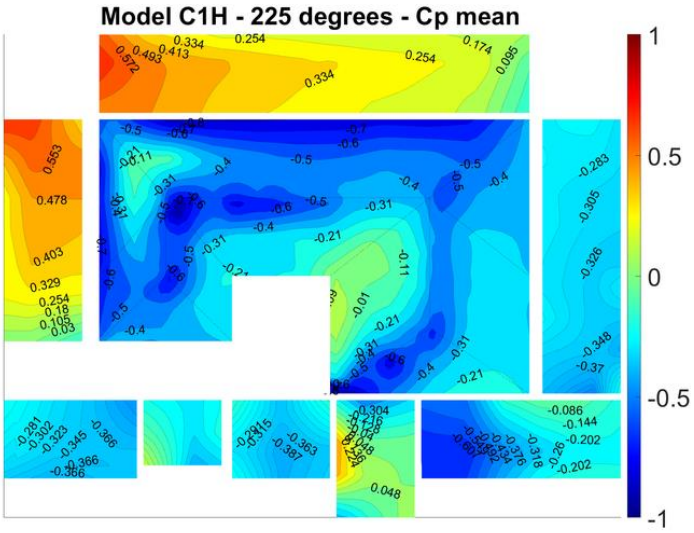
Model C1H - 225 degrees - Cp mean
1
0.5
0
-0.5
-1

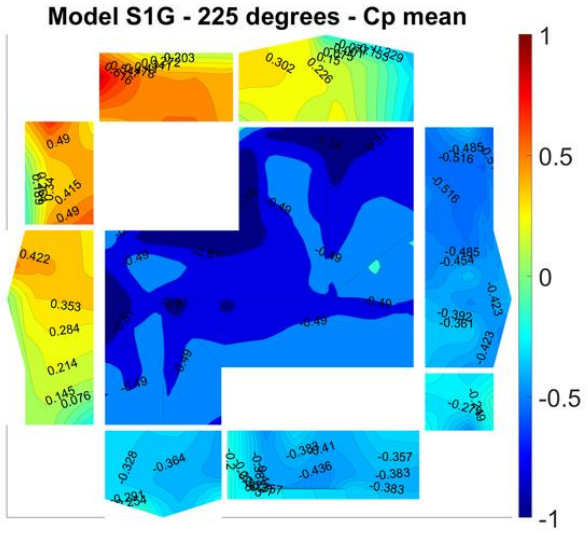
Model S1G - 225 degrees - Cp mean
1
0.5
0
-0.5
-1

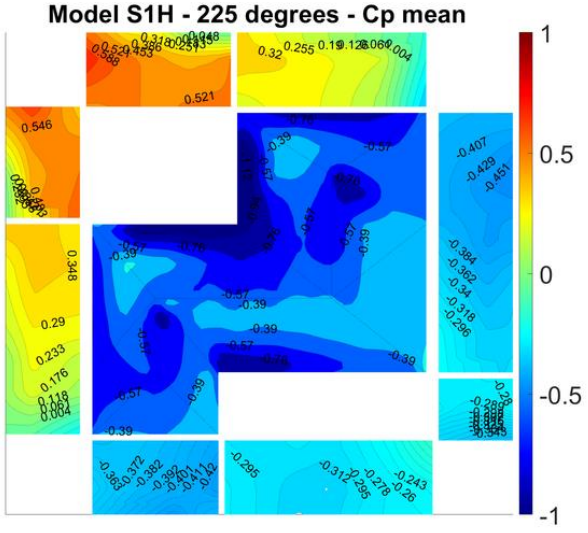
Model S1H - 225 degrees - Cp mean
1
0.5
0
-0.5
-1

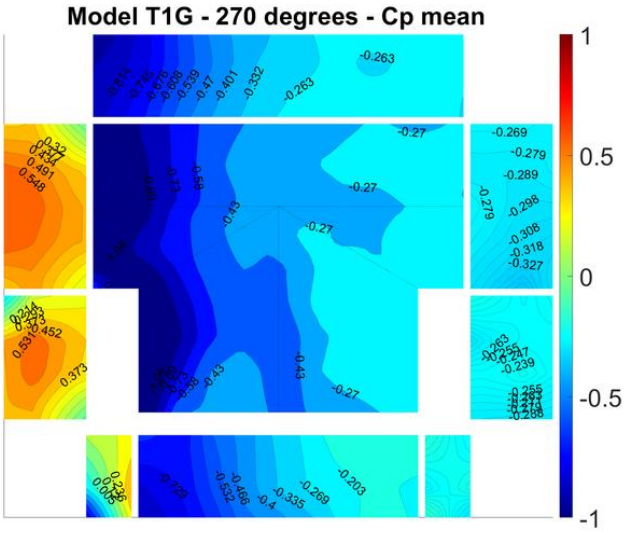
Model T1G - 270 degrees - Cp mean
1
0.5
0
-0.5
-1

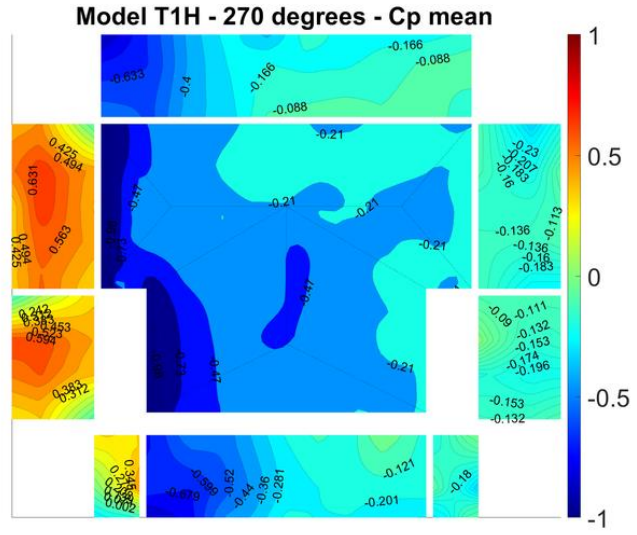
Model T1H - 270 degrees - Cp mean
1
0.5
0
-0.5
-1

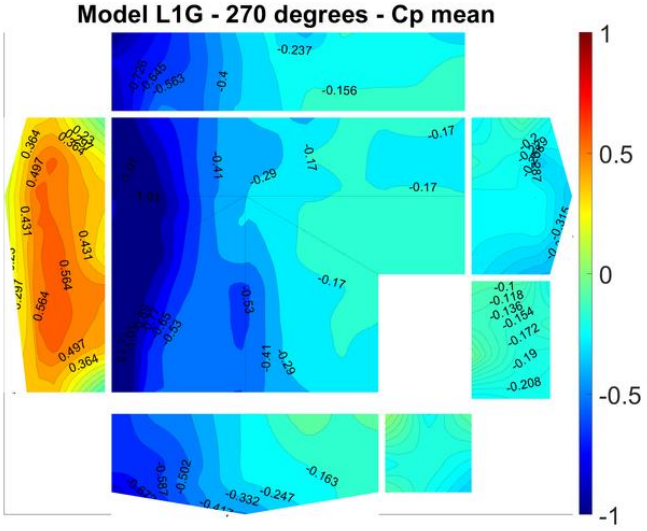
Model L1G - 270 degrees - Cp mean
1
0.5
0
-0.5
-1

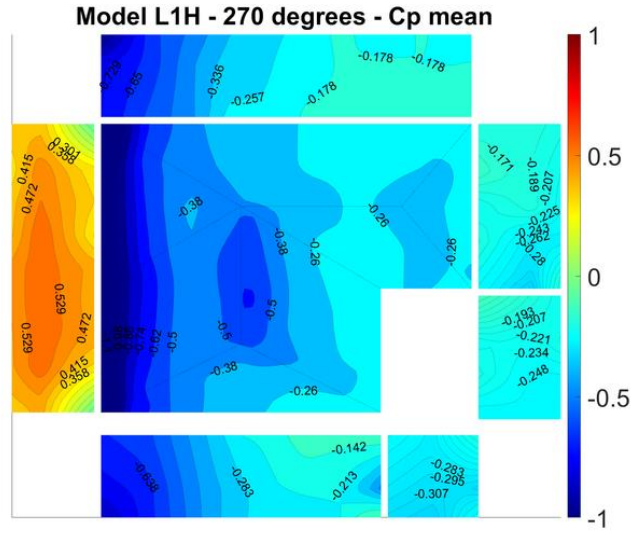
Model L1H - 270 degrees - Cp mean
1
0.5
0
-0.5
-1

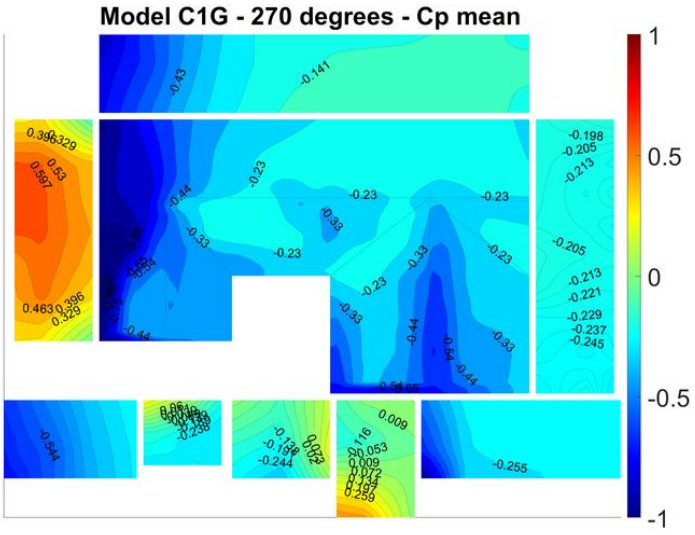
Model C1G - 270 degrees - Cp mean
1
0.5
0
-0.5
-1

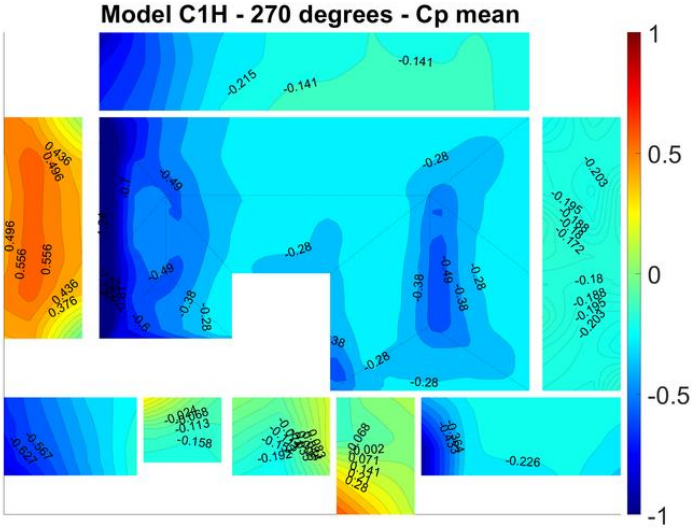
Model C1H - 270 degrees - Cp mean
1
0.5
0
-0.5
-1

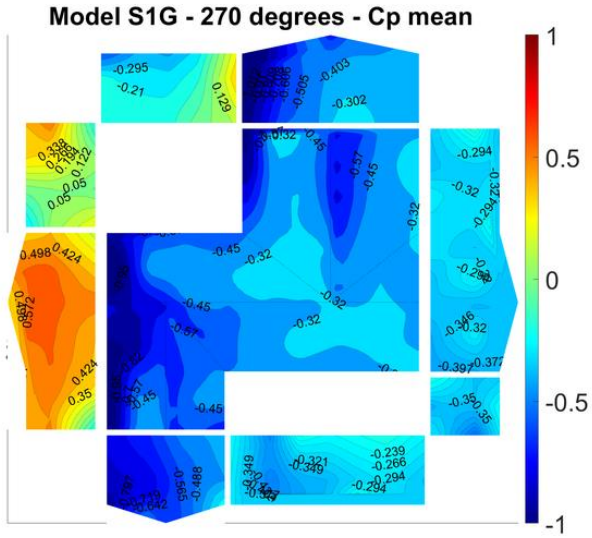
Model S1G - 270 degrees - Cp mean
1
0.5
0
-0.5
-1

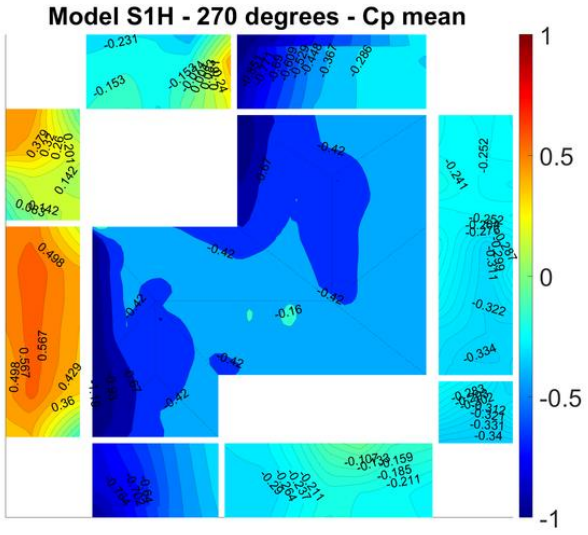
Model S1H - 270 degrees - Cp mean
1
0.5
0
-0.5
-1

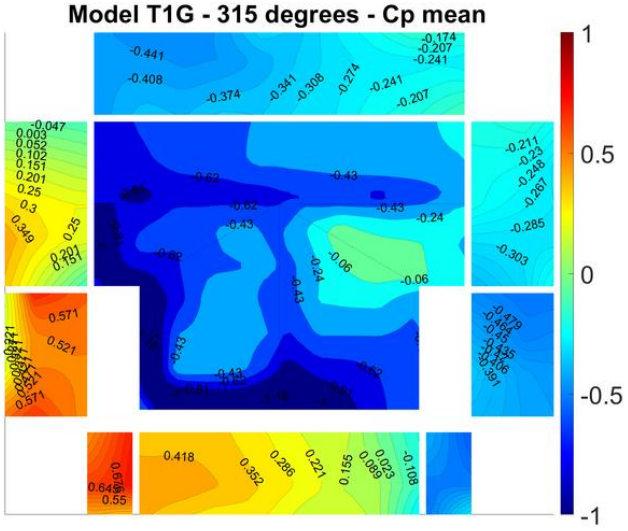
Model T1G - 315 degrees - Cp mean
1
0.5
0
-0.5
-1

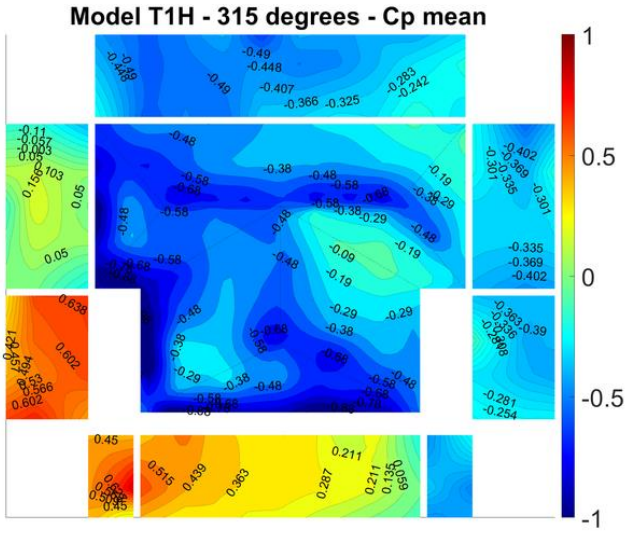
Model T1H - 315 degrees - Cp mean
1
0.5
0
-0.5
-1

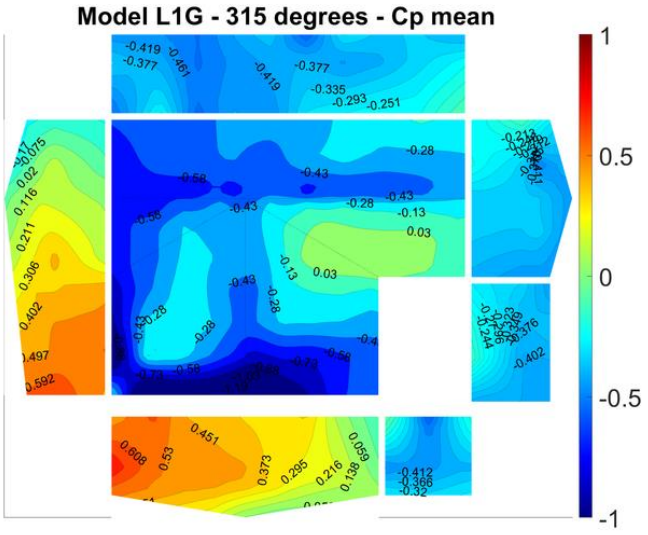
Model L1G - 315 degrees - Cp mean
1
0.5
0
-0.5
-1

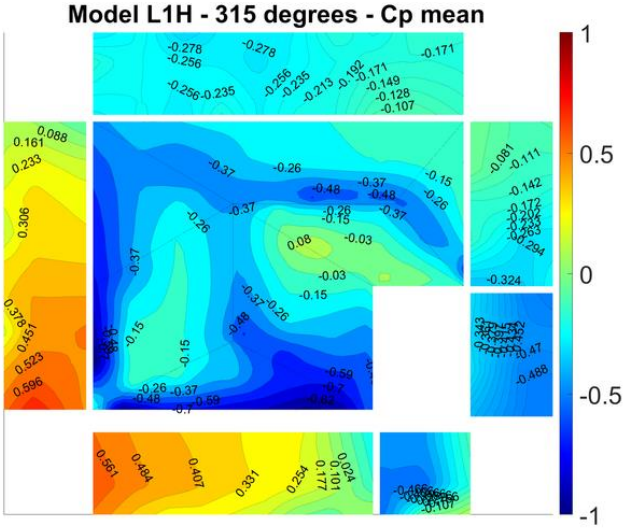
Model L1H - 315 degrees - Cp mean
1
0.5
0
-0.5
-1

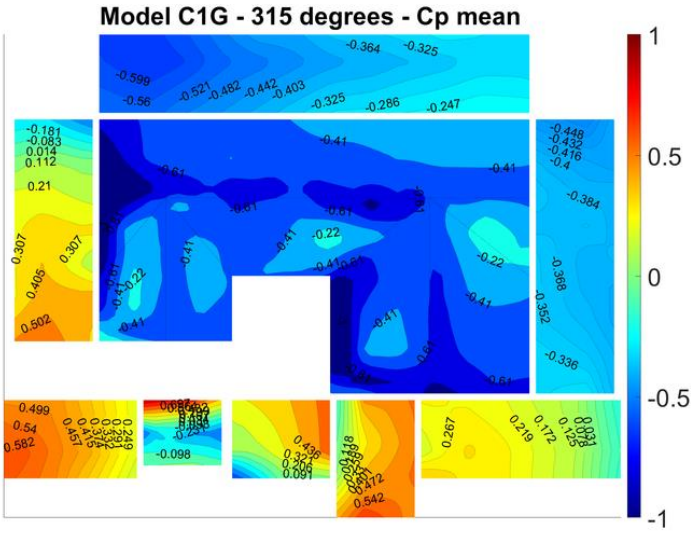
Model C1G - 315 degrees - Cp mean
1
0.5
0
-0.5
-1

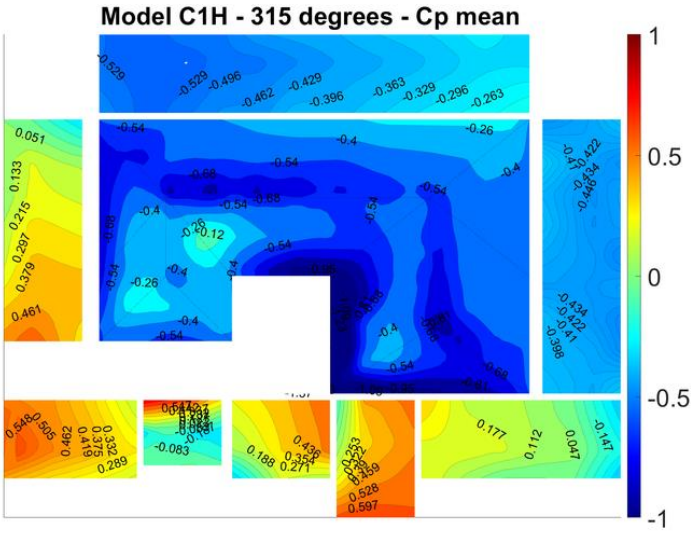
Model C1H - 315 degrees - Cp mean
1
0.5
0
-0.5
-1

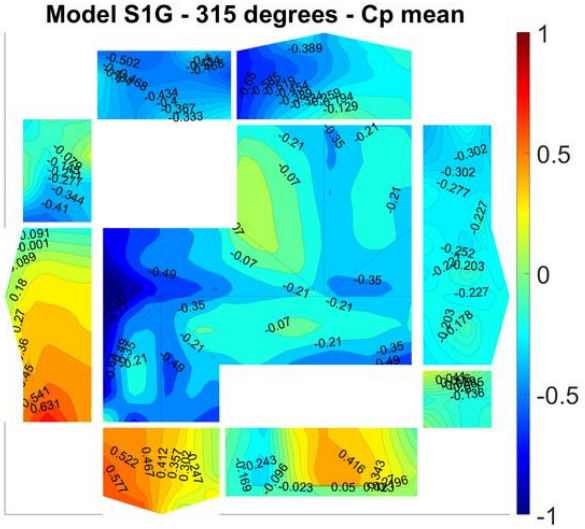
Model S1G - 315 degrees - Cp mean
1
0.5
0
-0.5
-1

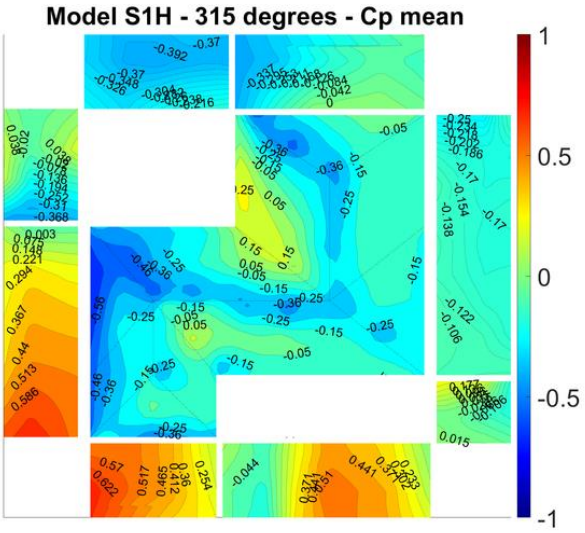
Model S1H - 315 degrees - Cp mean
1
0.5
0
-0.5
-1

VITA

MANUEL A. MATUS

Born, San Carlos, Chile

2014-2017	B.S., Civil Engineering (Structural Engineering) Florida International University Miami, Florida
2016-2017	Undergraduate Research Assistant Florida International University Miami, Florida
2017-2018	M.S., Civil Engineering (Structural Engineering) Florida International University Miami, Florida
2017-2021	Graduate Research Assistant Florida International University Miami, Florida
2018-2023	Doctoral Candidate (Structural Engineering) Florida International University Miami, Florida
2021	Research Specialist Wall of Wind Experimental Facility, Florida International University Miami, Florida

PUBLICATIONS AND PRESENTATIONS

Matus, M. 2018. "Experimental Investigation of Wind-Induced Response of Span-Wire Traffic Signal Systems." Florida International University (FIU) Electronic Theses and Dissertations. http://doi.org/10.25148/etd.FIDC006546.

Azzi, Z. Elawady, A. Matus, M., Zisis, I., Irwin, P. 2019. "Buffeting Response of Span-Wire Traffic Signals using Large-Scale Aeroelastic Wind Testing." Proceedings of the 15th International Conference on Wind Engineering, Beijing, China.

Zisis, I. Irwin, P., Chowdhury, A.G., Azizinamini, A., Matus, M., Berlanga, B., Azzi, Z., Estephan, J. 2019. "Development of a Test Method for Assessing the Performance of Vehicular Traffic Signal Assemblies during Hurricane Force Winds." Submitted to Florida Department of Transportation Research Center, Final Report BVD29 977-20, March 2019.

Zisis, I. Irwin, P., Chowdhury, A.G., Matus, M., Azzi, Z., Estepha, J., Hajra, B. 2019. “Assessment of the Performance of Vehicular Traffic Signal Assemblies during Hurricane Force Winds.” Submitted to Florida Department of Transportation Research Center, Final Report BVD29 977-27, March 2019.

Matus, M., Zisis, I. 2020. “Parametric Study to Investigate Span-Wire Traffic Signal System Performance,” Submitted to Transportation Research Board as a Final Report for the Grant Award 693JJ32045135.

Azzi, Z. Matus, M., Elawady, A., Zisis, I., Irwin, P., Chowdhury, A.G. 2020. “Aeroelastic Testing of Span-Wire Traffic Signal Systems.” Frontiers in Built Environment. https://doi.org/10.3389/fbuil.2020.00111.

Yin, Z., Matus, M., Zisis, I., Leon A. 2021. “Numerical Investigation on the Wind-Excited Dynamic Response of Span-Wire Traffic Signal Systems.” Journal of Fluids and Structures. http://doi.org/10.11648/j.fm.20220801.12.

Khandaker, M.A., Mohammadi, F.G., Matus, M., Shenavarmasouleh, F., Pereira, L.M., Zisis, I., Amini, Hadi. 2021. “Towards Real-time House Detection in Aerial Images Using Faster Region-based Convolutional Neural Network.” Journal of Engineering Applications of Artificial Intelligence. http://dx.doi.org/10.2139/ssrn.3994191.

Naeiji, A., Moravej, M., Matus, M., Zisis, I. 2022. “Codification Study of Wind-Induced Loads on Canopies Attached to Mid-Rise Buildings.” Journal of Wind Engineering and Industrial Aerodynamics, Volume 227. https://doi.org/10.1016/j.jweia.2022.105050.

Zisis, I., Matus, M., Hajra, B., Irwin, P. 2022. “Development and Validation of a Test Method to Assess the Wind-Induced Response of Span Wire Traffic Signal Systems.” Journal of Sustainable and Resilient Infrastructure. https://doi.org/10.1080/23789689.2022.2123143

Sarma, H.D., Matus, M., Zisis, I. 2023. “Effect of Roof Shape on Wind Vulnerability of Roof Sheathing Panels.” Journal of Structural Safety, Volume 100, January 2023, 102283. http://doi.org/10.1016/j.strusafe.2022.102283.